

Pre-normative research for safety of hydrogen driven vehicles and transport through tunnels and similar confined spaces

Fuel Cells and Hydrogen Joint Undertaking (FCH JU)
Grant Agreement Number 826193

Deliverable 4.3 Final report on analytical, numerical and experimental studies on explosions, including innovative prevention and mitigation strategies

Lead authors: HSE (W. Rattigan, K. Moodie)

Contributing authors: UU (V. Molkov, D. Makarov, D. Cirrone, V. Shenstov, S. Kashkarov)

KIT (Z. Xu, M. Kuznetsov)

NCSR (A. Venetsanos, S. Gianissi, I. Tolias)

USN (K. Vågsæther)

HSE (W. Rattigan, K. Moodie)

CEA (D. Bouix, G. Bernard-Michel)

PS (J. Grune)

Version: 220218

Delivery date for internal review: 18 February 2022

Due date: 28 February 2022

Dissemination level: Public



FUEL CELLS AND HYDROGEN
JOINT UNDERTAKING

D4.3. Final report on analytical, numerical and experimental studies on explosions, including innovative prevention and mitigation strategies

Deliverable administration					
Work Package	WP4 Explosion prevention and mitigation				
N. and title	D4.3 (D13) Final report on analytical, numerical and experimental studies on explosions, including innovative prevention and mitigation strategies (M36, HSE)				
Type	Report				
Status	Draft/Working/Released	Due	M36	Date	28/02/22
Comments					
Development and revision					
Version N.	Date	Authors		Description	
220204	04-02-22	W. Rattigan (HSE)		1 st Draft based on M4.3	
220204	04-02-22	D. Bioux (CEA)		Updated contribution to CEA subtasks	
220204	04-02-22	J. Lundberg (USN)		Updated contribution to task 4.4.4	
220204	04-02-22	K. Vågsæther (USN)		Updated contribution to task 4.3	
220204	04-02-22	S. Gianissi (NCSRD)		Updated contribution to task 4.3	
220215	15-02-22	V. Shenstov (UU)		Updated contribution to task 4.4.9	
220218	18-02-22	E. Studer (CEA)		Updated contribution to task 4.4.1	
220224	24-02-22	L. Giuliani (DTU)		Updated contribution to task 4.3	
220226	26-02-22	D. Cirrone, S. Kashkarov (UU)		Internal review	
220228	28-02-22	A. Venetsanos		Internal Review	

Disclaimer

Despite the care that was taken while preparing this document the following disclaimer applies: the information in this document is provided as is and no guarantee or warranty is given that the information is fit for any particular purpose. The user thereof employs the information at his/her sole risk and liability.

The document reflects only the authors' views. The FCH JU and the European Union are not liable for any use that may be made of the information contained therein.

Acknowledgments

This project has received funding from the Fuel Cells and Hydrogen 2 Joint Undertaking (JU) under grant agreement No 826193. The JU receives support from the European Union's Horizon 2020 research and innovation programme and United Kingdom, Germany, Greece, Denmark, Spain, Italy, Netherlands, Belgium, France, Norway, Switzerland.



FUEL CELLS AND HYDROGEN
JOINT UNDERTAKING

D4.3. Final report on analytical, numerical and experimental studies on explosions, including innovative prevention and mitigation strategies

Summary

The HyTunnel-CS project aims to conduct internationally leading pre-normative research (PNR) to close knowledge gaps and technological bottlenecks in the provision of safety and acceptable level of risk, in the use of hydrogen and fuel cell cars as well as hydrogen delivery transport in underground transportation systems. Work Package 4 (WP4) of HyTunnel-CS will focus on the investigation of hydrogen releases and their subsequent ignition within underground transportation systems.

This document presents the deliverable (D4.3) on the results of experimental, analytical and numerical studies regarding releases and explosions in tunnels and other confined spaces.

Keywords

Hydrogen safety; hazards; consequence assessment; unignited release; jet fire; deflagration; detonation; quantitative risk assessment; hydrogen in tunnel; explosion; mitigation; engineering correlation; numerical simulation; experiment; tunnel safety; ventilation; water mist; hydrogen vehicle; hydrogen dispersion; hydrogen combustion.

Nomenclature and abbreviation

BLEVE	Boiling Liquid Expanding Vapor Explosion
FRR	Fire resistance rating
DDT	Deflagration-to-Detonation Transition
DNS	Direct Numerical Simulations
HPV	Hydrogen Powered Vehicle
HRR	Heat Release Rate
LES	Large Eddy Simulations
LFL	Lower Flammability Limit
LNB	Leak-no-burst
MIE	Minimum Ignition Energy
NTP	Normal Temperature and Pressure
PIARC	Permanent International Association of Road Congresses
PNR	Pre-Normative Research
PPP	Pressure Peaking Phenomena
QRA	Quantitative Risk Assessment
RUD	Run-Up Distance
SF	Safety
TPRD	Thermal Pressure Relief Device
UFL	Upper Flammability Limit

Definitions

Accident is an unforeseen and unplanned event or circumstance causing loss or injury.

Flammability range is the range of concentrations between the lower and the upper flammability limits. *The lower flammability limit (LFL)* is the lowest concentration of a combustible substance in a gaseous oxidizer that will propagate a flame. *The upper flammability limit (UFL)* is the highest concentration of a combustible substance in a gaseous oxidizer that will propagate a flame.

Deflagration is the phenomenon of combustion zone propagation at the velocity lower than the speed of sound (sub-sonic) into a fresh, unburned mixture.

Detonation is the process of combustion zone propagating at the velocity higher than the speed of sound (supersonic) in the unreacted mixture.

Fire resistance rating is a measure of time for which a passive fire protection system can withstand a standard fire resistance test.

Harm is physical injury or damage to health.

Hazard is any potential source or condition that has the potential for causing damage to people, property and the environment.

Hazard distance is a distance from the (source of) hazard to a determined (by physical or numerical modelling, or by regulation) physical effect value (normally, thermal or pressure) that may lead to a harm condition (ranging from “no harm” to “max harm”) to people, equipment or environment.

D4.3. Final report on analytical, numerical and experimental studies on explosions, including innovative prevention and mitigation strategies

Hydrogen safety engineering is the application of scientific and engineering principles to the protection of life, property and the environment from adverse effects of incidents/accidents involving hydrogen.

Incident is something that occurs casually in connection with something else.

Limiting oxygen index is the minimum concentration of oxygen that will support flame propagation in a mixture of fuel, air, and nitrogen.

Mach disk is a strong shock normal to the under-expanded jet flow direction.

Minimum ignition energy of flammable gases and vapours is the minimum value of the electric energy, stored in the discharge circuit with as small a loss in the leads as possible, which (upon discharge across a spark gap) just ignites the quiescent mixture in the most ignitable composition. For a given mixture composition the following parameters of the discharge circuit must be varied to get the optimum conditions: capacitance, inductivity, charging voltage, as well as shape and dimensions of the electrodes and the distance between electrodes.

Normal temperature and pressure (NTP) conditions are temperature 293.15 K and pressure 101.325 kPa.

Permeation is the movement of atoms, molecules, or ions into or through a porous or permeable substance.

Separation distance is the minimum separation between a hazard source and an object (human, equipment or environment) which will mitigate the effect of a likely foreseeable incident and prevent a minor incident escalating into a larger incident.

D4.3. Final report on analytical, numerical and experimental studies on explosions, including innovative prevention and mitigation strategies

Table of contents

Summary	3
Keywords	3
Nomenclature and abbreviation	4
Definitions.....	4
Table of contents.....	6
List of figures	14
List of tables	21
1 Introduction	23
1.1 Work Package overview	23
1.1.1 Structure and synergy with HyTunnel-CS work plan	23
2 Analytical studies, development, and validation of engineering correlations (Task 4.2 / UU) 25	
2.1 Engineering models for assessment of blast wave and fireball of hydrogen tank rupture (4.2, UU).....	25
2.1.1 Universal correlation of blast wave attenuation in a tunnel	25
2.1.1.1 Background.....	25
2.1.1.2 Problem formulation	25
2.1.1.3 Dimensionless variables	26
2.1.1.4 Contribution of energies	26
2.1.1.5 Graphical determination of blast wave decay in tunnels.....	27
2.1.2 Fireball model	28
2.1.2.1 The analysis of experiments	28
2.1.2.2 Fireball in open space.....	30
2.1.2.3 Fireball in tunnel.....	32
2.1.2.4 Simulation of fireball in a tunnel	33
2.1.2.5 Conclusions.....	36
2.2 Engineering model for assessment of overpressure during spurious hydrogen release (4.2, UU)	37
2.2.5 Background	37
2.2.6 Validation experiments	37
2.2.7 The similitude analysis.....	37
2.2.8 Results and discussion.....	38
2.2.8.1 Concluding remarks.....	39

D4.3. Final report on analytical, numerical and experimental studies on explosions, including innovative prevention and mitigation strategies	
2.3 Engineering tool for prevention and mitigation of composite hydrogen storage tank explosion in a fire (4.2, UU)	39
2.3.5 Background	39
2.3.6 Effect of heat release rate on fire rupture resistance	39
2.3.7 Parametric study of effect of TPRD diameter and time of TPRD initiation on tank rupture	41
2.4 Correlation for DDT in horizontal and vertical ventilation systems with non-uniform hydrogen-air mixtures in the presence of obstacles (4.2, KIT)	42
2.4.5 Introduction	42
2.4.6 Nomenclature	43
2.4.7 Model description	43
2.4.8 Option 1: Uniform hydrogen concentration distributed over the full tunnel cross-section for the given hydrogen inventory	53
2.4.8.1 Input data	53
2.4.8.2 Calculation procedure	54
2.4.8.3 Output values	57
2.4.9 Option 2: Uniform hydrogen concentration distributed inside a layer of hydrogen-air mixture for the given hydrogen inventory	57
2.4.9.1 Input data	58
2.4.9.2 Calculation procedure	58
2.4.9.3 Output values	59
2.4.10 Option 3: Stratified layer of hydrogen-air mixture for the given hydrogen inventory	60
2.4.10.1 Input values	60
2.4.10.2 Calculation procedure	61
2.4.10.3 Output values	62
2.4.11 Option 4: Stratified hydrogen-air mixture filled the whole tunnel cross-section for the given hydrogen inventory	63
2.4.11.1 Input values	64
2.4.11.2 Calculation procedure	64
2.4.11.3 Output values	65
2.4.12 Conversion units	66
2.5 Analytical model for water spray/mist system effect on hydrogen combustion and a shock wave attenuation (4.2, KIT)	67
2.5.1 Background	67
2.5.2 Objectives	67
2.5.3 Knowledge gaps and accident scenarios assessed	68

D4.3. Final report on analytical, numerical and experimental studies on explosions, including innovative prevention and mitigation strategies

2.5.4	Engineering model development.....	68
2.5.4.1	Water spray model.....	68
2.5.4.2	Droplet breakup model	71
2.5.5	Discussion	72
2.5.6	Application of research findings	72
3	Numerical studies (Task 4.3 / NCSR D).....	73
3.1	Deflagration of non-uniform hydrogen-air cloud created by release in HSE tunnel experiments Task 4.4 (4.3, NCSR D).....	73
3.1.5	Introduction	73
3.1.6	Simulations details	73
3.1.7	Empty tunnel case	74
3.1.7.1	Examined deflagration cases.....	74
3.1.7.2	Deflagration results	75
3.1.8	Non-empty tunnel case.....	78
3.1.8.1	Examined scenarios.....	78
3.1.8.2	Deflagration results	80
3.1.9	Conclusions	84
3.2	Deflagration of non-uniform hydrogen-air cloud created by release in tunnel (4.3, KIT) 85	
3.2.5	Background	85
3.2.6	Objectives.....	85
3.2.7	Knowledge gaps and accident scenarios assessed.....	85
3.2.8	Numerical simulation development	85
3.2.9	Validation / optimisation.....	85
3.2.10	Results	85
3.2.10.1	Without tunnel ventilation.....	85
3.2.10.2	With tunnel ventilation	88
3.2.10.2.1	COM3D code	88
3.2.10.2.2	Modelling of the tunnel.....	89
3.2.10.2.3	Main results.....	91
3.2.11	Conclusions	95
3.3	Numerical Study of deflagration interaction with mist systems (4.3, NCSR D)	96
3.3.5	Introduction – literature review.....	96
3.3.6	Examined cases	97
3.3.7	Simulation details.....	97

D4.3. Final report on analytical, numerical and experimental studies on explosions, including innovative prevention and mitigation strategies	
3.3.8 Simulation results.....	98
3.3.9 Conclusions.....	99
3.4 Simulation of water injection effect on shock wave attenuation (4.3, KIT)	99
3.4.5 Background	99
3.4.6 Simulation code.....	100
3.4.7 Modelling	100
3.4.8 Results	103
3.4.8.1 Hydrogen distribution	103
3.4.8.2 Pressure	106
3.4.9 Conclusions	110
3.5 Simulation of water injection effect on shock wave attenuation validation against experiments (4.3, KIT)	110
3.5.5 Background	110
3.5.6 Objectives.....	110
3.5.7 Knowledge gaps and accident scenarios assessed.....	110
3.5.8 Numerical simulation development	111
3.5.9 Validation / optimisation.....	111
3.5.10 Simulation of shockwave attenuation tests in A2 vessel.....	112
3.5.10.1 Numerical Models	113
3.5.10.2 Detonation with spray off	114
3.5.10.3 Shockwave attenuation by mist	115
3.5.11 Conclusions	116
3.6 Analysis of the interaction between absorbing materials and systems and shock wave attenuation (4.3, KIT).....	116
3.6.5 Background	116
3.6.6 Objectives.....	116
3.6.7 Methodology	116
3.6.8 Models.....	117
3.6.9 Results	117
3.7 Pre-test simulations and parametric study to find out the maximum allowed hydrogen inventory to mitigate the effect of blast wave and fireball (4.3, CEA/ NCSRD/ UU).....	118
3.7.1 Pre-tests, background	118
3.7.1.1 CEA tests	118
3.7.1.2 HSE pre-tests	118
3.7.2 Parametric study	118

D4.3. Final report on analytical, numerical and experimental studies on explosions, including innovative prevention and mitigation strategies	
3.7.3 CFD model	121
3.7.4 Remarks from the CFD Study	122
3.8 Simulations to validate multi-phenomena turbulent burning velocity deflagration model (spurious release) (4.3, UU)	122
3.8.5 Background	122
3.8.6 Description of experiments	123
3.8.7 CFD model and numerical details	123
3.8.7.1 Unignited release modelling	123
3.8.7.2 Deflagration modelling	123
3.8.7.3 Numerical grid and details	124
3.8.8 Results and discussion	125
3.8.8.1 Unignited release	125
3.8.8.2 Deflagration	126
3.8.9 Concluding remarks	127
3.9 Coupled CFD/FEM modelling and simulation of a tunnel structure reaction to the blast (4.3, UU/ DTU)	127
3.9.1 Problem formulation	127
3.9.2 CFD Analysis (UU)	128
3.9.2.1 Numerical set-up	128
3.9.2.2 Computational results	128
3.9.3 FEM Analysis (DTU)	128
3.9.3.1 Object of the analysis	128
3.9.3.2 Input pressure and characterization of the dynamic regime	129
3.9.3.3 Implementation and validation of the model	132
3.9.3.3.1 Static validation	135
3.9.3.4 Outcomes of the analysis and evaluation of the results	137
3.9.3.5 Conclusions	139
3.10 Simulations of flame acceleration and transition to detonation in tunnel structures (4.3, USN)	141
3.10.5 Background and accident scenario	141
3.10.6 Objectives	141
3.10.7 Numerical simulation set-up	142
3.10.8 Results and conclusions	143
3.10.8.1 Effects of the concentration gradient	143
3.10.8.2 Effect of velocity gradient	143
3.10.9 Conclusion	144

D4.3. Final report on analytical, numerical and experimental studies on explosions, including innovative prevention and mitigation strategies

4	Experiments (Task 4.4 / HSE).....	144
4.1	Blast wave and fireball of tank rupture in tunnel: Demonstrations of car tank failure in fire experiments in one real tunnel (4.4.1, CEA)	144
4.1.5	Introduction	144
4.1.6	Test geometry	145
4.1.7	Test sequence and test matrix.....	146
4.1.8	Test results.....	149
4.1.8.1	Morphology of the fireballs.....	151
4.1.8.2	Fireball characteristics.....	153
4.1.9	Conclusions and recommendations	157
4.2	Blast wave and fireball of tank rupture in tunnel: Experiments utilising the experimental tubular steel “explosion” tunnel (4.4.1, HSE)	157
4.2.5	Background	157
4.2.6	Objectives.....	158
4.2.7	Description of test facilities.....	158
4.2.8	Scaling and accident scenarios assessed	159
4.2.8.1	Car.....	160
4.2.8.2	Bus	160
4.2.8.3	Train 1.....	160
4.2.8.4	Train 2.....	160
4.2.9	Tunnel scaling	160
4.2.9.1	Road tunnels.....	161
4.2.9.2	Rail tunnels	161
4.2.9.3	HSE Buxton test tunnel.....	161
4.2.10	Scaling criteria.....	161
4.2.11	Test rig for scaled releases	163
4.2.12	Scaling of airflow in HSE tunnel	167
4.2.12.1	Test programme	168
4.2.13	Expected results.....	169
4.3	Pressure decay after Hydrogen Tanks explosion tests in a full-scale tunnel.....	169
4.3.1	Introduction	169
4.3.2	Tunnel geometry, Measurement Devices and Experimental Matrix.....	170
4.3.3	Test results.....	173
4.3.4	Comparison with a correlation (Molkov & Dery, 2020).....	181
4.3.5	Conclusions and recommendations	185

D4.3. Final report on analytical, numerical and experimental studies on explosions, including innovative prevention and mitigation strategies	
4.4 Deflagration of non-uniform cloud in a tunnel: Experiments on deflagration of non-uniform hydrogen-air cloud created by release in mock-up tunnel sections (4.4.3, PS)	185
4.4.5 Background	185
4.4.6 Objectives.....	185
4.4.7 Knowledge gaps and accident scenarios assessed.....	186
4.4.8 Description	186
4.4.9 Results	188
4.4.9.1 Flame speed and combustion overpressure	188
4.4.9.2 Flame speed and combustion overpressure in non-uniform hydrogen-air mixtures	189
4.4.10 Influence of obstacles on stratified mixture combustion	190
4.5 Tests on effect of water sprays and mist systems on combustion and DDT (4.4.4, PS)	191
4.5.5 Background	191
4.5.6 Objectives.....	191
4.5.7 Knowledge gaps and accident scenarios assessed.....	191
4.5.8 Description	191
4.5.9 Results	192
4.5.10 Delivery timeline.....	192
4.6 Effect of droplet size on mitigation of combustion and DDT (4.4.4, USN)	193
4.6.5 Background	193
4.6.6 Materials and method	193
4.6.7 Results and discussion.....	194
4.6.8 Concluding remarks	200
4.7 Shock wave attenuation: tests on tank rupture in a tunnel with shock attenuation material / system (4.4.5, HSE)	201
4.7.5 Background	201
4.7.6 Delivery timeline.....	201
4.8 Shock wave attenuation: Experiments on the effect of water spray / mist system on shock wave attenuation (4.4.5, PS)	202
4.8.5 Background	202
4.8.6 Objectives.....	202
4.8.7 Knowledge gaps and accident scenarios assessed.....	202
4.8.8 Description	202
4.8.9 Results	203
4.8.10 Delivery timeline.....	203

D4.3. Final report on analytical, numerical and experimental studies on explosions, including innovative prevention and mitigation strategies

4.9	Shock wave attenuation: Tests on shock wave attenuation by using shock absorbing materials, soft bulkheads and sacrificial pre-evacuated volumes (4.4.5, PS)	203
4.9.5	Objectives	203
4.9.6	Description	204
4.9.7	Results	204
4.9.8	Delivery Timeline	204
4.10	Safety technology to prevent tank rupture: Development and manufacturing of four leak no burst composite type IV tanks prototypes for testing in a tunnel fire at CEA and HSE tunnels (4.4.6, UU).....	204
4.10.5	Introduction	204
4.10.6	Safety technology description	205
4.10.7	Proof of the successful technology operation in other projects	207
4.10.8	Design and manufacture of the LNB tank prototypes in HyTunnel-CS project	209
4.11	Safety technology to prevent tank rupture: Tests on prototypes of “leak no burst” composite type 4 tanks at CEA	212
4.11.1	Introduction	212
4.11.2	Test geometry	213
4.11.3	Description of the piping system.....	214
4.11.4	Description of the Burner	216
4.11.5	Measurement devices	218
4.11.6	Test sequence	220
4.11.7	Test results.....	221
4.11.8	Conclusions	230
5	References	231
	Appendices	241
	A1. Scaling criteria.....	241
	A1.1 Matching the mixing zone by choice of source momentum	242

List of figures

Figure 1. Relationship between peak overpressure and distance in tunnels of various lanes (1, 2 and 5), expressed by their dimensionless values, $P1$ and $L1$, respectively.....	28
Figure 2. Experimental fireball size versus mass of hydrogen: comparison with correlations..	32
Figure 3. Comparison of open space and inside the tunnel correlations.....	33
Figure 4. Simulated tunnel cross-section, tunnel drawing (left), simulated geometry (right). ..	34
Figure 5. Fireball dynamics in a tunnel with cross-section area 83 m ² (temperature contours): 2D tunnel centreline cross-section (left), 3D walls (right).....	35
Figure 6. Derived correlation for predicting overpressure from delayed ignition of turbulent hydrogen jets versus experiments.	39
Figure 7. Hydrogen storage tank FRR vs fire source HRR/A (Molkov et al., 2021).....	40
Figure 8. Tank rupture in a fire with varying HRR/A: 1 MW/m ² , 0.62 MW/m ² and 0.29 MW/m ² (tank volume 36 L, initial pressure 700 bar); dynamics of tank wall decomposition, load-bearing wall thickness and tank storage pressure (Molkov et al., 2021).	41
Figure 9. 36 L, 70MPa bar tank performance in a fire with blow-down through TPRD Ø0.45 mm and Ø0.65 mm, activation at 180 s after fire initiation - dynamics of tank wall decomposition front, load-bearing wall thickness, storage pressure and liner melting front (Molkov et al., 2021).....	42
Figure 10. Examples of cross-sections (mined road tunnels). Grey area is the total cross-section, A ; blue area is blocked by turbo-fans and/or by cars, A_i . $BR = \sum A_i/A$	44
Figure 11. Critical conditions for effective flame acceleration as function of expansion ratio vs. dimensionless vent area: sonic flame and detonations (open points); subsonic flame (solid points). Different spacing is labelled (Kuznetsov et al., 2011).	45
Figure 12. Hydrogen distribution profiles in a tunnel: a) front view; b) side view (Li et al., 2019).....	47
Figure 13. Typical geometry of hydrogen-air cloud inside the tunnel: uniform composition (left); stratified composition (right); fully filled cross-section (top); a semiconfined layer (bottom).....	50
Figure 14. Hydrogen distribution profiles in a tunnel vs. time after release: a) 1 s; b) 4 s; c) 8s; d) 16 s.	51
Figure 15. Logarithm of water flow rate in L/min as a function of hydrogen mass flow rate in kg/s.	70
Figure 16. Different droplet breakup modes depending on the Weber number.....	71
Figure 17. Numerical grid for the deflagration simulations of the empty tunnel case.....	73
Figure 18. Numerical grid for the deflagration simulations of the non-empty tunnel case.	74
Figure 19. Hydrogen volumes in the range of 4-75% (flammable volume), 25-35% and 32-42% as a function of time.	74
Figure 20. Hydrogen volumetric concentration (left) and the turbulent kinetic energy (right) at 4, 8, 12 and 16 s from the release start.	75
Figure 21. Effect of ignition position. Overpressure time series at 35, 40, 50 and 60 m, for two ignition positions, 36 and 38 m (ignition 4.0 s after the release).	76
Figure 22. Effect of ignition delay. Overpressure time series at 35, 40, 50 and 60 m, for two different ignition times, 4.0 and 8.0 s (ignition at 38 m).....	77
Figure 23. Temperature (left) and the overpressure (right) at 0.20, 0.25, 0.30, 0.35, 0.40, 0.45 s from the ignition (ignition at 38 m, 8.0 s after the release).....	78

D4.3. Final report on analytical, numerical and experimental studies on explosions, including innovative prevention and mitigation strategies

Figure 24. Effect of ignition position. Overpressure time series at 35, 40, 50 and 60 m, for two ignition positions, 36 and 38 m (ignition 4.0 s after the release).	78
Figure 25. Effect of ignition delay. Overpressure time series at 35, 40, 50 and 60 m, for two different ignition times, 4.0 and 8.0 s (ignition at 38 m).....	79
Figure 26. Temperature (left) and the overpressure (right) at 0.20, 0.25, 0.30, 0.35, 0.40, 0.45 s from the ignition (ignition at 38 m, 8.0 s after the release).	80
Figure 27. Effect of ignition position. Overpressure time series at 35, 40, 50 and 60 m, for ignition at 38 and 42 m (4.0 s ignition delay).	81
Figure 28. Effect of ignition time. Overpressure time series at 35, 40, 50 and 60 m, for two different ignition times (ignition location at 38 m).	82
Figure 29. Hydrogen volume fraction (left) and turbulent kinetic energy (right) at 0.30, 0.35 and 0.40 s from the ignition (ignition at 38 m, 12.0 s ignition delay).....	82
Figure 30. Effect of ignition position. Overpressure time series at 35, 40, 50 and 60 m, for four different ignition positions (12.0 s ignition delay).	83
Figure 31. Temperature (left) and the overpressure (right) at 0.25, 0.30, 0.35, 0.40, 0.45, 0.50 s from the ignition (ignition at 38 m, 12.0s after the release).	84
Figure 32. A horse-shoe cross-section tunnel model with eight cars.	86
Figure 33. Discretized computational domain.	86
Figure 34. Injected hydrogen mass flow rate through three TPRD opens ($\Phi=2.5$ mm) in H_2 tanks @ 70 MPa and 293 K.	86
Figure 35. Flammable hydrogen clouds with greater than 4 vol. % H_2 in longitudinally vertical cut through the injection point at 1 s, 4 s, 8 s and 16 s, without tunnel ventilation.	87
Figure 36. Hydrogen concentration distribution in a transverse cut at 16 s showing the ignition position with the spark in red close to the ceiling.	87
Figure 37. Pressure distributions in the tunnel at 2 ms, 4 ms, 7 ms and 9 ms later than the ignition in case of no ventilation.	88
Figure 38. Diagram of the geometry model, (a) circular tunnel; (b) rectangular tunnel.....	90
Figure 39. Computational region of the circular tunnel and the location of sensors, (a) longitudinal cross section; (b) transverse cross section ($9.6 \times 6.6 \text{ m}^2$).	90
Figure 40. Computational region of the rectangular tunnel and the location of sensors, (a) longitudinal cross section; (b) transverse cross section ($6.3 \times 8.7 \text{ m}^2$).	91
Figure 41. Mass flow rate of the H_2 injection (2mm Φ TPRD, 5kg H_2 in 0.125 m^3 at 70MPa)... ..	91
Figure 42. Longitudinal view of hydrogen concentration contours at $t = 5$ s in (a) circular tunnel with ventilation; (b) circular tunnel without ventilation; (c) rectangular tunnel with ventilation; (d) rectangular tunnel without ventilation.....	93
Figure 43. Transverse view of hydrogen concentration contours at $t = 5$ s in (a) circular tunnel with ventilation; (b) circular tunnel without ventilation; (c) rectangular tunnel with ventilation; (d) rectangular tunnel without ventilation.	93
Figure 44. Pressure history in circular tunnel with ventilation, with ignition at 5.2 s.	94
Figure 45. Pressure history in rectangular tunnel with ventilation, with ignition at 5.2 s.	94
Figure 46. Pressure history in circular tunnel without ventilation, with ignition at 5.2 s.	94
Figure 47. Pressure history in rectangular tunnel without ventilation, with ignition at 5.2 s. ...	95
Figure 48. Pressure contour plot at 5.216s for cases with ventilation.....	95
Figure 49. Pressure contour plot at 5.275s for cases without ventilation.....	95
Figure 50. Effect of water mist. Overpressure time series at 35, 40 and 50 m, for different water concentrations.....	98

D4.3. Final report on analytical, numerical and experimental studies on explosions, including innovative prevention and mitigation strategies

Figure 51. Effect of water mist on maximum overpressure (at $x=50$ m) and on maximum temperature.....	99
Figure 52. Geometry model of the HSE experimental tunnel.....	102
Figure 53. Computational domain of the HSE experimental tunnel and the location of sensors, (a) vertical view; (b) horizontal view.....	102
Figure 54. Mass flow rate of the H_2 injection (TPRD diameter Φ 2.2 mm, 0.45 kg H_2 in 0.053 m^3 at 118 bar).....	102
Figure 55. Mist region in the tunnel.....	103
Figure 56. Hydrogen concentration contours in a longitudinal vertical cut along the tunnel axis without ventilation at $t =$ (a) 2.5 s; (b) 5 s; (c) 7 s; (d) 9 s.	104
Figure 57. Hydrogen concentration contours in a longitudinal vertical cut along the tunnel axis with 1.25 m/s ventilation at $t =$ (a) 2.5 s; (b) 5 s; (c) 7 s; (d) 9 s.....	104
Figure 58. Hydrogen concentration contours in a longitudinal vertical cut along the tunnel axis with 2.4 m/s ventilation at $t =$ (a) 2.5 s; (b) 5 s; (c) 7 s; (d) 9 s.....	105
Figure 59. Hydrogen concentration contours in a horizontal view right below the chassis of the leaking vehicle without ventilation at $t =$ (a) 2.5 s; (b) 5 s; (c) 7 s; (d) 9 s.	105
Figure 60. Hydrogen concentration contours in a horizontal view right below the chassis of the leaking vehicle with 1.25 m/s ventilation at $t =$ (a) 2.5 s; (b) 5 s; (c) 7 s; (d) 9 s.	106
Figure 61. Hydrogen concentration contours in a horizontal view right below the chassis of the leaking vehicle with 2.4m/s ventilation at $t =$ (a) 2.5 s; (b) 5 s; (c) 7 s; (d) 9 s.	106
Figure 62. Pressure history when the hydrogen cloud was ignited 5.1 s after the beginning of the hydrogen release without ventilation.	108
Figure 63. Pressure history when the hydrogen cloud was ignited 5.1 s after the beginning of the hydrogen release with 1.25m/s ventilation.....	108
Figure 64. Pressure history when the hydrogen cloud was ignited 5.1 s after the beginning of the hydrogen release with 2.4m/s ventilation.....	108
Figure 65. Pressure history when the hydrogen cloud was ignited 5.1 s after the beginning of the hydrogen release without ventilation (with mist section).	109
Figure 66. Pressure history when the hydrogen cloud was ignited 5.1 s after the beginning of the hydrogen release with 1.25m/s ventilation (with mist section).....	109
Figure 67. Pressure history when the hydrogen cloud was ignited 5.1 s after the beginning of the hydrogen release with 2.4m/s ventilation (with mist section).....	109
Figure 68. Schematic test channel of planar shockwave propagation through a water fog region to study its attenuation effect on shock pressure.....	110
Figure 69. Verification of the droplet breakup model in COM3D against experimental data of Chauvin et al. (2011) with droplet diameter 500 μm , Mach number 1.5, liquid phase concentration 10 kg/m^3 and fog region length 700 mm.	112
Figure 70. 3D views of the A2 vessel in the KIT hydrogen test centre.	113
Figure 71. (a) The snapshot of the A2 vessel; (b) The computational domain of the vessel; (c) The generated droplet cloud inside the vessel.....	113
Figure 72. Geometrical models of hydrogen detonation vessel with sprays, (a) CAD drawing of the vessel, (b) vertical cut view of the computational domain showing schematically the detonation unit, droplet cloud and pressure gauges, (c) horizontal cut view of the model.....	114
Figure 73. Detonation shockwave developing and propagating process and wave reflections on the vessel bottom plate and the wall.....	115

D4.3. Final report on analytical, numerical and experimental studies on explosions, including innovative prevention and mitigation strategies

Figure 74. Overpressures in cases with/ without mist attenuation, recorded by the column of gauges aligned horizontally in the line from the vessel centre to the conical centre at the same height of $Z = 1.22$ m, and at a distance from the vessel centre $X = 1.74$ m, 2.18 m, 2.61 m, 3.05 m, respectively.	116
Figure 75. Experiment of hydrogen explosion shockwave attenuation by absorbing materials with different thicknesses in the HYKA A2 vessel.....	117
Figure 76. Tunnel view: orange - concrete ceiling, location for fire and dispersion tests, green - location for the explosion.....	118
Figure 77. CFD + FEM problem formulation.	119
Figure 78. Pressure dynamics in CFD and application for FEM.	120
Figure 79. Energy losses for under vehicle tank rupture and chemical energy, $P_T=94.5$ MPa, $V_T=120$ L, $m_v=1800$ kg.	120
Figure 80. Hexahedral and tetrahedral numerical grids structure.	125
Figure 81. H_2 mole fraction distribution: CFD modelling versus INERIS experiment (Cirrone, 2018).....	126
Figure 82. Pressure transients at pressure sensors P1, P2 and P3 for INERIS test: simulations versus experiment.....	127
Figure 83. Cross-section of the investigated slab. Measures are in mm.	129
Figure 84. Maximum overpressure on the tunnel ceiling (stand-alone tank 62.4L, 700bar). ...	130
Figure 85. PLANE182 (left) and REINF263 elements (right) (ANSYS, 2022).	132
Figure 86. 2 HSD hardening yield function in compression Ωc (left) and tension Ωt (right) (ANSYS, 2022).	133
Figure 87. Results of the compressive (left) and tensile (right) reaction force vs, displacement of the free end obtained in Ansys (orange line) and comparison with the value calculated from the input material model (blue line).	135
Figure 88. Model of the slab for validation of the bending capacity.	137
Figure 89. Reaction at support vs vertical displacement of the free end obtained for three different mesh sizes (continuous lines) and expected value of the capacity calculated in INCA2 (dotted line).	137
Figure 90. Deflection of the mid-span as function of time.	138
Figure 91. Plot of the strain at the time of the maximum deflection.....	138
Figure 92. Hydrogen mass flow rate into air volume above the train to form 30% vol. hydrogen mixture as a function of volumetric air flow rate above the train in tunnel, assuming 6 m x 0.5 m free area above train.	141
Figure 93. Hydrogen concentration distribution (gradient) used in the simulations (shown in terms of the equivalence ratio). A lean hydrogen-air mixture in the whole domain is used to keep reactivity low in simulations.....	143
Figure 94. Top: 7 ms after ignition. Middle: 9.2 ms after ignition. Bottom: 10.1 ms.	143
Figure 95. Simulated pressure during accelerated flame propagating in velocity gradient of 110 s^{-1} ($0\text{--}55\text{ m/s}$ over 0.5 m) at 69 ms from the ignition. The domain is 32 m long.	144
Figure 96. Example of tank equipped with a detonation belt.....	145
Figure 97. Measurement devices used to monitor fireballs.	146
Figure 98. General sketch of the 2021 explosion and fireball tests.	146
Figure 99. Post-processing method to derive the hemispherical radius of fireballs.	149
Figure 100. 2020 pre-test 31: Left – example of fireball picture. Right – post processing of fireball surface.....	149

D4.3. Final report on analytical, numerical and experimental studies on explosions, including innovative prevention and mitigation strategies

Figure 101. 2020 pre-test 32: Thermocouple measurements.	150
Figure 102. 2021 test 32: Shapes of the fireball.....	151
Figure 103. 2021 test 42: Shapes of the fireball.....	152
Figure 104. 2021 test 37: Shapes of the fireball.....	152
Figure 105. 2021 test 38: Shapes of the fireball.....	153
Figure 106. 2021 fireball tests: Evolution of the equivalent hemispherical radius.....	153
Figure 107. 2021 fireball tests: Photodiode measurements.	154
Figure 108. 2021 test 37: Video camera images.	155
Figure 109. 2021 fireball tests: Ultrasonic anemometer measurements. Top velocity, Bottom Orientation.....	156
Figure 110. 2021 fireball tests: Thermocouple measurements.	157
Figure 111: Tunnel geometry.....	170
Figure 112 : Scheme of installation of blast wave pressure transducers (left) and photo of a PCB blast wave pencil.....	171
Figure 113 : Tanks used for explosion experiments: TYPE II (left) and TYPE IV (right). The detonation belt is attached to each of the tanks.	172
Figure 114 : Test 42. Raw and filtered pressure signal at P1 (left, 30 m from explosion) and the magnitude spectrum of the pressure signal (right).	174
Figure 115: Test 31. DB of 130 g TNT. Overpressure evolutions at different distances.	175
Figure 116: Test 33. DB of 228 g TNT. Overpressure evolutions at different distances	175
Figure 117: Test 30. He 185 bar, 50L Type II tank. Overpressure evolutions at different distances	177
Figure 118: Test 34. He 650 bar, 78L Type IV tank. Overpressure evolutions at different distances.	177
Figure 119: Test 32. H ₂ 90 bar, 78L Type IV tank. Overpressure evolutions at different distances	179
Figure 120: Test 42. H ₂ 194 bar, 50L Type II tank. Overpressure evolutions at different distances	179
Figure 121: Test 37. H ₂ 520 bar, 78L Type IV tank. Overpressure evolutions at different distances	180
Figure 122: Test 38. H ₂ 610 bar, 78L Type IV tank. Overpressure evolutions at different distances (top), the evolutions are shown for longer time scale (bottom).....	180
Figure 123: Sketch of the blast wave propagation near explosion zone.	180
Figure 124 : Blast wave velocity as a function of distance for 3 tests.	181
Figure 125: Comparison of experimental data with universal correlation. First peak of pressure is taken into account.	184
Figure 126: Comparison of experimental data with universal correlation. Second peak of pressure is taken into account.....	184
Figure 127. Test facility H110 (A1) of HYKA with large scale rectangular combustion channel 9 x 3 x 0.6 m ³ , open from below.	186
Figure 128. Various hydrogen layers are produced by injection of different air diluted hydrogen mixtures at different injection pressures.	187
Figure 129. Measured flame speed and combustion overpressure in case HyT242 with H ₂ concentration gradient of 0.6% H ₂ /cm and max. H ₂ concentration of 20% H ₂ , case HyT256 with H ₂ concentration gradient of 0.33% H ₂ /cm and max. H ₂ concentration of 20% H ₂	189

D4.3. Final report on analytical, numerical and experimental studies on explosions, including innovative prevention and mitigation strategies

Figure 130. Flame speed (left) and combustion overpressure (right) comparisons between uniform and non-uniform mixtures with different hydrogen concentration gradients (slopes).

.....	190
Figure 131. Influence of obstacles on combustion in case of HyT256 with H ₂ concentration gradient of 0.33% H ₂ /cm and max. H ₂ concentration of 20% H ₂	191
Figure 132. Test facility H110 (A1) of HYKA with large scale rectangular combustion channel 9 x 3 x 0.6 m ³ and section with water spray.	192
Figure 133. (a) Overview of mist spray,(b) shadow image with droplet data overlay from Particle Master by Davis	195
Figure 134. Normalized mass flow for 100 bar supply water pressure, 940 mm below mist nozzle.	196
Figure 135. Number mean diameter for 100 bar supply water pressure, 940 mm below mist nozzle.	196
Figure 136. (a) Relative span factor- and (b) number of droplets for 100 bar supply water pressure, 940 mm below mist nozzle.	197
Figure 137. (a) Mass flux of water droplets- and (b) Mass averaged velocity for 100 bar supply water pressure, 940 mm below mist nozzle.	197
Figure 138. Droplet density for 100 bar supply water pressure, 940 mm below mist nozzle..	198
Figure 139. Example of Normalized distributions for 100 bar supply water pressure, 940 mm below, 75 mm radial to the mist nozzle.	199
Figure 140. (a) Total number size distribution- and (b) total volume distribution for 100 bar supply water pressure, 940 mm below mist nozzle.....	199
Figure 141. Test facility V220 (A2) of HYKA for attenuation of water spray on hydrogen detonation shock waves. A) Sketch of the set up for suppression tests of water spray on shock waves. B) Combustion unit with 4 g H ₂ provided as stoichiometric H ₂ /air mixture. C) Results of free field tests of combustion units.	203
Figure 142. Schematic view of the LNB tank cross-section: 1-liner, 2-bosses, 3-primary FRP layer, 4-TPL layer (Molkov et al., 2018)	205
Figure 143. Schematic of LNB safety technology for composite Type IV tanks: original tank (left) and LNB tank (right) in a fire.....	206
Figure 144. Finished LNB tank prototypes following UU design: left – the first prototypes, right – the second prototypes.	208
Figure 145. Pressure histories of the first prototypes in fire tests: COPV1-4 and COPV1-5. .	208
Figure 146. Pressure and temperature histories of the COPV2-5 tank prototype in a fire test.	208
Figure 147. Snapshots of COPV2-5 LNB prototype performance in a fire test.	209
Figure 148. Example of achievement of the burst pressure for prototype No 1: P _{burst} =24,917 psi=1718 bar, giving the burst pressure ratio 2.45.	211
Figure 149. The exteriors of the LNB prototypes (No 1-7 are shown).	212
Figure 150. Schematic representation of the test.	213
Figure 151. Sketch of the two tanks and the associated measuring devices.	214
Figure 152. Pictures and numbering of the different elements associated to the piping system between the solenoid valve and the LNB tank.	215
Figure 153. Schematic description of the propane burner.	216
Figure 154. Picture of the propane burner with the two zones on the right picture: engulfing area (left side) and localized area (right side).	217
Figure 155. Position of the burner.....	218

D4.3. Final report on analytical, numerical and experimental studies on explosions, including innovative prevention and mitigation strategies

Figure 156. Location of dedicated N-Type thermocouples.....	219
Figure 157. Location of the radiative heat flux sensors.	219
Figure 158. Inside tanks and pipes behavior – Top: solenoid valve opening to fill the LNB tank – Center: Overpressure in the main tank and in measurement chambers – Bottom: Temperature in the main tank and in the measurement chambers.....	221
Figure 159. Behavior around the LNB tanks – Top: Temperatures – Bottom: Radiated heat fluxes.	222
Figure 160. Synchronized behavior between overpressure inside the LNB tank and picture of the fire during phase 4 and 5.	224
Figure 161. Mass flow rate of the leaks for test 1 and 2.	225
Figure 162. Comparison of mass flow rate's test 2 (Simulated and calculated).....	227
Figure 163. Measured wind velocity and angle during the tests.	228
Figure 164. Measured gas temperature close to the top of the tunnel at different distances along the tunnel axis.....	229
Figure 165. Schematic diagram showing modelling of jet and tunnel ventilation interactions.	241

List of tables

Table 1. Tunnel dimensions and hydrogen tank parameters used in rupture simulation.	26
Table 2. Variables of the problem together with the corresponding symbols and dimensions..	26
Table 3. Determined energies contributing to the leading shock, based on total energy, including coefficients α and β	27
Table 4. Summary of validation experiments.	29
Table 5. Dimensionless scale for different processes.	46
Table 6. Critical ratios for DDT as function of blockage ratio.	47
Table 7. Dimensions of European road tunnels.	52
Table 8. Dimensions of European rail tunnels.	52
Table 9. Initial hydrogen inventory, mass flow rate and discharge time for different vehicles.	52
Table 10. Hydrogen storage specifications for different car.	52
Table 11. Initial properties of the system.	53
Table 12. Main properties of hydrogen-air combustible mixtures.	56
Table 13. Laminar flame speed and speed of sound for combustion products.	56
Table 14. Output data for hydrogen inventory, $m = 2$ kg.	57
Table 15. Output data for hydrogen inventory, $m = 10$ kg.	57
Table 16. Initial properties of the system.	58
Table 17. Output data for hydrogen inventory, $m = 2$ kg, and layer geometry, $h = 0.6$ m.	59
Table 18. Output data for hydrogen inventory, $m = 10$ kg, and layer geometry, $h = 0.6$ m.	59
Table 19. Initial properties of the system.	60
Table 20. Output data for hydrogen inventory, $m = 2$ kg, and stratified layer geometry, $h = 0.6$ m.	62
Table 21. Output data for hydrogen inventory, $m = 10$ kg, and stratified layer geometry, $h = 0.6$ m.	63
Table 22. Initial properties of the system.	64
Table 23. Output data for hydrogen inventory, $m = 2$ kg, and stratified hydrogen-air mixture.	65
Table 24. Output data for hydrogen inventory, $m = 10$ kg, and stratified hydrogen-air mixture.	66
Table 25. Correlation between hydrogen mass flow rate and water spray flow rate.	70
Table 26. Deflagration scenarios for the empty tunnel case. Ignition delay and ignition location.	75
Table 27. Deflagration scenarios. Water concentration and initial mass fractions.	97
Table 28. Maximum Overpressure (Pa) for various cases.	109
Table 29. Test channel parameter setup for shockwave propagation.	111
Table 30. Experimental tests available in literature modelled in CFD simulations.	123
Table 31. Notional nozzle parameters.	125
Table 32. Parameters of the numerical grids employed for simulations.	125
Table 33. Material parameters.	129
Table 34. Limit for dynamic regimes in literature.	130
Table 35. Calculation data and results of the natural period of the simply supported R.C. slab.	131
Table 36. Parameters of the concrete material model	134
Table 37. Table 1. Reaction at support in the FEM for 3 different mesh and comparison with the expected values.	137

D4.3. Final report on analytical, numerical and experimental studies on explosions, including innovative prevention and mitigation strategies

Table 38. Limit on the maximum deflection for collapse according to different regulations.	139
Table 39. Explosion test matrix.....	147
Table 40. Some global characteristics of fireball tests performed in 2021	148
Table 41. Examples of European road tunnels showing relevant geometry.	161
Table 42. Examples of European rail tunnels showing relevant geometry.	161
Table 43. Geometry of the HSE Buxton test tunnel.....	161
Table 44. Scaling factors to be applied for tests carried out at HSE Buxton.	162
Table 45. Scaled hydrogen inventories for cars, buses and trains (values highlighted in bold i.e. double-bore only, are those to be used for the actual modelling exercise).	163
Table 46. Correlation of proposed hydrogen to actual tank inventories.	164
Table 47. Equivalent diameter of TPRDs on cars, buses and trains.	165
Table 48. Initial mass flow rates and discharge times for full size and for scaled inventories.	166
Table 49. Scaled orifice size for experimental releases.	167
Table 50. Scaled ventilation velocities in HSE tunnel.	168
Table 51. Proposed matrix of tests.	169
Table 52. Timeline of pre-test and experimental delivery activities.....	169
Table 53. Blast wave sensors positions	171
Table 54. Specifications of Pressurized Tanks used in explosion tests	172
Table 55. Test Matrix	173
Table 56. Tests 31-33 (fragments). Maximum overpressures recorded at different distances	176
Table 57. Tests 30-34 (Helium tanks). Maximum overpressures recorded at different distances	178
Table 58. Tests 32, 42, 37 and 38 (Hydrogen tanks). Maximum overpressures recorded at different distances	181
Table 59. The tests used for comparison. The mechanical and chemical energies are given ..	183
Table 60. Maximum overpressure values measured at different distances for pre-Test 20.....	183
Table 61. Test matrix of non-uniform and uniform hydrogen-air cloud in a tunnel.....	188
Table 62. Test matrix of water injection effect on hydrogen combustion and DDT.	192
Table 63. Settings for Particle Master	194
Table 64. Averaged properties of the entire spray	200
Table 65. Numerical values for droplet size distributions of mist spray.....	200
Table 66. Test matrix of attenuation of water injection on shock wave of hydrogen detonation.	203
Table 67. Test matrix of absorbing materials' attenuation effect on shock wave.....	204
Table 68. List of the first successful LNB prototypes.....	207
Table 69. List of LNB prototypes designed and manufactured in Hy-Tunnel-CS project: materials and objectives.	210
Table 70. List of results of LNB prototypes undergone hydro burst and hydrostatic tests.....	211
Table 71. Description and estimated internal volumes of the various parts of the connection between the main tank valve and the LNB tank.....	216
Table 72. Time occurrence of the main events.	223

D4.3. Final report on analytical, numerical and experimental studies on explosions, including innovative prevention and mitigation strategies

1 Introduction

The HyTunnel-CS project aims to conduct internationally leading pre-normative research (PNR) to close knowledge gaps and technological bottlenecks, in the provision of safety and acceptable level of risk, in the use of hydrogen and fuel cell cars as well as hydrogen delivery transport in underground transportation systems. Work Package 4 (WP4) of HyTunnel-CS will focus on the investigation of hydrogen releases and their subsequent ignition within underground transportation systems.

This document presents the deliverable (D4.3) *Final report on analytical, numerical and experimental studies on explosions, including innovative prevention and mitigation strategies* regarding ignited releases and explosions in tunnels and underground parking.

The activities within this report follow the detailed programme and plan defined in deliverable D4.1 “Detailed research programme on explosion in underground transportation systems” (HyTunnel-CS D4.1, 2019). Some of the planned activities have been updated in response to developments and findings within the project. A first step to the preparation of this document was given by Milestone “M4.3. Results of experimental, analytical and numerical studies for final report” which presented a first version of the report on the research outcomes.

1.1 Work Package overview

The experimental campaigns, analytical and numerical studies in WP4 aim to address the identified knowledge gaps on explosion prevention and mitigation. These were defined through the critical review of the state of the art conducted in HyTunnel-CS D1.2 “Report on hydrogen hazards and risks in tunnels and similar confined spaces” (HyTunnel-CS D1.2, 2019). The analytical, numerical and experimental studies aim to improve the understanding of hydrogen explosion hazards in tunnels and similar confined spaces, generating unique experimental data to support the validation of engineering and numerical models to be used in hydrogen safety engineering. The final scope is the identification and evaluation of innovative safety strategies and engineering solutions to prevent and mitigate hydrogen explosions in underground transportation systems. The outcomes of the research will be used as an input to the recommendations for RCS and for an inherently safer use of hydrogen vehicles in underground transportation systems. A detailed list of the work-package objectives can be found in (HyTunnel-CS D4.1, 2019).

1.1.1 Structure and synergy with HyTunnel-CS work plan

Work Package 4 is structured in 5 tasks closely interconnected with each other and with HyTunnel-CS work plan. The first task, 4.1, aimed at the design of the research programme. Task 4.2 focuses on the development of analytical models and engineering-based correlations. Task 4.3 aims at the development and validation of CFD model against experiments available in literature or performed within HyTunnel-CS programme. Task 4.3 aims at performing the experimental work that will enhance the current understanding of explosion prevention and mitigation, along with supporting Tasks 4.2 and 4.3 by providing experimental data for validation. Thus, it is of utmost importance that a close collaboration is ensured between modellers and experimentalists during all phases of the experimental campaign, from design of tests to discussion of results. Finally, Task 4.5 draws on the findings from each of the Tasks 4.2 to 4.4 to produce mid-term and the final deliverables report, D4.2 and D4.3 respectively.

D4.3. Final report on analytical, numerical and experimental studies on explosions, including innovative prevention and mitigation strategies

WP4 activities are closely connected with WP2 research on release and dispersion of unignited hydrogen jets in tunnels and similar confined spaces. Finally, the outcomes developed within tasks 4.2-4.4 will be translated into a suitable language and format to be integrated into the guidelines and recommendations for RCSs developed within WP6. A complete list of the work-package activities within Tasks 4.2-4.4 can be found in (HyTunnel-CS D4.1, 2019 – see Table 1).

D4.3. Final report on analytical, numerical and experimental studies on explosions, including innovative prevention and mitigation strategies

2 Analytical studies, development, and validation of engineering correlations (Task 4.2 / UU)

2.1 Engineering models for assessment of blast wave and fireball of hydrogen tank rupture (4.2, UU)

2.1.1 Universal correlation of blast wave attenuation in a tunnel

2.1.1.1 Background

State-of-the-art research done on high-pressure hydrogen tank rupture and the attenuation of blast waves in tunnels is very limited. Several parameters such as, the energy of the hydrogen stored based on volume and pressure, and the tunnel dimensions, all have a significant influence on peak overpressure and its attenuation in a tunnel. The condensed material used for explosive sources for the generation of blast wave in tunnels is mostly TNT, or its equivalent mass in form of another explosive charge. The initial form of the blast wave decay law, as shown in equation (1), indicates the dependence of the peak overpressure, P , on the ratio of charge weight, m , to volume of enclosure or tunnel, V , taking the general form:

$$P \propto A \left(\frac{m}{V} \right)^b, \quad (1)$$

where A and b are derived empirically from best curve fits, and therefore mostly defined within specific parameters, such as distance or overpressure (Smith and Sapko, 2005; Curran et al., 1966; Fang et al., 2019; Skjeltnor, 1968). However, this method limits the fitted values of A and b to one -tunnel-case applicability. Furthermore, the constraint in the power law method suffers from the omission of other factors, such as the geometrical shape of the tunnel (i.e., aspect ratio), the percentage of energy of tank that becomes blast wave and minor and friction losses along the tunnel distance. With the aim of developing a universally applicable model across various tunnel sizes, these additional parameters are all considered in the novel methodology developed for blast wave decay in tunnel in this study.

2.1.1.2 Problem formulation

In the absence of experimental data, a CFD model, previously validated for high-pressure tank rupture in open atmosphere, is used in this study, to analyse the effect of high-pressure hydrogen tank rupture in a tunnel. This model development and the related validation processes are described elsewhere (Molkov et al., 2018a). Within this project, building on the previous CFD model for open atmosphere conditions, a parametric numerical study is conducted with the aim of developing a correlation between blast wave decay and tunnel confinements. This includes tunnels with cross-sections 24, 40 and 139 m² (corresponding to tunnels with 1, 2 and 5 traffic lanes) and tank masses of hydrogen ranging from 0.58 kg to 6.96 kg with pressure before burst values of 95 MPa, 70 MPa and 35 MPa. The dimensions and parameter of the tunnels and tanks used in the simulations are summarised in Table 1 below.

D4.3. Final report on analytical, numerical and experimental studies on explosions, including innovative prevention and mitigation strategies

Table 1. Tunnel dimensions and hydrogen tank parameters used in rupture simulation.

Tunnel cross section, m ²	Tunnel length, m	Tank volume, L	Tank mass, kg	Tank pressure, MPa
24, 40, 139	150 m	10	0.58	95
		30	1.7	
		60	3.5	
		120	6.9	
40	1500 m	120	5.2	70
40	1500 m		2.6	35

2.1.1.3 Dimensionless variables

To determine a decay law for blast wave overpressure in a tunnel, the main impact parameters of influence are required. There are various interpretations of these parameters, but the most commonly ascertained are the following: atmospheric pressure, P_0 , energy of the blast, E , the cross-section area of the tunnel, A , and the distance of the wave from the energy release point, L . To find the relationships between these four physical quantities, dimensional analysis is firstly performed, identifying the three basic dimensions as mass, $M = kg$, length, $L = m$, time, $T = s$. Table 2 shows the variables for the parameters mentioned together with their dimensions.

Table 2. Variables of the problem together with the corresponding symbols and dimensions.

Variable	Symbol	Basic dimensions
Atmospheric pressure	P_0	$M^1L^{-1}T^{-2}$
Energy	E	$M^1L^2T^{-2}$
Tunnel cross-section area	A	$M^0L^2T^0$
Distance from release	L	$M^0L^1T^0$

Using the Buckingham π theorem, a relationship between the variables can be represented as follows; with four physical quantities presented and three dimensions, there is one ($4 - 3 = 1$) independent dimensionless π parameter. Choosing three parameters (i.e., P , L , E) to be repeating variables, the one dimensionless quantity is derived as $\pi_1 = \frac{(P_0LA)}{E}$. This derived quantity may be considered as a dimensionless distance based on storage tank energy and tunnel dimensions and represented as:

$$\bar{L} = \frac{P_0LA}{E} \quad (2)$$

To convert overpressure, ΔP , from dimensional to dimensionless form it is divided by the surrounding (atmospheric) pressure:

$$\bar{P} = \frac{\Delta P}{P_0} \quad (3)$$

2.1.1.4 Contribution of energies

The total energy released on tank rupture in a car fire accident includes not only the instantaneously released mechanical energy of compressed hydrogen (i.e., “physical

D4.3. Final report on analytical, numerical and experimental studies on explosions, including innovative prevention and mitigation strategies
explosion”), but also the energy of chemically reacting hydrogen (i.e., combustion energy). In calculations, the total released energy is defined as:

$$E = \alpha \cdot E_m + \beta \cdot E_{ch} \quad (4)$$

with E_m and E_{ch} being the total mechanical compression and chemical energies of hydrogen in the vessel respectively; α is a mechanical energy coefficient; β is a chemical energy coefficient. For high-pressure tank rupture, close to the ground surface, the shock wave is reflected back in its entirety, and therefore, the energy associated with the generated blast wave will be twice as large. However, due to energy lost to partial reflections and ground cratering, a factor of $\alpha = 1.8$ is used. The chemical energy coefficient, β , indicates the fraction of the total hydrogen chemical energy gradually released during complete combustion contributing to the blast wave. This is determined either by the inverse problem method based on experimental values (found to be 5 % for the open atmosphere tank rupture and described by (Molkov and Kashkarov, 2015)), or by identifying, through simulation, when the primary (or leading) shock leaves the combustion zone. The contribution from combustion energy occurs only when the leading shock is still within the combustion zone. Once propagated away from the combustion zone, the secondary wave inhibits the energy feedback, by acoustic waves overcoming the positive temperature gradient generated spatially ahead, towards the leading front. In the absence of detailed experimental data on hydrogen tank rupture in tunnels, the second method to determine the chemical energy coefficient β is used in this study. The determined fractions of α and β , together with the calculated energies are listed in Table 3 below.

Table 3. Determined energies contributing to the leading shock, based on total energy, including coefficients α and β .

Tank mass, kg	Tank pressure, MPa	α	β	$\alpha \cdot E_m$, MJ	$\beta \cdot E_{ch}$, MJ
0.6	95 MPa	1.8	0.12	6.3	8.2
1.7			0.11	18.9	22.9
3.5			0.11	37.8	45.9
6.9			0.095	75.6	79.2
5.2	70 MPa		0.10	51.5	61.8
2.6	35 MPa		0.11	12.5	30.9

2.1.1.5 Graphical determination of blast wave decay in tunnels

Tunnels have different width to height ratios and the length of the tunnel influences resultant friction and other minor losses. To account for these phenomena, the original dimensionless parameters \bar{L} and \bar{P} are further modified using the similitude analysis to become \bar{L}_1 and \bar{P}_1 . As shown in Figure 1, simulated overpressure, for all tank volumes, pressures and tunnel cross-section areas, collapse in a single line when presented using these new dimensionless coordinates \bar{L}_1 and \bar{P}_1 . Figure 1 presents the peak overpressures obtained in CFD simulations, the best fit line and the upper limit conservative fit line.

D4.3. Final report on analytical, numerical and experimental studies on explosions, including innovative prevention and mitigation strategies

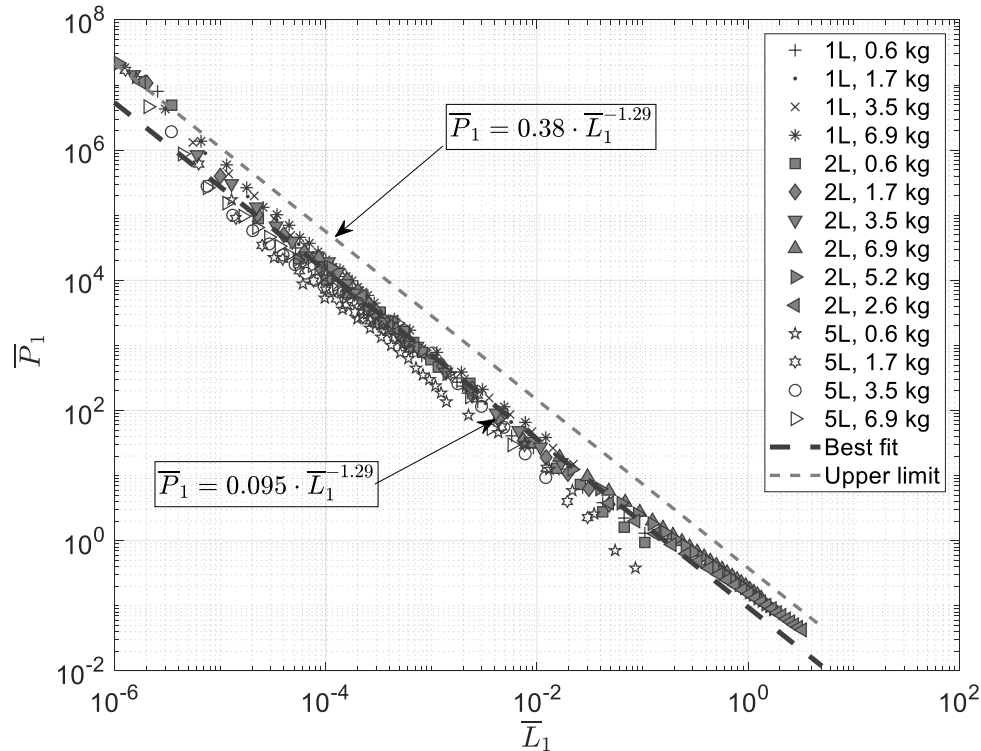


Figure 1. Relationship between peak overpressure and distance in tunnels of various lanes (1, 2 and 5), expressed by their dimensionless values, \bar{P}_1 and \bar{L}_1 , respectively.

This is a preliminary study of mainly academic interest rather than a source of safety guidelines for storage tanks and hydrogen-powered vehicle developers. However, with the current absence of experimental studies on high-pressure hydrogen tank rupture in a tunnel, it demonstrates a methodology on how to develop a universal dimensionless correlation to be used for safety guidelines and pre-test calculations.

2.1.2 Fireball model

The work focuses on the assessment of hazard distances arising from the fireball following the high-pressure hydrogen tank rupture in a fire. The semi-empirical correlation to assess the fireball size in an open space is proposed. Correlation for the open space is compared against experimental data on compressed hydrogen tank rupture in a fire and liquefied hydrogen spills. The validation process is available e-Laboratory of Hydrogen Safety developed in NET-Tools <https://fch2edu.eu/home/e-laboratory/> project where the tool for the assessment of the fireball size is proposed, based on the amount of the combustion products, generated after full combustion of all fuel and approximated to the hemisphere. The proposed correlation reproduces the model prediction and is in good agreement with experimental data.

2.1.2.1 The analysis of experiments

A model for calculation of the maximum fireball size diameter is required for the use in hydrogen safety engineering, for the assessment of hydrogen tank rupture hazards both in open and confined spaces. There is a lack of experimental data on the subject which can be used for the validation of the theory and numerical models. A few experiments available in the literature and suitable for the fireball model validation are described briefly below.

D4.3. Final report on analytical, numerical and experimental studies on explosions, including innovative prevention and mitigation strategies

A Type HGV-4 hydrogen storage tank rupture in the bonfire test, performed in the USA, is described by (Weyandt, 2005; Zalosh and Weyandt, 2005). The tank had an internal volume of 72.4 L, initial storage pressure was 34.3 MPa and the initial temperature was equal to 300 K (corresponding to 1.64 kg of hydrogen). At the time of rupture, i.e., 6 min 27 sec after initiation, (fire heat release rate was 350 kW), the pressure and temperature raised to 35.7 MPa and 312.15 K respectively. The reported diameter of the fireball was about 7.6 m at time 45 ms after the tank rupture. The second test, using a Type 3 tank (aluminium liner) of 88 L installed under a typical sport utility vehicle (SUV) (Weyandt, 2006) had a slightly lower initial storage pressure of 31.8 MPa and resulted in a fireball of 24 m.

Two fire tests were conducted in Japan (Tamura et al., 2006) on tanks with design pressure 70 MPa. Fire Test 1 was conducted with a Type 4 tank of 35 L volume. The last recorded pressure in the tank was 94.54 MPa. Fire Test 2 was conducted with a Type 3 tank of 36 L volume. The pressure measured just before the tank burst at 11 min after the fire exposure was 99.47 MPa. Both tests resulted in a fireball with a diameter of approximately 20 m as reported in the paper. However, the simulated maximum fireball diameter is smaller than the fireball size reported in the experiments (Molkov et al., 2020). There was no time indicated in the experimental paper when it was achieved. Based on the photographs taken during the experiment the fireball diameter was approximately 13 m (at 330 ms) by scaling from the size of the burner of 1.8 m, not 20 m as stated in the original paper.

Two experiments were performed by a Chinese group of researchers (Shen et al., 2018) with high-pressure tank rupture during fire test in 2018; Type 3 tanks were used in both tests and had a volume of 165 L and initial pressure of 35 MPa. The last measured pressure at the time of rupture was 43.73 and 44 MPa respectively. According to the size of large stones around the fire test, the maximum fireball diameter was estimated between 7-8 m.

Maximum fireball width and height produced by ignition of the hydrogen-air mixture formed by the sudden release of liquefied hydrogen in the range between 2.8-89 litres has been assessed in the report by (Zabetakis, 1964). The correlation proposed for the liquefied hydrogen is represented by equation $D = 8.5 \times M^{0.33}$, where D – is the fireball diameter (m) and M – is the hydrogen mass, (kg). The summary of validation experiments is presented in Table 4 below.

Table 4. Summary of validation experiments.

Experiments	Pressure, MPa	Volume, L	Hydrogen mass, kg	Fireball, m	Mechanical energy, MJ
(Weyandt, 2005)	35.7	72.4	1.64	7.6	5.45
(Weyandt, 2006) (Under-vehicle)	34.5	88	1.87	24	6.44
(Tamura et al., 2006)	94.54	36	1.406	20 (13)	5.97
(Tamura et al., 2006)	99.47	35	1.367	20 (13)	6.04
(Shen et al., 2018)	35	168	3.9	7-8	15.53
(Zabetakis, 1964)	LH ₂ (9 tests)	2.7-87.7	0.2-6.2	12-60	-

Experiments on fireball formation and thermal effects were carried out using 0.1-100 tons of industrial fuels, namely, gasoline, kerosene and diesel fuel by (Dorofeev et al., 1995). In the

D4.3. Final report on analytical, numerical and experimental studies on explosions, including innovative prevention and mitigation strategies

tests, the fireball started to rise from the ground, forming the mushroom shape between 1 and 2 seconds after ignition. The correlations proposed for maximum radius R (m) of fireball versus fuel mass M (tonne) were $R=33\pm4\cdot M^{(0.32\pm0.04)}$. A correlation, developed by Roberts (1981), relates the mass of fuel involved, in this study a propane BLEVE tests is considered, to the maximum fireball diameter; the resultant equation takes the form $D=5.8M^{1/3}$. A further correlation, proposed for propane-air detonation, for the fireball diameter $D=6.96M^{0.33}$ was given by (Dorofeev et al., 1996). Another proposed correlation was applied for propane BLEVE at pressures of $p=0.2-1.3\text{MPa}$ and takes the form $D=5.33M^{0.327}$ (Hasegawa and Sato, 1978). The empirical correlation reported by Hord (Hord, 1978), based on tests with rocket propellants, was used by (Zalosh and Weyandt, 2005), to calculate the fireball size as $D=7.93M^{0.327}$. A recent publication (Li, 2019) gives a correlation for the fireball of $D=5.8M^{1/3}$, which is close to those mentioned above and the same as in (Roberts, 1981). This is developed and validated mostly for hydrocarbon fuels i.e., propane at the stoichiometric condition; it is suggested that the same correlations can be applied for the hydrogen, based on one test done in (Zalosh and Weyandt, 2005).

Analysis of the described experimental results shows a scatter in the observed fireball size. Comparing the USA (Weyandt, 2005) and Chinese (Shen et al., 2018) cases, for the larger volume tank, i.e., 2.3 times larger at 165L and with a pressure just before burst at 23% higher, the fireball is shown to be almost the same size as that of the 72.4L tank. While looking at the Japanese set of experiments, with tank volume half that of the USA test and 4.7 times less than that of the Chinese test, the pressure was higher by 2.65 and 2.15 times respectively and the fireball was more than twice the distance. It is thought that these variations may be due to several factors; the debris moved by the pressure wave affecting the appearance of the fireball, the entrainment of the gas outwards and non-uniformity of the tank opening during rupture, creating the momentum towards a one-directional jet. Let us try to prove it by comparing the mechanical energies stored in the tanks, keeping in mind that with higher energy there will be more debris involved. A summary of the parameters for the experiments are presented in Table 4, it can be seen that the mechanical energy is practically the same for USA (Weyandt, 2005) and Japan (Tamura et al., 2006) tests, but the smaller tank and higher overpressure produced a nearly 3 times bigger fireball in Japan. The LH_2 test parameters (Zabetakis, 1964) are mostly excluded from the table due to the nature of the storage and the absence of high-pressure storage and initial mechanical component.

2.1.2.2 Fireball in open space

A model for calculation of the fireball size, due to high pressure tank rupture, in a fire is available in the [e-Laboratory of Hydrogen Safety](#). The methodology is based on the work by Dadashzadeh (Dadashzadeh et al., 2017). Calculation of a fireball size after a stand-alone tank rupture is a part of the methodology for the calculation of the blast wave decay, considering compressed gas vessel rupture (Molkov and Kashkarov, 2015), and hazard distances attributed to the blast parameters. According to the technique, the fireball size is calculated as a hemisphere, occupied by combustion products, resulting from complete combustion of released hydrogen in air (non-premixed turbulent combustion at contact surface occurs at a stoichiometric concentration of reactants). The hydrogen mass in reservoir m_{H_2} is calculated using the Abel-Noble EOS based on storage pressure p_1 , temperature T_1 and tank volume V and has the form

D4.3. Final report on analytical, numerical and experimental studies on explosions, including innovative prevention and mitigation strategies

$$m_{H_2} = V \frac{p_1}{(p_1 b + R_{H_2} T_1)} \quad (5)$$

where R_{H_2} is the hydrogen specific gas constant (J/(kg K)) and $b=0.007691$ is the hydrogen co-volume constant (m^3/kg). The volume of hydrogen in the reservoir is

$$V_{H_2} = \frac{m_{H_2}}{M_{H_2}} * 22.4 \quad (6)$$

where M_{H_2} is the molecular mass of hydrogen (g/mol). The volume of air required to burn the hydrogen is

$$V_{air} = 2.38 * V_{H_2} \quad (7)$$

The fireball diameter is then

$$D = 2 * \left(\frac{3V_{burned}}{2\pi} \right)^{1/3} \quad (8)$$

where $V_{burned} = (V_{H_2} + V_{air}) * 6.85$, i.e., the product of the total volume of combustion products and the expansion coefficient, 6.85. This is equivalent to the empirical correlation

$$D = 9.8 * m_{H_2}^{1/3} \quad (9)$$

Figure 2 combines described hydrogen experimental data on the fireball size versus mass of fuel for several studies. The figure gives the new empirical correlations proposed for the stand-alone tank rupture in open atmosphere “best fit”, $D_{BF} = 9.8 * M^{0.33}$, (thick solid line), and also “conservative fit” $D_C = 11.5 * M^{0.33}$, (thick dashed line). The LH2 correlation as described by Zabetakis (Zabetakis, 1964) is also included. In Figure 2, “thick crosses” symbols show the fireball size prediction using the [e-Laboratory of Hydrogen Safety](#) tool for high-pressure tank tests and the LH₂ spills based on the mass of spilt hydrogen. As can be seen, there are two studies that fall substantially below all three empirical correlations. The upright “triangle” symbol indicates fireball size 7.7 m in the experiment by (Weyandt, 2005), which was measured at time 45 ms after the tank rupture and thought to be not the maximum that has been registered. The solid “diamond” symbol indicates the fireball size as measured in the experiment by (Shen et al., 2018), which might be due to non-instantaneous release and combustion decreasing the real size of the fireball. The e-Laboratory prediction for both cases has shown a bigger fireball size than deduced from experimental studies and is in line with the “best fit” correlation. Another light grey “square” symbol, which is above the empirical correlation, is the experiment for the under-vehicle tank rupture test by (Weyandt, 2006). This tank setup is out of scope for this study but has been added to show that the presence of the vehicle increases the fireball size compared to stand-alone tank rupture. Light grey “circles” and black “crosses” relate to the study by Tamura (Tamura et al., 2006), where the larger fireball size of 20 m suggests that the shape of the fireball was probably elongated and / or the

D4.3. Final report on analytical, numerical and experimental studies on explosions, including innovative prevention and mitigation strategies

directional jet caused by the shape of the tank opening is resulting in that value, For the model validation, 13 m size has been chosen based on the conclusions from (Molkov et al., 2020).

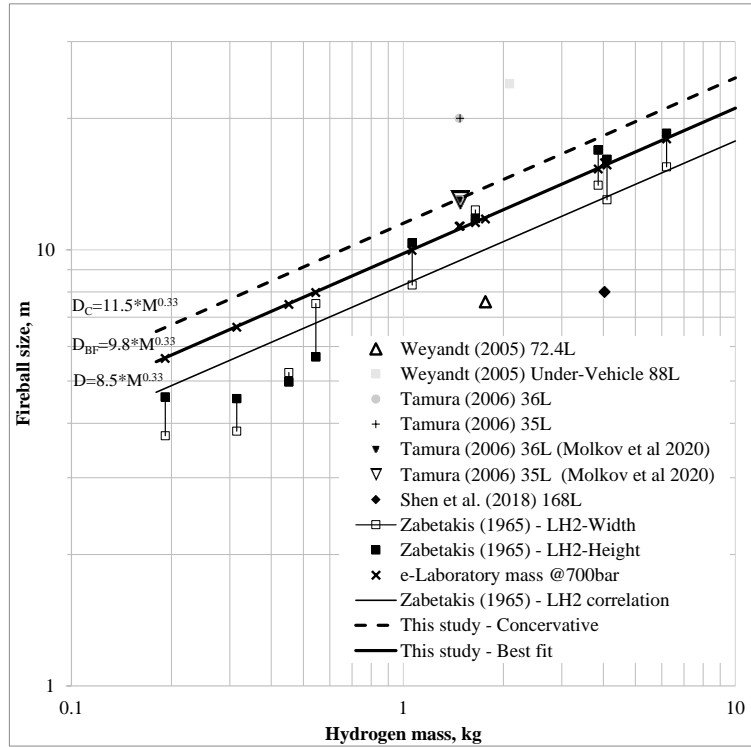


Figure 2. Experimental fireball size versus mass of hydrogen: comparison with correlations.

2.1.2.3 Fireball in tunnel

The same study by Li (Li, 2019) also suggests the correlation for the assessment of a maximum longitudinal length L_{max} of the fireball in a tunnel for a given cross-sectional area, is given by

$$L_{max} = 102 \frac{M_f}{A_T}, \quad (10)$$

where M_f – is the mass of fuel and A_T – is the tunnel cross-section area, again proposed for hydrocarbons. It was also shown that the fireball length in a tunnel of 50 m² cross-section area is much longer than the fireball diameter when the fuel mass exceeds around 5 kg for the proposed correlation in an open space.

Figure 3 shows the comparison of the best fit and conservative correlations, (correlations were described in the previous section of this report), which relate to open space fireballs (annotated as dotted lines). Figure 3 also shows the correlations derived by Li (Li, 2019) for a tunnel (annotated as solid lines) where, one, two and five traffic lanes with cross-sections of 24, 40 and 140 m² are considered. These tunnel cross-sectional areas are likewise considered by Shentsov (Shentsov et al., 2019), annotated as “this study” in Figure 3, where a simple equation, $L = \frac{V_{burned}}{A_T}$ has been incorporated to account for the amount of combustion products.

The correlation for the fireball in a tunnel is assumed to be one-dimensional, in contrast to the three-dimensional fireball in an open environment and hence, the difference in decay is clearly

D4.3. Final report on analytical, numerical and experimental studies on explosions, including innovative prevention and mitigation strategies

seen. For the smaller masses of fuel, this may lead to underestimation of the tunnel length occupied by the fireball. When the actual fireball size is less than the tunnel width the correlation presumes it still occupies the whole tunnel width, resulting in the decrease of the fireball length along the tunnel. In Figure 3 it is manifested by solid lines that the correlation for tunnels by (Li, 2019) is being below the dotted lines correlations for open atmosphere and underpredicts by 2.5 times the proposed one in this study justified by physical expansion of combustion products. It is worth noting that for the tunnel the effect of wind is not considered, and the model needs validation against realistic experiments which are absent to the best knowledge of authors. This can be addressed by the means of CFD simulations in the next study.

But the recent CFD calculation in Section 2.1.2.4 has shown that the shock propagation created the momentum which pulled the fireball inside the tunnel with the speed of 20 m/s; at this condition all such correlations cannot be applied in the realistic estimation. Even the comparison of the L_{max} with $L = \frac{V_{burned}}{A_T}$, for the same tunnel cross-section area A_T and mass of inventory which created the volume of combustion products burned at stoichiometry V_{burned} give under-prediction by 2.5 times. This means that none can be applied.

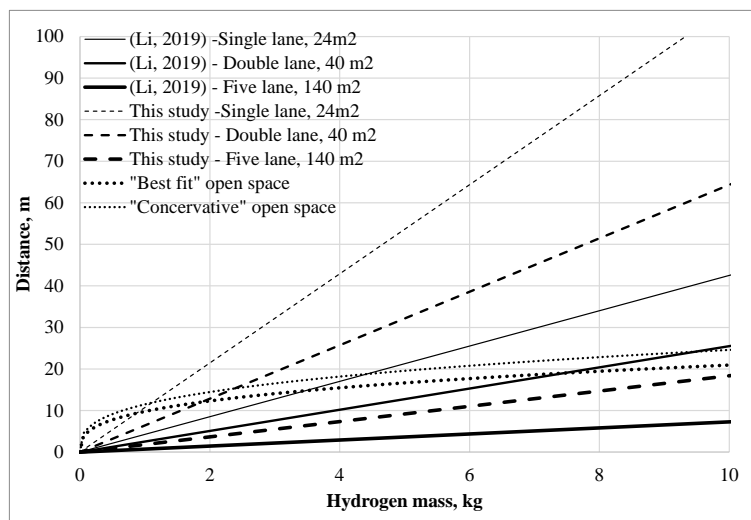


Figure 3. Comparison of open space and inside the tunnel correlations.

2.1.2.4 Simulation of fireball in a tunnel

CFD simulation of fireball dynamics after tank rupture has been performed in a tunnel with a cross-section area of 83 m², with a tank of 62.4 L and 700 bar, with the total mass of 2.5 kg and it was presented during HyTunnel-CS Stakeholders' Workshop (Shentsov, 2020). Figure 4 shows cross-section of the modelled tunnel design and corresponding cross-section of the calculation domain in CFD simulations. Figure 5 shows the simulated fireball dynamics in the tunnel cross-section and in projection to the tunnel walls using temperature field. Fireball size increases till 100 ms when reaching its maximum size of about 12 m in the longitudinal direction and 5.5 m in height. At the same moment, the fireball occupies the whole 13 m tunnel width. After 100 ms the fireball starts to rise above the ground and travel to the side dragged by the air force created by the blast wave. This creates a series of additional hazards to people and vehicles. The fireball velocity at the initial stage was 20 m/s.

D4.3. Final report on analytical, numerical and experimental studies on explosions, including innovative prevention and mitigation strategies

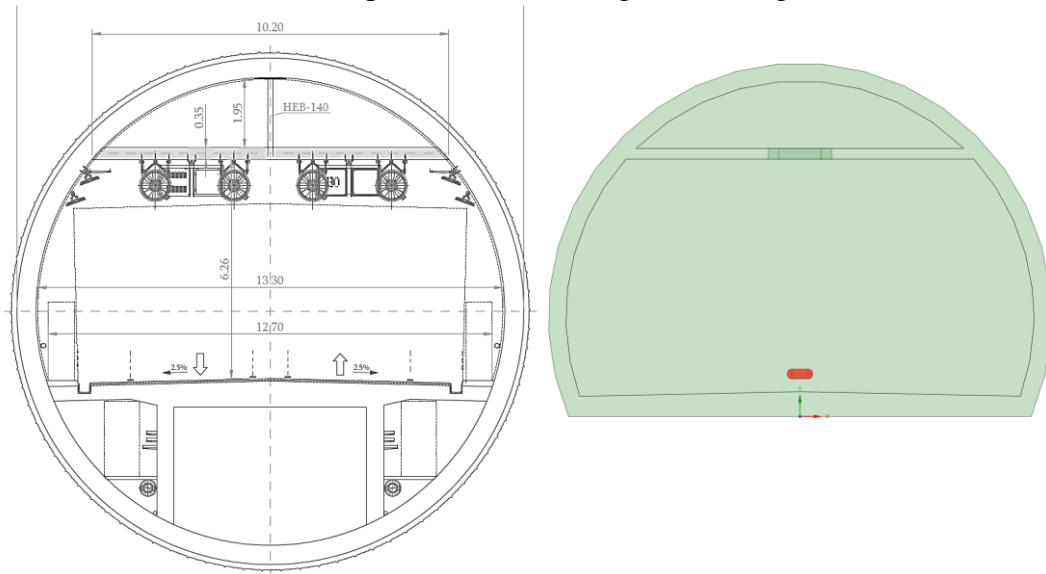


Figure 4. Simulated tunnel cross-section, tunnel drawing (left), simulated geometry (right).

In Figure 5 the left column shows the dynamics of the fireball propagation by temperature contours plane across the middle of the tunnel while on the right column the temperature contours are shown on the tunnel walls and ground. At the initial stage the fireball is not touching the side wall until 200 ms and then increases with the size starting to propagate towards the left.

In this particular example, the fireball is relatively small, fireball development is similar to the behaviour of fireball in open space and well reproduced by the “best fit” correlation in Figure 3 but further study are required to assess the hazard distance at which this fireball will propagate along the tunnel.

D4.3. Final report on analytical, numerical and experimental studies on explosions, including innovative prevention and mitigation strategies

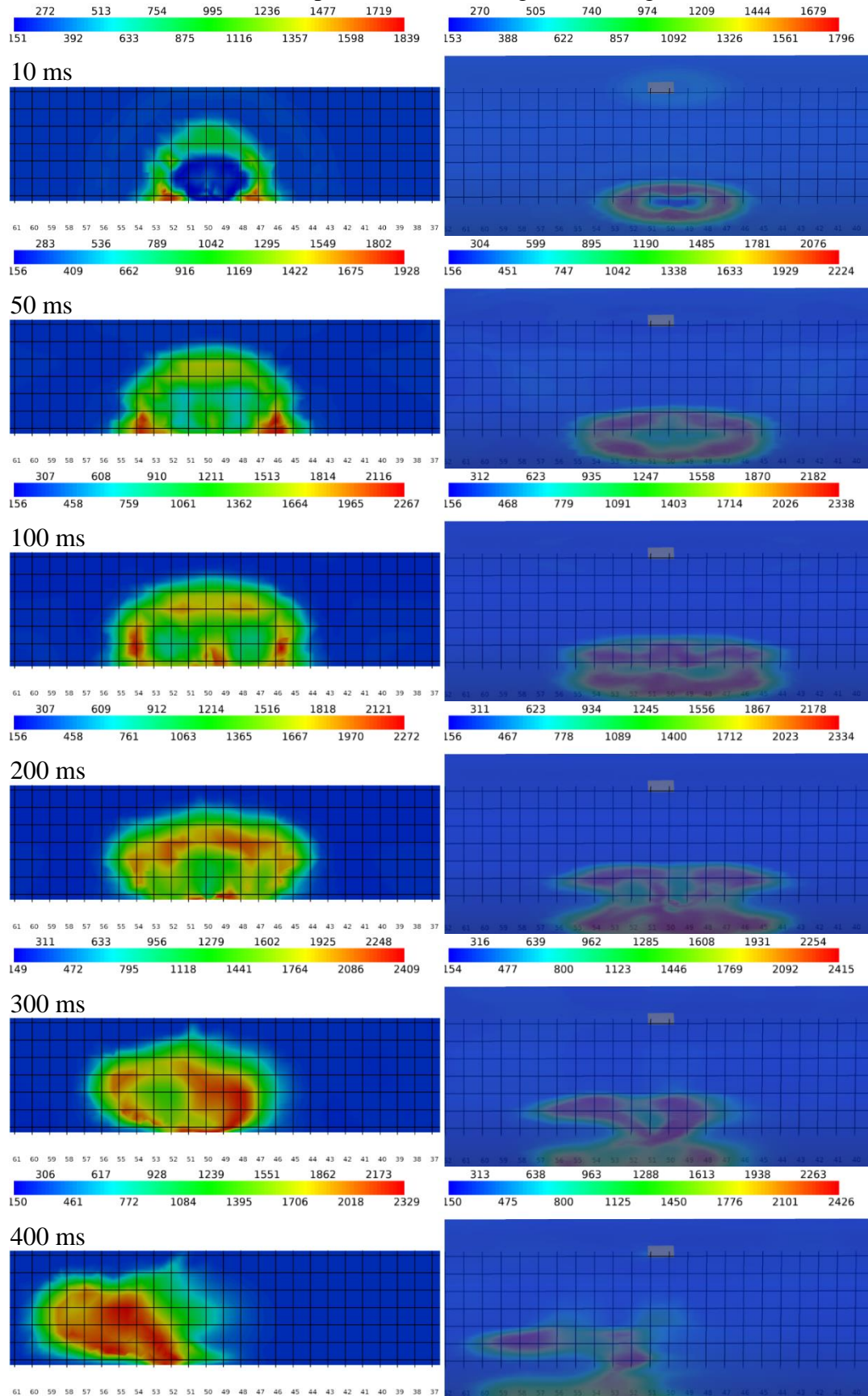


Figure 5. Fireball dynamics in a tunnel with cross-section area 83 m^2 (temperature contours): 2D tunnel centreline cross-section (left), 3D walls (right).

D4.3. Final report on analytical, numerical and experimental studies on explosions, including innovative prevention and mitigation strategies

2.1.2.5 Conclusions

The semi-empirical correlations to assess the fireball size after high-pressure hydrogen tank rupture in open space are proposed and compared with the experimental data on compressed hydrogen tank rupture in a fire and liquefied hydrogen spills. Due to the absence of tests inside the tunnel the correlations have been compared with the numerical simulation to assess the dynamics and the size of the fireball. As a preliminary conclusion it could be stated that none of simple correlations can be applied for the fireball hazard distance in a tunnel due to dynamics of its propagation. Further studies with different cross-sections and tank inventories that are required for verification of the proposed correlations and to support the preliminary conclusions will be performed in Section 3.7.

D4.3. Final report on analytical, numerical and experimental studies on explosions, including innovative prevention and mitigation strategies

2.2 Engineering model for assessment of overpressure during spurious hydrogen release (4.2, UU)

2.2.5 Background

In the case of an unscheduled hydrogen release from a high-pressure storage tank, there may be a delay between the beginning of release and ignition of flammable mixture created in the jet. This is a typical accident scenario with pressure hazards followed by thermal hazards produced from combustion products of the initial deflagration and the subsequent establishing jet fire. Pressure hazards associated with the turbulent hydrogen jet deflagration may be significant. For instance, experiments with a release orifice of 10 mm and spouting pressure of 40 MPa, generated an overpressure of 20 kPa at 4 m distance (Takeno et al., 2007), which is above the serious injury threshold (Lachance et al., 2011).

The study aimed to develop an engineering correlation for predicting the maximum overpressure that could be produced by a hydrogen jet, for a given storage pressure and release diameter. The engineering correlation was built through the similitude analysis and the use of 78 experiments with storage pressure in the range 0.5-65.0 MPa and release orifice diameter 0.5-52.5 mm. This approach is different from that suggested in D4.1 (HyTunnel-CS D4.1, 2019) as it was deemed more relevant and widely applicable. It is believed that a correlation developed for delayed ignition of hydrogen jets in an open space, may still be applicable to jets in enclosed spaces for defined boundary conditions.

2.2.6 Validation experiments

A total of 78 tests were selected to analyse the phenomenon and build the empirical correlation: (Royle and Willoughby, 2010) (Grune et al., 2013), (Grune, 2019) (Takeno et al., 2007), (Takeno, 2019) (Miller et al., 2015) (Daubech et al., 2015) (Friedrich et al., 2021). These include experiments on delayed ignition of both steady and unsteady, free, horizontal hydrogen jets. The location and number of sensors for overpressure measurements was variable and dependent on the experiment. Experiments had hydrogen storage pressure in the range 0.5-65 MPa, storage temperature 80-300 K, release diameter 0.5-52.5 mm. Maximum distance of the target from the release source was 50 m.

2.2.7 The similitude analysis

The storage pressure and release diameter determine the mass flow rate of hydrogen forming a flammable mixture and, therefore, affect the deflagration overpressure produced by delayed ignition of a hydrogen under-expanded jet. The first step in the similitude analysis was to consider the effect of storage conditions. In the assumption of storage temperature equal to ambient temperature, it is reasonable to suggest that deflagration overpressure grows with storage pressure, P_s . Thus, the first dimensionless parameter was: $\Pi_1 = P_s/P_0$, where P_0 is the ambient pressure. It was assumed that the fraction of flammable mixture with hydrogen concentration in air 25-35% defines the maximum overpressure in the blast wave. This range of concentration, characterises the most fast burning part of the cloud, as concluded in the study by (Makarov et al., 2018). In that study it was observed that only a small fraction of a non-uniform hydrogen-air mixture, with burning velocity within a narrow range 95-100% of the maximum value of burning velocity, defines the maximum vented deflagration pressure. This corresponds to hydrogen concentration range 25-35% by volume. The effect of combustion products expansion, turbulence generated by flame front itself and preferential

D4.3. Final report on analytical, numerical and experimental studies on explosions, including innovative prevention and mitigation strategies

diffusion instabilities were included into calculation of maximum burning velocity. The location with concentration 30% by vol. of hydrogen in air is assumed here as a centre of the mixture that will deflagrate and generate blast wave. The location of this centre was calculated using the similarity law for momentum expanded (Chen and Rodi, 1980) and under-expanded jets (Molkov, 2012). The distance between the centre of the 25-35% flammable cloud and the pressure sensor (in experiment) or “target” (person or structure) location is defined as R_w . The experimental studies demonstrated that the overpressure in the blast wave following the deflagration depends on the release diameter (Royle and Willoughby, 2010; Takeno et al., 2007). Apparently, the overpressure decreases with the increase of distance from the jet. Therefore, the second dimensionless parameter was defined here as the ratio of the orifice diameter, d , to the distance R_w , $\Pi_2 = d/R_w$. The derived dimensionless parameters were combined, following the similitude analysis rules, into a new dimensionless number:

$$\Pi = \Pi_1 \cdot \Pi_2^2 = \left(\frac{P_s}{P_0}\right) \cdot \left(\frac{d}{R_w}\right)^2 \quad (11)$$

The dimensionless overpressure in the deflagration blast wave, $\Delta P_{exp}/P_0$, can be represented as a function of the dimensionless number in previous equation:

$$\frac{\Delta P_{exp}}{P_0} = f\left(\left(\frac{P_s}{P_0}\right) \cdot \left(\frac{d}{R_w}\right)^2\right) \quad (12)$$

The derived correlation has been presented, analysed and calibrated against experimental data, and is shown in the next section.

2.2.8 Results and discussion

Figure 6 shows the distribution of the dimensionless, experimentally recorded, blast wave overpressure against the derived dimensionless number for all the tests available to the authors. Tests series by Health and Safety Executive (HSE) and Pro-Science (PS) present several values of $\Delta P_{exp}/P_0$ for the same dimensionless number Π . These tests are scattered by the ordinate as they were performed at different conditions of ignition delay and ignition point location. However, the main practical objective in the study is the derivation of an experimentally based, conservative correlation for determining the maximum overpressure that could be produced by delayed ignition of any hydrogen jet for arbitrary ignition conditions. Therefore, the maximum values of $\Delta P_{exp}/P_0$ will be used to build a conservative correlation. Figure 6 shows that the overpressure ratio ($\Delta P_{exp}/P_0$) correlates well to the dimensionless number $(P_s/P_0) \cdot (d/R_w)^2$.

D4.3. Final report on analytical, numerical and experimental studies on explosions, including innovative prevention and mitigation strategies

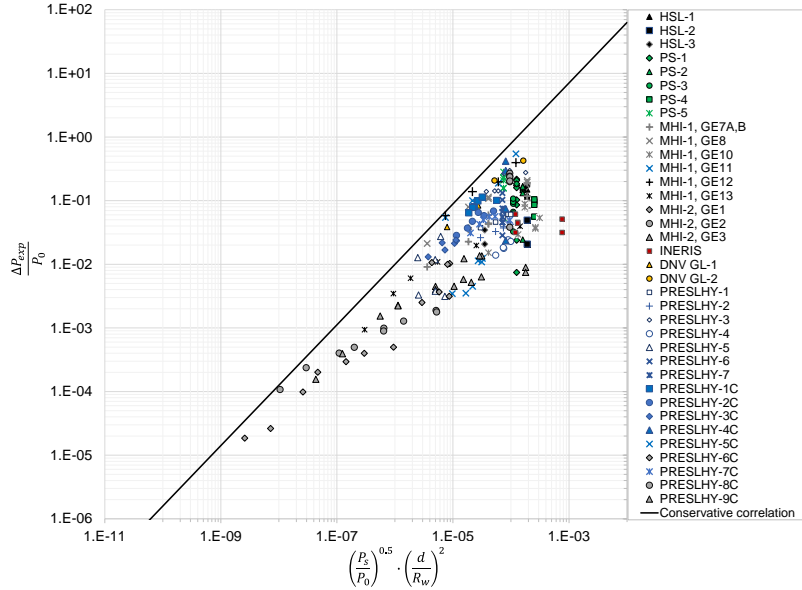


Figure 6. Derived correlation for predicting overpressure from delayed ignition of turbulent hydrogen jets versus experiments.

Thus, the conservative correlation for estimating the maximum overpressure from the release conditions and “target” location can be presented as:

$$\frac{\Delta P_{exp}}{P_0} = 5000 \cdot \left[\left(\frac{P_s}{P_0} \right)^{0.5} \cdot \left(\frac{d}{R_w} \right)^2 \right]^{0.95} \quad (13)$$

The present study may be further polished and finalised prior to intended publication into journal. The correlation is applicable to free jets in the open atmosphere and in the confined spaces with dimensions comparable to the jet axial distance to LFL.

2.2.8.1 Concluding remarks

An empirical correlation to estimate maximum overpressure from delayed ignition of hydrogen jets was derived and calibrated against experimental data available in literature.

2.3 Engineering tool for prevention and mitigation of composite hydrogen storage tank explosion in a fire (4.2, UU)

2.3.5 Background

The engineering tool for prevention and mitigation of composite hydrogen tank explosion in a fire is a part of the bigger model of tank-TPRD system performance in a fire, i.e., non-adiabatic blow-down model. The model was described in the publication presented at the International Conference on Hydrogen Safety (Dadashzadeh et al., 2019) and as a journal paper (Molkov et al., 2021). The parametric study and the results obtained in this section are based on the validation case presented in the paper (Dadashzadeh et al., 2019). The tank and the ambient (fire) parameters were described in the aforementioned papers.

2.3.6 Effect of heat release rate on fire rupture resistance

The engineering tools allow us to predict the time to tank rupture in a fire, i.e., its fire resistance rating, FRR, that can vary depending on the fire heat release rate, HRR, and the fire

D4.3. Final report on analytical, numerical and experimental studies on explosions, including innovative prevention and mitigation strategies

source size. It was previously demonstrated that the increase of the fire HRR decreases the tank's FRR (Kashkarov et al., 2018; Kim et al., 2015; Makarov et al., 2016) until, after a certain HRR value, it reaches saturation, when the FRR does not drastically decrease anymore and is equal about 4-6 min. Later, it was discovered at Ulster that a similar dependence trend and the FRR "saturation" occurs also for the fire source's specific heat release rate, i.e., fire source HRR divided by its area, A, i.e., HRR/A . It was revealed that the "saturation" onset occurs when the specific heat release rate of fire reaches values $HRR/A=1 \text{ MW/m}^2$, see Figure 7.

To obtain the relationship demonstrated in Figure 10 the engineering tool was used applying different values of heat flux to the tank surface. The graph demonstrates the saturation of the FRR with increase of the fire source specific HRR, HRR/A , above 1 MW/m^2 .

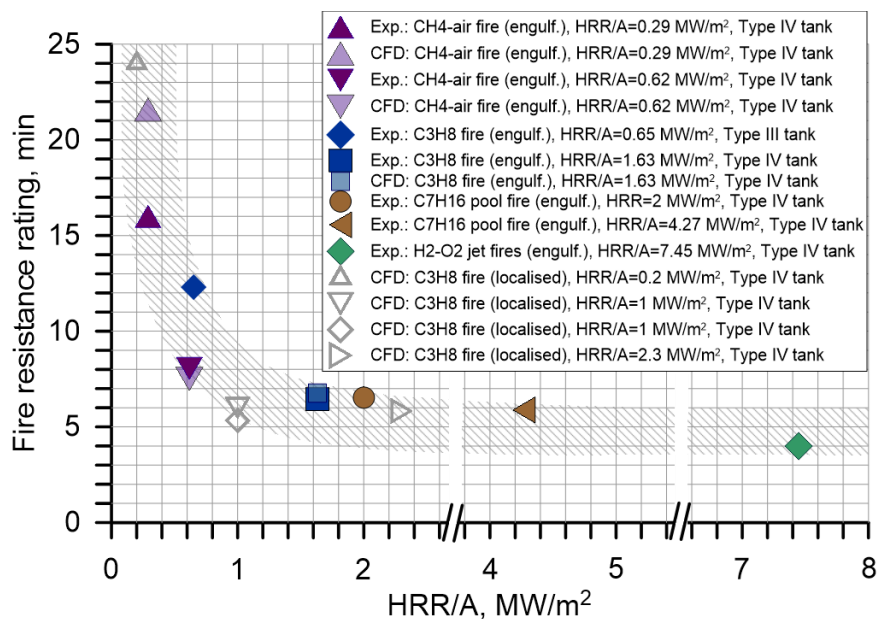


Figure 7. Hydrogen storage tank FRR vs fire source HRR/A (Molkov et al., 2021).

The heat flux values were obtained for fires with $HRR/A=1.0 \text{ MW/m}^2$, 0.62 MW/m^2 and 0.29 MW/m^2 (Figure 8 below). The parameters of the modelled 36 L and 700 bar Type IV tank and fire characteristics were described in the publication (Molkov et al., 2021).

D4.3. Final report on analytical, numerical and experimental studies on explosions, including innovative prevention and mitigation strategies

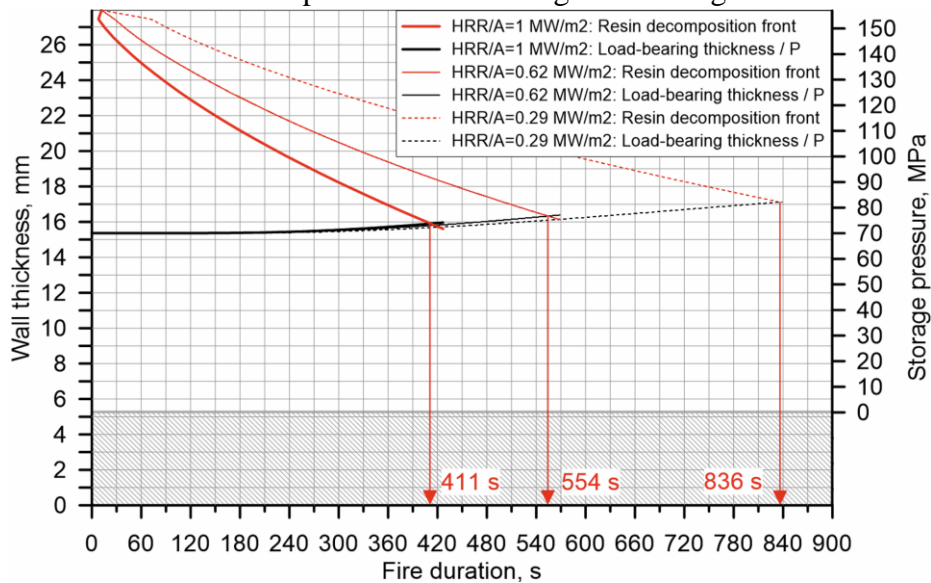


Figure 8. Tank rupture in a fire with varying HRR/A : 1 MW/m^2 , 0.62 MW/m^2 and 0.29 MW/m^2 (tank volume 36 L, initial pressure 700 bar); dynamics of tank wall decomposition, load-bearing wall thickness and tank storage pressure (Molkov et al., 2021).

In Figure 8 above, the Y-axis (left) is the tank wall thickness: liner (hatched bottom region) and carbon fibre reinforced polymer (CFRP) overwrap. The Y-axis (right) is the internal tank pressure. The pressure increases from 70 MPa at the start of the fire, to the final pressure at which the tank ruptures. The X-axis is the fire test duration. The black curves show the dynamics of load-bearing thickness and pressure; the red curves show the dynamics of resin decomposition front in the tank wall. The tank rupture criterion is defined as the contact of the resin decomposition front moving inwardly with the tank's dynamically changing (moving outwardly) load-bearing thickness. Using heat flux from fire with a given HRR/A as input the tool can easily predict the FRR of tank in the respective fire. Tank FRR can directly influence the risk of on-board hydrogen storage for different applications unless the tank is explosion-free in a fire.

2.3.7 Parametric study of effect of TPRD diameter and time of TPRD initiation on tank rupture

This section gives an example of the engineering tool application for modelling tank performance in a fire coupled with simulation of tank blowdown dynamics through a TPRD and effect of heat transfer to hydrogen. The goal of the study is to demonstrate how the engineering tool can help prevent tank rupture in a fire. The tool is accounting important physical phenomena behaviour, which can be observed in the fire test of high-pressure hydrogen storage tanks, such as: conjugate heat transfer from a fire to tank, tank materials degradation, internal hydrogen pressure dynamics, temperature dynamics and tank failure mechanism with determined FRR (validated in the study (Molkov et al., 2021)), initiation of hydrogen release through TPRD with non-adiabatic gas behaviour, liner melting causing the potential additional hydrogen leak etc. A number of assumptions were made in this parametric study. Firstly, two TPRD orifice sizes were used here – $\varnothing 0.45 \text{ mm}$ and $\varnothing 0.65 \text{ mm}$. The reduced orifices would help to prevent the pressure peaking phenomenon and exclude long jet fires. The TPRD activation time was 3 min after fire initiation and the fire HRR/A was 1

D4.3. Final report on analytical, numerical and experimental studies on explosions, including innovative prevention and mitigation strategies

MW/m², the tank was of Type IV, 36 L and charged to 70 MPa as mentioned in the previous section, see Figure 9 below.

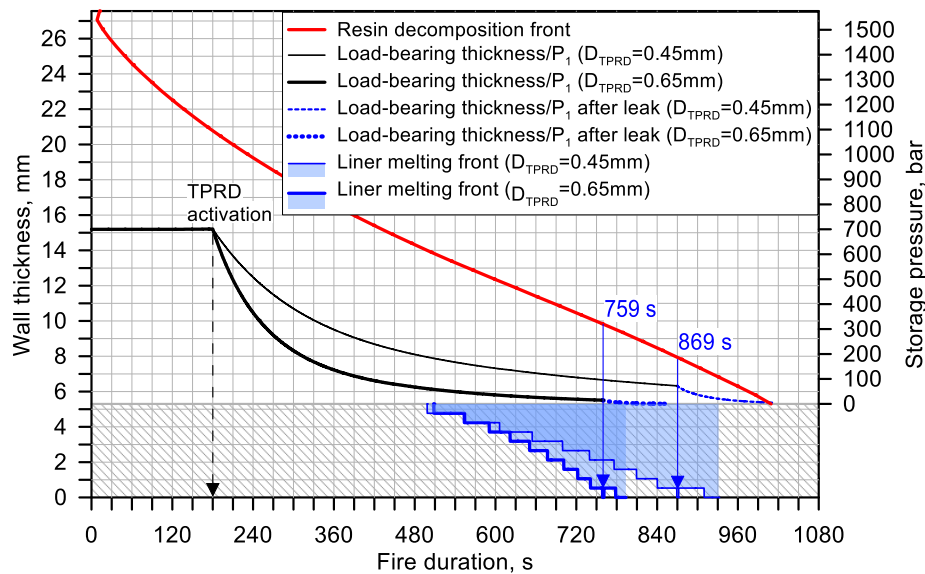


Figure 9. 36 L, 70MPa bar tank performance in a fire with blow-down through TPRD Ø0.45 mm and Ø0.65 mm, activation at 180 s after fire initiation - dynamics of tank wall decomposition front, load-bearing wall thickness, storage pressure and liner melting front (Molkov et al., 2021).

It is seen that after the TPRD initiation the load-bearing thickness of CFRP (and pressure) was slowly decreasing due to the pressure drop in the tank down to about 140 bar for orifice Ø0.45 mm, and below 50 bar for orifice Ø0.65 mm. The liner leakage occurred at 869 s and 759 s for TPRD orifices Ø0.45 mm and Ø0.65 mm respectively causing further pressure drop, down to atmospheric pressure, as shown with blue dash curves, because it created additional to TPRD orifice release areas.

2.4 Correlation for DDT in horizontal and vertical ventilation systems with non-uniform hydrogen-air mixtures in the presence of obstacles (4.2, KIT)

2.4.5 Introduction

The model allows the evaluation of the DDT conditions in a tunnel geometry for non-uniform hydrogen air mixtures. It consists of the four major parameters:

1. Geometry factors:
 - Confinement degree (confined, semiconfined, partially confined), lateral venting, end venting, smooth channel, rough channel, obstructions, fans, natural wind.
 - Scale (characteristic size – cross-section, length of the channel, length of the cloud of the hydrogen-air mixture).
 - The linearity of the channel (straight, bended, T-junction, Y-junction, zigzagging).
2. Mixture characterization:
 - Mixture uniformity/non-uniformity (longitudinal gradient, vertical stratification, vertical gradient).
 - Mixture reactivity (laminar flame velocity, expansion ratio, speed of sound, detonation velocity, detonation pressure, detonation cell size).

D4.3. Final report on analytical, numerical and experimental studies on explosions, including innovative prevention and mitigation strategies

3. Ignition source (electric spark, hot surface (glow plug), open flame, local explosion or blast wave)
4. History and dynamics of the process (run-up-distance, runway distance to flame acceleration and DDT)

2.4.6 Nomenclature

Parameter	Symbol	Unit
Height of the tunnel	H	m
Height of the hydrogen-air layer	h	m
Width of the tunnel	b	m
Cross section area	A	m ²
Blockage ratio	BR	(-)
Distance	x	m
Spacing between obstacles	s	m
Diameter	d, D	m
Gravity acceleration	g	m/s ²
Length	L	m
Universal gas constant	R	J/K/kmol
Volume fraction of hydrogen	X	(-)
Pressure	p	bar
Temperature	T	K
Molecular mass	M	kg/kmol
Density	ρ	kg/m ³
Characteristic time	t	s
Hydrogen inventory	m	kg

2.4.7 Model description

The model operates with several basic characteristics for DDT evaluation:

1. The mixture of hydrogen with air should be within the flammability limits 4 – 75 % H₂ (vol.). The criterion for flame acceleration is the critical expansion ratio for flame acceleration to speed of sound, $\sigma^*=3.75$ for hydrogen – air mixtures inside the enclosed channels (Dorofeev et al. 2001). It depends on the scale but not for the tunnel dimensions because the critical Peclet number $Pe = D/\delta \gg 100$ for tunnels. For partially confined envelope of hydrogen – air mixture, the critical expansion ratio depends on the opening degree, mixture uniformity and blockage ratio as the ratio of blocked area to the total cross-section area; see Figure 10 (Kuznetsov et al., 2011; Grune et al., 2013; Kuznetsov et al., 2015; Friedrich et al. 2019).

D4.3. Final report on analytical, numerical and experimental studies on explosions, including innovative prevention and mitigation strategies

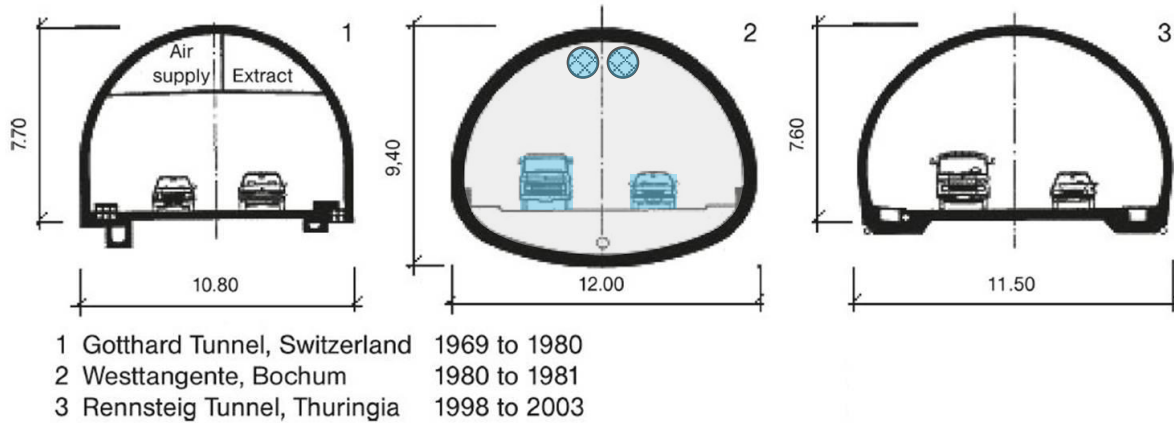


Figure 10. Examples of cross-sections (mined road tunnels). Grey area is the total cross-section, A ; blue area is blocked by turbo-fans and/or by cars, A_i . $BR = \sum A_i/A$.

A linear correlation between the critical expansion ratio σ^* and the ratio of the spacing between the obstacles and the layer thickness, s/h , was derived by Kuznetsov et al. (2011) for fast flame propagation based on large scale experiments (Figure 11) and theoretical considerations:

$$\sigma^* = \sigma_0^* \cdot (1 + K \cdot s/h) \quad (14)$$

where $\sigma_0^* = 3.75$ is the critical expansion ratio for uniform hydrogen-air mixture fully occupied the tunnel cross-section; $K = 0.175$ is a constant depending on the blockage ratio $BR = \sum A_i/A$, where A is the tunnel cross-section, A_i is the total visible blockage for cars, busses, trucks ventilators and other supporting equipment inside the tunnel; the spacing s can be a distance between cars in one lane. Eq. (14) is true for a layer of stratified hydrogen-air mixture; h is the layer thickness (Figure 13, left, bottom). It is valid for relatively small gradients (less than 30% H_2/m) in an assumption that the process of flame propagation governs by the highest hydrogen concentration at the ceiling. For a relatively high concentration gradient 40-60% H_2/m , efficiently, the only part of the mixture above 8-9% H_2 takes part in upward flame propagation. It results in a thinner layer of the mixture pushing the flame. This means that it requires higher hydrogen concentration to provide the flame acceleration to the speed of sound. For instance, it needs the maximum hydrogen concentration of 19% H_2 at the ceiling corresponding to 0.24 m of efficient layer thickness compared to 15 % H_2 and a layer thickness of 0.6 m for a uniform hydrogen-air composition to provide flame acceleration to speed of sound.

In case of a stratified hydrogen-air mixture fully occupied the cross-section of the system (Kudriakov et al., 2013; Kuznetsov et al., 2019), the process of combustion and flame acceleration is governed by the maximum hydrogen concentration at the top of the system with $h = H$ in Eq. (14).

D4.3. Final report on analytical, numerical and experimental studies on explosions, including innovative prevention and mitigation strategies

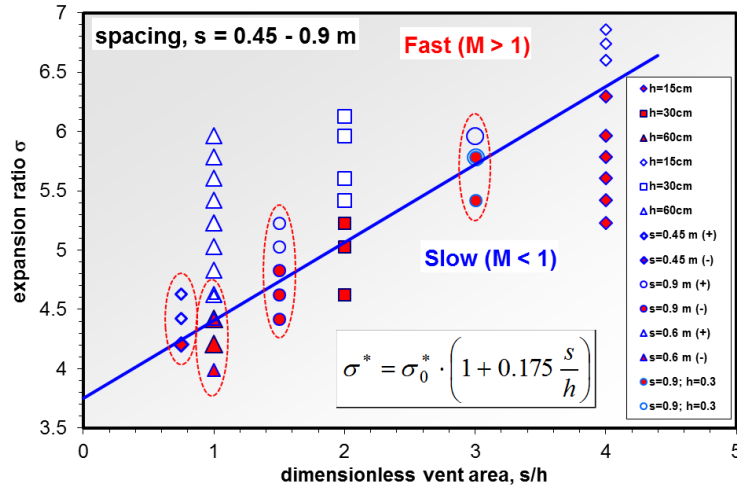


Figure 11. Critical conditions for effective flame acceleration as function of expansion ratio vs. dimensionless vent area: sonic flame and detonations (open points); subsonic flame (solid points). Different spacing is labelled (Kuznetsov et al., 2011).

- The DDT criterion is based on the ratio of characteristic tunnel dimension (for instance, an equivalent diameter $D = \sqrt{4A/\pi}$ to the detonation cell size, D/λ . The ratio D/λ should exceed the value N^* dependent on geometry, mixture reactivity, uniformity of the mixture (Moen et al., 1981; Teodorczyk et al., 1988; Dorofeev et al. 2001). Critical conditions for uniform or stratified semi-confined layer of hydrogen air mixture are given in terms of the ratio h/λ , where h is the layer thickness, see Figure 11, bottom (Kuznetsov et al., 2011; Grune et al., 2013; Kuznetsov et al., 2015; Rudy et al., 2013; Grune et al., 2013b).

The model includes the DDT criterion as dimensionless ratio L/λ of the characteristic size L over the detonation cell size λ as a measure of detonability of the mixture:

$$\frac{L}{\lambda} > N^* \quad (15)$$

where N^* is the critical value for detonation onset (DDT) or detonation propagation dependent on the geometry of the system. The tunnel relevant critical ratios of L/λ for detonation onset in a channel with obstacles fully filled with uniform mixture are summarized in Table 5.

D4.3. Final report on analytical, numerical and experimental studies on explosions, including innovative prevention and mitigation strategies

Table 5. Dimensionless scale for different processes.

Dimensionless scale	Critical value N^* , (-)	Detonation relevant phenomenon	References
D/λ	$1/\pi$	Detonation propagation in a smooth channel with diameter D	Moen et al. (1981)
d/λ	1	Detonation propagation in obstructed tubes with orifice size d ($BR^* < 0.43$)	Teodorczyk et al. (1988)
L/λ	7	Detonation onset in obstructed channels	Dorofeev et al. (2000)
L/λ	7	Detonation onset in multi-chamber structure	Dorofeev et al. (2000)

Most of the practical cases are covered by more universal criterion $L/\lambda > 7$ based on large scale experiments (Dorofeev et al., 2000). Characteristic size L for detonation onset is formulated depending on the size of the channel D , dimension of unobstructed passage between obstacle and sidewall d and spacing between repeating obstacles s :

$$L = \frac{D + s}{2 \left(1 - \frac{d}{D}\right)} \quad (16)$$

For tunnel geometry, it will be more convenient to express the ratio d/D through the blockage ratio BR because d -parameter is not well defined for the complex geometry of obstacles:

$$d/D = \sqrt{1 - BR} \quad (17)$$

The complex blockage ratio, in turn, can be expressed as follows

$$BR = \sum A_i/A \quad (18)$$

where A_i is the area of each visible object which is blocking the tunnel cross-section (a car or cars, a jet fan or ventilator, a truck or trucks). Then, assuming equidistant spacing $s = D$, Eq. (16) can be derived as a function of blockage ratio BR and an equivalent diameter D keeping constant the DDT condition $L/\lambda = 7$:

$$L = \frac{D}{1 - \sqrt{1 - BR}} = 7\lambda \quad (19)$$

Table 6 summarizes the results of such a practical transformation of Eq. (16). It may tell us several conclusions useful for tunnel safety assessment. For very small blockage $BR = 0.1$ characteristic length for DDT is about 20 diameters ($L/D = 19.5$). For practically unblocked tunnel ($BR=0.1$) the critical ratio $D/\lambda = 0.36$ approach to the ratio $D/\lambda = 1/\pi$ found by Moen et al. (1981) for smooth tubes. The critical ratio $d/\lambda = 0.96$ for $BR = 0.3$ and $d/\lambda = 1.22$ for $BR =$

D4.3. Final report on analytical, numerical and experimental studies on explosions, including innovative prevention and mitigation strategies

0.4 are very close to the DDT criterion $d/\lambda = 1$ found by Teodorczyk et al. (1988) for obstructed tube with $BR < 0.43$. The higher blockage leads to larger ratios D/λ and d/λ . For the tunnel geometry, we cannot expect the blockage larger than 30% except the rail tunnels where the blockage by the train can reach 50-60 %.

Table 6. Critical ratios for DDT as function of blockage ratio.

Blockage ratio BR	L/D	D/l	d/l
0.1	19.49	0.36	0.34
0.2	9.47	0.74	0.66
0.3	6.12	1.14	0.96
0.4	4.44	1.58	1.22
0.5	3.41	2.05	1.45
0.6	2.72	2.57	1.63

All of the aforementioned relationships for detonation onset are relevant to the very hypothetical scenario for uniform hydrogen-air mixture fully filled the tunnel cross-section. The most realistic scenario for tunnel geometry is the formation of a stratified layer of the hydrogen-air mixture on top of the channel (Figure 12). It was found by Li (2019) that due to open boundaries in the axial direction, the cloud grows only in the longitudinal direction with almost constant layer thickness remaining within 0.5-0.6 m.

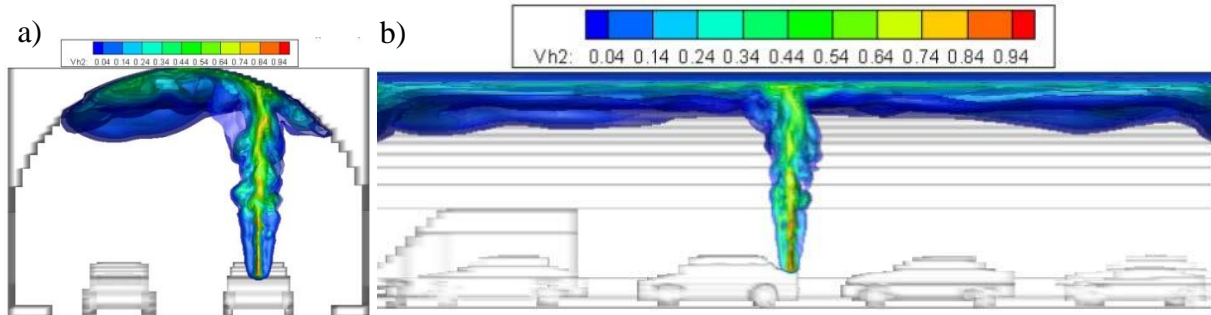


Figure 12. Hydrogen distribution profiles in a tunnel: a) front view; b) side view (Li et al., 2019).

Critical conditions for detonation onset in a semi-confined layer of the uniform hydrogen-air mixture have been experimentally found in a cylinder vessel of 3.5 m ID (Kuznetsov et al., 2011; Kuznetsov et al., 2015):

$$H/\lambda = 13 - 14 \quad (20)$$

where h is the layer thickness. For the stratified layer, similar to shown in Figure 12, If the hydrogen concentration gradient is not larger than $60\% \text{H}_2/\text{m}$, the critical condition for a detonation onset is the same (see Eq. (20)) as for uniform hydrogen composition of the same hydrogen concentration as the maximum concentration of the stratified composition. It happens when the efficient layer thickness is not less than the corresponding layer thickness for the uniform mixture.

$$h^* = X_{\text{H}_2} / \text{grad}(X_{\text{H}_2}) \quad (21)$$

D4.3. Final report on analytical, numerical and experimental studies on explosions, including innovative prevention and mitigation strategies

For instance the efficient layer thickness $h^* = 1.05$ m for $\text{grad}(X_{H_2}) = 20\% \text{ H}_2/\text{m}$ and $h^* = 0.7$ m for $\text{grad}(X_{H_2}) = 30\% \text{ H}_2/\text{m}$ for stratified compositions, which are larger than 0.6 m of detonable uniform composition. In the case of a very steep gradient (more than $60\% \text{ H}_2/\text{m}$) the effective layer thickness $h^* = 0.33$ m becomes too thin to be detonable. For such a layer thickness the maximum hydrogen concentration should be higher than $23\% \text{ H}_2$. This value is very close to the experimental one $23.6\% \text{ H}_2$ (Kuznetsov et al., 2015). Then, for the stratified semiconfined layer the critical DDT condition

$$h^*/\lambda = 13 - 14 \quad (22)$$

3. Both of the aforementioned criteria for flame acceleration and DDT require the satisfaction of so-called “run-up-distance (RUD) criterion”, $X_s < L$, where L is a characteristic length of hydrogen - air cloud along the channel (Veser et al., 2002; Kuznetsov et al., 2005; Ciccarelli et al., 2008). If the cloud dimension L is longer than the run-up-distance to speed of sound X_s then the detonation may occur.

The run-up distance to detonation depends on mixture reactivity and the level of turbulence. Both factors can promote flame acceleration and shorten the run-up distance X_s . A high level of turbulence can be introduced by fans or by other obstacles. In a tunnel it can be a ventilation system or traffic of the cars. If there are no obstacles and the channel is relatively smooth, then the boundary layer is the only source of the turbulent motion. Based on the critical thickness of the boundary layer for detonation onset $\delta = 10\lambda$ a run-up-distance to detonation was experimentally evaluated depending on the tube roughness (Kuznetsov et al., 2005):

$$X_s = 550\lambda \quad (23)$$

Eq. (23) is valid for very thick tubes similar to a tunnel with $D > 20\lambda$. For relatively narrow tubes with $10\lambda < D < 20\lambda$ the run-up-distance X_s is proportional to tube diameter D depending on roughness Δ :

$$X_s = (24 - 27)D, \quad \Delta = 100\mu \quad (24)$$

$$X_s = (18 - 19)D, \quad \Delta = 1000\mu \quad (25)$$

$$X_s = (12 - 14)D, \quad \Delta = 5000\mu \quad (26)$$

These values fit very well to $X_s = (15-40) D$ according to papers Bollinger et al. (1961) and Laffitte and Dumanois (1926). To take into account the effect of roughness and involving the boundary layer theory Equations (24) to (26) have been transformed as follows (Ciccarelli et al., 2008)

$$X_s = D \frac{\gamma}{C} \left[\frac{1}{\kappa} \ln \left(\gamma \frac{D}{h} \right) + K \right] \quad (27)$$

D4.3. Final report on analytical, numerical and experimental studies on explosions, including innovative prevention and mitigation strategies

where κ , K , and C are the physical constant from turbulent boundary layer theory (Landau and Lifshitz, 1986): $\kappa = 0.4$, $K = 5.5$, and $C = 0.2$; D/h can be expressed through the blockage ratio:

$$\frac{D}{h} = \frac{2}{1 - \sqrt{1 - BR}} \quad (28)$$

$$\gamma = \left[\frac{a_p}{\eta S_L (\sigma - 1)^2} \left(\frac{\delta}{D} \right)^{1/3} \right]^{\frac{1}{2m+7/3}} \quad (29)$$

where S_L is the laminar flame speed; $\delta = \nu/S_L$ is the laminar flame thickness; ν is the kinematic viscosity; η and m are two incognita derived from experimental data (Kuznetsov et al., 1999; Lindstedt et al., 1989; Kuznetsov et al., 2005b; Kuznetsov et al., 2003): $\eta=2.1$ and $m=-0.18$. Relations Eq. (27) to (29) consider roughness as a measure of blockage but the relations are valid only up to very small blockage ratio $BR < 0.1$. There is another relationship to calculate the run-up-distance to supersonic flame within the range $BR = 0.3 - 0.75$ (Veser et al., 2002):

$$X_s = \frac{a_p D \cdot (1 - BR)}{(1 + 1.5 \cdot BR) \cdot 10 S_L (\sigma - 1)} \quad (30)$$

Due to the gap of blockage ratios for the validity of Eq. (27) and Eq. (30) between $BR = 0.1$ and $BR = 0.3$, a linear interpolation between two bounding points X_s/D ($BR=0.3$) and X_s/D ($BR=0.1$) can be used (Ciccarelli et al., 2008). For the practical application, we can propose to extend the correlation Eq. (30) to blockage ratio $BR = 0.1$ with 3 times under-prediction compared to Eq. (27).

Both relationships Eq. (27) and Eq. (30) include laminar flame speed S_L and laminar flame thickness δ as the measures of reactivity of the mixture. The detonability factor detonation cell size λ is not included in the consideration. Then, it might be a curious result obtained that the distance is enough for the detonation onset, but the detonation cell size is too big for the system to make the system detonable. In such a case, a supersonic flame should be considered. One of the disadvantages and also a conservatism of the correlations Eq. (27) and Eq. (30) is that they cover the cases of uniform mixtures in an enclosed channel. So that for a semi-confined layer of a stratified hydrogen-air mixture it might be an under-predicted result (a shorten run-up-distance). The under-prediction can be compensated by the existence of local zones enriched with hydrogen in the vicinity of the source and also by some barriers of the tunnel structure or big trucks carrying huge cargo reducing the run-up-distance.

4. Characteristic reactivity, geometry, the scale/dimension of the hydrogen-air cloud produced by accidental hydrogen release should be defined depending on the release scenario, total hydrogen inventory, and characteristic time. Characteristic time is the time span between hydrogen release and ignition moments required for hydrogen distribution and cloud formation.

The cloud can be uniform (Figure 13, left, very hypothetical) or a more realistic stratified layer (Figure 13, right). It can be fully filled the tunnel cross-section (Figure 13, top) or formed as a

D4.3. Final report on analytical, numerical and experimental studies on explosions, including innovative prevention and mitigation strategies

layer on top of the compartment (Figure 13, bottom). The typical layer geometry of the cloud is shown in Figure 12 and Figure 14 based on GASFLOW numerical simulations. The case of uniform hydrogen distribution is more typical for vertical vents from a tunnel to the atmosphere. The case of high-pressure hydrogen jet cloud with a radial hydrogen distribution will not be considered in the tool. The average hydrogen concentration in the case of a uniform hydrogen-air cloud and the maximum hydrogen concentration at the ceiling of the tunnel is assumed to be the characteristic concentration of hydrogen to evaluate the reactivity of the cloud.

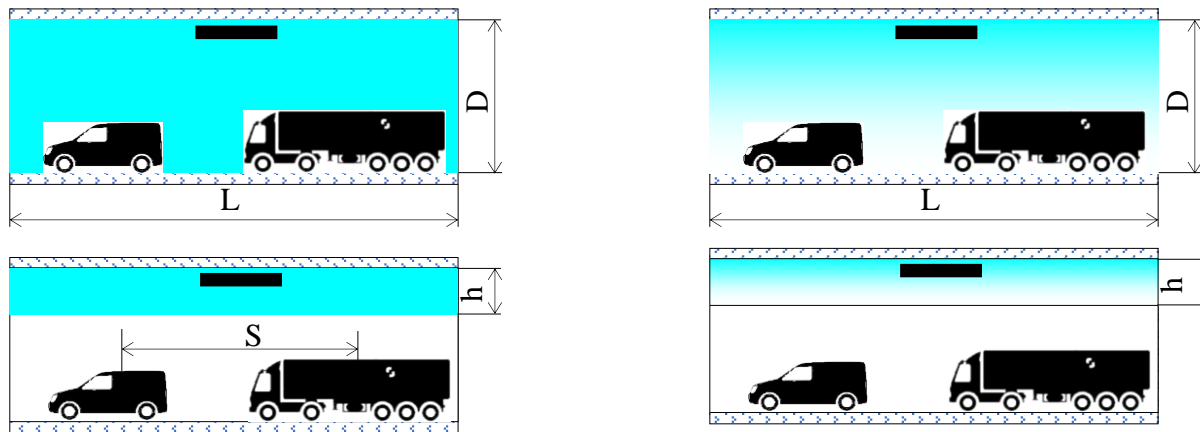


Figure 13. Typical geometry of hydrogen-air cloud inside the tunnel: uniform composition (left); stratified composition (right); fully filled cross-section (top); a semiconfined layer (bottom).

As follows from GASFLOW numerical simulations (Li et al., 2019) for 3.5 kg of hydrogen distribution from high pressure tank (70 MPa, 5 mm TPRD device) in a tunnel ($D = 9.6$ m, $H = 6.6$ m) the most realistic cloud geometry is a semiconfined layer of stratified hydrogen in air along the tunnel (Figure 14). The figure shows the flammable hydrogen cloud (H_2 vol $>4\%$) in the tunnel at different times. The hydrogen cloud is gathering at the ceiling and is pushed sidewise along the tunnel by the continuous hydrogen jet. Hence, a layer of combustible hydrogen with thickness 0.5-0.6 m is formed at the tunnel ceiling. Figure 14 (d) at 16 s corresponds to the time when hydrogen inventory within the flammability limits has a maximum of about 2.5 kg. The mass flow rate drops down from 0.5 kg/s to 0.1 kg/s at this moment. This time is about a third of the total release time of about 50 s. However, almost 70% of the total hydrogen inventory was released during this time. The hydrogen concentration has a strong vertical gradient with the maximum hydrogen concentration near the ceiling around 40% decreasing to 0% at the bottom of the layer. It is supposed to be the most dangerous moment with respect to the severity of the hydrogen explosion. We may take the region of the hydrogen layer (0.6 m below the ceiling) at the time of the third of the total release time to evaluate the hydrogen risk with respect to the flame acceleration and DDT. Such evaluation can be quite conservative because for a smaller nozzle diameter of TPRD device it can be a smaller fraction of total hydrogen inventory as a maximum amount of hydrogen contained within the hydrogen flammability limits.

D4.3. Final report on analytical, numerical and experimental studies on explosions, including innovative prevention and mitigation strategies

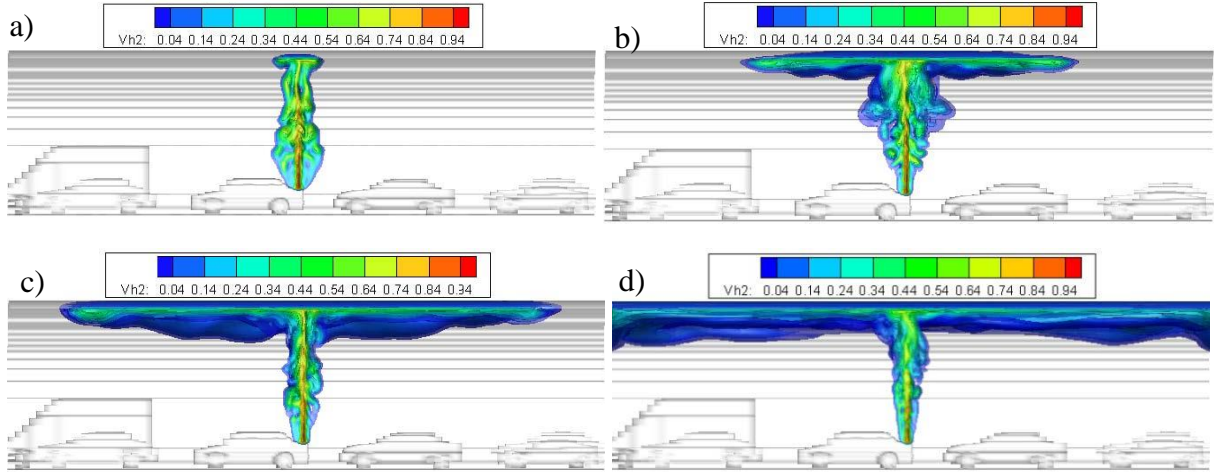


Figure 14. Hydrogen distribution profiles in a tunnel vs. time after release: a) 1 s; b) 4 s; c) 8s; d) 16 s.

Now, we can specify the geometry of hydrogen-air clouds for different tunnel geometries. Three most typical tunnel cross-sections are given in Figure 10. A round shape (4) and a rectangular cross-section (5) can also be introduced as the simplest and the basic ones to be combined to reproduce the real tunnel cross-sections. Within the Hytunnel-CS project (D2.2, Ch. 4.3), typical dimensions for different tunnels and hydrogen inventories for typical vehicles are summarized to be used as input data for safety evaluations (Table 7, Table 8, Table 9, Table 10). Depending on the hydrogen inventory, the volume and dimension of the cloud a characteristic hydrogen concentration can be calculated for uniform and stratified hydrogen clouds.

The characteristic length of the cloud L for the given average hydrogen concentration X_{H_2} can be calculated for hydrogen inventory m of uniform hydrogen distribution (Figure 13, left):

$$L = V/A, \quad (31)$$

where V is the volume of hydrogen-air mixture as a function of average hydrogen concentration X_{H_2}

$$V = \frac{1}{X_{H_2}} \cdot \frac{pM}{mRT} \quad (32)$$

A is the tunnel cross-section area (CSA) (Table 7, Table 8) of a layer cross-section area:

$$A = b \cdot h \quad \text{for rectangular tunnel } b \cdot H \quad (33)$$

D4.3. Final report on analytical, numerical and experimental studies on explosions, including innovative prevention and mitigation strategies

Table 7. Dimensions of European road tunnels.

	Tunnel Description	Cross-section Area, CSA (m ²)	Real Diameter, D (m)	Equivalent Diameter, D (m)
1	Single lane tunnel	24.10	N/A	5.54
2	Double lane tunnel	39.50	N/A	7.09
3	Gotthard tunnel, double lane	49.35	7.74	7.93
4	Rennsteig tunnel, double lane	72.95	7.5	9.64
5	Tyne tunnel (Original), double lane	48.10	7.3	7.83

Table 8. Dimensions of European rail tunnels.

	Tunnel Description	Cross-section Area, CSA (m ²)	Real Diameter, D (m)	Equivalent Diameter, D (m)
1	High speed traffic, two rail	92.0	N/A	10.82
2	Express traffic tunnel, two rail	79.2	N/A	10.04
3	Metro type traffic, single rail	44.6	N/A	7.54
4	Rectangular section urban rail, two rail	56.3	N/A	8.47
5	Severn tunnel, two rail	60.0	7.93	8.74
6	Channel tunnel single rail	53.5	7.6	8.25

Table 9. Initial hydrogen inventory, mass flow rate and discharge time for different vehicles.

Vehicle	Total Vehicle Inventory (kg)	Single Tank Inventory (kg)	Initial mass flow rate (kg/s)	Discharge time (secs)
Car (700 Bar)	5.4	2.7	0.215	168
Bus (350 bar)	40.0	4.97	1.638	134
Train 1 (350 bar)	96.0	4.14	7.85	67
Train 2 (350 bar)	105.0	5.80	5.89	97

Table 10. Hydrogen storage specifications for different car.

Car/Model	Year	No tanks	Vessel pressure (MPa)	Mass per tank / total (kg)	Volume per tank / total (liters)
Mercedes-Benz GLC F-CELL.	2018	2	70	2.2 / 4.4	57.5 / 115
Hyundai NEXO Fuel Cell	2018	3	70	2 / 6	52 / 156
Honda Clarity Fuel Cell	2016	2	70	? / 5.46	144
Toyota Mirai	2015	2	70	2.3 / 4.6	60 + 62.4 / 122.4
Hyundai Tucson/ix35 FCEV	2013	2	70	? / 5.6	/ 133

D4.3. Final report on analytical, numerical and experimental studies on explosions, including innovative prevention and mitigation strategies

$$A = \frac{\Theta - \sin\Theta}{2} R^2, \text{ for a circular cross-section of the tunnel} \quad (34)$$

where $R=D/2$; Θ is a vision angle for the segment of hydrogen layer of the height h :

$$\frac{\Theta}{2} = \arccos\left(\frac{R-h}{R}\right), \text{ for a circular cross-section of the tunnel} \quad (35)$$

The average hydrogen concentration X_{H_2} in Eq. (32) and the layer thickness h should be the input parameters. For a stratified hydrogen distribution, the average maximum hydrogen concentration at the top of the tunnel should be an input parameter. A linear gradient of hydrogen concentration from X_{H_2} (MAX, AVERAGE) to 0 within the layer thickness h is assumed. Then, the gradient of concentration is calculated as follows

$$\text{grad}(X_{H_2}) = X_{H_2}/h \quad (36)$$

The volume of the cloud of hydrogen – air mixture will be two times larger compared to the uniform cloud with the same hydrogen concentration X_{H_2} :

$$V = \frac{2}{X_{H_2}} \frac{pM}{mRT} \quad (37)$$

The height of the layer in a tunnel geometry with quite a large TPRD device (about 5 mm ID) is recommended to be by default $h = 0.6$ m supported by the natural gravity and density differences.

2.4.8 Option 1: Uniform hydrogen concentration distributed over the full tunnel cross-section for the given hydrogen inventory

This option allows the user to calculate the detonability of the uniform hydrogen-air cloud formed by the release of 2 and 10 kg of hydrogen in an assumption of the total cross-section filled with the cloud. Five levels of average hydrogen mole fraction in the cloud from 10% to 30% H_2 are analysed.

2.4.8.1 Input data

Table 11. Initial properties of the system.

Parameter name	Symbol	Value		Range	Unit
Cloud uniformity and geometry	U, N	U1 (Figure 13)		(U1, U2, N1, N2)	(-)
Hydrogen inventory	m_{H_2}	2	10	0.1-100	kg
Mole fraction of hydrogen	X_{H_2}	0.1		8-75	(-)
Mole fraction of hydrogen	X_{H_2}	0.11		8-75	(-)
Mole fraction of hydrogen	X_{H_2}	0.15		8-75	8-75

D4.3. Final report on analytical, numerical and experimental studies on explosions, including innovative prevention and mitigation strategies

Mole fraction of hydrogen	X_{H2}	0.20	8-75	(-)
Mole fraction of hydrogen	X_{H2}	0.30	8-75	(-)
Ambient pressure	p	1e5	(1-2)e5	Pa
Ambient temperature	T	293	253-313	K
Area of the tunnel cross-section	A	85.8	0.1-100	m ²
Height of the tunnel cross-section	H	8.89	1-15	m
Diameter of the tunnel cross-section	D	10.46	1-15	m
Spacing between cars	S	10.46	0.1-50	m
Blocked area by three cars	ΣA_i	17.79 (Table 9)	m	m ²

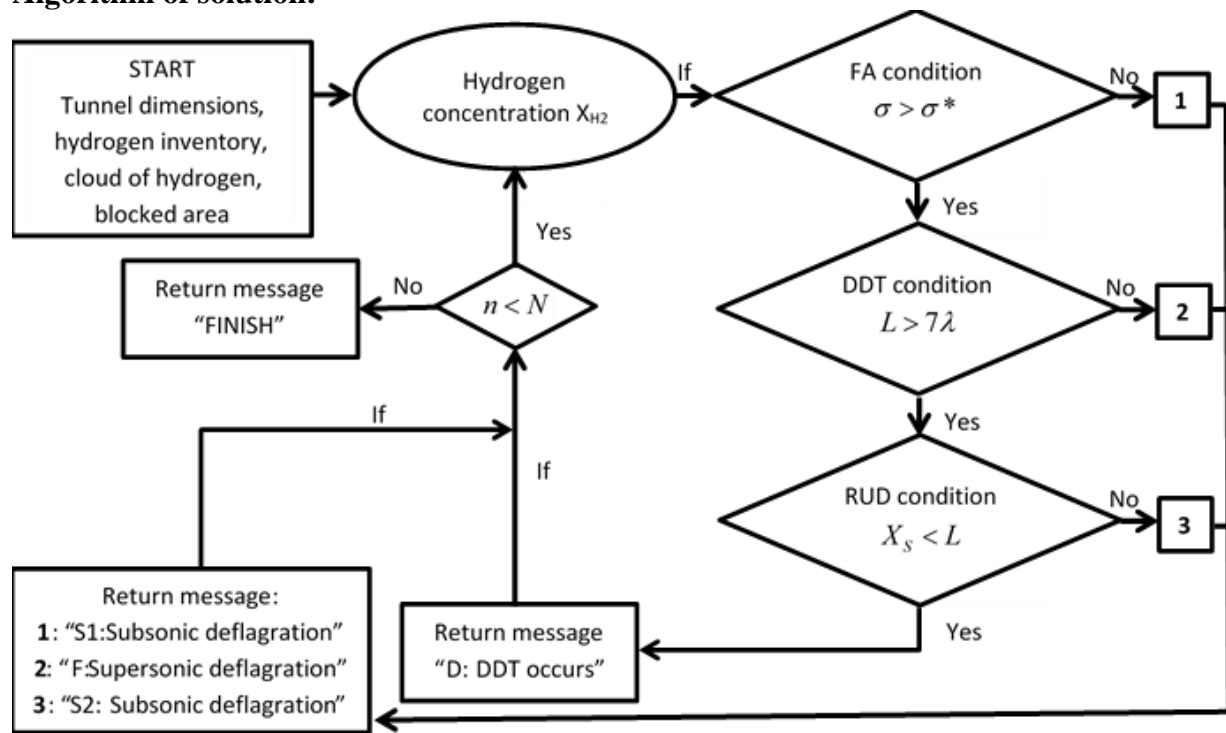
2.4.8.2 Calculation procedure

Steps 1,2,3...

1	Hydrogen-air cloud geometry	Figure 13	(-)
2	Expansion ratio, s	Table 12	(-)
3	Flame acceleration evaluation	$\sigma > \sigma^* = 3.75$	Yes / No
4	Detonation cell size, l	Table 12	m
5	Pre-detonation length, L	$L = \frac{D+S}{2\left(1-\frac{d}{D}\right)}$ or $L = \frac{D}{1-\sqrt{1-BR}}$ if ($S=D$)	m
6	Blockage ratio	$BR = \Sigma A_i / A$	(-)
7	Ratio d/D	$\frac{d}{D} = \sqrt{1-BR}$	(-)
8	Detonation evaluation	$L > 7\lambda$	Yes/No
9	DDT run-up-distance, X_s	$X_s = \frac{a_p D \cdot (1-BR)}{(1+1.5 \cdot BR) 10 S_L (\sigma-1)}$	m
10	a_p , S_L evaluation	Table 13	m/s
11	Length of hydrogen cloud	$L = V / A$	m
12	Volume of hydrogen cloud	$V = \frac{1}{X_{H2}} \frac{pM}{mRT}$	m ³
13	Universal gas constant, R	$R = 8314.47$	J/K/kmol
14	Final detonability evaluation	$X_s < L$	Yes/No

D4.3. Final report on analytical, numerical and experimental studies on explosions, including innovative prevention and mitigation strategies

Algorithm of solution:



D4.3. Final report on analytical, numerical and experimental studies on explosions, including innovative prevention and mitigation strategies

Table 12. Main properties of hydrogen-air combustible mixtures.

H ₂ mole fraction* X _{H2}	Expansion ratio** s	Detonation cell size*** l, mm	H ₂ mole fraction X _{H2}	Expansion ratio s	Detonation cell size l, mm
0.09	3.31	18040	0.296	7.00	9.8
0.1	3.54	5095	0.3	7.02	9.7
0.11	3.77	2319	0.35	6.90	9.7
0.12	3.99	1289	0.4	6.60	11.9
0.13	4.21	798	0.45	6.27	16.8
0.14	4.42	531	0.5	5.91	27.3
0.15	4.63	361	0.55	5.53	57.4
0.16	4.83	252	0.6	5.12	148
0.18	5.23	114	0.65	4.69	362
0.2	5.60	44.6	0.7	4.24	930
0.22	5.96	24.6	0.75	3.76	2957
0.25	6.45	14.5	0.8	3.25	21230

* The data for intermediate concentration can be linearly or by spline interpolated.

** Expansion ratios are calculated by STANJAN and Cantera codes (Reynolds, 1986; Goodwin, 2001).

*** Detonation cell sizes are calculated with CELL_ H₂ program based on Gavrikov et al. (2000) paper.

Table 13. Laminar flame speed and speed of sound for combustion products.

H ₂ mole fraction* X _{H2}	Laminar velocity** SL, m/s	Speed of sound** a _p , m/s	Kin. viscosity** ν, cm ² /s	H ₂ mole fraction X _{H2}	Laminar velocity SL, m/s	Speed of sound a _p , m/s	Kin. viscosity ν, cm ² /s
0.09	0.171	636	0.165	0.296	2.677	980	0.202
0.1	0.246	659	0.167	0.3	2.719	983	0.203
0.11	0.334	682	0.168	0.35	3.131	1024	0.214
0.12	0.432	703	0.170	0.4	3.333	1047	0.227
0.13	0.541	724	0.171	0.45	3.313	1068	0.242
0.14	0.657	745	0.173	0.5	3.082	1087	0.258
0.15	0.781	765	0.175	0.55	2.672	1106	0.277
0.16	0.910	784	0.176	0.6	2.129	1125	0.299
0.18	1.180	821	0.180	0.65	1.516	1145	0.325
0.2	1.458	855	0.183	0.7	0.905	1165	0.356
0.22	1.737	888	0.187	0.75	0.375	1186	0.393
0.25	2.139	931	0.192	0.8	0.009	1206	0.441

* The data for intermediate concentration can be linearly or by spline interpolated.

** The data are calculated by STANJAN and Cantera codes (Reynolds, 1986; Goodwin, 2001).

D4.3. Final report on analytical, numerical and experimental studies on explosions, including innovative prevention and mitigation strategies

2.4.8.3 Output values

Table 14. Output data for hydrogen inventory, $m = 2$ kg.

Hydrogen inventory, $m = 2$ kg							
Parameter name	Symbol	Unit	Output values				
			Hydrogen mole fraction, X_{H_2}				
			0.1	0.11	0.15	0.2	0.3
Expansion ratio, s	s	(-)	3.54	3.77	4.63	5.6	7.02
Detonation cell size, l	l	mm	5095	2320	361	44.6	9.7
Blockage ratio, BR	BR	(-)	0.207	0.207	0.207	0.207	0.207
Pre-detonation length, L	L	m	95	95	95	95	95
DDT length	$7l$	m	35.7	16.2	2.53	0.31	0.07
Volume of hydrogen cloud	V	m^3	240	219	160	120	80
Length of hydrogen cloud	L	m	2.8	2.5	1.9	1.4	0.93
Sound speed in products	a_p	m/s	659	682	765	855	983
Laminar velocity	S_L	m/s	0.25	0.33	0.78	1.46	2.7
Run-up-distance (RUD)	X_s	m	666	467	171	81	39
Result			S1	S2	S2	S2	S2

Note: S1 – subsonic deflagration ($\sigma < \sigma^* = 3.75$); S2 - supersonic deflagration ($\sigma > \sigma^*$, $X_s \gg L$).

Table 15. Output data for hydrogen inventory, $m = 10$ kg.

Hydrogen inventory, $m = 10$ kg							
Parameter name	Symbol	Unit	Output values				
			Hydrogen mole fraction, X_{H_2}				
			0.1	0.11	0.15	0.2	0.3
Expansion ratio, s	s	(-)	3.54	3.77	4.63	5.6	7.02
Detonation cell size, l	l	mm	5095	2320	361	44.6	9.7
Blockage ratio, BR	BR	(-)	0.207	0.207	0.207	0.207	0.207
Pre-detonation length, L	L	m	95	95	95	95	95
DDT length	$7l$	m	35.7	16.2	2.53	0.31	0.07
Volume of hydrogen cloud	V	m^3	1200	1095	800	600	400
Length of hydrogen cloud	L	m	14	12.5	9.5	7	4.65
Sound speed in products	a_p	m/s	659	682	765	855	983
Laminar velocity	S_L	m/s	0.25	0.33	0.78	1.46	2.7
Run-up-distance (RUD)	X_s	m	666	467	171	81	39
Result			S1	S2	S2	S2	S2

Note: S1 – subsonic deflagration ($\sigma < \sigma^* = 3.75$); S2 - supersonic deflagration ($\sigma > \sigma^*$, $X_s \gg L$).

2.4.9 Option 2: Uniform hydrogen concentration distributed inside a layer of hydrogen-air mixture for the given hydrogen inventory

This option allows user calculating the detonability of the uniform cloud formed as a layer of hydrogen-air mixture by the release of 2 and 10 kg of hydrogen. Five levels of average hydrogen mole fraction in the cloud from 10 to 30% H_2 are analysed.

D4.3. Final report on analytical, numerical and experimental studies on explosions, including innovative prevention and mitigation strategies

2.4.9.1 Input data

Table 16. Initial properties of the system.

Parameter name	Symbol	Value		Unit
Hydrogen inventory	m_{H_2}	2	10	kg
Mole fraction of hydrogen	X_{H_2}	0.1		(-)
Mole fraction of hydrogen	X_{H_2}	0.11		(-)
Mole fraction of hydrogen	X_{H_2}	0.15		(-)
Mole fraction of hydrogen	X_{H_2}	0.20		(-)
Mole fraction of hydrogen	X_{H_2}	0.30		(-)
Ambient pressure	p	1		bar
Ambient temperature	T	293		K
Area of the tunnel cross-section	A	85.8		m ²
Height of the tunnel cross-section	H	8.89		m
Diameter of the tunnel cross-section	D	10.46		m
Thickness of the layer	h	0.6		m
Conventional blockage ratio*	BR	0.05		(-)

Note: * Since the vehicles in the tunnel do not block the flame propagation in a layer on top of the tunnel, a conventional blockage ratio of $BR = 0.05$ corresponding to the natural roughness of the tunnel surface of about 10 cm is assumed.

2.4.9.2 Calculation procedure

1	Expansion ratio, s	Table 12	(-)
2	Critical expansion ratio, s^*	$\sigma^* = \sigma_0^* (1 + K \cdot s/h)$	(-)
3	Flame acceleration evaluation	$\sigma > \sigma^*$	Yes / No
4	Detonation cell size, l	Table 12	mm
5	Critical layer thickness, h^*	$h^* = 13.5\lambda$	m
6	Blockage ratio	$BR = 0.05$	(-)
6	Spacing, s	$s = \frac{D}{2} (1 - \sqrt{1 - BR})$	(-)
7	Detonation evaluation	$h > h^* = 13.5\lambda$	Yes/No
8	DDT run-up-distance, X_s	$X_s = \frac{\gamma}{C} \left[\frac{1}{\kappa} \ln \left(\gamma \frac{D}{h} \right) + K \right]$	m
9	a_p , S_L evaluation	Table 13	m/s
10	γ evaluation	$\gamma = \left[\frac{a_p}{\eta S_L (\sigma - 1)^2} \left(\frac{\delta}{D} \right)^{1/3} \right]^{\frac{1}{2m+7/3}}$	(-)
11	D/h evaluation	$\frac{D}{h} = \frac{2}{1 - \sqrt{1 - BR}}$	(-)
12	Kinematic viscosity, ν	Table 13	cm ² /s
13	Laminar flame thickness	$\delta = \frac{\nu}{S_L}$	mm
14	Length of hydrogen cloud	$L = V / A$	m

D4.3. Final report on analytical, numerical and experimental studies on explosions, including innovative prevention and mitigation strategies

15	Volume of hydrogen cloud	$L > 7\lambda$	m ³
16	Layer cross-section area	$A = \frac{\Theta - \sin \Theta}{2} R^2$	m ²
17	Visible angle	$\frac{\Theta}{2} = \arccos\left(\frac{R-h}{R}\right)$	rad
18	Final detonability evaluation	$X_s < L$	Yes/No

2.4.9.3 Output values

Table 17. Output data for hydrogen inventory, $m = 2$ kg, and layer geometry, $h = 0.6$ m.

Hydrogen inventory, $m = 2$ kg							
Parameter name	Symbol	Unit	Output values				
			Hydrogen mole fraction, X_{H_2}				
			0.1	0.11	0.15	0.2	0.3
Expansion ratio, s	s	(-)	3.54	3.77	4.63	5.6	7.02
Critical expansion ratio, s	s*	(-)	3.89	3.89	3.89	3.89	3.89
Detonation cell size, l	l	mm	5095	2320	361	44.6	9.7
Blockage ratio, BR	BR	(-)	0.05	0.05	0.05	0.05	0.05
Spacing, s	s	m	0.13	0.13	0.13	0.13	0.13
Critical layer thickness, h*	h*	m	69	31	4.87	0.60	0.13
Volume of hydrogen cloud	V	m ³	240	219	160	120	80
Layer cross-section area	A	m ²	1.97	1.97	1.97	1.97	1.97
Layer thickness	h	m	0.6	0.6	0.6	0.6	0.6
Visible angle	Q	rad	0.968	0.968	0.968	0.968	0.968
Length of hydrogen cloud	L	m	122	111	81	61	41
Sound speed in products	a _p	m/s	659	682	765	855	983
Laminar velocity	S _L	m/s	0.25	0.33	0.78	1.46	2.7
Laminar flame thickness, δ	δ	mm	0.1342	0.1023	0.0425	0.0203	0.0092
γ - parameter	γ	(-)	3.068	2.372	1.037	0.510	0.233
D/h - parameter	D/h	(-)	79.0	79.0	79.0	79.0	79.0
Run-up-distance (RUD)	X _s	m	3084	2304	896	393	155
Result			S1	S1	S2	S2	S2

Table 18. Output data for hydrogen inventory, $m = 10$ kg, and layer geometry, $h = 0.6$ m.

Hydrogen inventory, $m = 10$ kg							
Parameter name	Symbol	Unit	Output values				
			Hydrogen mole fraction, X_{H_2}				
			0.1	0.11	0.15	0.2	0.3
Expansion ratio, s	s	(-)	3.54	3.77	4.63	5.6	7.02
Critical expansion ratio, s	s*	(-)	3.89	3.89	3.89	3.89	3.89
Detonation cell size, l	l	mm	5095	2320	361	44.6	9.7
Blockage ratio, BR	BR	(-)	0.05	0.05	0.05	0.05	0.05
Spacing, s	s	m	0.13	0.13	0.13	0.13	0.13
Critical layer thickness, h*	h*	m	69	31	4.87	0.60	0.13
Volume of hydrogen cloud	V	m ³	1200	1095	800	600	400

D4.3. Final report on analytical, numerical and experimental studies on explosions, including innovative prevention and mitigation strategies

Layer cross-section area	A	m ²	1.97	1.97	1.97	1.97	1.97
Layer thickness	h	m	0.6	0.6	0.6	0.6	0.6
Visible angle	Q	rad	0.968	0.968	0.968	0.968	0.968
Length of hydrogen cloud	L	m	610	556	406	305	203
Sound speed in products	a _p	m/s	659	682	765	855	983
Laminar velocity	S _L	m/s	0.25	0.33	0.78	1.46	2.7
Laminar flame thickness, δ	δ	mm	0.1342	0.1023	0.0425	0.0203	0.0092
γ - parameter	γ	(-)	3.068	2.372	1.037	0.510	0.233
D/h - parameter	D/h	(-)	79.0	79.0	79.0	79.0	79.0
Run-up-distance (RUD)	X _s	m	3084	2304	896	393	155
Result			S1	S1	S2	S2	D

Note: S1 – subsonic deflagration ($\sigma < \sigma^* = 3.75$); S2 - supersonic deflagration ($\sigma > \sigma^*$, $X_s \gg L$); D – Detonation $X_s < L$.

2.4.10 Option 3: Stratified layer of hydrogen-air mixture for the given hydrogen inventory

This option allows user calculating the detonability of the stratified layer of hydrogen-air mixture by the release of 2 and 10 kg of hydrogen. Five levels of maximum hydrogen mole fraction at the top of the cloud from 10 to 30% H₂ are analysed.

2.4.10.1 Input values

Table 19. Initial properties of the system.

Parameter name	Symbol	Value		Unit
Hydrogen inventory	m_{H_2}	2	10	kg
Mole fraction of hydrogen at the top	X_{H_2}	0.1		(-)
Mole fraction of hydrogen at the top	X_{H_2}	0.11		(-)
Mole fraction of hydrogen at the top	X_{H_2}	0.15		(-)
Mole fraction of hydrogen at the top	X_{H_2}	0.20		(-)
Mole fraction of hydrogen at the top	X_{H_2}	0.30		(-)
Ambient pressure	p	1		bar
Ambient temperature	T	293		K
Area of the tunnel cross-section	A	85.8		m ²
Height of the tunnel cross-section	H	8.89		m
Diameter of the tunnel cross-section	D	10.46		m
Thickness of the layer	h	0.6		m
Conventional blockage ratio*	BR	0.05		(-)

Note: * Since the vehicles in the tunnel do not block the flame propagation in a layer on top of the tunnel, a conventional blockage ratio of $BR = 0.05$ corresponding to the natural roughness of the tunnel surface of about 10 cm is assumed.

D4.3. Final report on analytical, numerical and experimental studies on explosions, including innovative prevention and mitigation strategies

2.4.10.2 Calculation procedure

1	Expansion ratio, s	Table 12	(-)
2	Gradient of concentration, $\text{grad}(X_{H_2})$	$\text{grad}(X_{H_2}) = X_{H_2} / h$	(-)
3	Efficient layer thickness, h^*	$h^* = X_{H_2} / \text{grad}(X_{H_2})^*$	(-)
4	Critical expansion ratio, s^*	$\sigma^* = \sigma_0^* (1 + K \cdot s/h)$	(-)
5	Flame acceleration evaluation	$\sigma > \sigma^*$	Yes / No
6	Detonation cell size, l	Table 12	mm
7	Blockage ratio	$BR = 0.05$	(-)
8	Critical layer thickness, h^*	$h^* = 13.5\lambda$	m
9	Detonation evaluation	$h > h^* = 13.5\lambda$	Yes/No
10	DDT run-up-distance, X_s	$X_s = \frac{\gamma}{C} \left[\frac{1}{\kappa} \ln \left(\gamma \frac{D}{h} \right) + K \right]$	m
11	a_p , S_L evaluation	Table 13	m/s
12	γ evaluation	$\gamma = \left[\frac{a_p}{\eta S_L (\sigma - 1)^2} \left(\frac{\delta}{D} \right)^{1/3} \right]^{\frac{1}{2m+7/3}}$	(-)
13	D/h evaluation	$\frac{D}{h} = \frac{2}{1 - \sqrt{1 - BR}}$	(-)
14	Kinematic viscosity, ν	Table 13	cm ² /s
15	Laminar flame thickness	$\delta = \frac{\nu}{S_L}$	mm
16	Length of hydrogen cloud	$L = V / A$	m
17	Volume of hydrogen cloud	$V = \frac{2}{X_{H_2}} \frac{pM}{mRT}$	m ³
18	Layer cross-section area	$A = \frac{\Theta - \sin \Theta}{2} R^2$	m ²
19	Visible angle	$\frac{\Theta}{2} = \arccos \left(\frac{R-h}{R} \right)$	rad
20	Final detonability evaluation	$X_s < L$	Yes/No

Note: * If the gradient is an input parameter, then $h = h^*$.

D4.3. Final report on analytical, numerical and experimental studies on explosions, including innovative prevention and mitigation strategies

2.4.10.3 Output values

Table 20. Output data for hydrogen inventory, $m = 2$ kg, and stratified layer geometry, $h = 0.6$ m.

Hydrogen inventory, $m = 2$ kg							
Parameter name	Symbol	Unit	Output values				
			Hydrogen mole fraction, X_{H_2}				
			0.1	0.11	0.15	0.2	0.3
Expansion ratio, s	s	(-)	3.54	3.77	4.63	5.6	7.02
Gradient of concentration	$\text{grad}(X_{H_2})$	% H_2 /m	16.7	18.3	25	33.3	50
Critical expansion ratio, s	s^*	(-)	3.89	3.89	3.89	3.89	3.89
Detonation cell size, l	l	mm	5095	2320	361	44.6	9.7
Blockage ratio, BR	BR	(-)	0.05	0.05	0.05	0.05	0.05
Spacing, s	s	m	0.13	0.13	0.13	0.13	0.13
Critical layer thickness, h^*	h^*	m	69	31	4.87	0.60	0.13
Volume of hydrogen cloud	V	m^3	481	437	321	240	160
Layer cross-section area	A	m^2	1.97	1.97	1.97	1.97	1.97
Layer thickness	h	m	0.6	0.6	0.6	0.6	0.6
Visible angle	Q	rad	0.968	0.968	0.968	0.968	0.968
Length of hydrogen cloud	L	m	244	222	163	122	81
Sound speed in products	a_p	m/s	659	682	765	855	983
Laminar velocity	S_L	m/s	0.25	0.33	0.78	1.46	2.7
Laminar flame thickness, δ	δ	mm	0.1342	0.1023	0.0425	0.0203	0.0092
γ - parameter	γ	(-)	3.068	2.372	1.037	0.510	0.233
D/h - parameter	D/h	(-)	79.0	79.0	79.0	79.0	79.0
Run-up-distance (RUD)	X_s	m	3084	2304	896	393	155
Result			S1	S1	S2	S2	S2

Note: S1 – subsonic deflagration ($\sigma < \sigma^* = 3.75$); S2 - supersonic deflagration ($\sigma > \sigma^*$, $X_s \gg L$); D – Detonation $X_s < L$.

D4.3. Final report on analytical, numerical and experimental studies on explosions, including innovative prevention and mitigation strategies

Table 21. Output data for hydrogen inventory, $m = 10$ kg, and stratified layer geometry, $h = 0.6$ m.

Hydrogen inventory, $m = 10$ kg							
Parameter name	Symbol	Unit	Output values				
			Hydrogen mole fraction, X_{H_2}				
			0.1	0.11	0.15	0.2	0.3
Expansion ratio, s	s	(-)	3.54	3.77	4.63	5.6	7.02
Gradient of concentration	$\text{grad}(X_{H_2})$	% H_2 /m	16.7	18.3	25	33.3	50
Detonation cell size, l	l	mm	5095	2320	361	44.6	9.7
Blockage ratio, BR	BR	(-)	0.05	0.05	0.05	0.05	0.05
Critical layer thickness, h^*	h^*	m	69	31	4.87	0.60	0.13
Volume of hydrogen cloud	V	m^3	2404	2186	1603	1202	801
Layer cross-section area	A	m^2	1.97	1.97	1.97	1.97	1.97
Layer thickness	h	m	0.6	0.6	0.6	0.6	0.6
Visible angle	Q	rad	0.968	0.968	0.968	0.968	0.968
Length of hydrogen cloud	L	m	1221	1110	814	611	407
Sound speed in products	a_p	m/s	659	682	765	855	983
Laminar velocity	S_L	m/s	0.25	0.33	0.78	1.46	2.7
Laminar flame thickness, δ	δ	mm	0.1342	0.1023	0.0425	0.0203	0.0092
γ - parameter	γ	(-)	3.068	2.372	1.037	0.510	0.233
D/h - parameter	D/h	(-)	79.0	79.0	79.0	79.0	79.0
Run-up-distance (RUD)	X_s	m	3084	2304	896	393	155
Result			S1	S1	S2	D	D

Note: S1 – subsonic deflagration ($\sigma < \sigma^* = 3.75$); S2 - supersonic deflagration ($\sigma > \sigma^*$, $X_s \gg L$); D – Detonation $X_s < L$.

2.4.11 Option 4: Stratified hydrogen-air mixture filled the whole tunnel cross-section for the given hydrogen inventory

This option allows the user to calculate the detonability of the stratified hydrogen-air mixture filling the total tunnel cross-section by the release of 2 and 10 kg of hydrogen. This option was chosen to be more realistic for a very long release time in the case of a very large hydrogen inventory or smaller nozzle diameter (0.5, 1 mm ID) for TPRD devices. Five levels of maximum hydrogen mole fraction at the top of the cloud from 10 to 30% H_2 are analysed. The concentrations above 15% seemed to be less probable.

D4.3. Final report on analytical, numerical and experimental studies on explosions, including innovative prevention and mitigation strategies

2.4.11.1 Input values

Table 22. Initial properties of the system.

Parameter name	Symbol	Value		Unit
Hydrogen inventory	m_{H_2}	2	10	kg
Mole fraction of hydrogen at the top	X_{H_2}	0.1		(-)
Mole fraction of hydrogen at the top	X_{H_2}	0.11		(-)
Mole fraction of hydrogen at the top	X_{H_2}	0.15		(-)
Mole fraction of hydrogen at the top	X_{H_2}	0.20		(-)
Mole fraction of hydrogen at the top	X_{H_2}	0.30		(-)
Ambient pressure	p	1		bar
Ambient temperature	T	293		K
Area of the tunnel cross-section	A	85.8		m ²
Height of the tunnel cross-section	H	8.89		m
Diameter of the tunnel cross-section	D	10.46		m
Thickness of the layer	H	8.89		m
Blockage ratio*	BR	0.207		(-)

Note: * The stratified mixture covers total tunnel cross-section. Then the channel will be blocked by cars and trucks.

2.4.11.2 Calculation procedure

1	Expansion ratio, s	Table 12	(-)
2	Gradient of concentration, $grad(X_{H_2})$	$grad(X_{H_2}) = X_{H_2} / h$	(-)
3	Layer thickness, h	$h = H$	(-)
3	Spacing between cars, s	$s = D$	(-)
3	Efficient layer thickness, h^*	$h^* = X_{H_2} / grad(X_{H_2})^*$	(-)
4	Critical expansion ratio, s^*	$\sigma^* = \sigma_0^* (1 + K \cdot s/h)$	(-)
5	Flame acceleration evaluation	$\sigma > \sigma^*$	Yes / No
6	Detonation cell size, l	Table 12	mm
8	Critical layer thickness, h^*	$h^* = 13.5\lambda$	m
9	Detonation evaluation 1**	$H > h^* = 13.5\lambda$	Yes/No
4	Pre-detonation length, L	$L = \frac{D+S}{2\left(1-\frac{d}{D}\right)}$ or $L = \frac{D}{1-\sqrt{1-BR}}$ if ($S = D$)	m
5	Blockage ratio	$BR = \Sigma A_i / A = 0.207$	(-)
6	Ratio d/D	$\frac{d}{D} = \sqrt{1-BR}$	(-)

D4.3. Final report on analytical, numerical and experimental studies on explosions, including innovative prevention and mitigation strategies

7	Detonation evaluation 2*	$L > 7\lambda$	Yes/No
8	DDT run-up-distance, X_s	$X_s = \frac{a_p D \cdot (1 - BR)}{(1 + 1.5 \cdot BR) \cdot 10 S_L (\sigma - 1)}$	m
9	a_p , S_L evaluation	Table 13	m/s
16	Length of hydrogen cloud	$L = V / A$	m
17	Volume of hydrogen cloud	$V = \frac{2}{X_{H_2}} \frac{pM}{mRT}$	m ³
18	Layer cross-section area	$A = A_{tunnel} - \frac{\Theta - \sin \Theta}{2} R^2$	m ²
19	Visible angle	$\frac{\Theta}{2} = \arccos\left(\frac{H - R}{R}\right)$	rad
20	Final detonability evaluation	$X_s < L$	Yes/No

Note: * If the gradient is an input parameter then $h = h^*$.

** The most dangerous DDT criterion should be chosen

2.4.11.3 Output values

Table 23. Output data for hydrogen inventory, $m = 2$ kg, and stratified hydrogen-air mixture.

Hydrogen inventory, $m = 2$ kg							
Parameter name	Symbol	Unit	Output values				
			Hydrogen mole fraction, X_{H_2}				
			0.1	0.11	0.15	0.2	0.3
Expansion ratio, s	s	(-)	3.54	3.77	4.63	5.6	7.02
Gradient of concentration	$\text{grad}(X_{H_2})$	% H_2 /m	1.1	1.2	1.7	2.2	3.4
Critical expansion ratio, s	s^*	(-)	4.52	4.52	4.52	4.52	4.52
Detonation cell size, l	l	mm	5095	2320	361	44.6	9.7
Critical layer thickness, h^*	h^*	m	68.8	31.3	4.87	0.60	0.13
Volume of hydrogen cloud	V	m ³	481	437	321	240	160
Cloud cross-section area	A	m ²	77.8	77.8	77.8	77.8	77.8
Cloud thickness	h	m	8.89	8.89	8.89	8.89	8.89
Visible angle	Q	rad	1.589	1.589	1.589	1.589	1.589
Length of hydrogen cloud	L	m	6.2	5.6	4.1	3.1	2.1
Sound speed in products	a_p	m/s	659	682	765	855	983
Laminar velocity	S_L	m/s	0.25	0.33	0.78	1.46	2.7
Run-up-distance (RUD)	X_s	m	656	472	171	80	38
Result			S1	S1	S1	S2	S2

Note: S1 – subsonic deflagration ($\sigma < \sigma^* = 4.52$); S2 - supersonic deflagration ($\sigma > \sigma^*$, $X_s \gg L$); D – Detonation $X_s < L$.

D4.3. Final report on analytical, numerical and experimental studies on explosions, including innovative prevention and mitigation strategies

Table 24. Output data for hydrogen inventory, $m = 10$ kg, and stratified hydrogen-air mixture.

Hydrogen inventory, $m = 10$ kg							
Parameter name	Symbol	Unit	Output values				
			Hydrogen mole fraction, X_{H_2}				
			0.1	0.11	0.15	0.2	0.3
Expansion ratio, s	s	(-)	3.54	3.77	4.63	5.6	7.02
Gradient of concentration	$\text{grad}(X_{H_2})$	% H_2 /m	1.1	1.2	1.7	2.2	3.4
Critical expansion ratio, s	s^*	(-)	4.52	4.52	4.52	4.52	4.52
Detonation cell size, l	l	mm	5095	2320	361	44.6	9.7
Critical layer thickness, h^*	h^*	m	68.8	31.3	4.87	0.60	0.13
Volume of hydrogen cloud	V	m^3	2404	2186	1603	1202	801
Layer cross-section area	A	m^2	77.8	77.8	77.8	77.8	77.8
Cloud thickness	h	m	8.89	8.89	8.89	8.89	8.89
Visible angle	Q	rad	1.589	1.589	1.589	1.589	1.589
Length of hydrogen cloud	L	m	30.9	28.1	20.6	15.5	10.3
Sound speed in products	a_p	m/s	659	682	765	855	983
Laminar velocity	S_L	m/s	0.25	0.33	0.78	1.46	2.7
Run-up-distance (RUD)	X_s	m	656	472	171	80	38
Result			S1	S1	S2	S2	S2

Note: S1 – subsonic deflagration ($\sigma < \sigma^* = 4.52$); S2 - supersonic deflagration ($\sigma > \sigma^*$, $X_s \gg L$); D – Detonation $X_s < L$.

2.4.12 Conversion units

Pressure P should be in Pascal (Pa). So whatever unit the user selects (bar, Pa, atm, MPa, kPa or psi), pressure should be converted to Pa:

- $P_{(Pa)} = P_{(atm)} \times 101325$
- $P_{(Pa)} = P_{(bar)} \times 100000$
- $P_{(Pa)} = P_{(psi)} \times 6894.76$
- $P_{(Pa)} = P_{(MPa)} \times 1000000$
- $P_{(Pa)} = P_{(kPa)} \times 1000$

Following the completion of the calculations, for the purposes of the creation of the results table, the units of pressure should be converted back into the units initially chosen by the user:

- $P_{(atm)} = \frac{P_{(Pa)}}{101325}$
- $P_{(bar)} = \frac{P_{(Pa)}}{100000}$
- $P_{(psi)} = \frac{P_{(Pa)}}{6894.76}$
- $P_{(MPa)} = \frac{P_{(Pa)}}{1000000}$
- $P_{(kPa)} = \frac{P_{(Pa)}}{1000}$

Temperature T should be in Kelvin (K). So whatever unit the user selects (C or F), temperature should be converted to K:

D4.3. Final report on analytical, numerical and experimental studies on explosions, including innovative prevention and mitigation strategies

- $T_{(K)} = T_{(C)} + 273.15$
- $T_{(K)} = (T_{(F)} + 459.67) * \frac{5}{9}$

Following the completion of the calculations, for the purposes of the creation of the results table, the units of temperature should be converted back into the units initially chosen by the user:

- $T_{(C)} = T_{(K)} - 273.15$
- $T_{(F)} = T_{(K)} * \frac{9}{5} - 459.67$

Distance (length) L (in our case height and width H&W) should be in meters (m). Whatever unit the user selects (ft, inch, cm), it should be converted to m:

- $L_{(m)} = L_{(ft)} \times 0.3048$
- $L_{(m)} = L_{(inch)} \times 0.0254$
- $L_{(m)} = L_{(cm)} \times 0.01$

Following the completion of the calculations, for the purposes of the creation of the results table, the units of distance should be converted back into the units initially chosen by the user:

- $L_{(ft)} = \frac{L_{(m)}}{0.3048}$
- $L_{(inch)} = \frac{L_{(m)}}{0.0254}$
- $L_{(cm)} = \frac{L_{(m)}}{0.01}$

2.5 Analytical model for water spray/mist system effect on hydrogen combustion and a shock wave attenuation (4.2, KIT)

2.5.1 Background

Water injections like spray or mist generation system are traditionally applied to extinguish fires in conventional accident scenarios. However, it might be a challenge for the conventional fire protection systems when hydrogen vehicles are involved in fire due to hydrogen release in confined spaces like traffic tunnels. It is still a question whether a water spray is able to extinguish effectively a hydrogen fire. Nuclear containment safety studies for water reactors have shown that water spray is not a sufficiently good extinguisher to hydrogen fire in some circumstances, but the injected water droplets and vaporized steam can change the composition of the atmosphere in the containment and the chemical sensitivities of the gas mixtures.

In case of hydrogen deflagration or detonation in confined spaces like tunnels, injected water mist interacts with shockwave caused by explosion. The pressure waves are supposed to be attenuated by the interaction. The attenuation effect is still unclear and has to be investigated.

2.5.2 Objectives

The cooling mechanism of the sprayed water droplets acting on the hot products of hydrogen combustion is to be investigated by means of theoretical analysis of the heat and mass transfer laws between the liquid phase and the gas phase. An empirical correlation between hydrogen release rate and the required water spray flow rate is proposed if the fire ambient gas temperatures are cooled down to the same level.

D4.3. Final report on analytical, numerical and experimental studies on explosions, including innovative prevention and mitigation strategies

The interaction between droplets and pressure shock front is investigated to reveal the attenuation mechanism of water mist on shockwave. A theoretical model - droplet breakup model is established for implementation.

2.5.3 Knowledge gaps and accident scenarios assessed

In view of fire protection, water spray brings both advantages and disadvantages. The advantage is to cool down the hot gases of combustion, while the disadvantage is that the spray action can, in some circumstances, intensify the turbulent effect in gas flow then to intensify the combustion of gaseous fuel like hydrogen.

2.5.4 Engineering model development

2.5.4.1 Water spray model

In the transport process of a water particle from the spray nozzle to the gas volume of e.g. a tunnel model, a phase change occurs, due to vaporization and condensation. In the scenario of tunnel hydrogen fire, vaporization of the liquid particle certainly dominates. Besides the convective heat and radiative heat transfer, the latent heat of the vaporized steam brings away the major part of the explicit heat of hot gases of combustion. The heat and mass transfers between the two phases are the essential mechanisms of the cooling effect of the spray.

The heat transfer is formulated by

$$m_l c_l \frac{dT_l}{dt} = A_{p,s} h (T_g - T_l) + \dot{q}_r + \frac{dm_l}{dt} h_v, \quad (38)$$

where,

m_l – liquid particle mass, kg,

c_l – specific heat of water, J/kg,

T_l – liquid temperature, K,

T_g – gas temperature, K

$A_{p,s}$ – surface area of particle, m²,

h – heat transfer coefficient between liquid and gas, W/(m²•K),

\dot{q}_r – rate of radiative heating of the particle, W,

h_v – vaporization latent heat of liquid particle, J/kg,

t – physical time, s.

Accordingly, the mass transfer between the liquid-gas phases is modeled as,

$$\frac{dm_l}{dt} = -A_{p,s} h_m \rho_g (Y_{\alpha,l} - Y_{\alpha,g}), \quad (39)$$

where,

D4.3. Final report on analytical, numerical and experimental studies on explosions, including innovative prevention and mitigation strategies

h_m – mass transfer coefficient due to phase change, m/s,

ρ_g – gas density, kg/m³,

$Y_{\alpha,l}$ – liquid equilibrium vapor mass fraction,

$Y_{\alpha,g}$ – vapor mass fraction in gas phase.

Due to far insufficient data available at KIT, the FDS code being implemented in the above-described phase change model is applied to analyse the relationship between the hydrogen injection flow rate and the sprayed water flow rate.

In a simplified rectangular cross-section tunnel model, hydrogen is released from a 70 MPa storage tank into the tunnel with a longitudinal ventilation velocity of 3 m/s. The hydrogen mass flow rate decays as time goes by owing to the blowdown flow feature. Hydrogen is ignited from the starting point of the release; meanwhile, water spray is activated, which is positioned on the tunnel ceiling right above the hydrogen release location. For a given hydrogen fire scale corresponding to a hydrogen release rate, the water spray flow rate is tuned that the high temperature of hot products of hydrogen combustion is decreased by the spray to the same low temperature, e.g., with the average gas temperature in the whole tunnel model as the reference temperature.

In afore-described assumptions, the obtained water spray flow rates are listed in Table 25 and shown in Figure 15.

D4.3. Final report on analytical, numerical and experimental studies on explosions, including innovative prevention and mitigation strategies

Table 25. Correlation between hydrogen mass flow rate and water spray flow rate.

Hydrogen mass flow rate, \dot{m}_{H_2} , kg/s	Water spray mass flow rate, \dot{m}_{H_2O} , L/min
0.05	80
0.10	690
0.11	1600
0.12	3100
0.13	6000

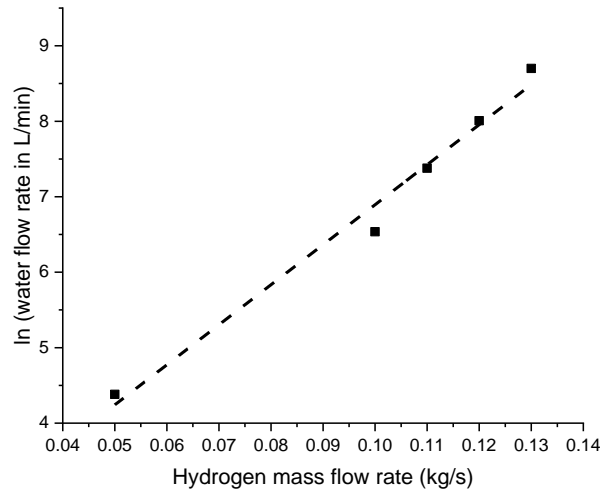


Figure 15. Logarithm of water flow rate in L/min as a function of hydrogen mass flow rate in kg/s.

According to Figure 15, an empirical correlation between the water spray flow rate and the hydrogen release mass flow rate can be obtained by a linear fitting of the data points.

$$\dot{m}_{H_2O} = \exp (53\dot{m}_{H_2} + 1.59), \quad (40)$$

where,

\dot{m}_{H_2} – hydrogen release mass flow rate in kg/s,

\dot{m}_{H_2O} – water spray flow rate in L/min.

It manifests that the water spray mass flow rate increases exponentially if the hydrogen release rate increases, in order to cool the hot gas mixture after burning down to the same low temperature level. Attention should be paid hereby that, this is not a general conclusion, but valid only for the specific scenario defined in the FDS simulations, e.g.,

- Tunnel ventilation 3 m/s.
- Spray nozzle is right above the H_2 release location.
- Ignition occurs from the H_2 release start.

The required fast increasing water flow rate to cool down the hydrogen combustion mixture with increasing leak rate is caused maybe by the ventilation flow, which can readily blow the hot gases away from the spray region. Therefore, a larger coolant water flow rate is necessary to cool down the combustion products before they are blown away.

D4.3. Final report on analytical, numerical and experimental studies on explosions, including innovative prevention and mitigation strategies

2.5.4.2 Droplet breakup model

Droplet break-up is an important mechanism in the shockwave attenuation process by water mist. The theoretical break-up model contains three key model parameters, i.e., the critical Weber number, the droplet breakup time and the secondary droplet size.

Critical Weber number

Figure 13 shows the different droplet breakup modes depending on varying Weber number (We), which in principle dominates the breakup mode of the droplet. The starting of breakup process is also controlled by the Ohnesorge number (Oh). By considering both factors, the correlations to determine the critical Weber number is formulated as,

$$We_c = \begin{cases} 12(1 + 1.077Oh^{1.6}), & \text{if } 4 \leq Oh < 10 \\ 12(1 + 1.50Oh^{0.74}), & \text{if } Oh < 4 \end{cases} \quad (41)$$

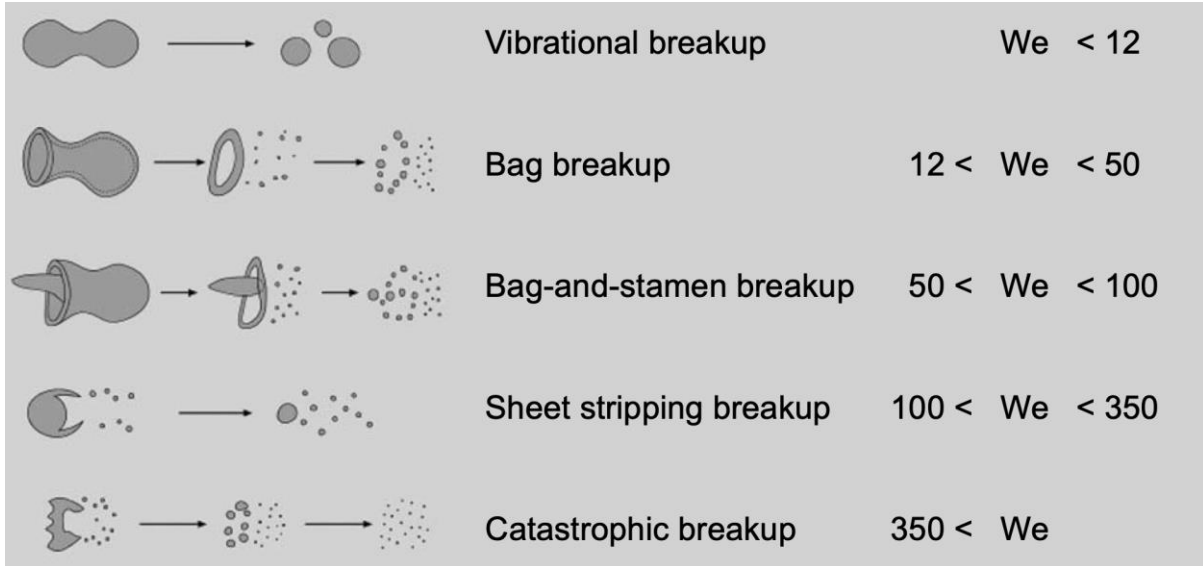


Figure 16. Different droplet breakup modes depending on the Weber number

Droplet breakup time

The droplet breakup time depends on a characteristic time (t_{char}) and a factor (T_{tot}^*), namely,

$$t_{tot} = t_{char} * T_{tot}^*, \quad (42)$$

where, the characteristic time t_{char} is formulated as,

$$t_{char} = \frac{D_d}{|u_g - u_d|} \sqrt{\frac{\rho_d}{\rho_g}} \quad (43)$$

with D_d – droplet diameter, u_d – droplet velocity, ρ_d – droplet density, u_g – gas flow velocity, ρ_g – gas density. And the factor T_{tot}^* is depending on the Weber number and the Ohnesorge number, formulated as,

D4.3. Final report on analytical, numerical and experimental studies on explosions, including innovative prevention and mitigation strategies

$$T_{tot}^* = T_{tot}^* = \begin{cases} 6 \cdot (We - 12)^{-0.25} & ; 12 < We < 18 \text{ and } Oh < 0.1 \\ 2.45 \cdot (We - 12)^{0.25} & ; 18 < We < 45 \text{ and } Oh < 0.1 \\ 14.1 \cdot (We - 12)^{-0.25} & ; 45 < We < 351 \text{ and } Oh < 0.1 \\ 0.766 \cdot (We - 12)^{0.25} & ; 351 < We < 2670 \text{ and } Oh < 0.1 \\ 5.5 & ; 2670 < We \text{ and } Oh < 0.1 \\ 4.5 \cdot (1 + 1.2Oh^{0.74}) & ; Oh \geq 0.1 \end{cases} \quad (44)$$

Secondary droplet size

After the breakup process, the original droplet is broken into smaller droplets, which are called secondary droplets. The size of the secondary droplet is determined by,

$$D_{d_{sec}} = D_d \cdot 1.5 \cdot Oh^{0.2} We_{corr}^{-0.25} \quad (45)$$

where, the corrected Weber number We_{corr} is defined as,

$$We_{corr} = \frac{We}{1 + 1.077Oh^{1.6}} \quad (46)$$

The droplet breakup model has been implemented into the COM3D code.

2.5.5 Discussion

The obtained empirical correlation is valid only for the specific tunnel model with the specifically configured water spray e.g., spray position and droplet size and tunnel ventilation condition etc., and under the specific assumptions made in the study. Nevertheless, it shows an exponential increase feature of the water flow rate if hydrogen release increases. In other words, the water spray design for a tunnel is highly dependent on the TPRD design of a hydrogen vehicle.

2.5.6 Application of research findings

In general, the manufacturing cost (~ 2M Euro per km) and maintenance cost (~ 40k Euro per km) of a water spray system for a tunnel is quite expensive. Due to the exponential increasing feature of water spray flow rate along the increasing TPRD opening diameter, the capacity design of the water spray system must be referenced to the TPRD design of hydrogen vehicles. It means the tunnel engineering entities must have sufficiently detailed communications with the automobile industry.

3 Numerical studies (Task 4.3 / NCSR)

3.1 Deflagration of non-uniform hydrogen-air cloud created by release in HSE tunnel experiments Task 4.4 (4.3, NCSR)

3.1.5 Introduction

Pre-test deflagration simulations of hydrogen released from a train inside the HSE tunnel (HyTunnel-CS-D2.3), (HyTunnel-CS-D4.4) were conducted. The length of the tunnel is equal to 70 m and the maximum height equal to 3.25 m. Initially dispersion simulation was performed, in order to define the initial conditions for the deflagration simulations. Both the empty and the non-empty cases were studied. In the non-empty case, the train obstacles are included. Ventilation equal to 1.25 m/s from the one opening of the tunnel was considered. The hydrogen volume is equal to 159 liters stored at 511 bars. The release diameter is equal to 5.7 mm and the release direction is upwards. For more details, please refer to (HyTunnel-CS-D2.3), (HyTunnel-CS-D4.4).

3.1.6 Simulations details

For the simulations the ADREA-HF CFD code (Venetsanos et al. 2010) was used. For turbulence, the Kato-Launders modification (Kato et al. 1993) of k- ϵ model was utilized. The equations were discretized using the second order upwind bounded numerical scheme for the convection terms and a first order upwind discretization for time. Release was modelled using the Birch (Birch et al. 1984) notional nozzle approach. For deflagration simulation a recently developed model was used. The model utilized the Schmid's formula for turbulent flame speed and several wrinkling factors to account for flame instabilities. Model details and validation can be found in (Tolias et al. 2018), (Tolias et al. 2020) and (Momferatos et al. 2021).

The release was discretized using 4 cells. For the deflagration simulations the total number of (active) cells was equal to 650,000 in the empty tunnel case and equal to 960,000 in the non-empty case. A denser grid was used in the non-empty tunnel case at the area with the obstacles. The grid was extended beyond both openings and also in the vertical direction. Picture of the domain and grid details are presented in Figure 17 and Figure 18.

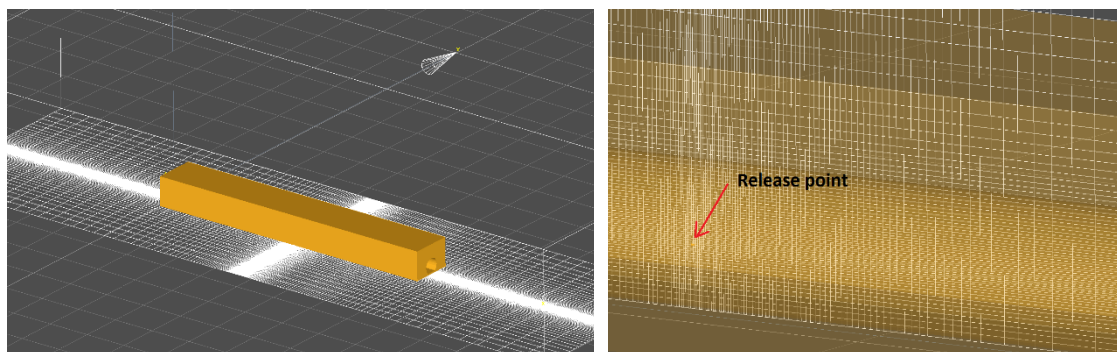


Figure 17. Numerical grid for the deflagration simulations of the empty tunnel case.

D4.3. Final report on analytical, numerical and experimental studies on explosions, including innovative prevention and mitigation strategies

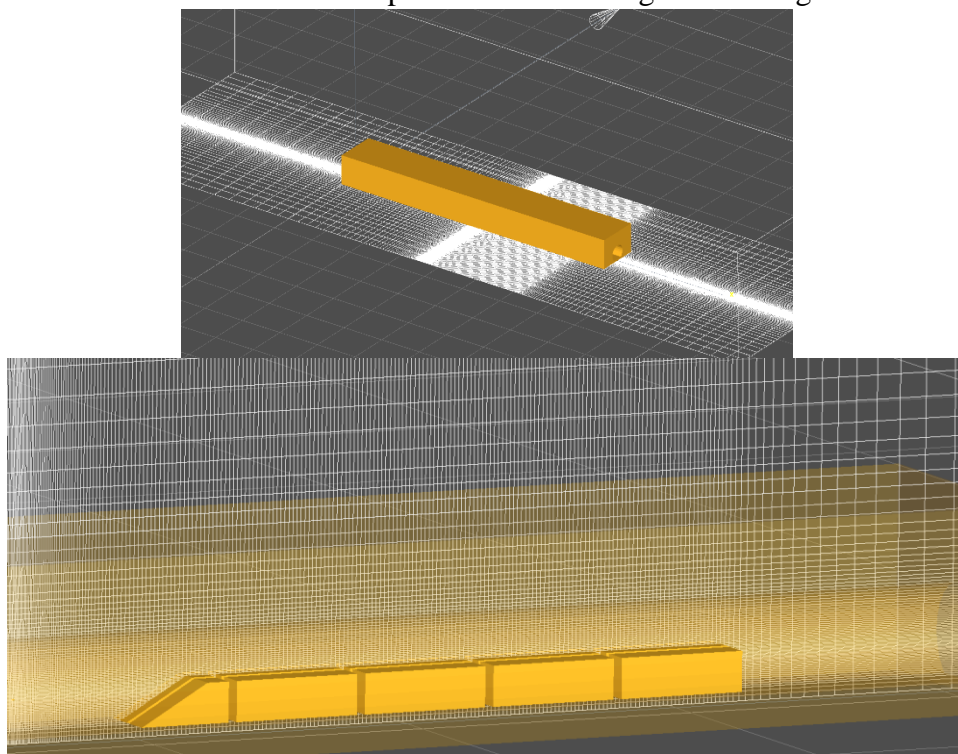


Figure 18. Numerical grid for the deflagration simulations of the non-empty tunnel case.

3.1.7 Empty tunnel case

3.1.7.1 Examined deflagration cases

The results of the empty tunnel case are presented in this Section. In Figure 19 the results of the dispersion simulations are presented. The volume of hydrogen clouds at various ranges are shown as a function of time. The maximum flammable volume inside the tunnel is equal to 350 m³ at 19 s from the release start. The maximum 25-35% cloud is equal to 4.1 m³ at 4.4 s from the release start whereas the maximum 32-42% cloud is equal to 0.6 m³ at 2.6 s. Hydrogen concentrations at the 32-42% range are observed only in the core of the hydrogen jet, below the ceiling.

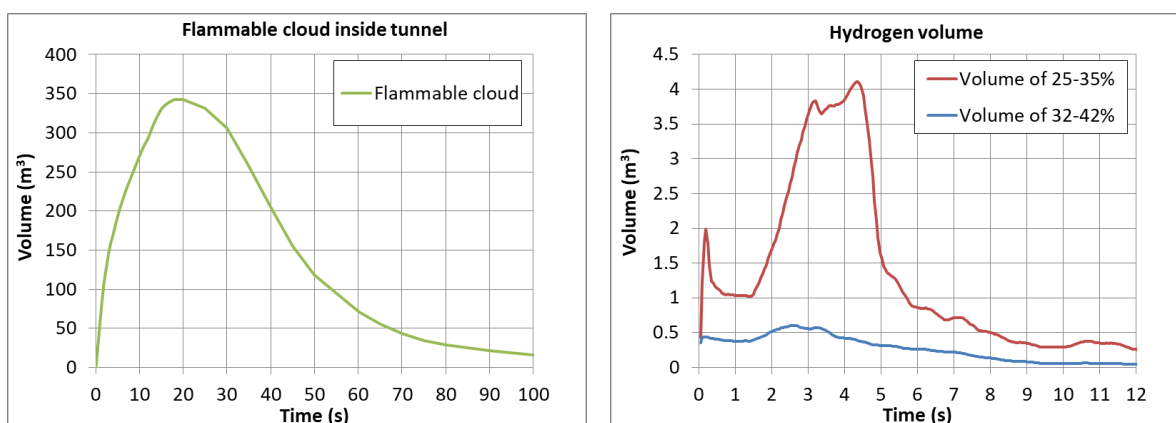


Figure 19. Hydrogen volumes in the range of 4-75% (flammable volume), 25-35% and 32-42% as a function of time.

D4.3. Final report on analytical, numerical and experimental studies on explosions, including innovative prevention and mitigation strategies

In Figure 20 the hydrogen volume concentration and the turbulent kinetic energy are shown at four characteristic times, 4, 8, 12 and 16 s. We observe that the average concentration in hydrogen cloud is around 16%. Moreover, high levels of turbulence are developed downwind the release area at short release durations. Due to the release blowdown turbulence decreases with time.

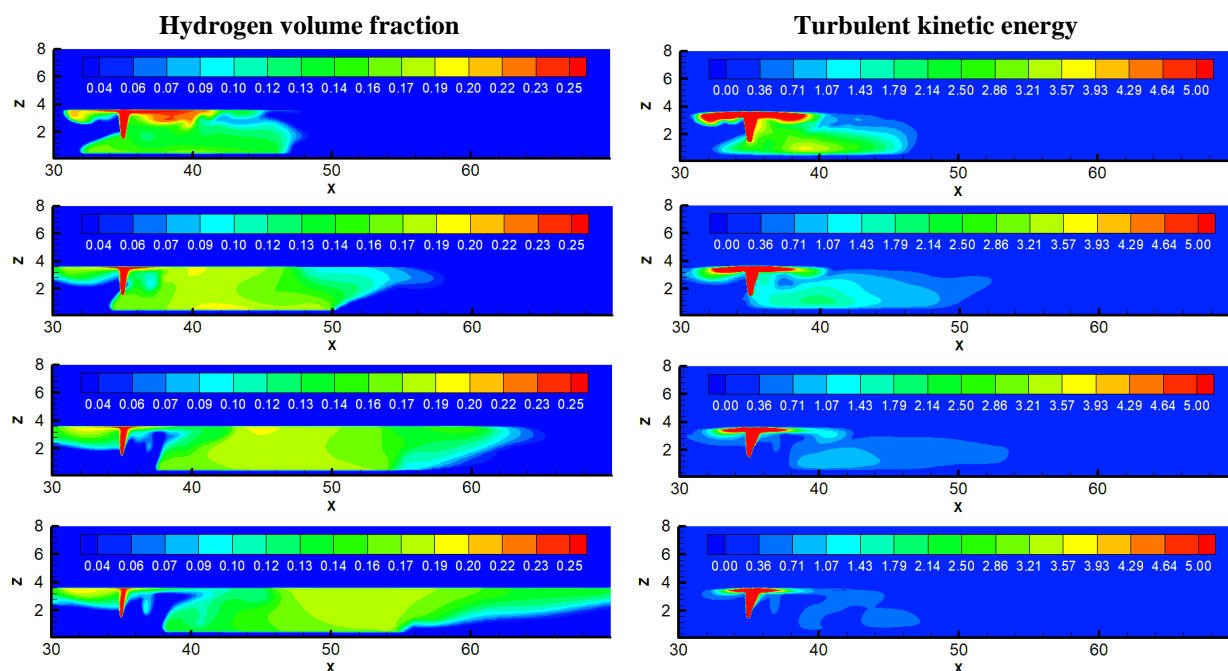


Figure 20. Hydrogen volumetric concentration (left) and the turbulent kinetic energy (right) at 4, 8, 12 and 16 s from the release start.

In Table 26 the times and the positions at which ignition was considered for deflagration simulations are presented. In total 3 deflagration simulations were carried out. Two ignition locations were studied at the time of 4.0 s in order to assess the sensitivity of the results on the ignition position. A higher ignition delay was also considered in which the hydrogen cloud has increased in size and has been moved away from the high turbulence area. The height of ignition location in all case was near the ceiling.

Table 26. Deflagration scenarios for the empty tunnel case. Ignition delay and ignition location.

Time (s)	Description	Horizontal Distance from release (m)
4.0	High turbulence	36
4.0	High turbulence	38
8.0	Large cloud	38

3.1.7.2 Deflagration results

In Figure 21 the effect of ignition position on overpressure for a 4.0 s ignition delay is shown at four sensor positions in the tunnel (35, 40, 50 and 60 m from the opening with the ventilation). We observe that both ignition positions (at 36 and 38 m) give similar results. Notable

D4.3. Final report on analytical, numerical and experimental studies on explosions, including innovative prevention and mitigation strategies

differences in the maximum overpressure are observed only at 60 m distance. The maximum overpressure among all sensors is approximately equal to 36 kPa.

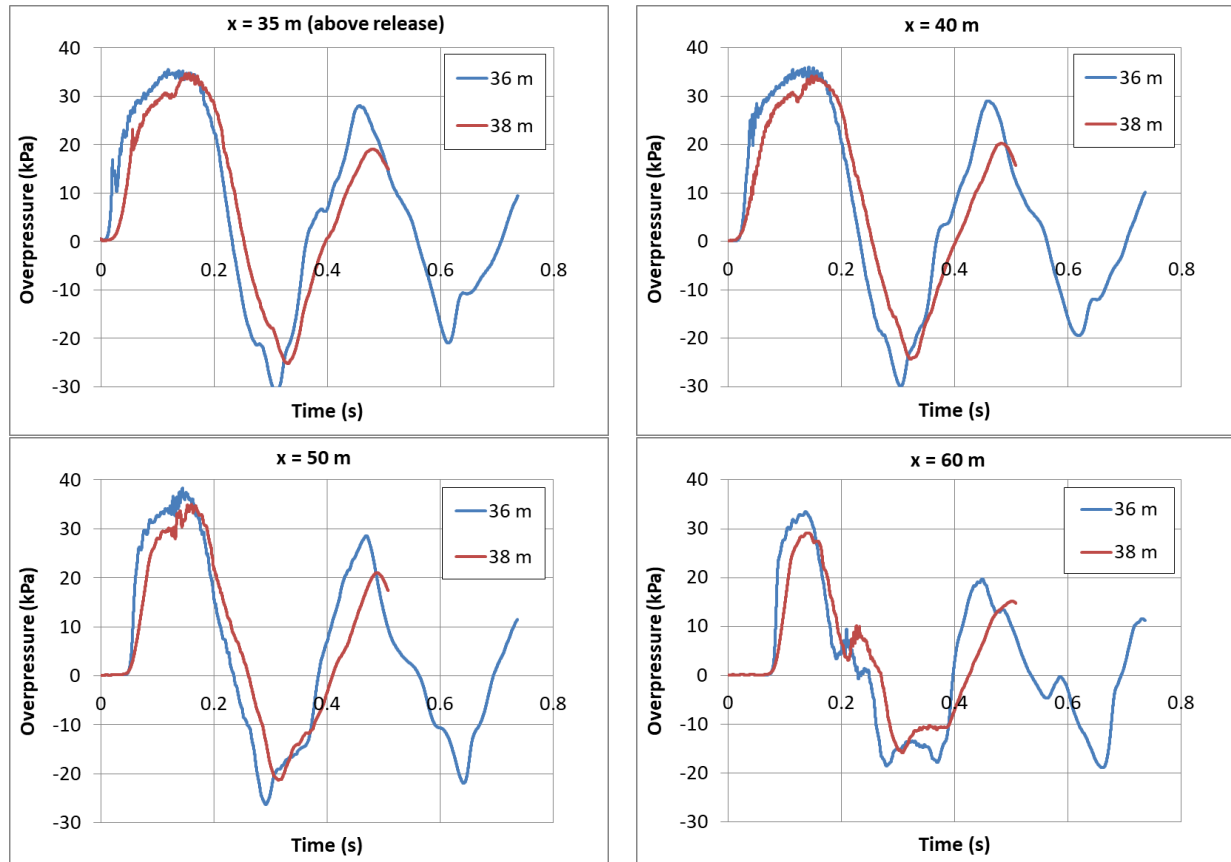
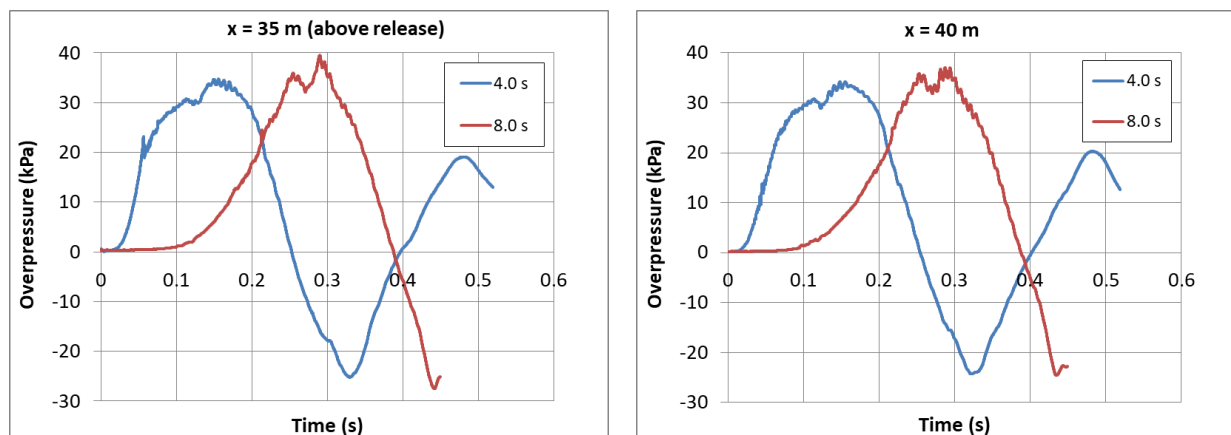


Figure 21. Effect of ignition position. Overpressure time series at 35, 40, 50 and 60 m, for two ignition positions, 36 and 38 m (ignition 4.0 s after the release).

In Figure 22 the effect of ignition delay is shown. The 4.0 s case is compared to the 8.0 s case. In both cases the ignition was positioned at 38 m. We observe that the ignition at 8.0 s achieves higher maximum overpressures in most of the sensors. The maximum overpressure at 35, 40, 50 and 60 m is equal to 40, 36, 37 and 28 kPa, respectively, in the case of ignition at 8.0 s.



D4.3. Final report on analytical, numerical and experimental studies on explosions, including innovative prevention and mitigation strategies

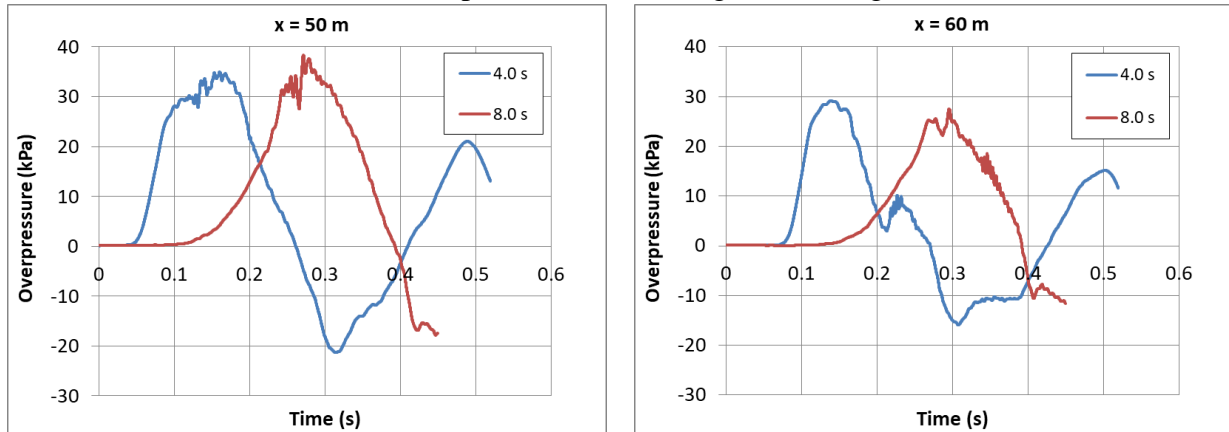
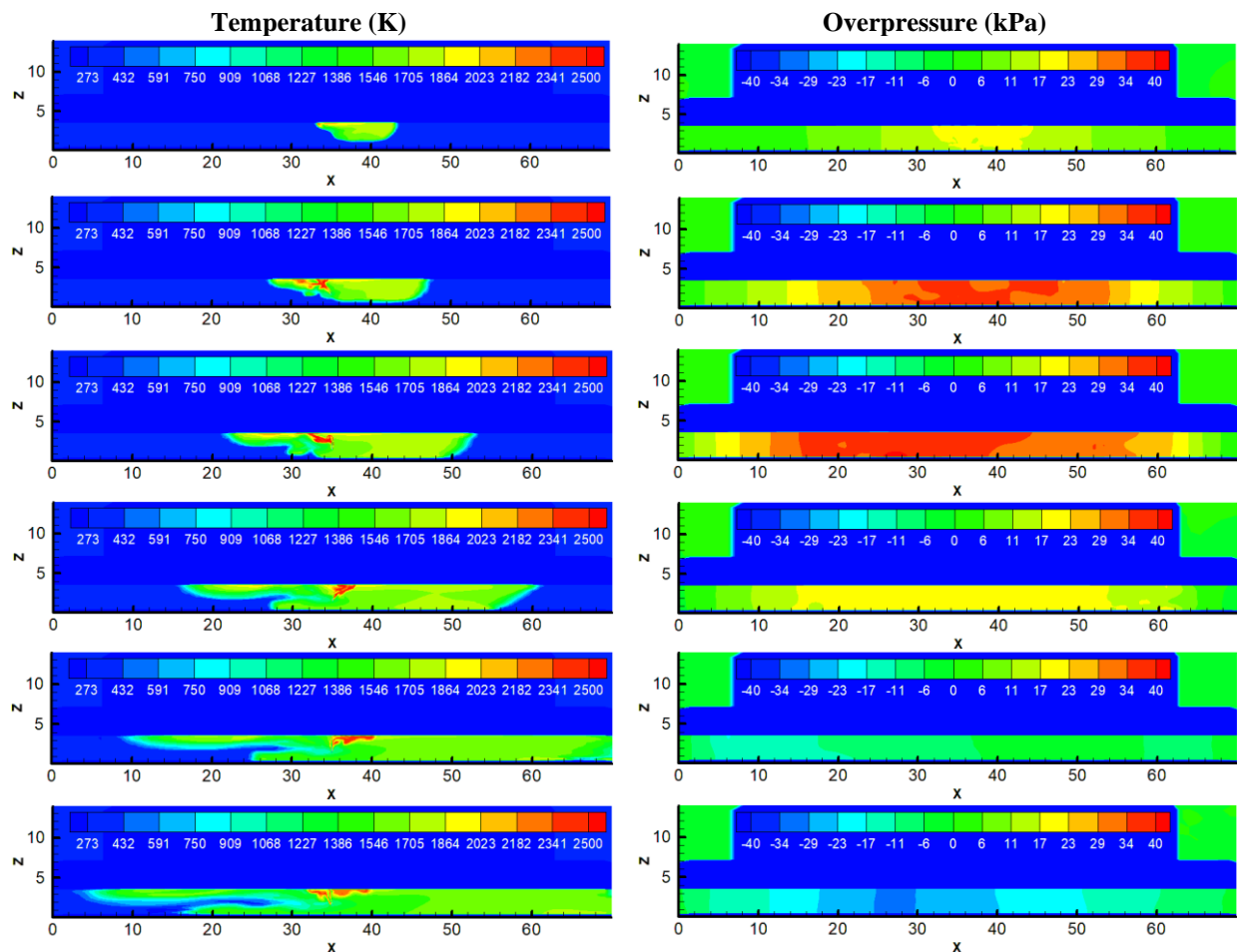


Figure 22. Effect of ignition delay. Overpressure time series at 35, 40, 50 and 60 m, for two different ignition times, 4.0 and 8.0 s (ignition at 38 m).

In Figure 23, the deflagration dynamics are presented through the temperature and overpressure contours for the case of ignition at 38 m and 8.0 s. We observe that the average temperature inside the tunnel at the end of combustion is around 1500 K. The high temperature cloud occupied mainly the area downwind the release point where the flammable cloud was accumulated. The maximum overpressures are achieved at around 0.30 s. At this time the high value of pressure occupies the entire tunnel length.



D4.3. Final report on analytical, numerical and experimental studies on explosions, including innovative prevention and mitigation strategies

Figure 23. Temperature (left) and the overpressure (right) at 0.20, 0.25, 0.30, 0.35, 0.40, 0.45 s from the ignition (ignition at 38 m, 8.0 s after the release).

3.1.8 Non-empty tunnel case

3.1.8.1 Examined scenarios

In Figure 24 the effect of ignition position on overpressure for a 4.0 s ignition delay is shown at four sensor positions in the tunnel (35, 40, 50 and 60 m from the opening with the ventilation). We observe that both ignition positions (at 36 and 38 m) give similar results. Notable differences in the maximum overpressure are observed only at 60 m distance. The maximum overpressure among all sensors is approximately equal to 36 kPa.

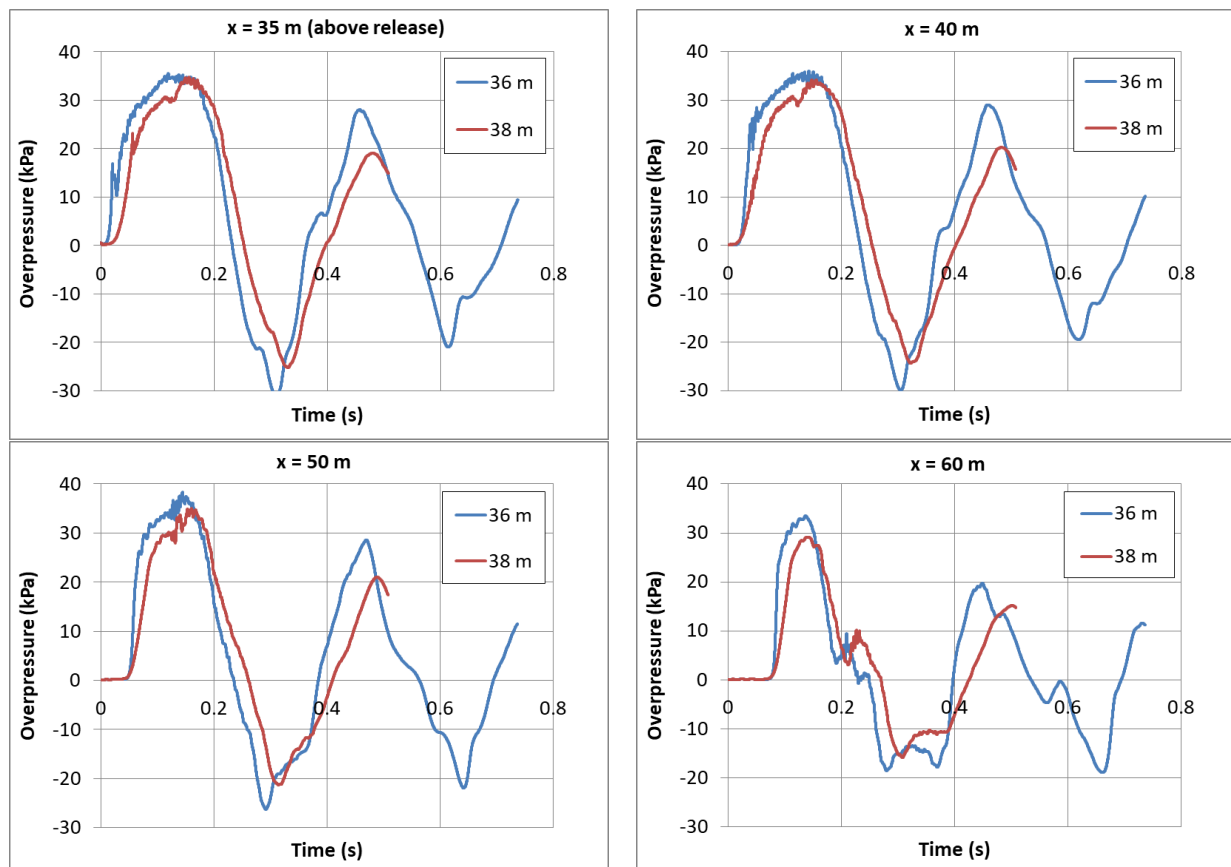


Figure 24. Effect of ignition position. Overpressure time series at 35, 40, 50 and 60 m, for two ignition positions, 36 and 38 m (ignition 4.0 s after the release).

In Figure 25 the effect of ignition delay is shown. The 4.0 s case is compared to the 8.0 s case. In both cases, the ignition was positioned at 38 m. We observe that the ignition at 8.0 s achieves higher maximum overpressures in most of the sensors. The maximum overpressure at 35, 40, 50 and 60 m is equal to 40, 36, 37 and 28 kPa, respectively, in the case of ignition at 8.0 s.

D4.3. Final report on analytical, numerical and experimental studies on explosions, including innovative prevention and mitigation strategies

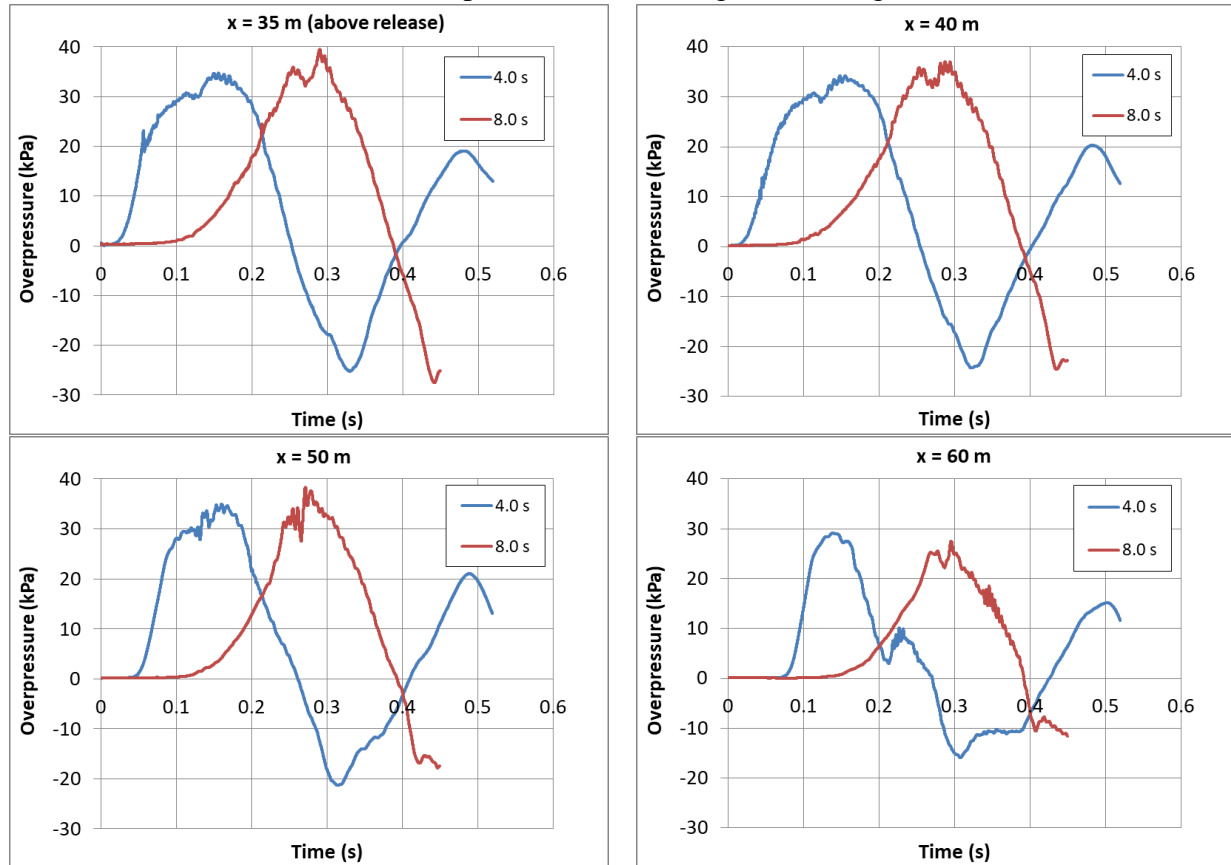
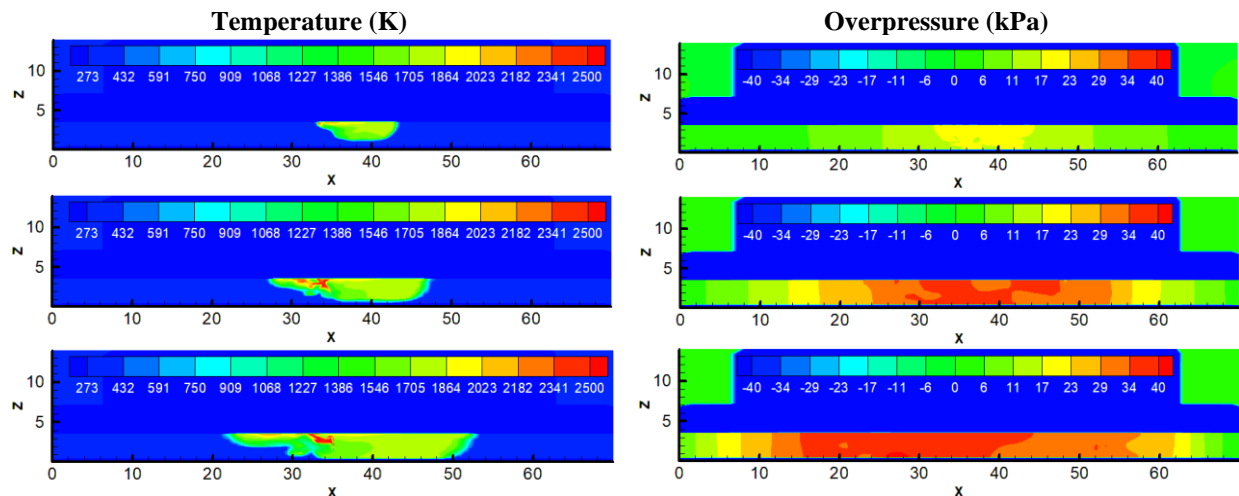


Figure 25. Effect of ignition delay. Overpressure time series at 35, 40, 50 and 60 m, for two different ignition times, 4.0 and 8.0 s (ignition at 38 m).

In Figure 26, the deflagration dynamics are presented through the temperature and overpressure contours for the case of ignition at 38 m and 8.0 s. We observe that the average temperature inside the tunnel at the end of combustion is around 1500 K. The high temperature cloud occupied mainly the area downwind the release point where the flammable cloud was accumulated. The maximum overpressures are achieved at around 0.30 s. At this time, the high value of pressure occupies the entire tunnel length.



D4.3. Final report on analytical, numerical and experimental studies on explosions, including innovative prevention and mitigation strategies

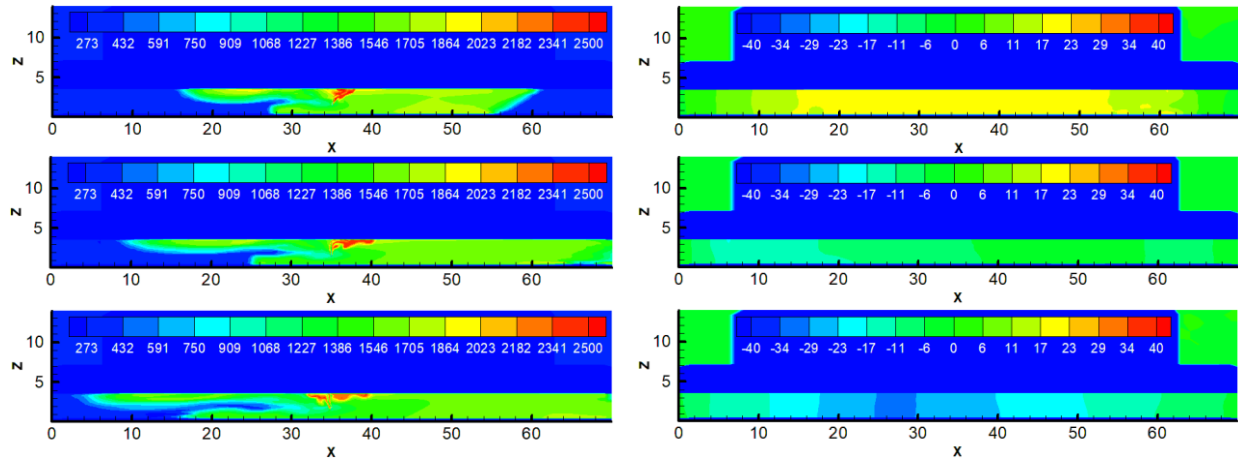


Figure 26. Temperature (left) and the overpressure (right) at 0.20, 0.25, 0.30, 0.35, 0.40, 0.45 s from the ignition (ignition at 38 m, 8.0 s after the release).

3.1.8.2 Deflagration results

In Figure 27 the effect of ignition position, for 4.0 s (after the start of the release) ignition delay is shown at four sensor positions in the tunnel (35, 40, 50 and 60 m from tunnel entrance, i.e., the opening with the ventilation). We observe that the ignition at 38 m generates much higher overpressures. The reason for this behavior is that this ignition point is at the center of the hydrogen cloud inside the high turbulence area whereas the 42 m ignition point is at the right end of the cloud (see Figure 28). The maximum overpressure is close to 50 kPa which is higher than the maximum overpressure of the worst-case scenario of the empty tunnel case which was equal to 40 kPa.

D4.3. Final report on analytical, numerical and experimental studies on explosions, including innovative prevention and mitigation strategies

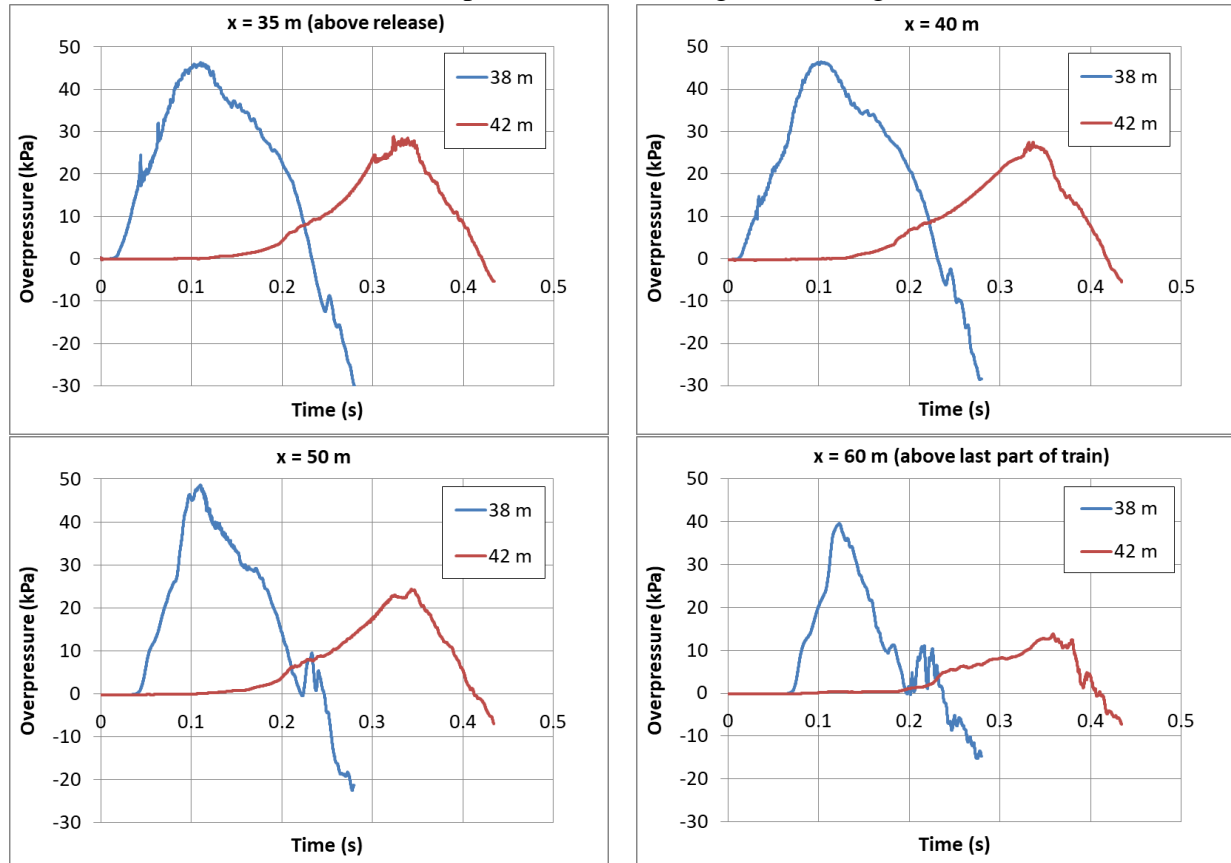


Figure 27. Effect of ignition position. Overpressure time series at 35, 40, 50 and 60 m, for ignition at 38 and 42 m (4.0 s ignition delay).

In Figure 28 the effect of ignition delay is shown. The 4.0 s case is compared with the 12.0 s case. In both cases the ignition point was set at 38 m (near the ceiling). We observe that the ignition with 4.0 s delay achieves much higher maximum overpressures. The reason for this is the high turbulence area that exists at 4.0 s near the release. Moreover, the hydrogen concentration around the ignition position is higher at 4.0 s compared to 12.0 s.

We observe that in 12.0 s case, two pressure peaks are formed. The second one is higher, especially in longer distances from the release. At 60 m, this peak has the highest value being equal 30 kPa. This peak is generated due to the high turbulence area that is developed behind the last part of the train as deflagration progresses. Deflagration imposes high velocity field which leads to the development of the high turbulence at the recirculation area. These observations can be seen in Figure 29 where the hydrogen volume fraction and turbulent kinetic energy are presented for different times of the deflagration.

D4.3. Final report on analytical, numerical and experimental studies on explosions, including innovative prevention and mitigation strategies

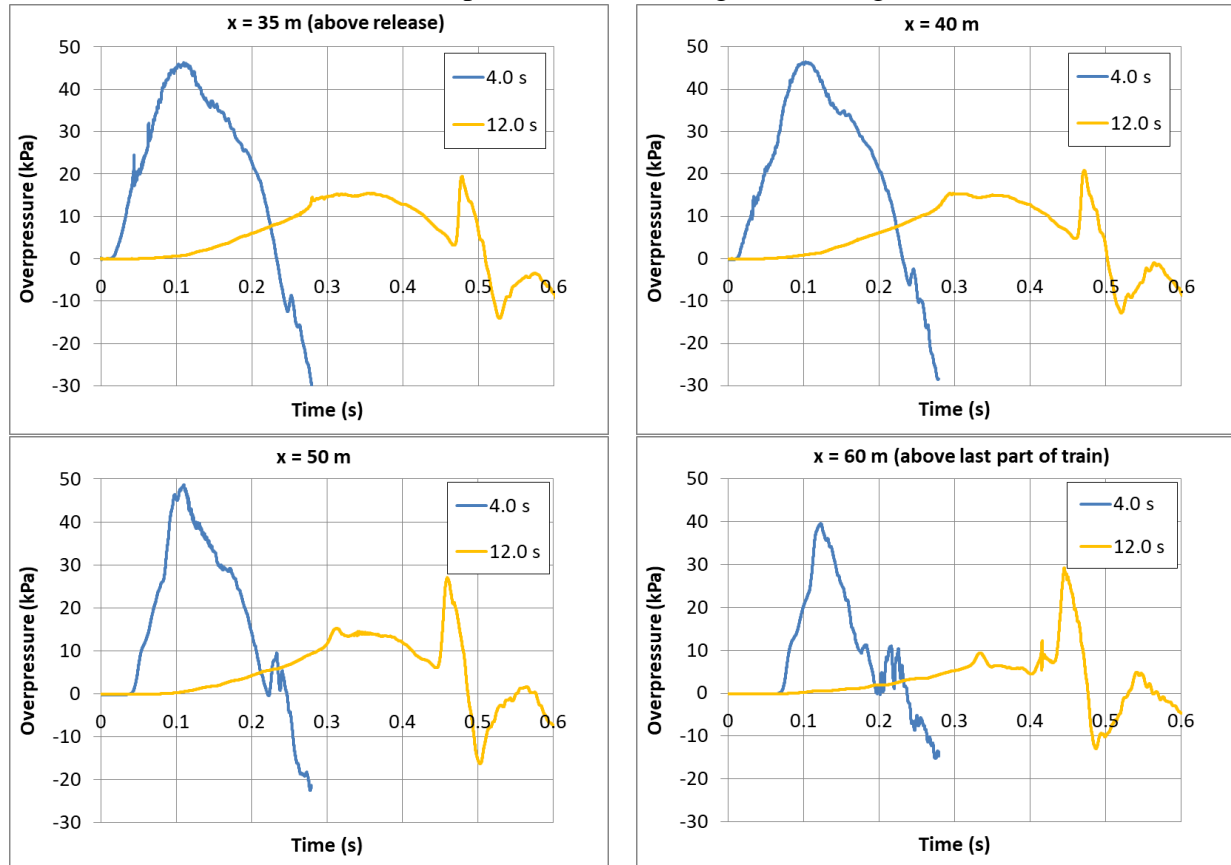


Figure 28. Effect of ignition time. Overpressure time series at 35, 40, 50 and 60 m, for two different ignition times (ignition location at 38 m).

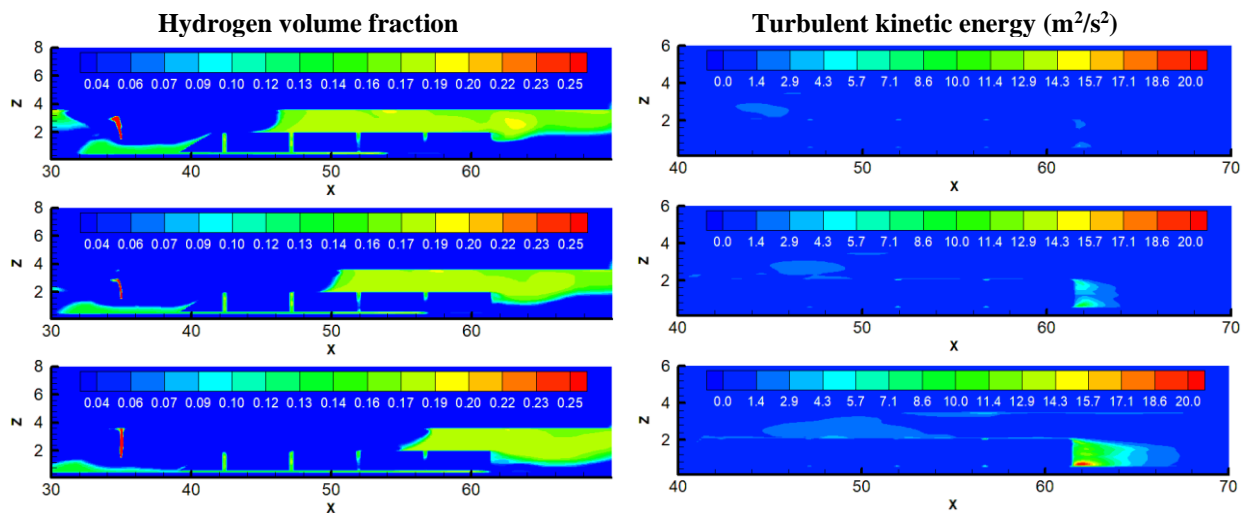


Figure 29. Hydrogen volume fraction (left) and turbulent kinetic energy (right) at 0.30, 0.35 and 0.40 s from the ignition (ignition at 38 m, 12.0 s ignition delay).

In Figure 30 the effect of ignition location is shown for ignition delay 12.0 s. We observe that the worst-case scenario in terms of maximum overpressure is the ignition near the release at 38 m. As we move away from the release, both pressure peaks are reduced. In the ignition at 56 m case, only one pressure peak is observed in all sensors. This ignition point is very near the end of the train and as a result turbulence does not have enough time to develop in that area.

D4.3. Final report on analytical, numerical and experimental studies on explosions, including innovative prevention and mitigation strategies

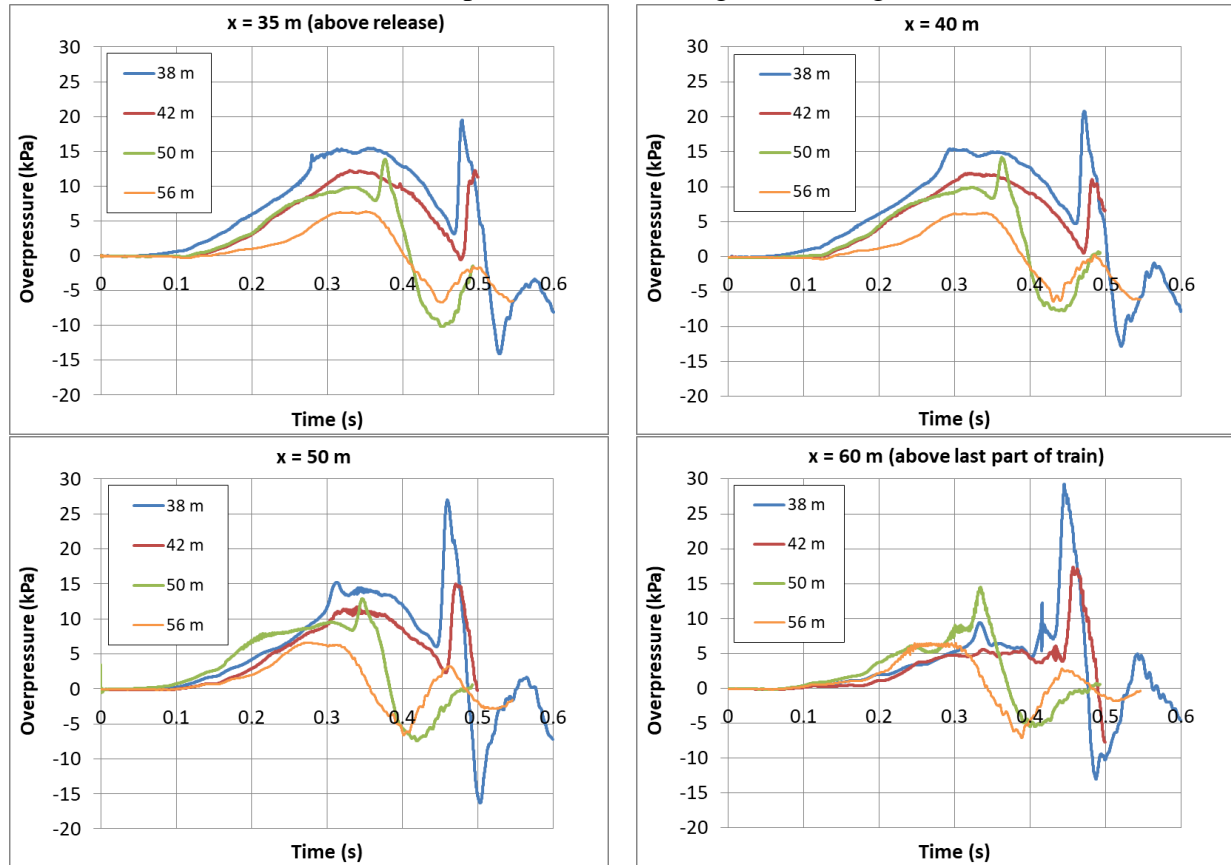
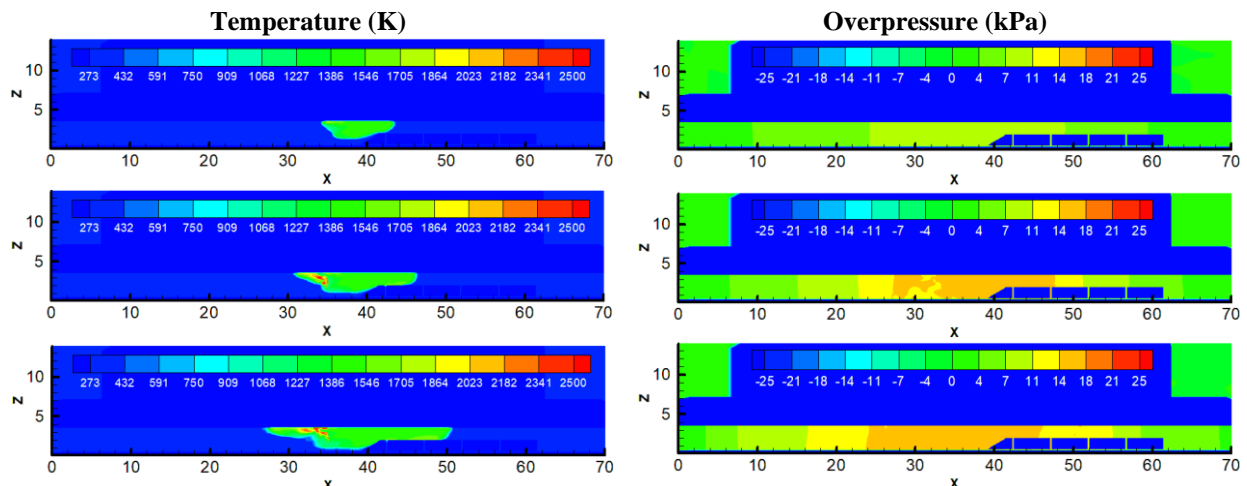


Figure 30. Effect of ignition position. Overpressure time series at 35, 40, 50 and 60 m, for four different ignition positions (12.0 s ignition delay).

In Figure 31, the deflagration dynamics are presented through the temperature and overpressure contours for ignition at 38 m, 12.0 s after the release. We observe that the average temperature inside the tunnel at the end of the combustion is around 1500 K. The high temperature cloud occupied mainly the area downwind the release point where the flammable cloud was accumulated. At 0.35 s when the first overpressure peak occurs, pressure is high at the central area of the tunnel. After that time pressure decreases. However, at 0.45 s a sudden pressure increase occurs at the end of the train due to the violent combustion that occurs in the high turbulence region. The pressure wave then propagates throughout the tunnel.



D4.3. Final report on analytical, numerical and experimental studies on explosions, including innovative prevention and mitigation strategies

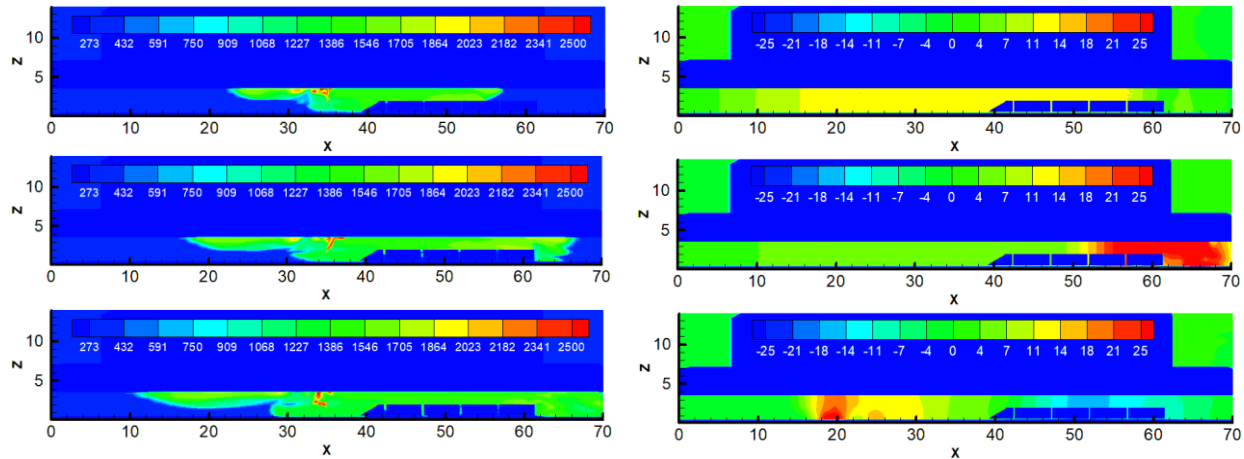


Figure 31. Temperature (left) and the overpressure (right) at 0.25, 0.30, 0.35, 0.40, 0.45, 0.50 s from the ignition (ignition at 38 m, 12.0s after the release).

3.1.9 Conclusions

CFD pre-tests simulations were conducted in the HSE tunnel geometry. Two geometrical configurations were considered, the empty tunnel case and the non-empty tunnel case. The effect of ignition location and of ignition delay was investigated. The generated overpressure highly depends on ignition position and ignition delay. The maximum overpressure among all examined cases was equal to 50 kPa. This pressure was generated in the non-empty tunnel case (with train carriages), with ignition delay equal to 4.0 s after the release and ignition location at 38 m (i.e., 3 m downwind the release). This time corresponds to the time that the maximum 25-35 % hydrogen volume concentration occurs. In the empty tunnel case, the maximum overpressure is equal to 40 kPa. This value is achieved with ignition delay 8.0 s after the release and ignition position at 38 m.

In the non-empty tunnel case, a secondary pressure peak was developed due to the deflagration of hydrogen behind the back end of the train. At this area high turbulence exists increasing the reaction rate and thus the pressure. The violence of this secondary explosion depends on the ignition position. The further the ignition position from the back of the train is, the higher the overpressure in this area is. In order for this explosion to happen, the ignition needs to occur after some time from the release (in our case after 12.0 s) in order hydrogen to reach the area.

The above results suggest to the experimentalists that different ignition delays may be studied for the same release scenario. Ignition positions near the release should be included because they correspond to the worst-case scenarios. Finally, repetitions of some experiments would be useful to be conducted for model validation in order to assess the uncertainty of the experimental results. Small changes in the ignition condition (e.g., exact ignition location or initial mixture concentration) may lead to not negligible changes in the overpressure. Finally, special caution needs to be taken at the area of the end of the train because high values of pressure may be developed.

D4.3. Final report on analytical, numerical and experimental studies on explosions, including innovative prevention and mitigation strategies

3.2 Deflagration of non-uniform hydrogen-air cloud created by release in tunnel (4.3, KIT)

3.2.5 Background

Many studies have been dedicated to the combustion of the homogeneous hydrogen-air mixture. In hydrogen release accident scenarios in confined spaces like tunnels, the released hydrogen could not have sufficient time to mix with the ambient air before ignition. Thus, the hydrogen combustion occurs mostly in a non-uniform mixed state, e.g., in stratified layers on the top side of the tunnel. Such an accumulation of hydrogen is the consequence of a delayed ignition, which is supposed to take place with a certain possibility in the hydrogen leak accident. In this section the hydrogen combustion of a non-uniform cloud is studied by means of numerical simulations.

3.2.6 Objectives

The pressure and thermal loads of the non-uniform hydrogen-air mixture combustion in the semi-confined tunnel model are mainly concerned through the simulations, with special focuses on the peak pressure caused by hydrogen deflagration. As one of the mitigation measures, the influence of tunnel ventilation on hydrogen behaviour is discussed.

3.2.7 Knowledge gaps and accident scenarios assessed

A horse-shoe cross section tunnel is modeled in 3D with eight cars in it. Hydrogen is released through the TPRD of one of the eight car models. Non-uniform hydrogen cloud is formed in the tunnel domain. An artificially delayed ignition source starts the hydrogen combustion process. The caused peak pressure is evaluated.

3.2.8 Numerical simulation development

The 3D compressible Navier-Stokes flow dynamics equations with multiple gas species transport models are solved. The flow turbulence is formulated by a two-equation standard k-epsilon model. An adiabatic boundary condition is assumed at the overall boundaries of the tunnel model. A simplified chemistry of hydrogen combustion is adopted.

3.2.9 Validation / optimisation

The hydrogen distribution and combustion models in the KIT in-house HyCodes have been widely validated in many nuclear applications and hydrogen energy applications and been verified against experiments performed on the KIT hydrogen test facilities as well as the experiments carried out by the collaborating institutes.

3.2.10 Results

3.2.10.1 Without tunnel ventilation

Model

A tunnel section is modelled in 12 m long, 9.6 m wide and 6.6 m high, which has two lanes with eight operating cars, as shown in Figure 32. The whole domain is meshed by 130 x 80 x 120 cells with an average cell size of 10 cm for hydrogen distribution simulation, but a refined mesh by 130 x 80 160 x 120 cells with an average cell size of 7 cm for hydrogen combustion simulation. The discretized computational domain is shown in Figure 33.

D4.3. Final report on analytical, numerical and experimental studies on explosions, including innovative prevention and mitigation strategies

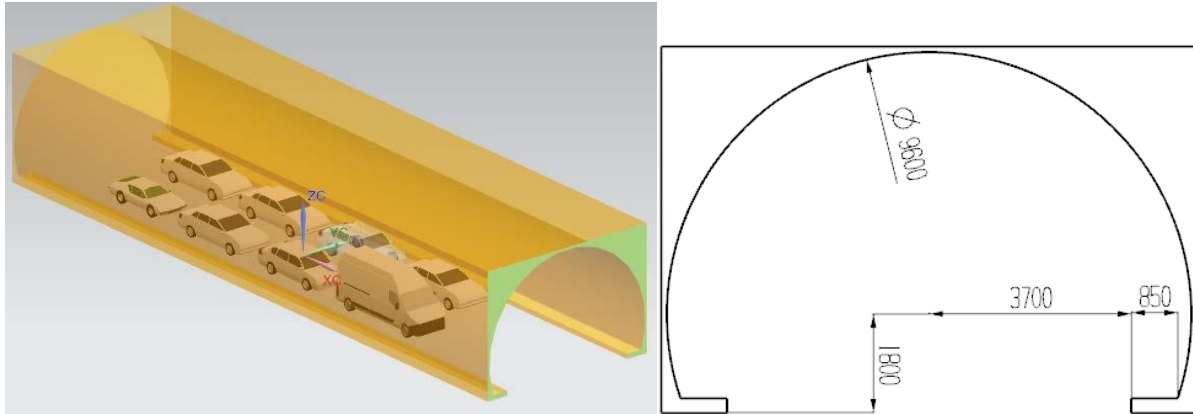


Figure 32. A horse-shoe cross-section tunnel model with eight cars.

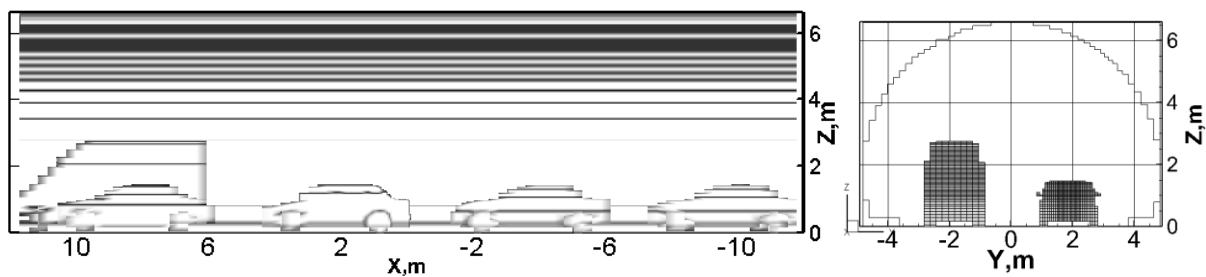


Figure 33. Discretized computational domain.

Hydrogen source

Hydrogen is released at the rear of the second car with a vertical upwards injection. The hydrogen mass flow rate is shown in Figure 34, which is equivalent to three TPRD openings of 70 MPa storage tanks of fuel cell vehicle.

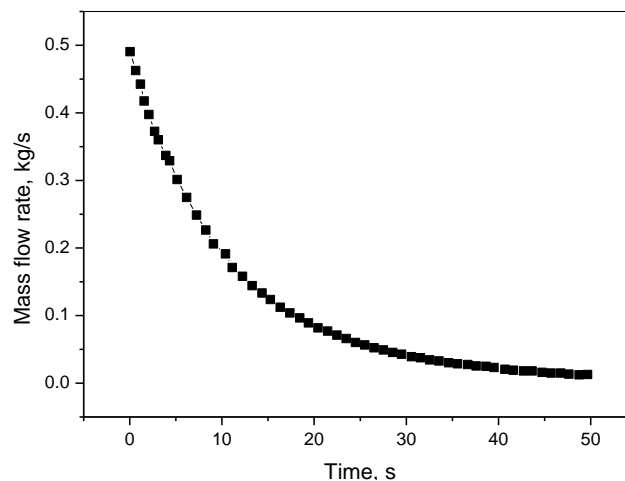


Figure 34. Injected hydrogen mass flow rate through three TPRD opens ($\Phi=2.5$ mm) in H_2 tanks @ 70 MPa and 293 K.

Hydrogen distribution

Figure 35 presents the released hydrogen cloud developing process. The hydrogen plume rises upwards and spreads bi-directionally along the ceiling after it touches the tunnel ceiling, which

D4.3. Final report on analytical, numerical and experimental studies on explosions, including innovative prevention and mitigation strategies
is due to unavailable tunnel ventilation. The gas mixing is very limited and strongly stratified hydrogen layers are formed on the top side.

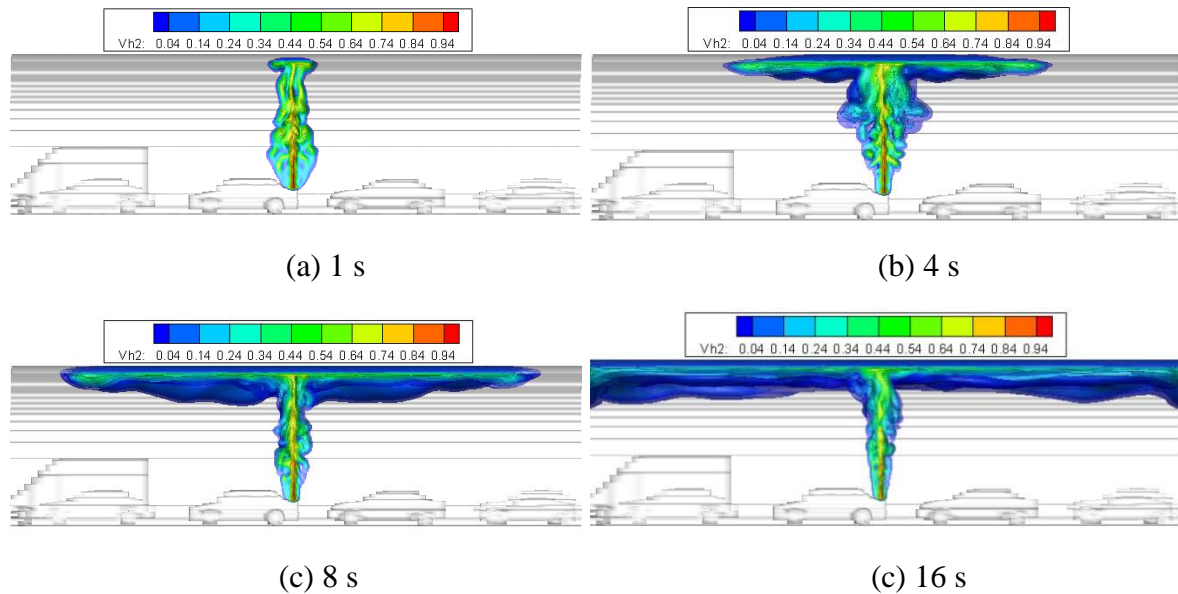


Figure 35. Flammable hydrogen clouds with greater than 4 vol. % H_2 in longitudinally vertical cut through the injection point at 1 s, 4 s, 8 s and 16 s, without tunnel ventilation.

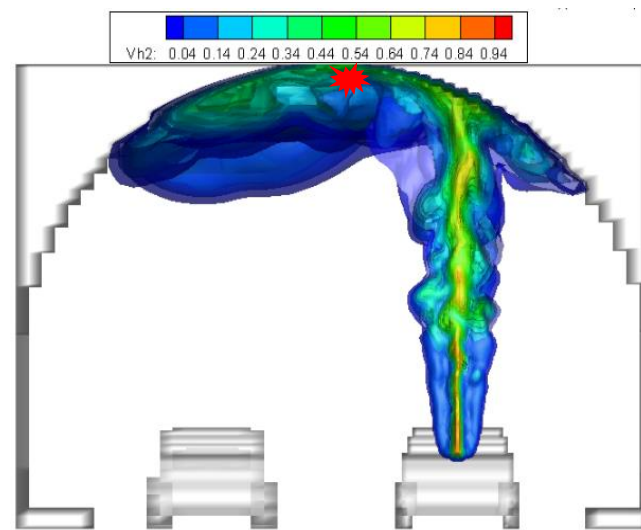


Figure 36. Hydrogen concentration distribution in a transverse cut at 16 s showing the ignition position with the spark in red close to the ceiling.

Hydrogen combustion

The hydrogen cloud is ignited at 16 s. The distributed hydrogen in the whole domain at the moment is about 3.5 kg. The artificial ignition spark is located at the ceiling as shown in Figure 36.

D4.3. Final report on analytical, numerical and experimental studies on explosions, including innovative prevention and mitigation strategies

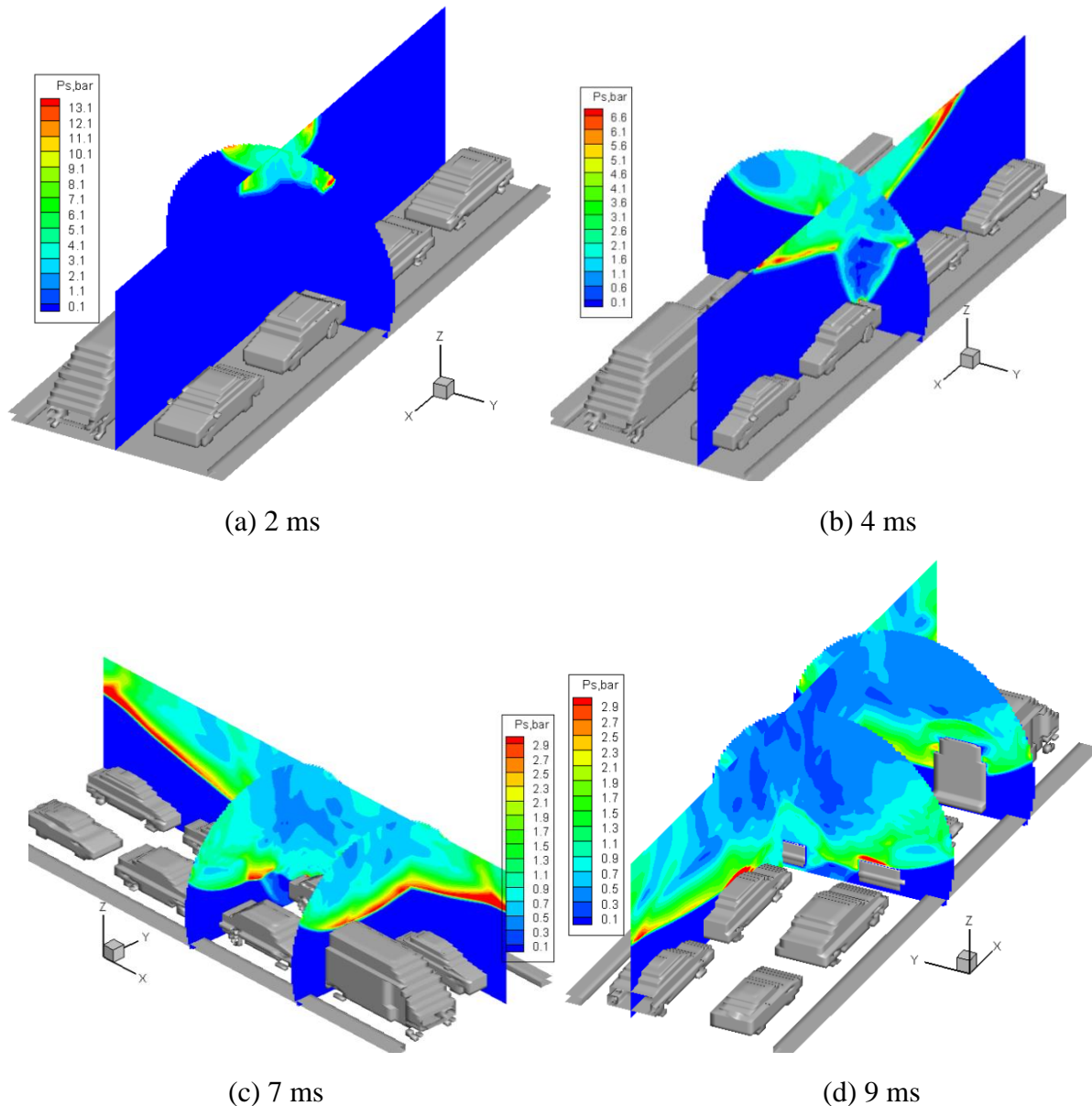


Figure 37. Pressure distributions in the tunnel at 2 ms, 4 ms, 7 ms and 9 ms later than the ignition in case of no ventilation.

The pressure distributions at transverse and longitudinal cuts of the tunnel are shown in Figure 37. Significantly high pressure appears due to the hydrogen deflagration of the non-uniform mixture. Attention should be paid to that the tunnel has no ventilation and the hydrogen release rate is significantly high. Although the assumed scenario is somehow beyond the real situation, the computed high overpressure proves that ventilation is indispensable for tunnels of any length to avoid potential hydrogen risk.

3.2.10.2 With tunnel ventilation

3.2.10.2.1 COM3D code

The numerical simulation of the hydrogen release, dispersion and explosion in a tunnel was carried out by using the in-house COM3D code developed in the Karlsruhe Institute of Technology.

D4.3. Final report on analytical, numerical and experimental studies on explosions, including innovative prevention and mitigation strategies

At the hydrogen dispersion stage,

- implicit solver (ALE) was utilized,
- the flow turbulence was modelled by the RNG k- ϵ model.

After the ignition,

- the simulation of the turbulence was carried out with the RNG k- ϵ model and,
- the TVD 2nd order solver was utilized in present simulations,
- the combustion was modelled utilizing the KYLCOM model coupled with the turbulence burning velocity correlation proposed by Schmidt.

3.2.10.2.2 Modelling of the tunnel

The geometry model of the circular tunnel consists of an actual scaled tunnel and eight cars, as shown in Figure 38 (a), and the geometry model of rectangular tunnel adopts the same road width (8.7 m) and the cross-sectional area (54.8 m²) as the circular tunnel, as shown in Figure 38 (b). The geometry information for the longitudinal and transverse cross section view of the tunnel is given in Figure 39 and Figure 40, respectively. The cross-sectional diameter of the circular tunnel is 4.8 m. The cross-sectional dimension of the rectangular tunnel is 6.3 × 8.7 m². The actual model consists of eight cars placed in two lanes in the tunnel. Each of the cars is located at the centre of each lane with a spacing distance of 1 m between cars to simulate a tight traffic condition. The length and width of the car model are 4 m and 2 m, respectively. The hydrogen injection location is at the rear of the second car, venting upwards to the tunnel ceiling which is assumed as the most severe scenario based on the reference (Lafleur et al., 2017). The mass flow rate of H₂ injection given in is equivalent to the flow rate when TPRD with 2 mm diameter is activated in a hydrogen fuel cell car equipped by an inventory of 5kg H₂ in 0.125 m³ at 70 MPa.

For the circular tunnel, the calculation domain of the tunnel is given with a length of 25 m, width of 9.6 m, and height of 6.6 m. For the rectangular tunnel, the calculation domain of the tunnel is given with a length of 25 m, width of 8.7 m, and height of 6.3 m. For the ventilation case, an extra gas volume is set on the exit end of the tunnel to ensure the stability of the flow field and the non-reflecting boundary conditions are imposed at all boundaries of the extra volume except the bottom boundary. The velocity boundary condition with 3 m/s ventilation is specified at another end of the tunnel as the entrance of venting air. The calculation region is discretized into 4,698,000 numerical cells with a cell size of 0.1 m. For the non-ventilation case, the two additional volumes are imposed at both ends of the tunnel, respectively. The none-reflecting boundary conditions are also set at all boundaries of extra volumes except bottom boundary. The calculation region is discretized into 5,742,000 numerical cells with a cell size of 0.1 m.

Two rows of sensors are set to record pressure histories in the tunnel. One line of sensors (P₁) is in the centre of the tunnel, two metres above the ground. Another line of sensors (P₂) is above the leak, 5 meters above the ground. Both rows of sensors are separated by 2 m from each other. P₁₃ and P₁₄ are 0.4 m and 1.6 m horizontally away from the leakage point, respectively. The position of the pressure sensor and the hydrogen leakage are shown in Figure 38 and Figure 39. For the cases with ventilation, the ignition point is at 1.8 m downstream of

D4.3. Final report on analytical, numerical and experimental studies on explosions, including innovative prevention and mitigation strategies

the leak and 4 m above the ground. For the cases without ventilation, the ignition point is directly above the leak, 6 m above the ground.

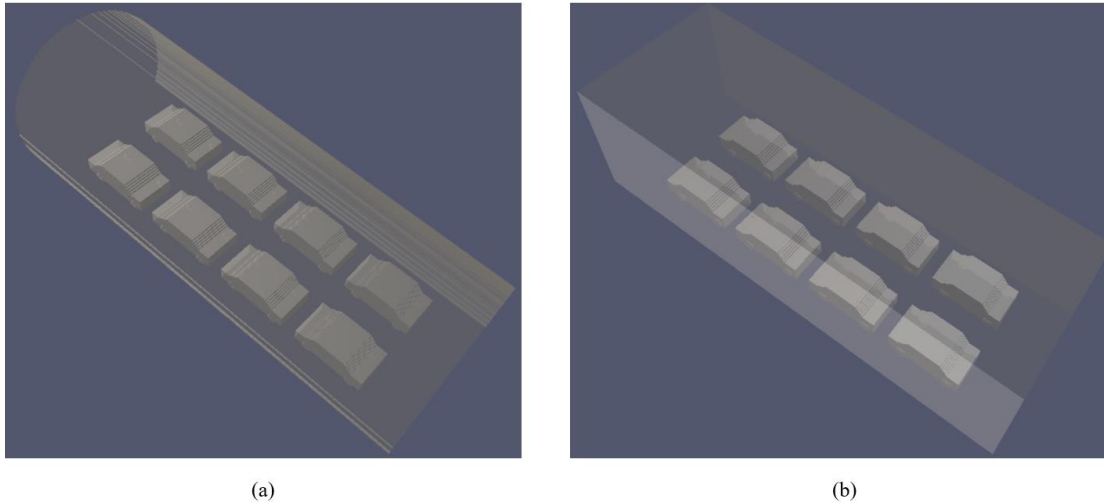


Figure 38. Diagram of the geometry model, (a) circular tunnel; (b) rectangular tunnel.

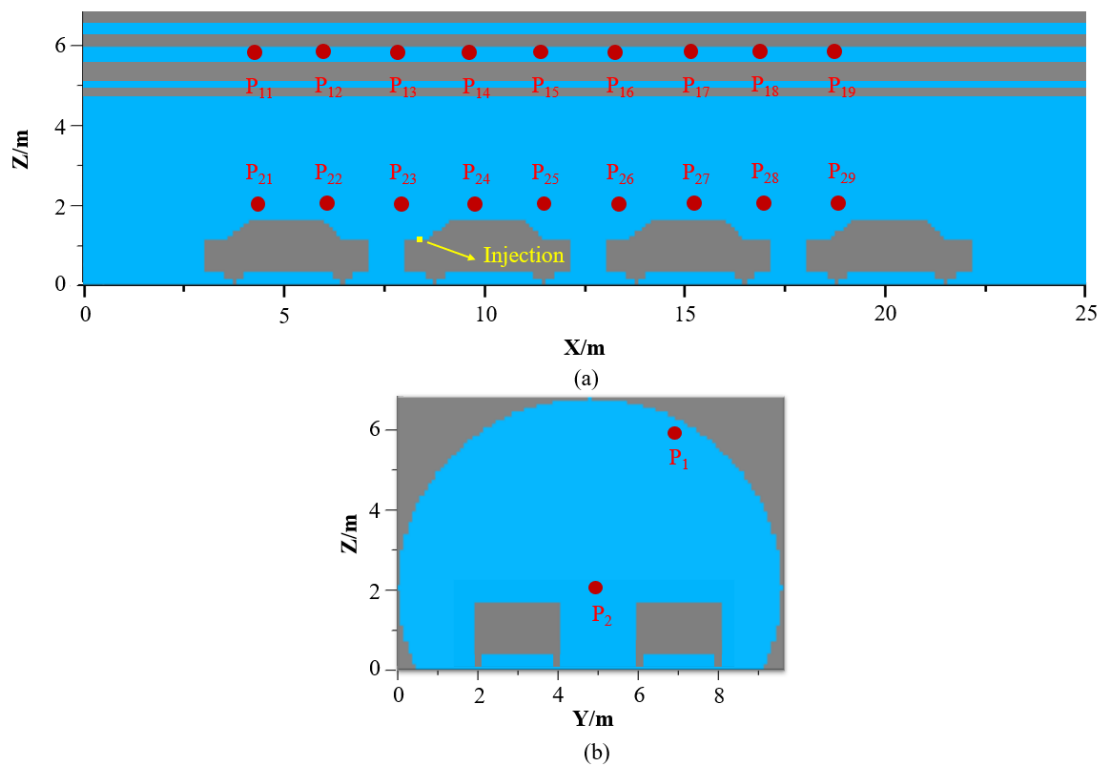


Figure 39. Computational region of the circular tunnel and the location of sensors, (a) longitudinal cross section; (b) transverse cross section ($9.6 \times 6.6 \text{ m}^2$).

D4.3. Final report on analytical, numerical and experimental studies on explosions, including innovative prevention and mitigation strategies

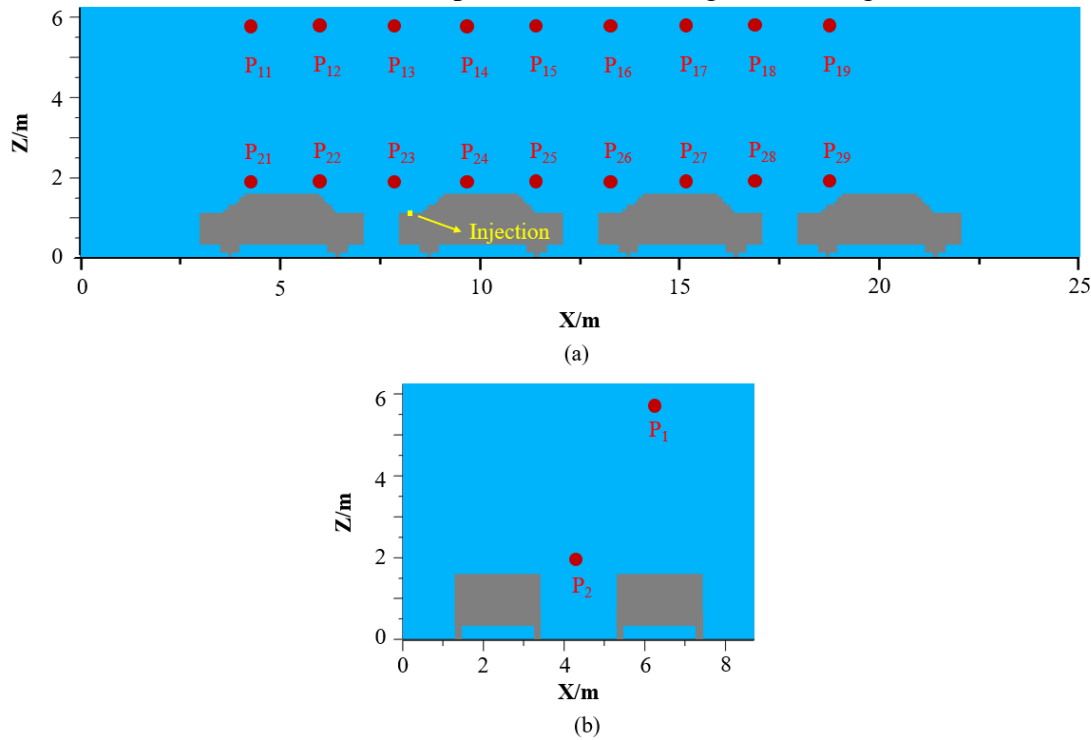


Figure 40. Computational region of the rectangular tunnel and the location of sensors, (a) longitudinal cross section; (b) transverse cross section ($6.3 \times 8.7 \text{ m}^2$).

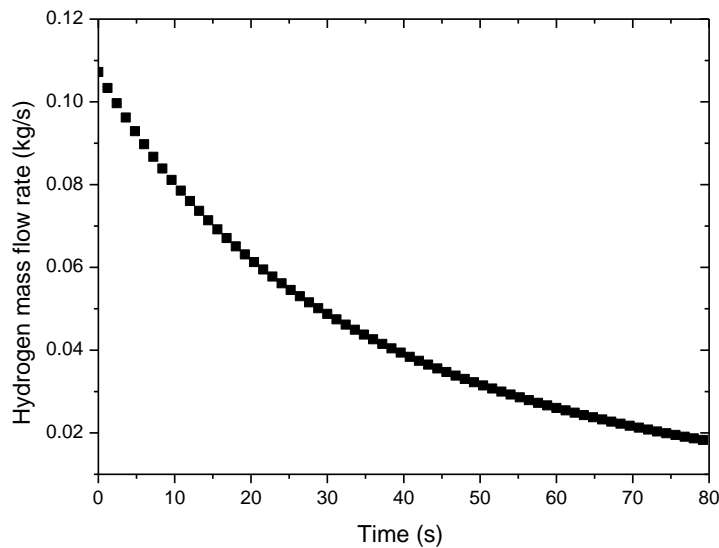


Figure 41. Mass flow rate of the H₂ injection (2mm Φ TPRD, 5kg H₂ in 0.125m³ at 70MPa).

3.2.10.2.3 Main results

3.2.10.2.3.1 Hydrogen distribution

When the hydrogen stored in the 70 MPa high pressure cylinders is released, a hydrogen jet is generated and H₂ diffuses rapidly. Figure 42 shows the longitudinal hydrogen concentration contours with H₂ concentration > 4 vol. % along the tunnel axis at t = 5 s with and without ventilation in circular and rectangular tunnels, respectively. The flammable hydrogen cloud

D4.3. Final report on analytical, numerical and experimental studies on explosions, including innovative prevention and mitigation strategies

was several metres long at the time of 5 s. When the 3 m/s ventilation was set in the tunnel, almost all the hydrogen clouds were blown downstream. The hydrogen clouds with ventilation in the circular tunnel (Figure 42a) and rectangular tunnel (Figure 42c) was similar. The position where the hydrogen cloud touches the tunnel ceiling is at the downstream of the leakage location. Figure 42(b) and Figure 42(d) show the hydrogen distribution without ventilation. A hydrogen jet was generated and quickly reached to the top of the tunnel, and then rapidly diffused. The hydrogen accumulated at the tunnel ceiling due to the density difference between hydrogen and air. In addition, the hydrogen diffusion length in the rectangular tunnel was shorter than that in the circular tunnel, which means the hydrogen is more likely to accumulate in rectangular tunnels. Comparing with the ventilation cases, the higher hydrogen concentration was observed in the tunnel with the non-ventilation cases.

Figure 43 shows the hydrogen concentration contours in a transverse direction of the tunnel at $t = 5$ s under different configurations. The result shows that ventilation promotes hydrogen diffusion. The hydrogen did not accumulate right below the ceiling, as shown in Figure 43(a) and Figure 43(c), but for the non-ventilation case, the hydrogen jet flows impinge on the ceiling of the tunnel and then spread along the ceiling. The flammable hydrogen cloud was very close to the ceiling and have a stratified high concentration. Therefore, it can be concluded that ventilation can greatly influence the distribution of hydrogen when hydrogen released from the TPRDs.

D4.3. Final report on analytical, numerical and experimental studies on explosions, including innovative prevention and mitigation strategies

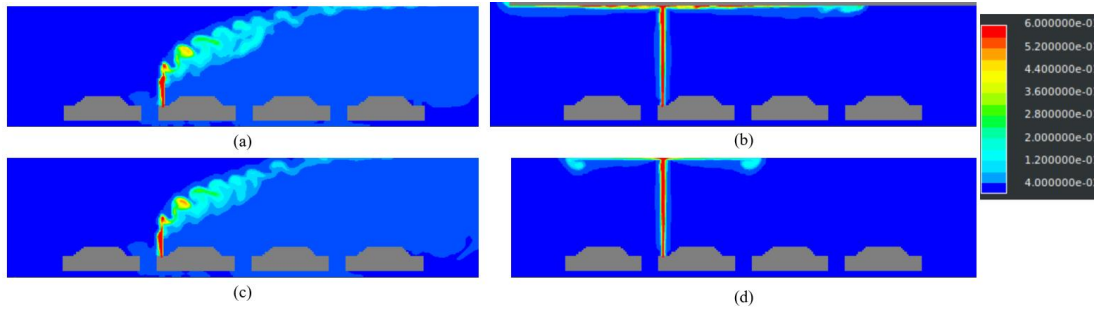


Figure 42. Longitudinal view of hydrogen concentration contours at $t = 5$ s in (a) circular tunnel with ventilation; (b) circular tunnel without ventilation; (c) rectangular tunnel with ventilation; (d) rectangular tunnel without ventilation.

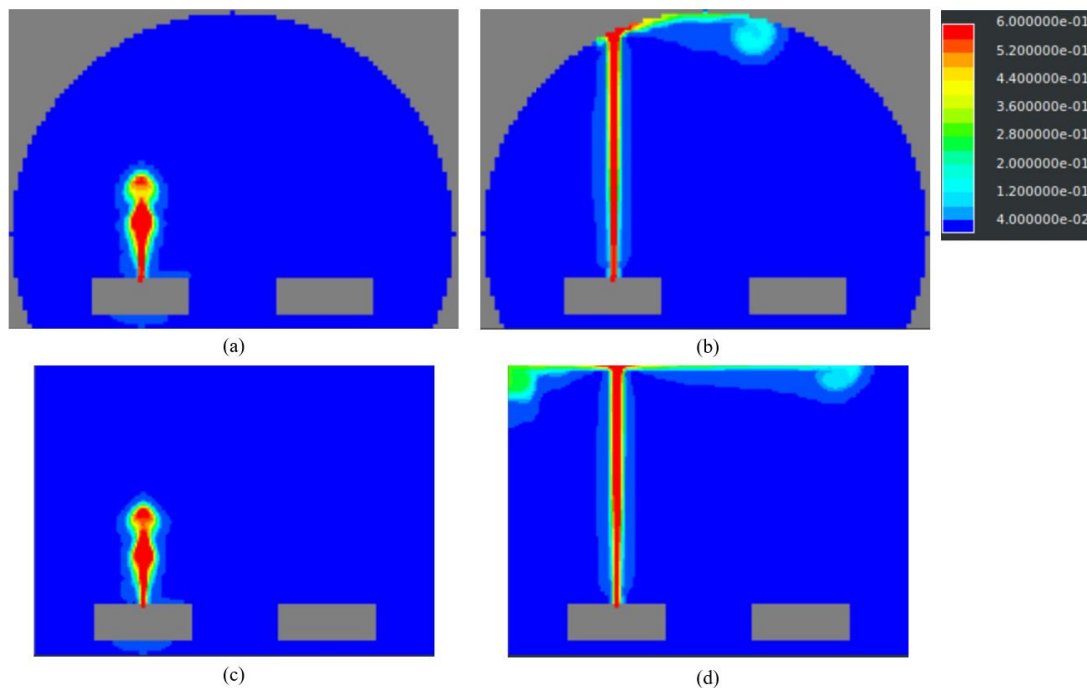


Figure 43. Transverse view of hydrogen concentration contours at $t = 5$ s in (a) circular tunnel with ventilation; (b) circular tunnel without ventilation; (c) rectangular tunnel with ventilation; (d) rectangular tunnel without ventilation.

3.2.10.2.3.2 Pressure

The hydrogen cloud was ignited at 5.2 s after the start of the release. The pressure history of H_2 deflagration in different configurations is shown in Figure 44 to Figure 47. As shown in Figure 44 and Figure 45, the peak of the pressure in both circular tunnel and the rectangular tunnel is similar for cases with ventilation, which agrees with the distribution of H_2 mole fraction as mentioned in last section. The overpressure for both cases is very low, about 0.04 bar. The pressure field has a spatially and temporally uneven distribution. A maximum overpressure of about 0.07 bar can be observed in the pressure contour plot, as shown in Figure 48. Besides, the pressure changes of both lines of sensors are similar in the same tunnel. As shown in Figure 46 and Figure 47, a higher overpressure is obtained in the cases without ventilation, with a narrow pressure peak distribution. The data points are farther from the release location, the pressure rise occurs with a longer delay, which presents the flame propagation process. For the upper line of P1 sensors, the maximum overpressures are about 0.15 bar and 0.17 bar for the

D4.3. Final report on analytical, numerical and experimental studies on explosions, including innovative prevention and mitigation strategies

circular and rectangular tunnel, respectively. However, for the lower line of P2 sensors, the maximum overpressures are about 0.03 bar and 0.045 bar for circular and rectangular tunnel, respectively. Like the ventilation condition, the pressure distribution is uneven spatially and temporally, and the maximum overpressure can be obtained near the ceiling, which is nearly 0.7 bar, as shown in Figure 49. The comparison of Figure 44 to Figure 47 shows that the maximum deflagration overpressure is reduced if ventilation was present.

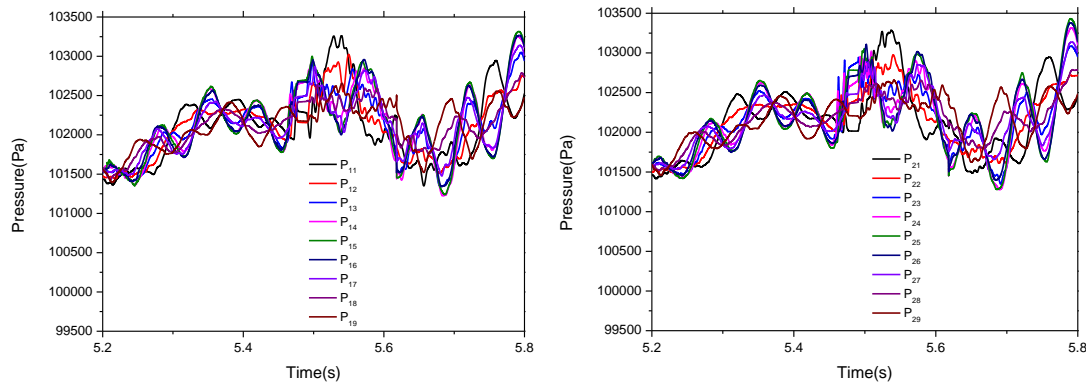


Figure 44. Pressure history in circular tunnel with ventilation, with ignition at 5.2 s.

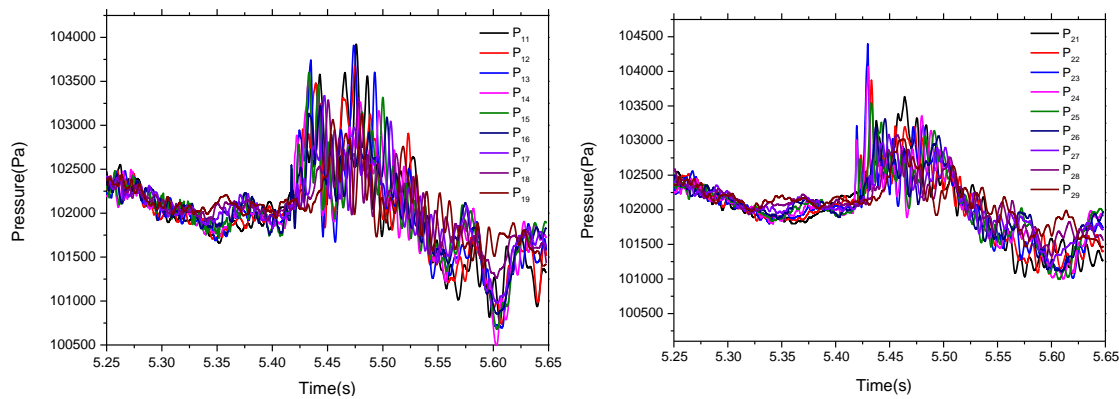


Figure 45. Pressure history in rectangular tunnel with ventilation, with ignition at 5.2 s.

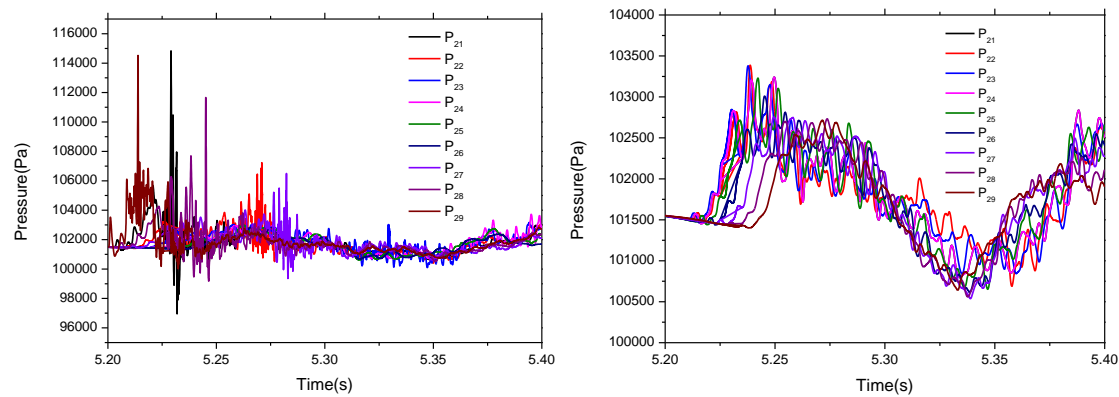


Figure 46. Pressure history in circular tunnel without ventilation, with ignition at 5.2 s.

D4.3. Final report on analytical, numerical and experimental studies on explosions, including innovative prevention and mitigation strategies

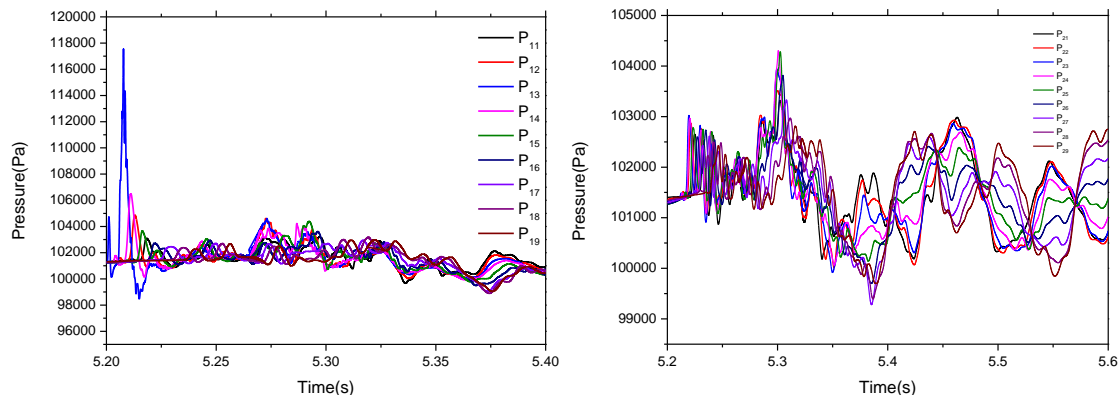


Figure 47. Pressure history in rectangular tunnel without ventilation, with ignition at 5.2 s.



Figure 48. Pressure contour plot at 5.216s for cases with ventilation.



Figure 49. Pressure contour plot at 5.275s for cases without ventilation.

3.2.11 Conclusions

For the H₂ distribution stage, ventilation can greatly influence the distribution of hydrogen when hydrogen released from the TPRDs. When the 3 m/s ventilation was set in the tunnel, almost all of the hydrogen clouds were blown downstream. The upstream of the ventilation was less hazardous than the downstream and the risk around the hydrogen leaking vehicle was reduced significantly. Hydrogen is more likely to be accumulated and pose a higher risk in the rectangular tunnel than that in the circular tunnel.

After ignition, the H₂ deflagration overpressure is reduced by the ventilation effectively. For the cases without ventilation, the overpressure is obviously higher than that with ventilation. The local pressure near the ceiling even exceeds 1.4 bar. Nevertheless, the overpressure at the lower space of the tunnel, recorded by the low line of sensor, keeps very low.

According to the simulation results, the tunnel is advised to be ventilated in the same direction as the road traffic. Thus, once the hydrogen was released, the hydrogen would disperse along

D4.3. Final report on analytical, numerical and experimental studies on explosions, including innovative prevention and mitigation strategies
the ventilation, and people in the vehicles blocked in the upstream would have more time to escape.

3.3 Numerical Study of deflagration interaction with mist systems (4.3, NCSR)

3.3.5 Introduction – literature review

Adding water mist in a reactive mixture can have significant effects on flame properties. These effects are a result of different mechanisms such as the reduction of reactants' concentration, reduction of temperature due to heat absorption and chemical effects (Yoshida et al. 2015). In case of water droplets, additional effects are introduced due to the interaction of the flow-field with the droplets. There are some studies in the literature, which have investigated the effect of water mist or water droplets on the deflagrations and on shock waves.

Ye et al. 2005 performed experiments in a tube of 25 m length and 0.7 m diameter using a homogeneous methane-air mixture of 8% concentration. To form a shock wave at the beginning of ignition 5 g (TNT) were used. Various mist densities were examined such as 24, 33 and 49 kg/m³. The larger the water volume, the better the suppression effect was.

Schwer et al. 2007 investigated numerically the effect of water-mist on shock waves generated by a TNT explosive. The water-mist mitigated the shockwave through vaporization and momentum reduction. Momentum extraction had the dominant role in mitigating the leading shock wave. The ratio of water mass to gas mass within a cell was equal to 0.5 in most cases but also smaller ratios were tested with the smallest to be equal to 0.25. The maximum droplet sizes were equal to 15-50 µm. Despite the large latent heat of vaporization and heat capacity of water, it was found that the role of vaporization on shock wave mitigation was small, particularly close to the explosive. Two reasons were given for this phenomenon: Firstly, the amount of water that is vaporized directly in the shock wave is small due to the moderate temperature and the short duration of the phenomenon. Secondly, the water that is vaporized leads to gas pressure increase, cancelling out the effect of lowering the pressure through lower gas temperatures. Thus, the main mechanism for pressure mitigation in the examined case was momentum extraction.

Song et al. 2019 studied the influence of droplet size and concentrations on explosion using 2D numerical model in an 8.9 m long tube of 0.108 m diameter. Methane explosions of 9.5 % were considered. The methane-air mixture was placed at the first 2.5 m of the tube whereas the mist region was placed from 3 to 4 m. The model considered the breakup of the droplets at the explosion phase ignoring collisions and coalescence. Standard k-e model was used for turbulence and finite rate/eddy dissipation model for combustion. A Lagrangian approach for the droplets was used. The discrete and the continuous phase exchanged heat, mass and momentum. The range of droplet size of 50 to 150 µm was found to be more effective compared to larger or smaller sizes. Water concentrations were ranged between 0.3 to 1.5 kg/m³. Simulations showed that the overpressure decreases with the increase of initial mist concentration. However, the decrease was small. The effect on temperature was more pronounced.

Cao et al. 2019 investigated experimentally the suppression affected by ultrafine water mist containing different additives. A closed combustion vessel of 23.2 L was used filled with a homogeneous 9.5 % methane-air mixture. The water particles diameter ranged from 5 to 10 µm

D4.3. Final report on analytical, numerical and experimental studies on explosions, including innovative prevention and mitigation strategies and the water concentrations that were investigated were equal to 56, 112, 168, 224 and 280 g/m³. Alkali metal additions were also used with mass fraction equal to 5 %. It was found that adding alkali metal can significantly enhance the effect of water mist.

Battersby et al. 2012 also investigated the effect of fine water mist on hydrogen-oxygen-nitrogen explosions. Water concentration values of 90, 200 and 250 mg/l were used. The effect on the pressure rise was significant. The Sauter mean diameter of the particle was close to 5-6 μm .

Liang et al. 2010 studied numerically the effect of water addition on methane explosion in the constant volume bomb. Mole fraction of water in the mixed gas equal to 0, 5, 10 and 20 % were studied (with methane mole fraction equal to 0.07, 0.063, 0.0595 and 0.056, respectively). It was found that 10 % water fraction decrease the temperature after explosion from 2700 K to 2600 K whereas 20 % water fraction decrease the temperature to 2380 K.

3.3.6 Examined cases

In order to examine the effect of water mist on hydrogen deflagrations, the HSE tunnel geometry was utilized. The length of the tunnel is equal to 70 m and the maximum height equal to 3.25 m. For simplicity, uniform hydrogen-air mixture of 30 % was used. The mixture is assumed to occupy an area of 10 m length around the center of the tunnel, from $x=30$ to $x=40$ m from the tunnel exit. The above assumptions are close to the findings of the pre-test simulations of hydrogen release from a train inside the empty tunnel. The ignition was located at a vertical distance approximately equal to 1.2 m from the ground and at the center of its length. Deflagration simulation without water was first conducted and then 5 different water concentrations were used to examine the effect of mist on the overpressure. Water was distributed uniformly inside the hydrogen-air mixture.

3.3.7 Simulation details

The simulations were made in 2D domain, to obtain a first insight of the effect of water concentrations on the results within reasonable computational time. The 2D grid was positioned on the symmetry plane of the tunnel. In Table 27 the examined scenarios are presented. Water concentration and species mass fractions are presented. Hydrogen to hydrogen-air ratio remains constant in all cases. We observe that most of water is in liquid state. Estimations made about the displaced (from water) hydrogen-air mixture, revealed that its volume is very small and thus it was ignored in all examined cases.

Table 27. Deflagration scenarios. Water concentration and initial mass fractions.

Water concentration (kg/m ³)	Hydrogen mass fraction (kg/kg)	Oxygen mass fraction (kg/kg)	Water mass fraction (kg/kg)	Liquid water mass fraction (kg/kg)
0	0.0291	0.226	0.0	0.0
0.05	0.0275	0.214	0.0538	0.040
0.10	0.0261	0.203	0.102	0.089
0.20	0.0237	0.184	0.185	0.173
0.50	0.0185	0.144	0.362	0.353
1.00	0.0136	0.106	0.532	0.525

D4.3. Final report on analytical, numerical and experimental studies on explosions, including innovative prevention and mitigation strategies

Homogeneous equilibrium model was used for the two-phase mixture. Both liquid and vapor phase have the same temperature and the phase distribution is estimated using Raoult's law. As a result, the evaporation of water droplets occurs very fast. This assumption is valid in a very fine water mist (very small droplet size). The effect of liquid phase on the velocity field due to the imposed drag is ignored in this study. Thus, no water droplet diameter needs to be defined.

For the simulations the ADREA-HF CFD code (Venetsanos et al. 2010) was used. For turbulence, the Kato-Launders modification (Kato et al. 1993) of k- ϵ model was utilized. The equations were discretized using the second order upwind bounded numerical scheme for the convection terms and a first order upwind discretization for time. Combustion model utilized the Schmid's formula for turbulent flame speed and several wrinkling factors to account for flame instabilities. Model details and validation can be found in (Tolias et al. 20180, (Tolias et al. 2020) and (Momferatos et al. 2021). The computational grid consists of 12,240 cells. Uniform cell size was used at the area of the flammable mixture with cell length equal to 0.125 m.

3.3.8 Simulation results

In Figure 50 overpressure time series at three different distances from tunnel entrance are presented ($x=35$ m is at the middle of the tunnel and of the flammable cloud). The effect of water mist is shown. We observe that small additions of water mist lower than 0.1 kg/m^3 , have small effect on the generated overpressure. However, mist concentration higher than 0.2 kg/m^3 can reduce the pressure significantly. Maximum overpressure in 0.2 , 0.5 and 1.0 kg/m^3 cases is 1.27 , 1.75 and 4.7 times smaller compared to the dry case. The more pronounced effect on pressure is achieved with 1.0 kg/m^3 water concentration.

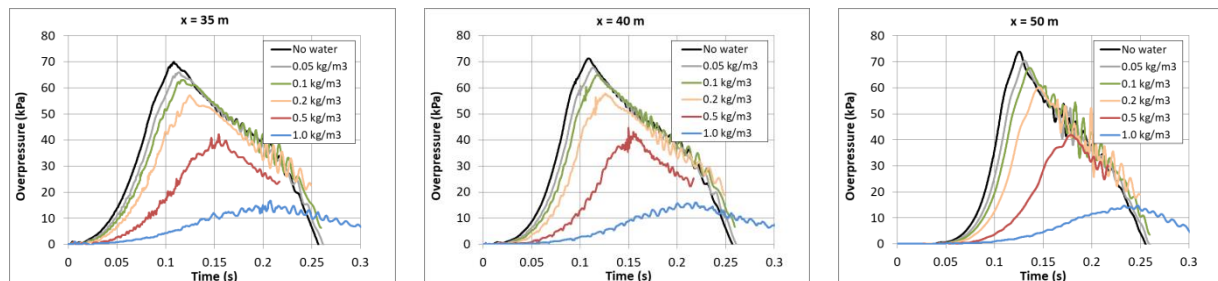


Figure 50. Effect of water mist. Overpressure time series at 35, 40 and 50 m, for different water concentrations.

In Figure 51 the effect of water concentration on maximum overpressure and on maximum temperature are presented. We observe that overpressure is reduced approximately linearly with the increase of water concentration. On the other hand, temperature relation with water deviates from linearity. Water cooling effect is very strong, and it is the main reason for the decrease of overpressure.

D4.3. Final report on analytical, numerical and experimental studies on explosions, including innovative prevention and mitigation strategies

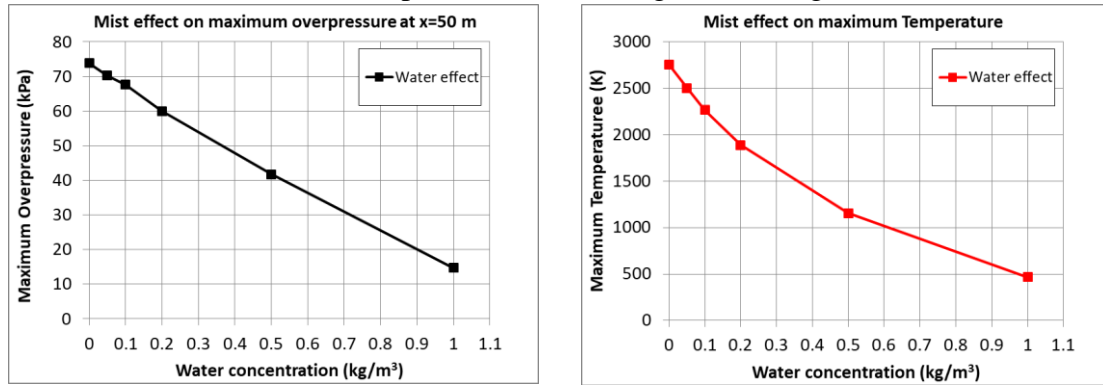


Figure 51. Effect of water mist on maximum overpressure (at $x=50$ m) and on maximum temperature.

3.3.9 Conclusions

The effect of water mist on hydrogen-air stoichiometric mixture was examined using 2D simulation inside the HSE tunnel geometry. The following assumptions were made:

- 1) Water droplets are uniformly distributed inside the whole volume of hydrogen-air mixture.
- 2) Heat exchange between the vapor and the liquid phase is very fast and thus the homogeneous equilibrium model can be used.
- 3) The effect of water droplets on the velocity field is negligible.
- 4) Water evaporation is very fast.

The last three assumptions can be valid in the case of a very small droplet diameter. The first two assumptions favor pressure reduction whereas the third one does not. However, if particles are very small and heat exchange is fast the effect of the momentum extraction due to drag and droplet division is expected to be negligible. The fourth assumption favors pressure reduction because of temperature reduction but hinders pressure reduction due to the increase of water volume. However, simulation results indicate that the effect of temperature dominates in high water concentrations. Thus, in overall, the observed pressure reduction can be considered as one of the best-case scenarios that can occur. For the examined case, water concentration equal to 1 kg/m^3 was found to be sufficient to reduce the overpressure significantly, leading to 4.7 times smaller overpressure compared to the no-mist case.

3.4 Simulation of water injection effect on shock wave attenuation (4.3, KIT)

3.4.5 Background

Tunnels are an increasingly important part of the traffic infrastructure especially in territorially uneven mountain areas. They create challenges for prevention and management of incidents/accidents, fire and explosion protection and security against attacks or sabotage. The use of alternative fuels, including compressed gaseous hydrogen (CGH_2) and cryogenic liquid hydrogen (LH_2), in tunnels and similar confined spaces creates new challenges to provision of life safety, property and environment protection at an acceptable level of risk.

The confined feature of traffic tunnel may amplify the potential risk of hydrogen fuel cell vehicles (HFCVs) in accident scenarios. Due to the narrow space and auxiliary facilities and devices acting as blockages in a tunnel, the tube might become an ideal place for hydrogen flame acceleration even detonation if the hydrogen involved accidents are not properly

D4.3. Final report on analytical, numerical and experimental studies on explosions, including innovative prevention and mitigation strategies

mitigated. Ventilations are designed for tunnels traditionally, to purify contaminants in air in normal operation and to control smoke in hydrogen-carbon fires caused by, e.g., conventional petroleum product fuelled vehicle accidents. In case of HFCV accident, ventilation can also facilitate to disperse and exhaust unintentionally released hydrogen.

Another important mitigation measure is water spray or mist in tunnels, which can decrease fire growth, spread and heat release rate of tunnel fires due to its cooling effect. It is an interesting topic to study the interaction between the distributed liquid droplets and hydrogen behaviours in tunnels.

Numerical modelling and CFD simulations of hydrogen distribution and combustion in tunnels or tunnel-like facilities were performed without water intervention. This study focuses on hydrogen deflagration suppressed by water mist in a tunnel.

3.4.6 Simulation code

The configurations of turbulence and combustion in the present simulations are consistent with that in previous circular and rectangular tunnel simulations. Namely, the RNG k - ε turbulence model and the implicit solver (ALE) were utilized for the hydrogen dispersion stage; the RNG k - ε turbulence model and the TVD 2nd order solver were utilized for the deflagration stage. The KYLCOM combustion model coupled with the turbulence burning velocity correlation proposed by Schmidt is specified in the current simulations. The drag coefficient correlation of Niansheng and Cheng (Cheng et al., 2009) was used the droplet dynamics. For the calculation of the total breakup factor, the correlation of Pilch and Erdman (Pilch et al., 1987) for $Oh \leq 0.1$ and the proposal from Gelfand (Gelfand et al., 1973) for $Oh > 0.1$ were used.

3.4.7 Modelling

The geometry model consists of HSE experimental tubular steel “explosion” tunnel and nine scaled vehicle models, as shown in Figure 52. The geometry information for the cross-section views of the tunnel is given in Figure 53. The tunnel region is given with a length of 70 m, width of 3.7 m, and height of 3.4 m. The cross-sectional diameter is 1.9 m. The vehicle models consist of seven cars, a van and a bus placed in two lanes in the tunnel. Each of the vehicles is located at the centre of each lane with a spacing distance of 2 m between vehicles except the first car. The scaled size of the car, the van and the bus model are $2 \times 0.9 \times 0.6 \text{ m}^3$, $2.4 \times 0.9 \times 1.1 \text{ m}^3$ and $4.5 \times 1.1 \times 1.6 \text{ m}^3$, respectively. Each vehicle was set on the rails with a height of 0.1 m and a space of 0.5 m. The hydrogen injection location is at the base of the first car. The release location is 4 m from the first row of vehicles and 35 m from the exit of the tunnel. The H_2 mass flow rate of injection given in Figure 54, is equivalent to the flow rate when a 2.2 mm diameter TPRD opens in a hydrogen fuel cell car with a scaled H_2 inventory of 0.45 kg in 0.053 m^3 at 118 bar. For the ventilation case, a velocity boundary condition with 3 m/s is specified at the entrance of the tunnel, and a non-reflection boundary condition is at the tunnel exit, as shown in Figure 53. For the non-ventilation case, both tunnel ends were set as the non-reflection boundary condition. The calculation domain is discretized into 880,600 numerical cells with a cell size of 0.1 m.

The length of the section with water mist injection is configured from the first vehicle to the last, covering the entire gas volume of the tunnel section, as shown in Figure 54. A droplet diameter of 500 μm and liquid phase (water) concentration of about 10 kg/m^3 for the

D4.3. Final report on analytical, numerical and experimental studies on explosions, including innovative prevention and mitigation strategies

experiments were assumed, which lead to a total number of droplets of 29×10^9 . For the huge number of droplets, it is not feasible to simulate every single droplet. Therefore, the code uses a droplet multiplication factor, which determines the number of droplets that are initialised in one cell and are calculated collectively. By using a droplet multiplication factor of 1.45×10^6 , only a number of 20,000 droplets are simulated representatively.

Two rows of sensors are set to record pressure evolutions in the tunnel. Both lines of sensors are above the leaking location, 3 m and 1 m above the ground, respectively. The detailed position of the pressure sensor and the hydrogen leakage are also shown in Figure 52. The ignition point is at 0.8 m downstream of the leak and 0.5 m above the ground.

D4.3. Final report on analytical, numerical and experimental studies on explosions, including innovative prevention and mitigation strategies

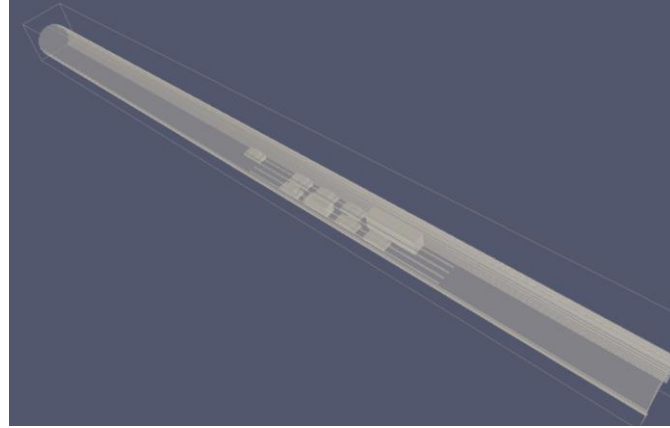


Figure 52. Geometry model of the HSE experimental tunnel.

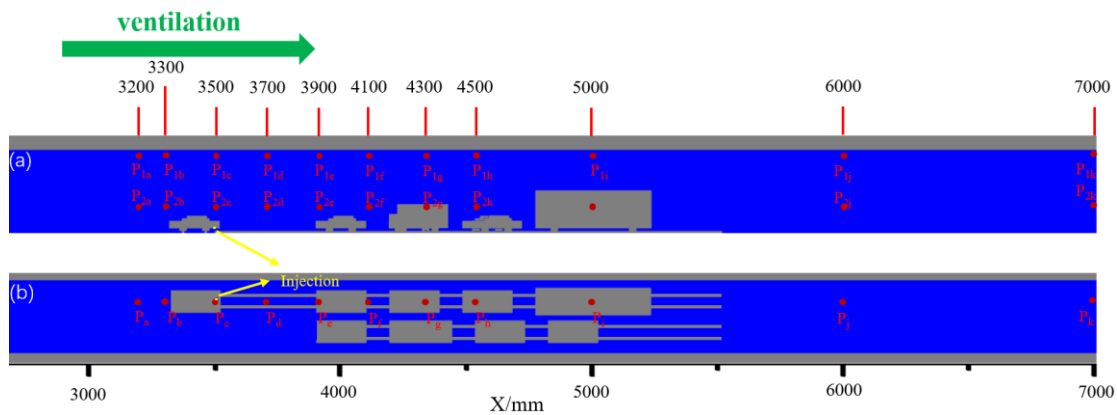


Figure 53. Computational domain of the HSE experimental tunnel and the location of sensors, (a) vertical view; (b) horizontal view.

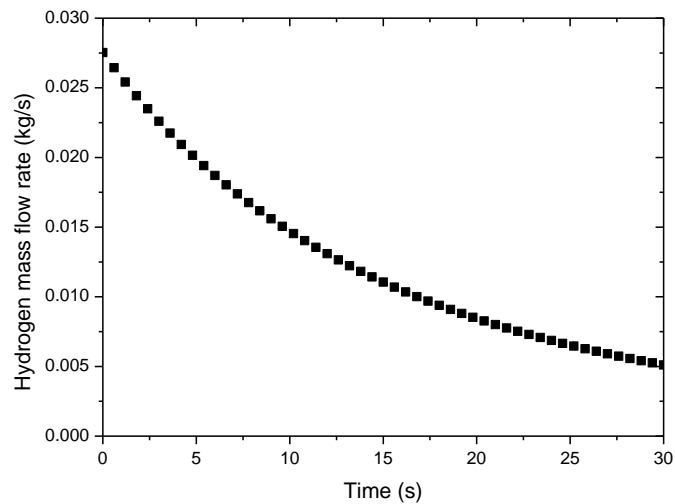


Figure 54. Mass flow rate of the H_2 injection (TPRD diameter Φ 2.2 mm, 0.45 kg H_2 in 0.053 m^3 at 118 bar).

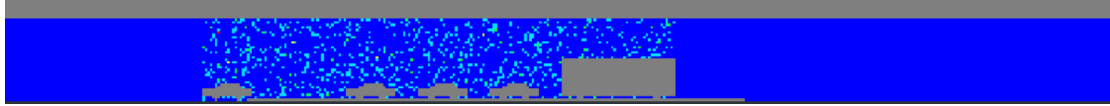


Figure 55. Mist region in the tunnel.

3.4.8 Results

3.4.8.1 Hydrogen distribution

Due to the downward injection of hydrogen, the hydrogen jet impinges the ground and bounces back. The hydrogen rises slowly due to the dominated buoyancy effect. Figure 56 to Figure 58 show the hydrogen concentration (> 4 vol. H_2 %) contours in the longitudinal vertical cut along the tunnel axis at different times with the ventilation of 0, 1.25 m/s and 2.4 m/s, respectively. For the non-ventilation tunnel (Figure 56), hydrogen overflowed from the rear of the car firstly, and then gradually flowed out around the car. When hydrogen reached the ceiling, it spread to both sides of the tunnel and accumulated at the ceiling to form a flammable hydrogen cloud. For the ventilation of 1.25 m/s in the tunnel (Figure 57), almost all the hydrogen cloud was blown downstream. The position where the hydrogen reached the ceiling was 2.5m downstream away from the leakage point. Then most of hydrogen was flowed downstream along the ceiling. When the 2.4 m/s ventilation was proposed, the hydrogen cloud was leaned downstream and the position where the hydrogen reached the ceiling was 7.5m downstream away from the leak. The hydrogen cloud was more dispersed, not just spread along the ceiling. Figure 59 to Figure 61 show the hydrogen concentration (> 4 vol. H_2 %) contours in the horizontal view right below the chassis of the leaking vehicle at different times with the ventilation of 0, 1.25 m/s and 2.4 m/s, respectively. For the non-ventilation tunnel (Figure 59), hydrogen didn't diffuse upstream or downstream and had a high concentration. The hydrogen cloud was nearly invariant with time in Figure 59. For the ventilation cases, the hydrogen cloud was blown downstream. The 3.7 m and 15.2 m hydrogen cloud for the 1.25 m/s and 2.4 m/s ventilation can be observed in Figure 60(d) and Figure 61(d), respectively.

For the three cases, the high hydrogen concentration (30 vol. H_2 %) was concentrated near the leak point. However, for 2.4 m/s ventilation condition, the region of the high hydrogen concentration was obviously smaller than that for the 1.25 m/s ventilation and non-ventilation condition due to the higher ventilation speed.

D4.3. Final report on analytical, numerical and experimental studies on explosions, including innovative prevention and mitigation strategies

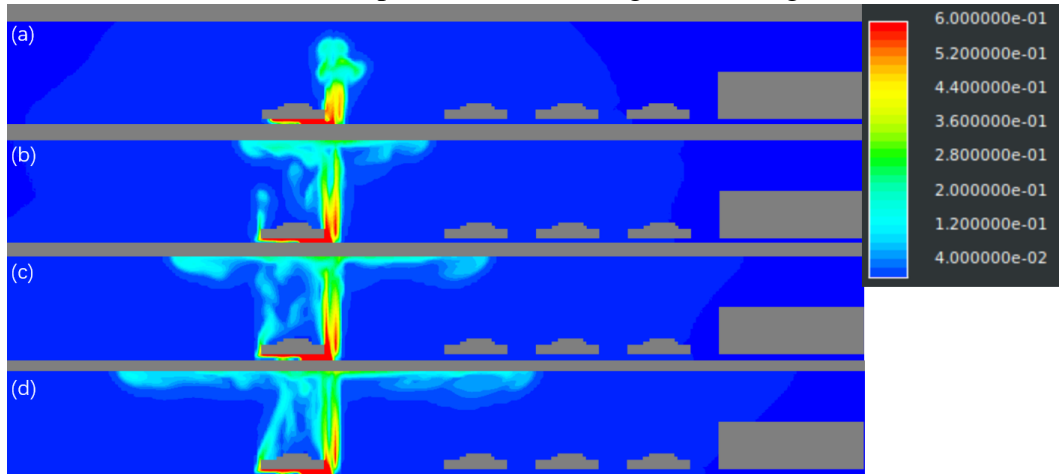


Figure 56. Hydrogen concentration contours in a longitudinal vertical cut along the tunnel axis without ventilation at $t = (a) 2.5 \text{ s}$; $(b) 5 \text{ s}$; $(c) 7 \text{ s}$; $(d) 9 \text{ s}$.

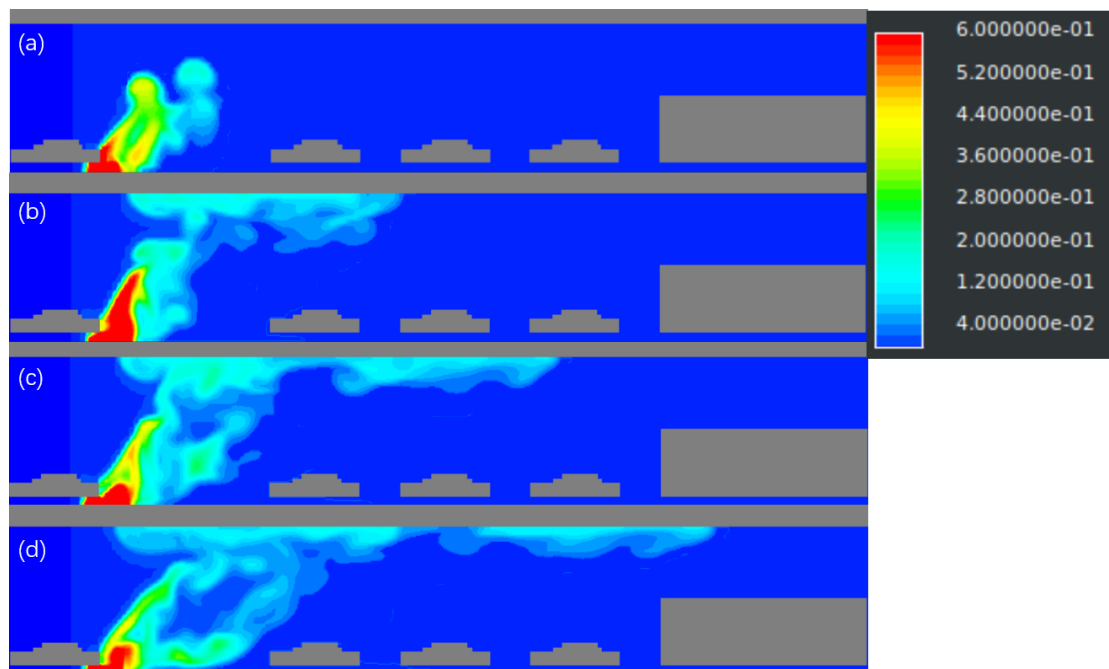


Figure 57. Hydrogen concentration contours in a longitudinal vertical cut along the tunnel axis with 1.25 m/s ventilation at $t = (a) 2.5 \text{ s}$; $(b) 5 \text{ s}$; $(c) 7 \text{ s}$; $(d) 9 \text{ s}$.

D4.3. Final report on analytical, numerical and experimental studies on explosions, including innovative prevention and mitigation strategies

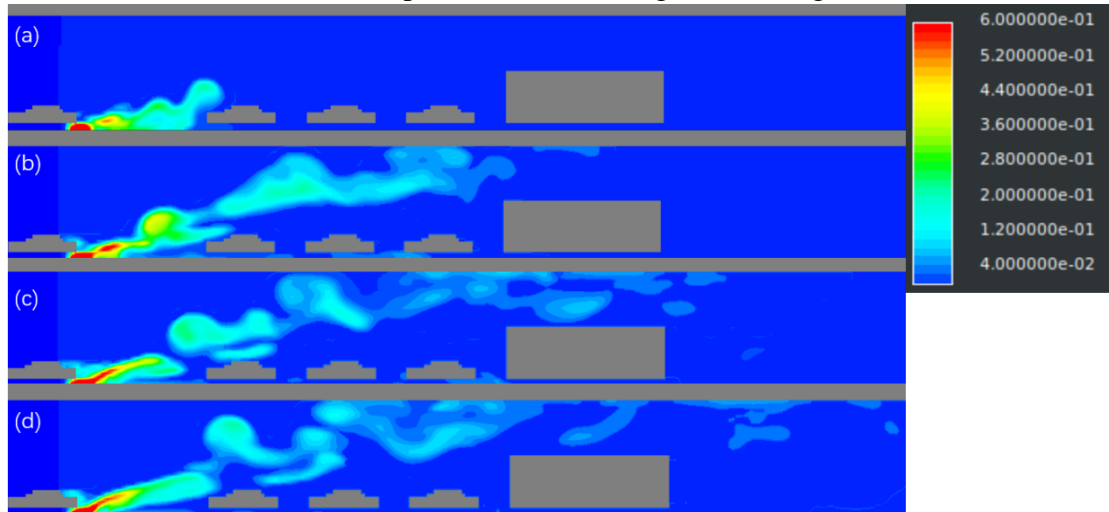


Figure 58. Hydrogen concentration contours in a longitudinal vertical cut along the tunnel axis with 2.4 m/s ventilation at $t = (a) 2.5$ s; $(b) 5$ s; $(c) 7$ s; $(d) 9$ s.

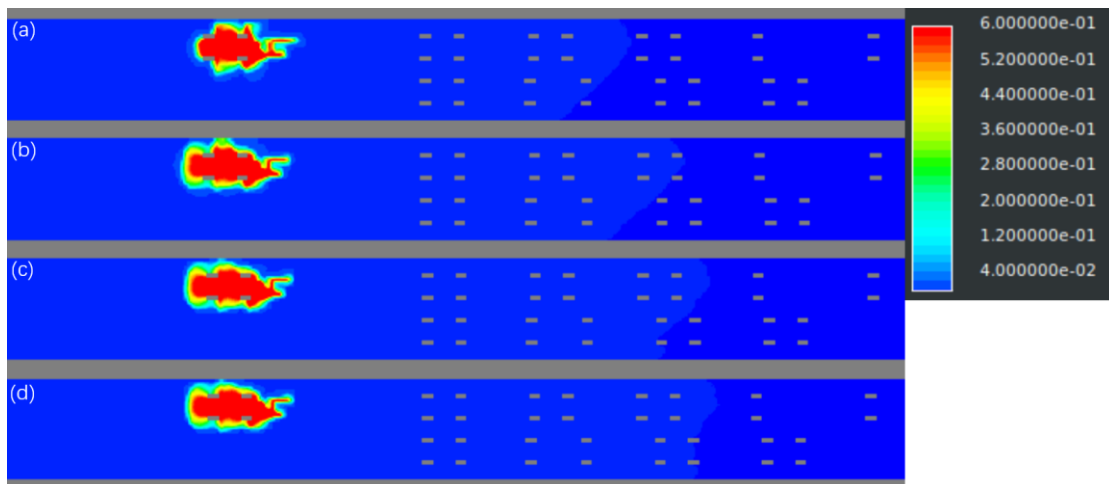


Figure 59. Hydrogen concentration contours in a horizontal view right below the chassis of the leaking vehicle without ventilation at $t = (a) 2.5$ s; $(b) 5$ s; $(c) 7$ s; $(d) 9$ s.

D4.3. Final report on analytical, numerical and experimental studies on explosions, including innovative prevention and mitigation strategies

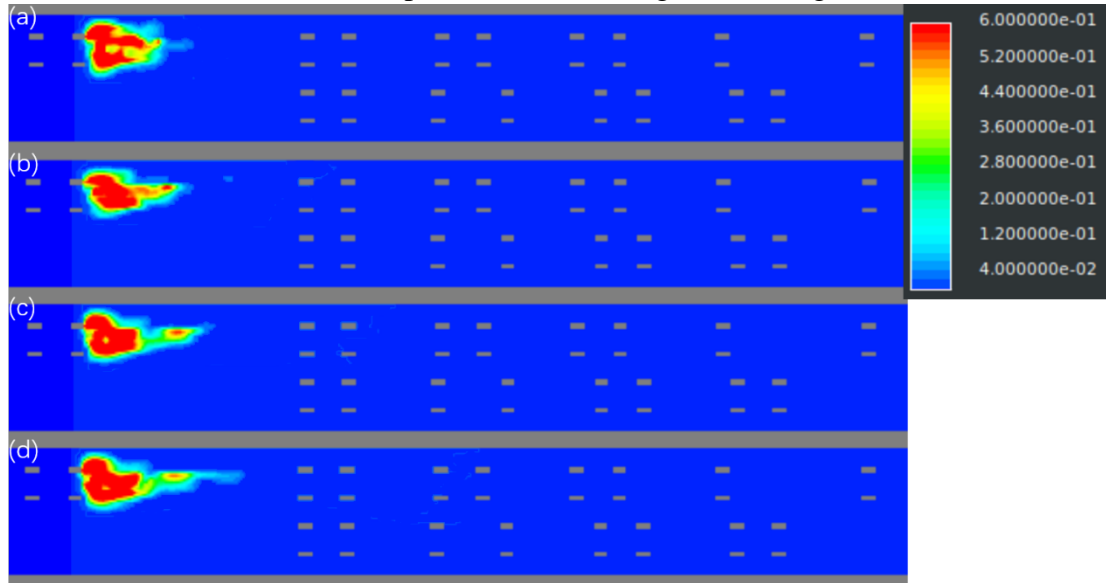


Figure 60. Hydrogen concentration contours in a horizontal view right below the chassis of the leaking vehicle with 1.25 m/s ventilation at $t =$ (a) 2.5 s; (b) 5 s; (c) 7 s; (d) 9 s.

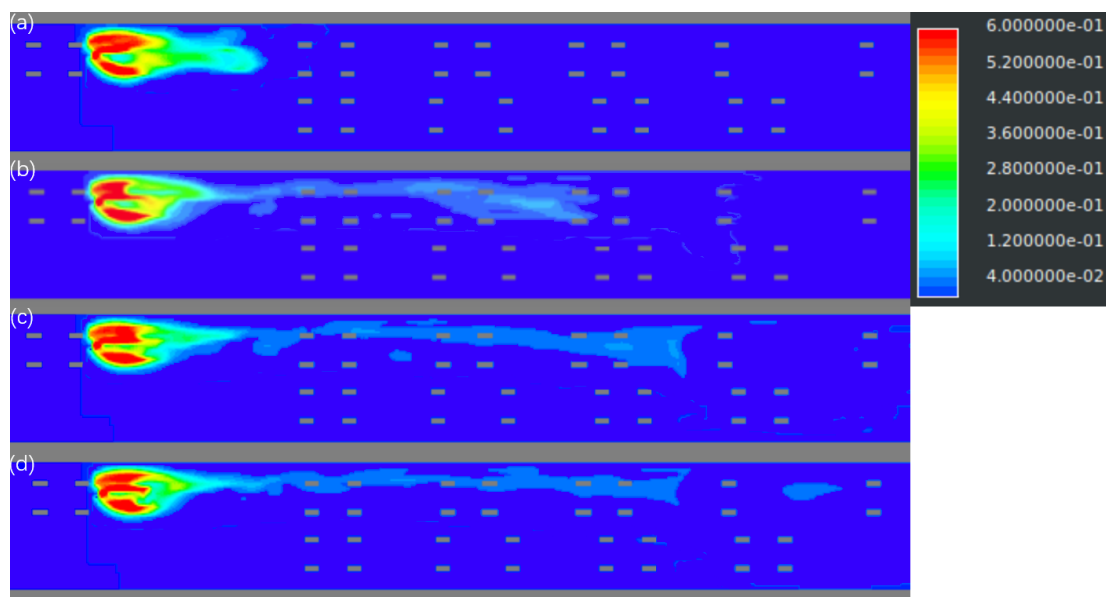


Figure 61. Hydrogen concentration contours in a horizontal view right below the chassis of the leaking vehicle with 2.4m/s ventilation at $t =$ (a) 2.5 s; (b) 5 s; (c) 7 s; (d) 9 s.

3.4.8.2 Pressure

The pressure histories of hydrogen combustion without water mist injection for different ventilation conditions are shown in Figure 62 to Figure 64, in which the hydrogen cloud is ignited at 5.1 s after the beginning of release. The overpressures have little difference between the points near the leaking location, e.g., between P_{1c} and P_{1d} , and between P_{2c} and P_{2d} . The data points are farther from the release location, the pressure rise occurs with a longer delay, which presents the flame propagation process. Meanwhile, the combustion overpressure decays both temporally and spatially, due to the H_2 concentration decay. The sharp peaks and frequent oscillations in the pressure histories manifest the stochastic character of combustion. The cases without mist for different ventilation conditions, but ignited at 2.5 s and 9.2 s, were also

D4.3. Final report on analytical, numerical and experimental studies on explosions, including innovative prevention and mitigation strategies

simulated, respectively. The maximum overpressures caused by H_2 combustion are shown in Table 28, for different ignition times and different ventilation conditions. Under the same ventilation condition, the maximum overpressures at various ignition times are little different. Moreover, the maximum overpressures for the ventilation of 1.25 m/s and 2.4 m/s are quite close, due to the similar hydrogen concentrations near the ignition point for the various ventilation conditions. However, both are larger than that of the non-ventilation case, because the H_2 can disperse only in one direction in case of ventilation, which brings a higher H_2 concentration. Another reason might be that the ventilation flow enhances the turbulence intensity, which promotes further combustion process.

Figure 65 to Figure 67 show the pressure histories with mist injection for different ventilation conditions when the hydrogen cloud was ignited at 5.2 s. The maximum pressure is also near the sensors of P_{1c} and P_{1d} , P_{2c} and P_{2d} , and the pressure decays similarly in space and in time. However, due to the suppression effect of the droplet, the pressure peaks with mist are lower than that without mist. Moreover, the pressure histories with mist are smoother. The maximum combustion overpressures with mist are also shown in Table 28. The suppression on pressure caused by the droplets is rather obvious, with a pressure decrease by more than 23.5%. The cooling effect of the water mist on the hot combustion products may be the major contribution to suppress the combustion overpressures.

D4.3. Final report on analytical, numerical and experimental studies on explosions, including innovative prevention and mitigation strategies

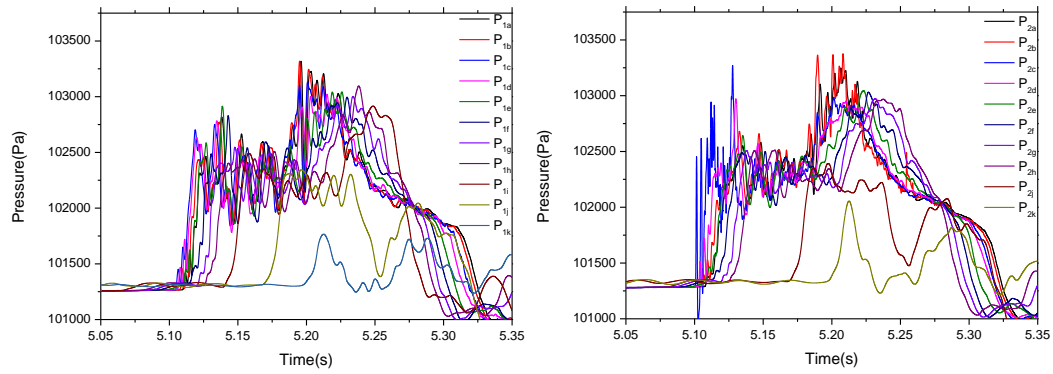


Figure 62. Pressure history when the hydrogen cloud was ignited 5.1 s after the beginning of the hydrogen release without ventilation.

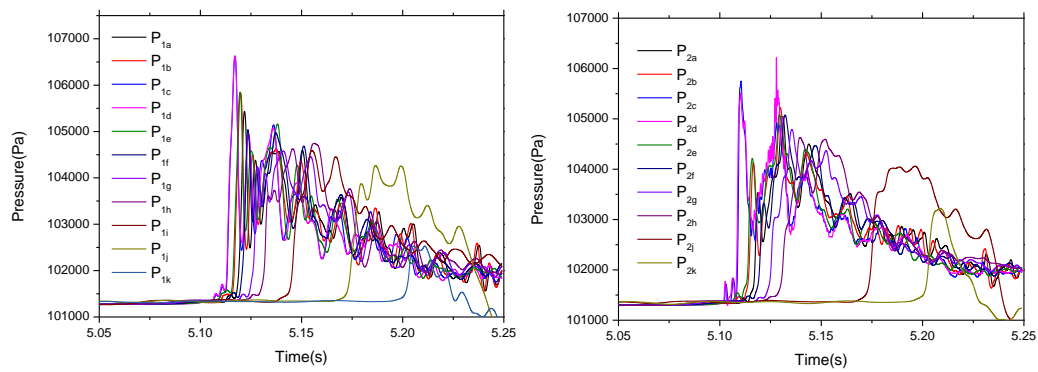


Figure 63. Pressure history when the hydrogen cloud was ignited 5.1 s after the beginning of the hydrogen release with 1.25 m/s ventilation.

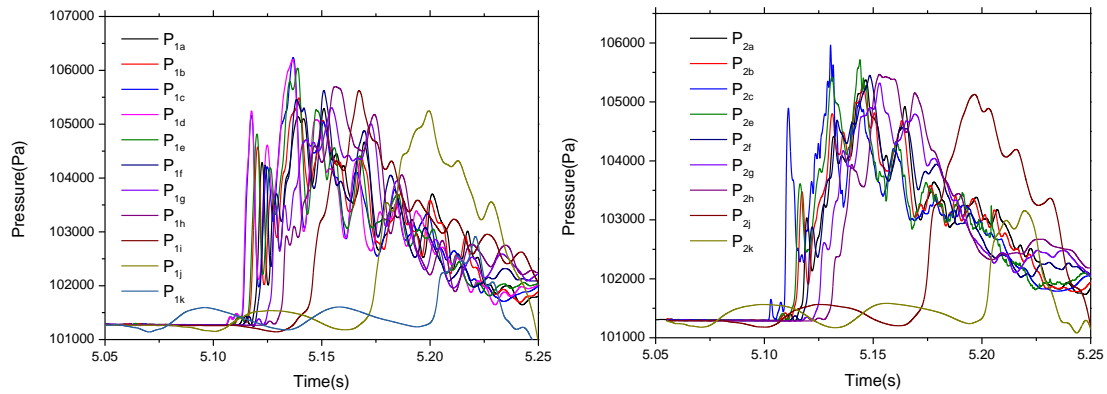


Figure 64. Pressure history when the hydrogen cloud was ignited 5.1 s after the beginning of the hydrogen release with 2.4 m/s ventilation.

D4.3. Final report on analytical, numerical and experimental studies on explosions, including innovative prevention and mitigation strategies

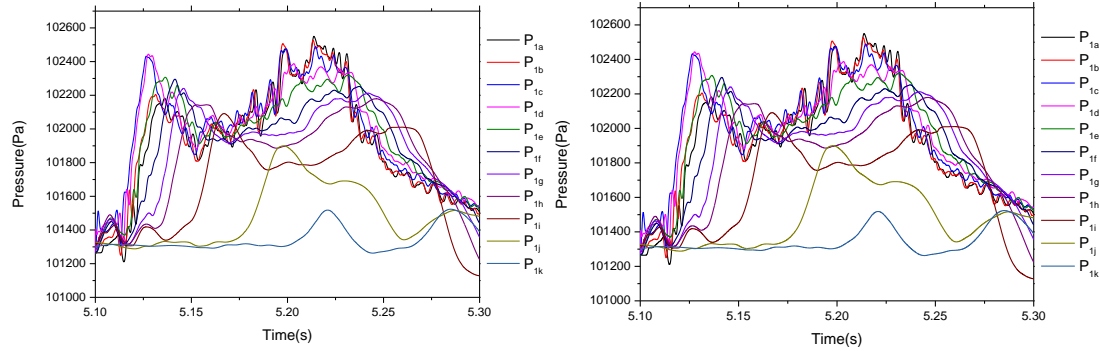


Figure 65. Pressure history when the hydrogen cloud was ignited 5.1 s after the beginning of the hydrogen release without ventilation (with mist section).

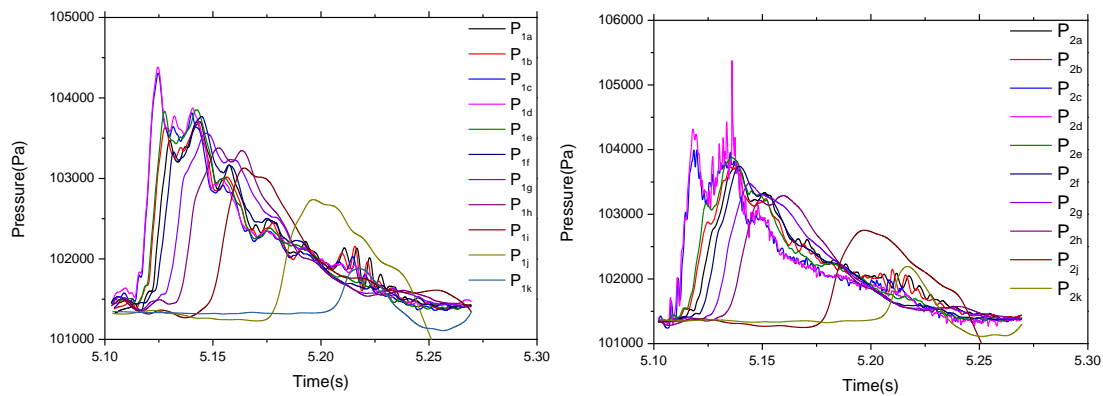


Figure 66. Pressure history when the hydrogen cloud was ignited 5.1 s after the beginning of the hydrogen release with 1.25 m/s ventilation (with mist section).

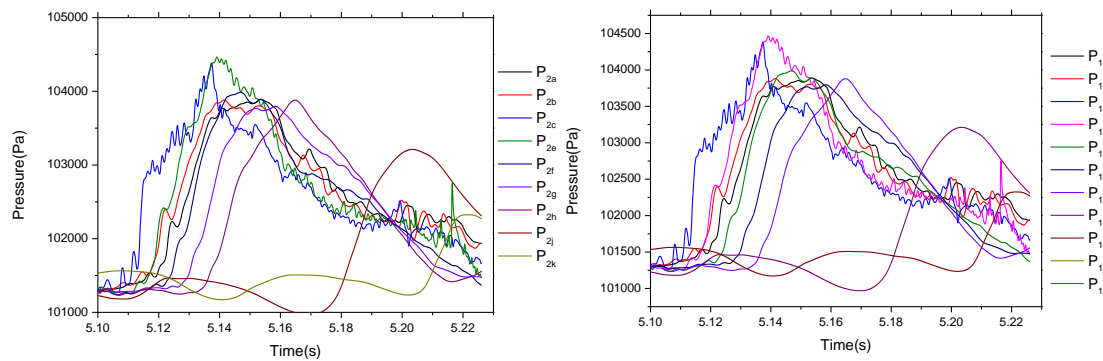


Figure 67. Pressure history when the hydrogen cloud was ignited 5.1 s after the beginning of the hydrogen release with 2.4 m/s ventilation (with mist section).

Table 28. Maximum Overpressure (Pa) for various cases.

		Without mist			With mist
Ventilation	Ignition time	2.5 s	5.1 s	9.2 s	5.1 s
0		2335	2075	1514	1438
1.25 m/s		4226	5330	3882	4076

D4.3. Final report on analytical, numerical and experimental studies on explosions, including innovative prevention and mitigation strategies

2.4 m/s	4550	4894	4473	3166
---------	------	------	------	------

3.4.9 Conclusions

Due to the downward leakage of hydrogen, the hydrogen cloud rises in the buoyancy dominated flow. Almost all the hydrogen cloud was blown downstream under the ventilation conditions. The H_2 concentration in the downstream is, therefore, higher than that without ventilation. Meanwhile, the ventilation accelerates the diffusion of the hydrogen and strengthens the flow turbulence intensity. Owing to the two reasons, the maximum overpressures for the ventilation cases are higher than that of the non-ventilation cases.

The suppression effect of mist on hydrogen combustion overpressure is remarkable, due to its cooling effect on the hot gases after combustion.

3.5 Simulation of water injection effect on shock wave attenuation validation against experiments (4.3, KIT)

3.5.5 Background

One of the major risks of hydrogen deflagration or detonation involved in tunnels is the pressure load caused by the detonation shockwave. Water mist injection into the tunnel in accidental scenarios is supposed to be able to attenuate the peak pressure of the shockwaves. Therefore, the in-house KIT HyCodes – COM3D is used to simulate the attenuation effect of water mist or fog on pressure waves.

3.5.6 Objectives

The purpose of the study is to implement the droplet breakup model in the COM3D code and to verify it, and to make simulations of the shockwave attenuation experiments by water mist carried out in the KIT test facility.

3.5.7 Knowledge gaps and accident scenarios assessed

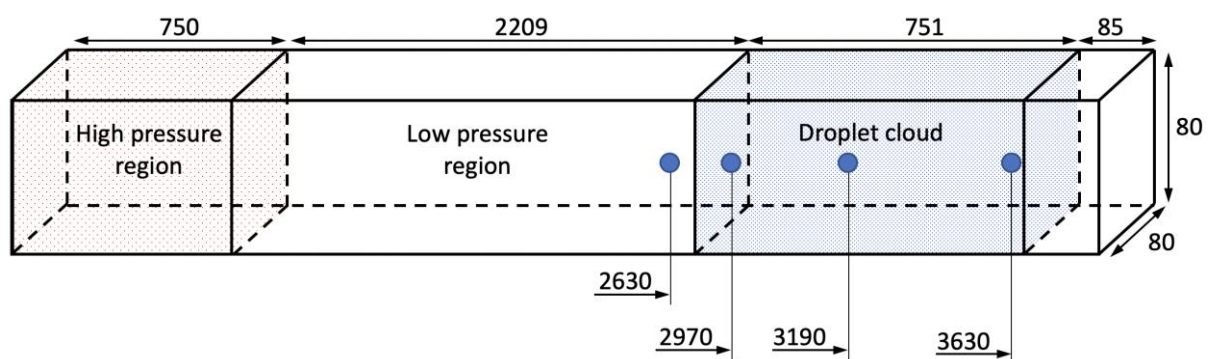


Figure 68. Schematic test channel of planar shockwave propagation through a water fog region to study its attenuation effect on shock pressure.

As shown in Figure 68, a pressure shock is generated due to the damage of the membrane separating the high- and low-pressure regions. The generated shock front propagates from left to right through the region full of water fog. The shock pressures are compared between the cases with and without the fog region, to verify the developed droplet breakup model.

D4.3. Final report on analytical, numerical and experimental studies on explosions, including innovative prevention and mitigation strategies

The parameter configuration of the test channel is shown in Table 29.

Table 29. Test channel parameter setup for shockwave propagation.

Parameter	Value
Initial high pressure	6.75 bar
Initial low pressure	1
Mach number	1.5
Shockwave velocity	522 m/s
Droplet diameter	500 μm
Liquid volume fraction	1 vol. %
Liquid phase concentration	10 kg/m^3
Shock temperature	400 K

3.5.8 Numerical simulation development

The detailed description of the droplet breakup model is formulated in Section 2.5.4.2.

3.5.9 Validation / optimisation

In order to verify the developed droplet breakup model, the simulations are performed for the shockwave propagation through the fog region in the channel. For the calculation of the total breakup factor (T_{tot}), we use the correlation of Pilch and Erdman for $Oh \leq 0.1$ and the correlation of Gelfand for $Oh > 0.1$ (see Section 3.4.6).

D4.3. Final report on analytical, numerical and experimental studies on explosions, including innovative prevention and mitigation strategies

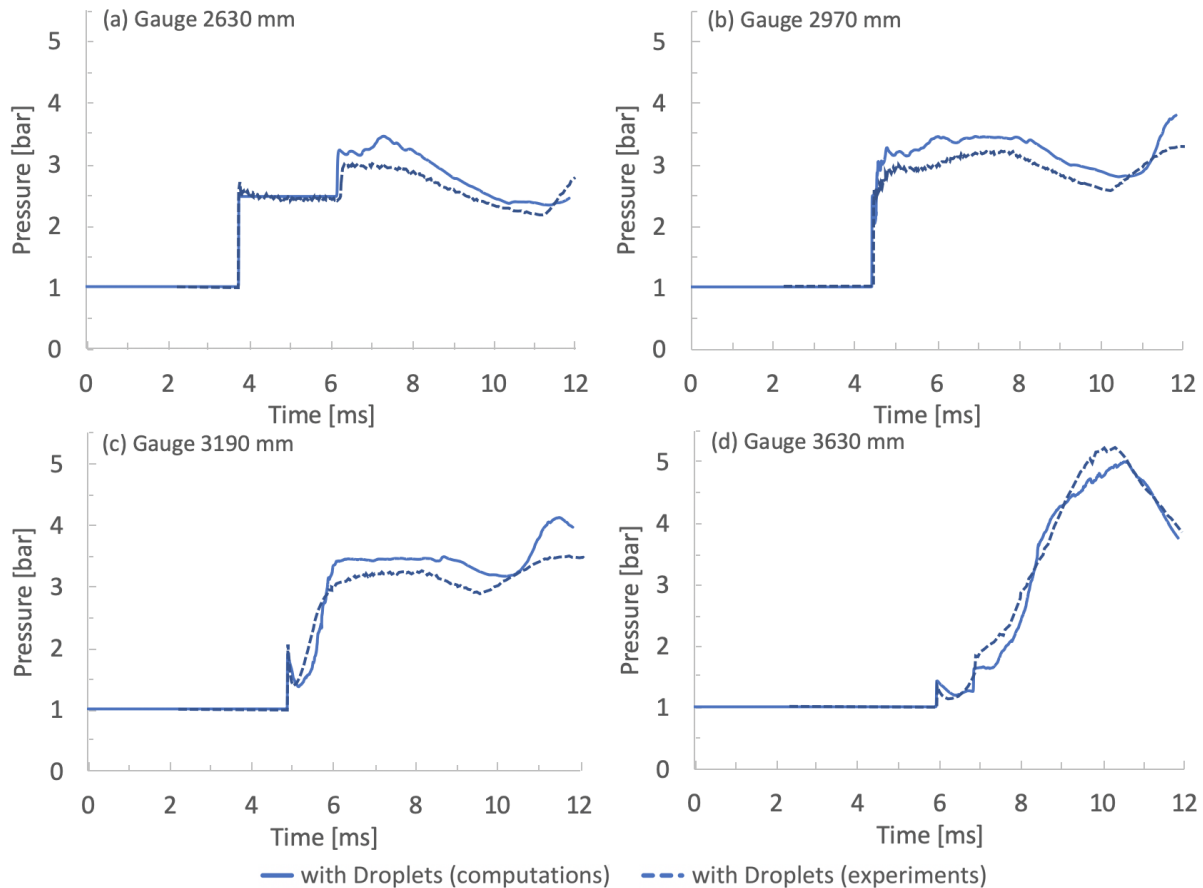


Figure 69. Verification of the droplet breakup model in COM3D against experimental data of Chauvin et al. (2011) with droplet diameter $500\ \mu\text{m}$, Mach number 1.5, liquid phase concentration $10\ \text{kg/m}^3$ and fog region length 700 mm.

Figure 69 shows the results the pressure histories of data and computed results. Evidently, the pressure courses agree well in both qualitative and quantitative terms, despite of slight deviations. So, in general, the model is able to emulate the droplet behaviour properly.

3.5.10 Simulation of shockwave attenuation tests in A2 vessel

The shockwave attenuation experiments by water mist are carried out at the A2 vessel of the KIT hydrogen test facility, as shown in Figure 70 and Figure 71.

D4.3. Final report on analytical, numerical and experimental studies on explosions, including innovative prevention and mitigation strategies

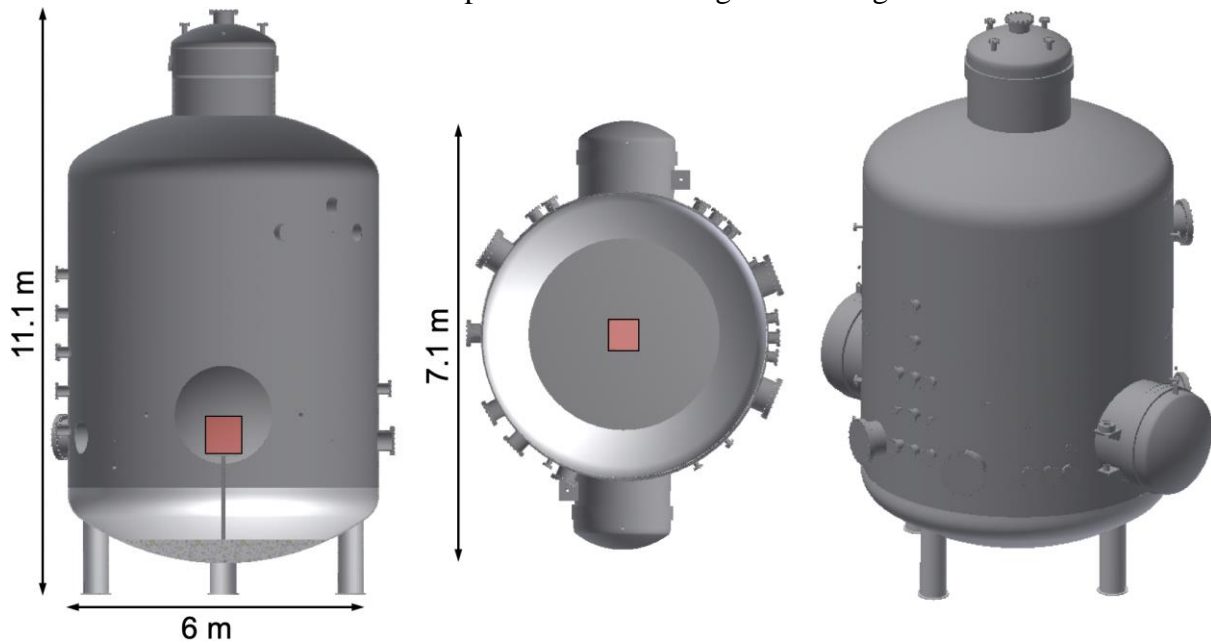


Figure 70. 3D views of the A2 vessel in the KIT hydrogen test centre.

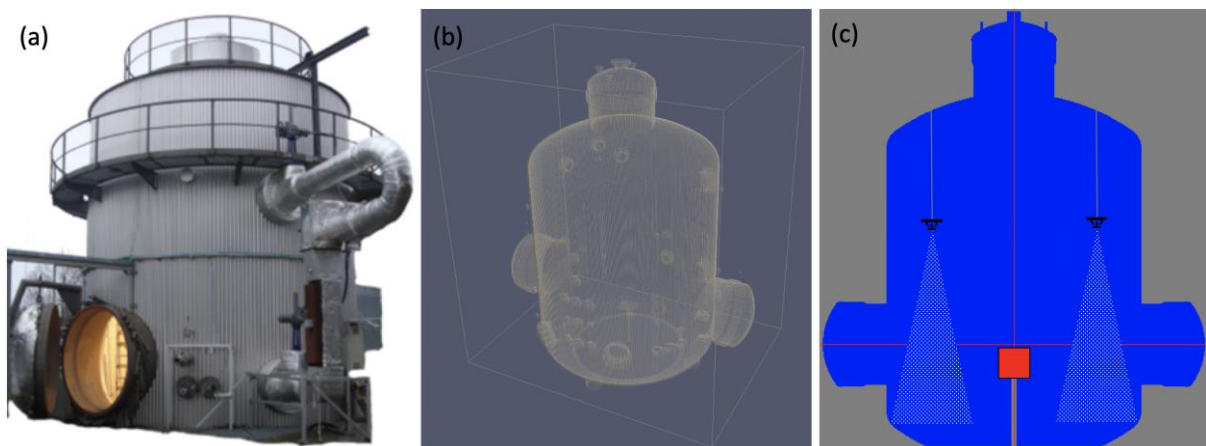


Figure 71. (a) The snapshot of the A2 vessel; (b) The computational domain of the vessel; (c) The generated droplet cloud inside the vessel.

3.5.10.1 Numerical Models

Detonation shockwaves are generated in plan by igniting 4 g hydrogen in a detonation unit positioned in a central place of the experimental facility – A2 vessel at Karlsruhe Institute of Technology with a gas volume of 220 m³, as shown in Figure 72(a). Symmetrically located four water spray devices are applied to make mist clouds to attenuate the shockwaves initiated by the hydrogen detonation.

A half of the facility volume is modeled due to its symmetry. A vertical and a horizontal cut view of the computational domain are shown in Figure 72(b) and (c), respectively.

D4.3. Final report on analytical, numerical and experimental studies on explosions, including innovative prevention and mitigation strategies

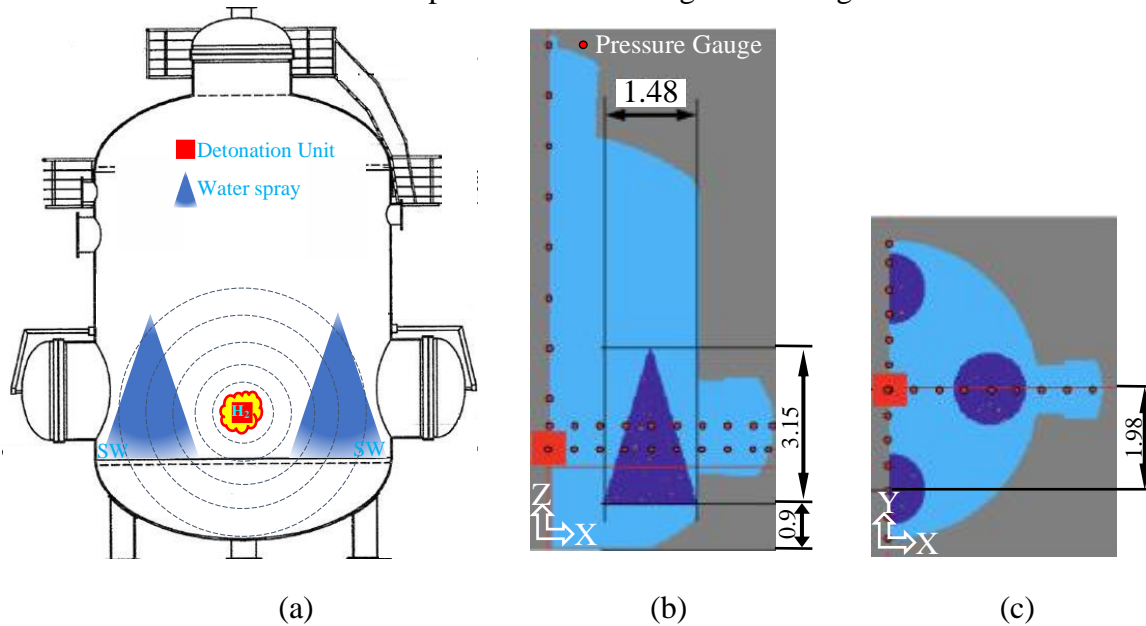


Figure 72. Geometrical models of hydrogen detonation vessel with sprays, (a) CAD drawing of the vessel, (b) vertical cut view of the computational domain showing schematically the detonation unit, droplet cloud and pressure gauges, (c) horizontal cut view of the model.

Each spray device generates a mist cloud in a conical shape with a height of 3.15 m and a bottom radius of 0.74 m, a volume of 1.8 m^3 . The droplet size is defined as $500 \text{ }\mu\text{m}$ and the liquid phase concentration as 1 kg/m^3 . In total 2.76×10^7 particles are defined. However, only 10^4 “representative” particles are computed by using a multiplication approach due to limited computing resource.

The half domain is modeled by 1.82 million cubic cells with a uniform size of 0.0435 m.

3.5.10.2 Detonation with spray off

As a base case, hydrogen detonation is simulated without water intervention. The 4 g hydrogen is ignited at time $t = 0 \text{ ms}$ in the detonation unit put on a solid tray. A high pressure up to 8 bar and a high temperature up to 2000 K caused by the acute $\text{H}_2\text{-O}_2$ reactions initiates pressure shockwaves, propagating spherically from the detonation unit. The shockwave developing process is shown in Figure 74 as pressure contour plots at different times. At $t = 1.32 \text{ ms}$, the spherical shock front is almost formed with a slight asymmetry in the vertical axis due to the solid plate where the detonation unit stands. A low-pressure region is formed at the center of the unit because of the fast expansion of the gases. At this time, the shockwave has a peak pressure of 2 bar with a Mach number of 1.41. At $t = 2.63 \text{ ms}$, the pressure shock is quite mature presenting a decayed pressure of 1.4 bar and a Mach number of 1.16. At $t = 5.17 \text{ ms}$, the shock front hits on the vessel bottom plate and is reflected there. The wave reflection forms a higher pressure indexed by red. At $t = 7.77 \text{ ms}$, the shock front hits on the vessel wall, where the shockwave is reflected. At $t = 11.23 \text{ ms}$, a complicated pressure distribution is formed owing to the superimpositions between the original incident shockwave and the reflected ones.

The pressures are recorded by the pressure gauges at the defined locations, which are compared to those attenuated by water mist in next sub-section.

D4.3. Final report on analytical, numerical and experimental studies on explosions, including innovative prevention and mitigation strategies

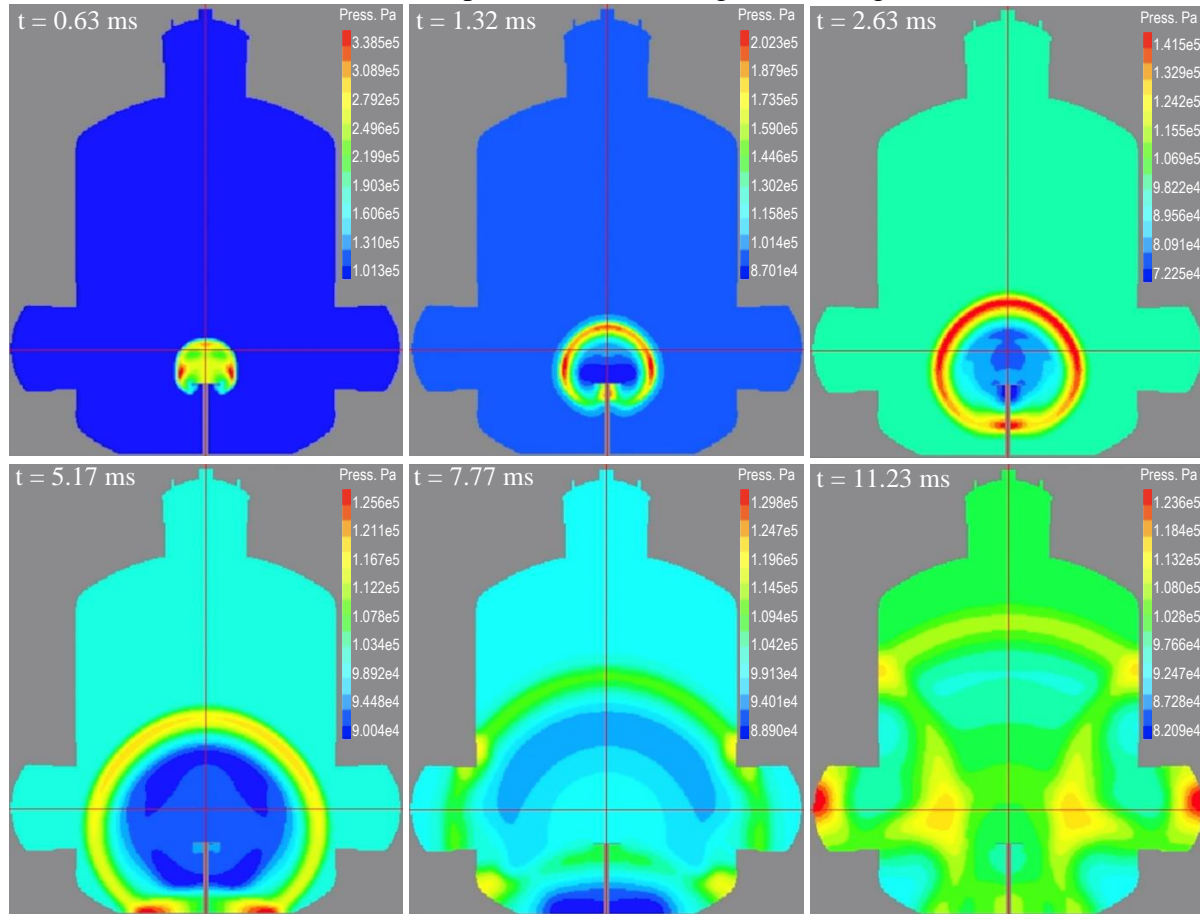


Figure 73. Detonation shockwave developing and propagating process and wave reflections on the vessel bottom plate and the wall.

3.5.10.3 Shockwave attenuation by mist

A wet case is simulated by restarting the base case with the presence of the defined droplet clouds from the time $t = 0$ ms. The shockwave overpressures caused by hydrogen detonation are compared between the case with mist attenuation and without mist. As shown in Figure 74, the compared shock front overpressures are the records of the column of gauges aligned horizontally in the line from the vessel centre to the conical cloud centre at the same height of $Z = 1.22$ m, and at a distance from the vessel centre $X = 1.74$ m, 2.18 m, 2.61 m, 3.05 m, respectively. The Gauge 1 locates in front of, not within, the cloud; the Gauge 4 behind the cloud. The Gauge 2 and 3 are within the cloud.

As expected, the peak pressure is not affected by the presence of cloud, as shown by the curves in black in Figure 74, where is outside of the misted region. However, the records of the other three gauges manifest that the overpressures are deducted by 15 – 20 % due to the presence of the droplet clouds. According to arrival times of the peak pressures, it seems that the mist clouds barely influence the shockwave propagating speed.

D4.3. Final report on analytical, numerical and experimental studies on explosions, including innovative prevention and mitigation strategies

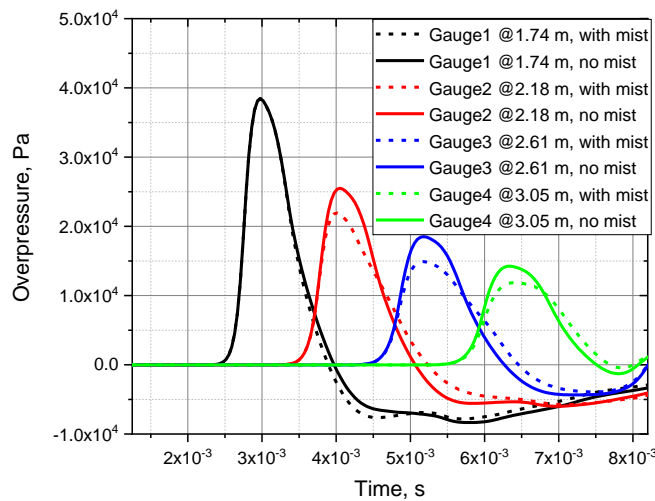


Figure 74. Overpressures in cases with/ without mist attenuation, recorded by the column of gauges aligned horizontally in the line from the vessel centre to the conical centre at the same height of $Z = 1.22$ m, and at a distance from the vessel centre $X = 1.74$ m, 2.18 m, 2.61 m, 3.05 m, respectively.

3.5.11 Conclusions

The attenuation mechanism of water droplet cloud against pressure shockwaves is elaborated. By using a turbulent combustion code with droplet models, the water mist attenuation phenomenon on shockwaves is studied by simulations in a conceptual mini-scaled tunnel and an experimental facility in a large scale. The attenuation effect of water mist on shock front pressures is observed in both cases. The simulation results of the experimental facility give insight to help design tests in laboratory. Further validation of the developed particle models is foreseen as a next step.

3.6 Analysis of the interaction between absorbing materials and systems and shock wave attenuation (4.3, KIT)

3.6.5 Background

Shockwaves can be mitigated by means of attenuation by water mist or absorbing materials, soft bulkheads or sacrificial pre-evacuated volumes etc. This subtask focuses on the analysis of effect of different absorbing materials of varying thickness on shockwaves. The mitigation capacity of different absorbing materials is discussed, and an optimal material is proposed.

3.6.6 Objectives

The scope of this work is to study the effectiveness of different absorbing materials with varying thickness to attenuate the strength of a blast or shock wave generated by an explosion.

3.6.7 Methodology

The hydrogen explosion tests are performed in the HYKA A2 vessel of 220 m^3 volume (6 m diameter, 9 m height). As shown in Figure 75, hydrogen detonation is initiated in a combustion unit located at the centre of the A2 vessel. Absorbing materials are put on the solid wall of the vessel. The interaction of the absorbing materials to the coming shockwave is measured,

D4.3. Final report on analytical, numerical and experimental studies on explosions, including innovative prevention and mitigation strategies including the reflected shock pressure amplitude, and the reflected positive shock pressure impulse.

The tested different absorbing materials are

- polystyrene,
- foam polyurethane and
- acoustic glass wool

with different thickness of 2 cm, 12 cm or 20 cm.

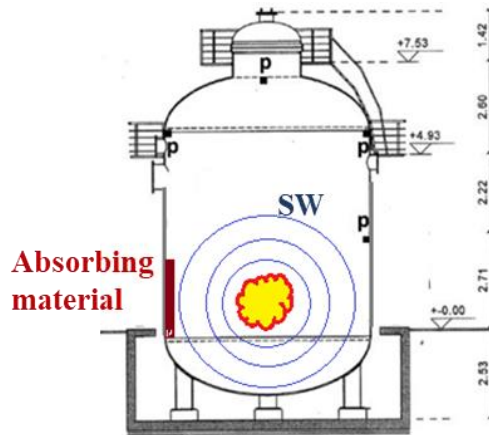


Figure 75. Experiment of hydrogen explosion shockwave attenuation by absorbing materials with different thicknesses in the HYKA A2 vessel.

3.6.8 Models

The hydrogen detonation and shockwave propagation are simulated by using COM3D code with a moving boundary at the surface of the absorbing material block. The soft material surface deforms due to the incoming shock pressure wave, which forms a moving boundary for the COM3D calculations.

The deformation of the soft materials is computed by using the ABAQUS code with the crushable foam plasticity model. The computed pressure by the COM3D code acts as a pressure boundary at the surface of the absorbing material block for the ABAQUS simulations. On the contrary, the computed deformation of the material surface by the ABAQUS supplies a moving boundary condition for the gas dynamics simulations of the COM3D.

Therefore, the COM3D and the ABAQUS calculations must be coupled at each time step for simulation.

3.6.9 Results

The results of the simulation will be reported in D4.4.

D4.3. Final report on analytical, numerical and experimental studies on explosions, including innovative prevention and mitigation strategies

3.7 Pre-test simulations and parametric study to find out the maximum allowed hydrogen inventory to mitigate the effect of blast wave and fireball (4.3, CEA/ NCSRD/ UU)

3.7.1 Pre-tests, background

UU is planning to perform pre-test simulations and parametric study to find out the maximum allowed hydrogen inventory, to mitigate the effect of blast wave and fireball, after a hydrogen tank rupture in a fire in a tunnel, on people and structure.

3.7.1.1 CEA tests

The initial Villarodin-Bourget- Modane tunnel selected for the simulations, is not available due to the fact that the TELT company has started a new excavation work in the gallery where the tests were about to commence and the pre-tests to be done. Another tunnel is proposed for the tests in October. The proposed tunnel is shown in Figure 76; this is a 500 m length tunnel, 5 m in height and 7.5m width minimum, there is a 2-lane road and a slope of 3.6%, the tunnel is open at both ends. The first 130 m are in concrete as are the last 50 m. The natural airflow circulation is from top to bottom with an average speed of 1.2 m/s.

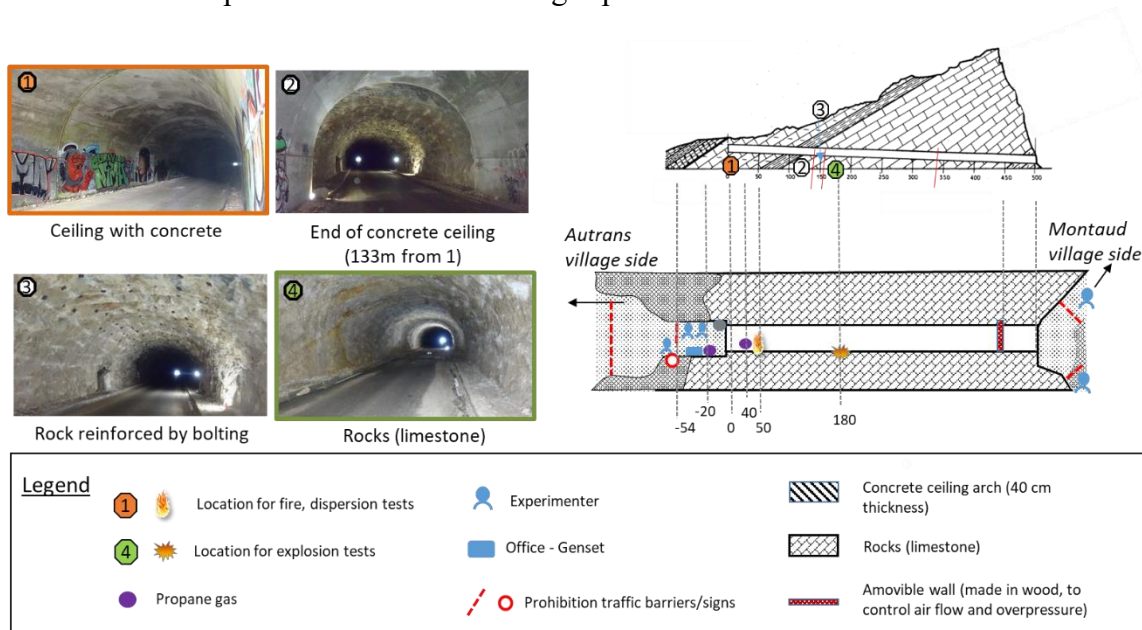


Figure 76. Tunnel view: orange - concrete ceiling, location for fire and dispersion tests, green - location for the explosion.

3.7.1.2 HSE pre-tests

Another set of pre-test simulations will be performed by UU for the HSE tunnel, as described in Section 4.2.

3.7.2 Parametric study

The CFD parametric study will be performed based on the problem formulation presented in section 2.1.1.2, to derive the correlation of blast wave attenuation in a tunnel with a presence of a vehicle. Currently, the correlation has been prepared and several numerical tests with stand-alone tank rupture in a tunnel conducted are described in the recent paper (Molkov and Dery, 2020).

D4.3. Final report on analytical, numerical and experimental studies on explosions, including innovative prevention and mitigation strategies

The work is ongoing to include the FEM analysis of the energy losses due to car deformation and dislocation. Methodology for the assessment of blast attenuation includes a two-step calculation of pressure dynamics by CFD and energy losses using the FEM:

- CFD simulation of blast wave dynamics after tank rupture in a fire. Rupture of under-vehicle hydrogen tanks of 10, 30, 60 and 120 L at storage pressure of 94.5 MPa and temperature 385 K and 1, 2 and 5 lane tunnels example of pressure dynamics is shown in Figure 81.
- FEM simulation of vehicle deformation and dislocation to obtain the energy losses. Pressure dynamics from 98 surfaces, calculated in CFD is applied in FEM to the vehicle of 1800 kg to obtain the energy losses.

Both approaches are shown in Figure 77. Figure 77 (top) presents the CFD model implemented in ANSYS Fluent showing the mesh (left) and solution of pressure contours on the car body (right). Figure 77 (bottom) presents the FEM model implemented in ANSYS Explicit Dynamic showing the mesh view in the car body (left) and frame (right). As can be seen the interior of the car is also presented by the car seats, parts mimicking the engine, fuel cell, battery and 2nd tank is also present to make sure that the car weight is the same as for the typical FC vehicle.

Figure 79 (top) shows the dynamics of the energy losses calculated using FEM on demolition and dislocation of the vehicle while Figure 79 (bottom) shows the calculated chemical energy released during tank rupture and combustion of hydrogen. Application of both methods will help to develop the methodology for calculation of blast wave decay with presence of realistic vehicles considering the energy losses.

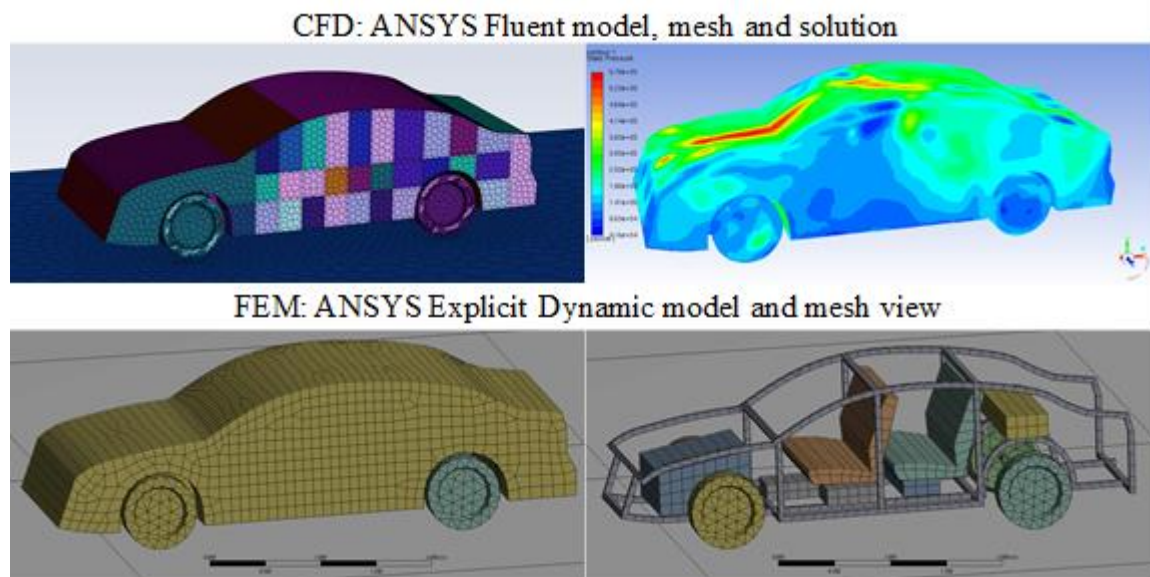


Figure 77. CFD + FEM problem formulation.

D4.3. Final report on analytical, numerical and experimental studies on explosions, including innovative prevention and mitigation strategies

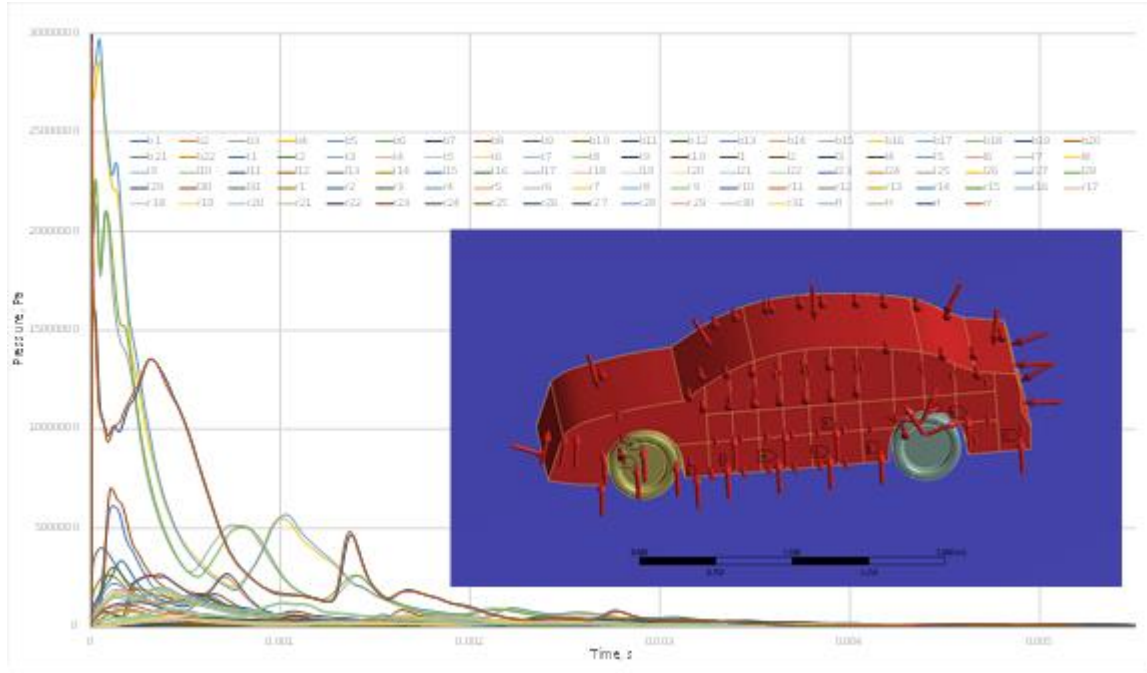


Figure 78. Pressure dynamics in CFD and application for FEM.

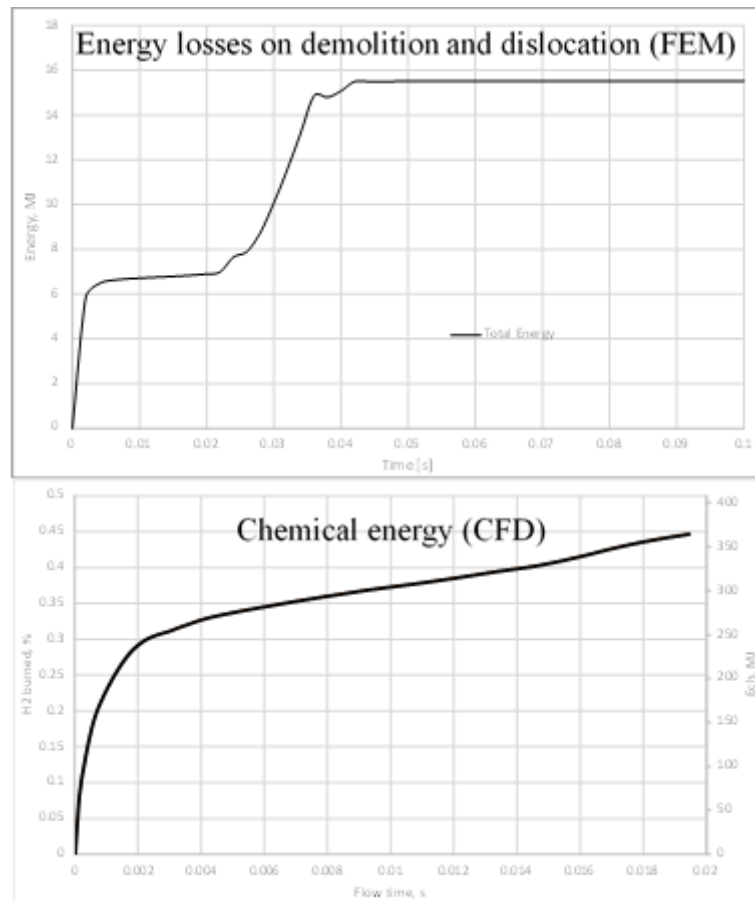


Figure 79. Energy losses for under vehicle tank rupture and chemical energy, $P_T=94.5$ MPa, $V_T=120$ L, $m_v=1800$ kg.

D4.3. Final report on analytical, numerical and experimental studies on explosions, including innovative prevention and mitigation strategies

The established harm criteria for humans and damage criteria for structures will be applied to find out the parameters of an inherently safer on-board storage tank. UU will develop and validate numerical techniques for understanding and quantifying hazards from hydrogen tank rupture in a tunnel.

3.7.3 CFD model

ANSYS Fluent has been used as a CFD engine and the model employed the LES approach coupled with Smagorinsky-Lilly as the sub-grid scale model for turbulence, and the eddy-dissipation-concept (EDC) for the simulation of combustion with direct integration. To conserve the mechanical energy of compressed hydrogen in real conditions, the tank volume with “ideal gas” (V_{ideal}) in simulations will be scaled using the following equation:

$V_{ideal} = V_{real} - mb$, where m is the hydrogen mass and b is the co-volume constant. The reduction of volume compared to the real tank allows to preserve the mechanical energy and the pressure as in experiment to get the same starting shock. The time step adapting technique will be used to maintain a constant Courant-Friedrichs-Lewy (CFL) number.

The numerical study will begin with validation of the CFD model using experimental data, from rupture tests on a stand-alone vessel (Tamura, Takahashi et al. 2006) (35 L at 945 bar) and (Weyandt 2005) (72.4 L at 350 bar).

The second stage of the CFD model development will include the problem formulation in order to define a maximum amount of hydrogen in an on-board vehicle storage tank that would not generate pressure loads capable of threatening life and destroying property along a tunnel. It is planned to perform realistic simulations of high-pressure tank rupture, in a tunnel with the presence of a vehicle etc. A series of numerical simulations will be performed, with the following tank and tunnel parameters:

- Different tunnel cross-sections comprising of 1, 2 and 5 traffic lanes with cross-section areas of 24, 40 and 140 m² respectively.
- The fixed tunnel length for all simulations of 1000 m.
- There will be 4 tanks with various volumes of 10, 30, 60 and 120 L at fixed storage pressure of 700 bar. The respective mass inventories are 0.40, 1.21, 2.43 and 4.86 kg.
- The simulations will be carried out to account for losses of mechanical energy required to damage and move the car and the effect of car geometry on the amount of released chemical energy.
- The model of a real car with a real tank on-board will be placed in those tunnels and simulations performed for the cases outlined above.
- There are a total of 12 simulations planned.

The established overpressure for the cases performed, will be compared against harm criteria for humans and damage criteria for structures to find the maximum allowed inventory.

The third stage of development will be undertaken, following the initial validation (stage 1) and identification of critical inventories (stage 2). The model will be tested against HyTunnel-CS experimental data, produced by CEA, from Task 4.4. In that work, experiments will be undertaken firstly with non-flammable nitrogen and helium, and then with flammable hydrogen in order to assess the impact of gas type, and the contribution of chemical energy of combustion on the strength of the blast wave. The numerical model and methodology will be

D4.3. Final report on analytical, numerical and experimental studies on explosions, including innovative prevention and mitigation strategies applied for the tests performed in Task 4.4.1 and the following results expected from validation:

- Effect of different non-reacting gases on the blast for the same mechanical energy.
- Effect of combustion contribution to the strength of the blast wave.
- Dynamics of the maximum blast pressure along the tunnel.
- Pressure profile throughout the whole length of the tunnel.
- Pressure-drop due to losses and presence of obstacles and tunnel structures (e.g., car and/or ventilation system).
- Temperature profile of the developing fireball.

At the final step the results and conclusions i.e., safe distances along the tunnel, maximum inventory of hydrogen that would not generate life threatening pressure loads, and effect of gases will be presented and summarised for recommendations. The developed model will be recommended as a tool for hydrogen safety engineering and design.

3.7.4 Remarks from the CFD Study

The main conclusion following the CFD study concluded that the analysis of the consequences based on the comparison of harm criteria with pressure and impulse generated at different locations from the tank rupture has shown that there is no “no-harm” zone and people in the tunnel would be either injured or killed by the blast. This is an unacceptable situation. It is worth mentioning that the worst-case scenario was considered with the maximum onboard inventory in one tank for currently available fuel cell cars and the tunnel with minimum cross-section area.

There is a non-zero probability of TPRD failure in a fire. The TPRD cannot be initiated by localised fire if the fire affects only a part of the tank where there is no TPRD, e.g., smouldering fire, it can be blocked from a fire during an incident, its response time depends on fire intensity and could be comparatively long for lower intensity fire; TPRD could fail to be open or could spontaneously open without fire due to fatigue stress as a result of numerous cycling during service life, etc. Therefore, the knowledge of the blast wave decay for a tank of a particular volume and NWP is required for the first responders and design of inherently safer FCEV. The universal correlation for the assessment of blast wave decay in a tunnel is available in (Molkov and Dery, 2020)-

Because the blast wave decays in a tunnel extremely slow, the general recommendation is to prevent hydrogen tank rupture in tunnel fire by all means. The most promising way that excludes disadvantages of storage systems with TPRD is an explosion free in a fire self-venting tank, which could be presented as a tank with virtual “TPRD” distributed over the whole tank surface.

3.8 Simulations to validate multi-phenomena turbulent burning velocity deflagration model (spurious release) (4.3, UU)

3.8.5 Background

The CFD model aims to assess pressure and thermal hazards from delayed ignition of hydrogen jets. The CFD model employs the Ulster’s multi-phenomena deflagration model, which is adapted to account for the non-uniformity of the hydrogen-air mixture and high-

D4.3. Final report on analytical, numerical and experimental studies on explosions, including innovative prevention and mitigation strategies
intensity turbulence in the jet. Simulations were performed and compared to experimental tests conducted in the open space and available in literature.

3.8.6 Description of experiments

The CFD simulation results have been compared against data from two experiments available in literature, on tests in the open space for release pressures 36 and 200 bar, and release diameters 12.0 and 6.4 mm, respectively. Details of the tests are given in Table 30, whereas a detailed description can be found in the associated sources.

Table 30. Experimental tests available in literature modelled in CFD simulations.

Test	Pressure [bar]	Diameter [mm]	Ignition location [m]	Ignition delay [s]	Literature source
1	36	12	1.8	5	(Daubech et al., 2015), (Jallais et al., 2017)
2	200	6.4	2.0	0.8	(Royle and Willoughby, 2010)

The CFD model is applicable to free jets in a tunnel. It is envisaged that the CFD model application will be extended to jet fires in enclosed spaces, as the experiments performed at HSE within sub-task 4.4.2 for releases at a higher pressure (700 bar).

3.8.7 CFD model and numerical details

A CFD simulation within this task is subdivided in two stages characterised by different models: unignited release and deflagration simulations.

3.8.7.1 Unignited release modelling

The flow is treated as an incompressible ideal gas. A pressure-based implicit solver is used. A time step equal to 10^{-3} s is used for calculations, as it was seen to provide a time step independent solution for the 200-bar release (Cirrone, 2018). A RANS approach is chosen to calculate the distribution of hydrogen concentration and the turbulence mapping of the flammable cloud at the time of ignition. RNG k- ϵ model is used for turbulence (Yakhot and Orszag, 1986).

3.8.7.2 Deflagration modelling

The distribution calculated for the unignited release is used as an initial condition for the second phase of the simulation. The gas is assumed as compressible and ideal. The CFD model is based on the density-based, coupled solver with explicit time stepping. A Courant Friedrichs Lewy (CFL) number equal to 0.9 is maintained in all simulations. The same turbulence model as per the unignited release simulation is maintained. The multi-phenomena deflagration model by Verbecke et al. (2009) is used for the premixed combustion. The premixed flame propagation is modelled through the progress variable, c , equation and the source term, S_c , which is calculated with the gradient method: $\bar{S}_c = \rho_u S_t |\text{grad} \tilde{c}|$, where ρ_u is the density of the unburnt mixture and S_t is the turbulent flame speed.

The laminar burning velocity, S_u , is calculated as a function of hydrogen mole fraction according to the data reported in (Lamoureux et al., 2002), pressure and temperature. The turbulent burning velocity includes the effect of flow turbulence (\mathcal{E}_{turb}), turbulence produced

D4.3. Final report on analytical, numerical and experimental studies on explosions, including innovative prevention and mitigation strategies by the flame front (\mathcal{E}_{karl}), preferential diffusion (\mathcal{E}_{lp}) and the increase of flame radius with respect to the flame thickness (\mathcal{E}_{fract}):

$$S_t = S_u \cdot \mathcal{E}_{turb} \cdot \mathcal{E}_{karl} \cdot \mathcal{E}_{lp} \cdot \mathcal{E}_{fract}, \quad (47)$$

The model by Verbecke et al. (2009), developed for modelling deflagration in initial quiescent conditions, was adapted to simulate the delayed ignition of a turbulent high-pressure hydrogen jet. This model takes into account a self-similar fully developed turbulent combustion regime since the moment of ignition, and thus, implements slightly modified wrinkling factors, \mathcal{E} , compared to original model. The effect of turbulence is calculated as: $\mathcal{E}_{turb} = \exp(u'/S_t)^2$, which is extracted from the renormalisation group theory for premixed turbulent combustion by Yakhot (1988). The turbulent velocity u' is calculated as: $u' = \sqrt{2/3 k}$. The turbulence generated by the flame front itself which further increases its extension is taken in account through the wrinkling factor: $\mathcal{E}_{karl} = \psi \cdot \mathcal{E}_{karl,max}$. ψ is an empirical coefficient, calculated as function of hydrogen concentration according to Molkov and Bragin (Molkov and Bragin, 2015). The maximum theoretical value of the factor is given by $\mathcal{E}_{karl,max} = (E_i - 1)/\sqrt{3}$ where E_i is the expansion coefficient of the combustion products (ρ_u/ρ_b). A further mechanism is represented by the preferential diffusion which increases in significance for lean-hydrogen mixtures. The associated factor, \mathcal{E}_{lp} , is calculated as function of hydrogen concentration according to (Zimont and Lipatnikov, 1995) and is assumed to be a maximum given the initial turbulence level of the jet. For the same reason, the flame is assumed to propagate with a fractal-like structure from the ignition moment and location. Following Verbecke et al. (2009)'s work, the fractal wrinkling factor was calculated as $\mathcal{E}_{fract} = (R_{flame}/\varepsilon_c)^{D-2}$, where R_{flame} is the radius of the flame, ε_c is the inner cut-off and D is the fractal dimension. The inner cut-off is considered comparable to the control volume size. In conclusion, the turbulent flame speed including all the mentioned effects is defined as:

$$S_t = S_u \cdot \exp(u'/S_t)^2 \cdot (\psi \cdot \mathcal{E}_{karl,max}) \cdot \mathcal{E}_{lp,max} \cdot \left(\frac{R_{flame}}{CV_{size}} \right)^{D-2}, \quad (48)$$

A detailed description of the model features and parameters can be found in Verbecke et al. (2009) and Cirrone (2018). The present work implements a modification of the combustion model based on the work by Arnzen (1998), as it is expected to have a grid size, CV_{size} , larger than the integral length scale, l_t . The correction aims at thickening the flame zone by increasing diffusivity, D_t , by a factor, CV_{size}/l_t , and correspondingly reducing the reaction rate of combustion products by the same factor. The integral length scale is defined according to Kurenkov & Oberlack (2005):

$$l_t = 0.37 \frac{u'^3}{\varepsilon}. \quad (49)$$

where, ε is the turbulent dissipation rate.

3.8.7.3 Numerical grid and details

A notional nozzle approach is employed to model the under-expanded jet (Molkov et al., 2009). The nozzle parameters for the INERIS and HSE tests are outlined in Table 31. It is

D4.3. Final report on analytical, numerical and experimental studies on explosions, including innovative prevention and mitigation strategies
assumed that given the short ignition delay for the HSE experimental test, variation of conditions in the tank, due to the blowdown, can be neglected.

Table 31. Notional nozzle parameters.

Parameter	INERIS test	HSE test
Diameter, cm	4.4	6.3
Velocity, m/s	1199	1189
Temperature, K	247.8	243.8

The numerical grid is realised through a hexahedral mesh in the zone where the release is located, surrounded by a hemispherical domain with radius 50 m, surrounding the hexahedral domain, as shown in Figure 80, to distance the domain boundaries and limit their effect on the simulation results. A tetrahedral and coarser mesh was employed to reduce the number of control volumes, as there is no need to accurately solve the flow in this portion of the domain as for the proximity of the release. The two numerical grids were coupled as interfaces.

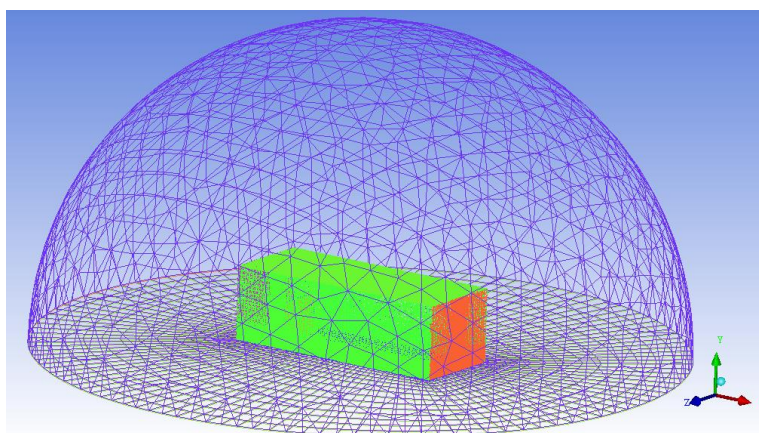


Figure 80. Hexahedral and tetrahedral numerical grids structure.

Table 32. Parameters of the numerical grids employed for simulations.

Parameter	INERIS test	HSE test
Hexahedral domain dimensions, m	9 x 4.5 x 15	25 x 8 x 10
Number of control volumes (CV)	1294000	1521803

The Semi-Implicit Method for Pressure-Linked Equations (SIMPLE) pressure-velocity scheme is employed, along with a second order upwind scheme for resolution of the convective terms.

3.8.8 Results and discussion

3.8.8.1 Unignited release

The hydrogen distributions used for deflagration modelling were numerically simulated in Cirrone (2018). Herein, results are only briefly presented and discussed to show initial conditions for deflagration modelling. Hydrogen concentration was sampled during INERIS tests at 9 radial locations and different axial distances from the nozzle. Measurements provide a mapping of the “steady-state”, hydrogen distribution achieved within the 5 s release prior to ignition. Figure 81 shows the comparison between the experimental measurements and the

D4.3. Final report on analytical, numerical and experimental studies on explosions, including innovative prevention and mitigation strategies

simulated distribution of hydrogen mole fraction. Simulations show an accurate calculation of concentration along the jet. The simulated jet presents a slightly slower radial decay of hydrogen concentration at a distance from the nozzle between 2 and 3 m. A finer discretisation of the release source may affect dispersion calculation in the near field. Discrepancies between simulations and experiments disappear beyond 3 m, and simulation reproduces well the overall hydrogen concentration.

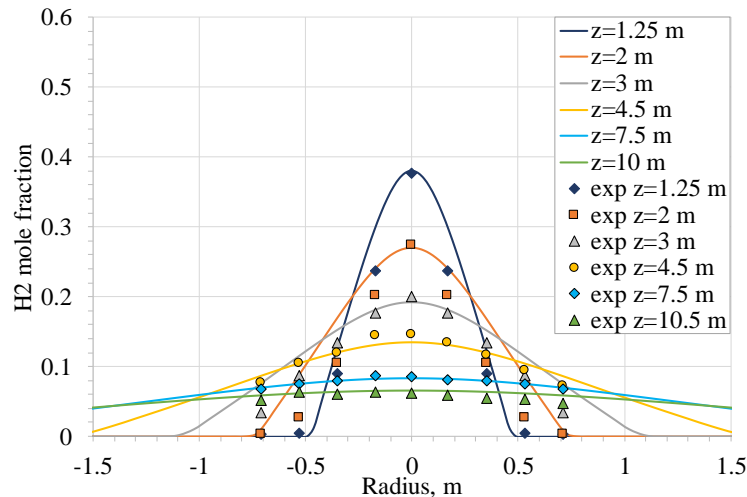


Figure 81. H_2 mole fraction distribution: CFD modelling versus INERIS experiment (Cirrone, 2018).

Experimental measurements on hydrogen distribution prior to ignition for the HSE test are not available. Since the CFD model is seen to predict well the hydrogen concentration for INERIS tests, it has been employed to calculate hydrogen distribution at the moment of ignition for the HSE test. Distributions for the HSE test indicate that the hydrogen-air mixture is rich at the time and location of ignition ($\approx 45\%$ by vol of H_2).

3.8.8.2 Deflagration

The hydrogen distribution simulated in the previous section is used as an initial condition for the deflagration modelling. Ignition is realised by increasing linearly, the progress variable, c , from 0 to 1 in a group of $4 \times 4 \times 4$ cells located at the ignition point for the respective tests. Simulation results were found to reasonably agree with experimental measurements. Figure 82 shows simulated overpressure dynamics for INERIS tests at the three pressure sensors P1, P2 and P3 and their locations with respect to the nozzle and the ignition point. Calculated overpressure dynamics are compared against two sets of experimental data. It should be highlighted that the two-test series, presenting some differences in the overpressure dynamics, were conducted in same experimental conditions. Overall, the simulated dynamics agrees with the trend showed by the experimental series 2. The simulation estimates well the first pressure peak reached at about 8 ms at sensor P1. Afterwards, the simulation slightly underestimates the experimentally measured pressure up to approximately 15 ms. Calculated pressure dynamics at sensor P3 well predicts experiments up to approximately 15 ms. After this time, sensor P3 in the experiment recorded a strong vacuum, of a magnitude even larger than the positive blast wave peak, which is not recorded in simulations. Maximum overpressure at the three sensors is predicted within reasonable engineering accuracy of $\pm 15\%$.

D4.3. Final report on analytical, numerical and experimental studies on explosions, including innovative prevention and mitigation strategies

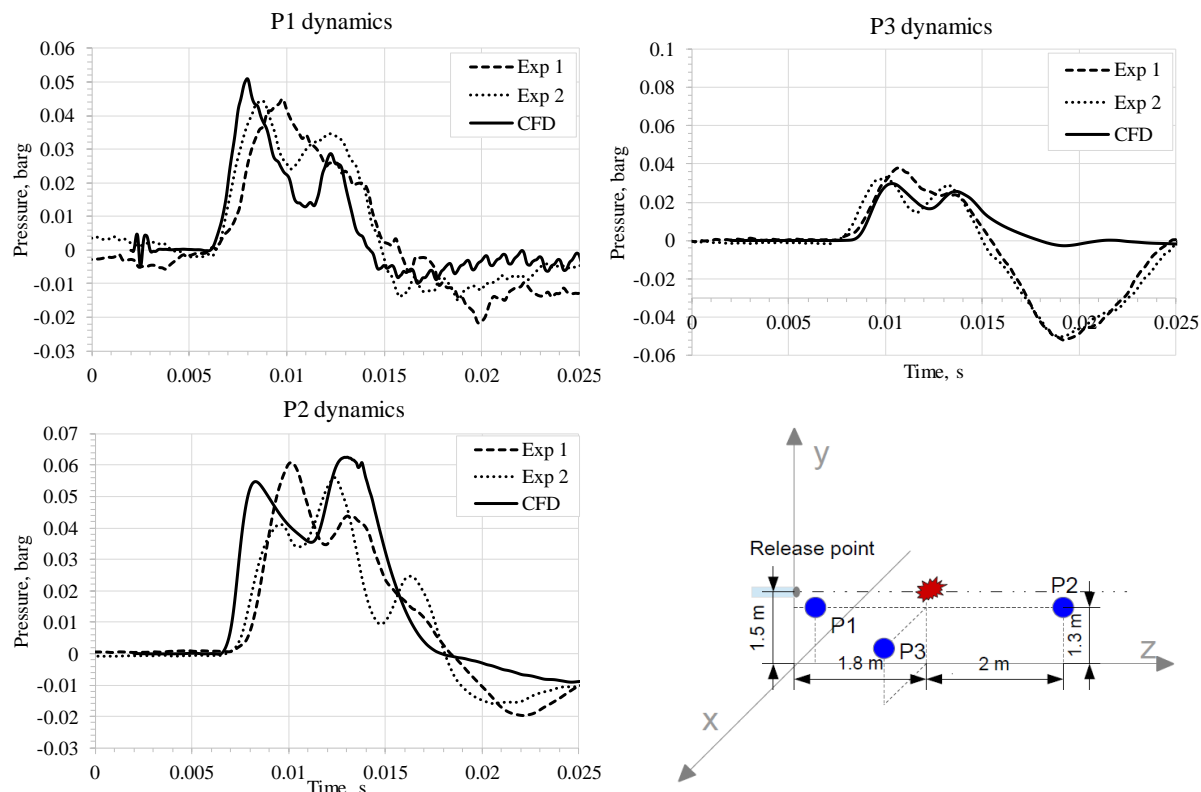


Figure 82. Pressure transients at pressure sensors P1, P2 and P3 for INERIS test: simulations versus experiment.

Simulation results for the HSE tests showed a similar overpressure dynamics to experiments, while underpredicting the maximum pressure peak. This discrepancy was resolved by considering the effect of the turbulence and flow instabilities produced by the inertial valve opening process (260 ms duration) on the hydrogen jet in the highly transitional and brief stage prior to ignition at 800 ms.

3.8.9 Concluding remarks

A CFD model was developed and applied to experiments on delayed ignition of hydrogen turbulent jets. Simulation results agree reasonably well with the experimental overpressure dynamics. Further research should be performed to advance the CFD approach and assess independence from the employed parameters characterizing the experimental conditions, e.g., ignition source, to gain insights into the delayed ignition phenomenon.

3.9 Coupled CFD/FEM modelling and simulation of a tunnel structure reaction to the blast (4.3, UU/ DTU)

3.9.1 Problem formulation

Pressure effects of high-pressure tank rupture, in a fire, in confined spaces, are not studied thoroughly. This CFD simulation of blast wave dynamics after tank rupture, in fire, is the first part of the joint work of UU (CFD) and DTU (FEM). Rupture of a hydrogen tank of 62.4 L (2.5 kg) at storage pressure of 94.5 MPa and temperature 385 K (at the moment of rupture), inside the road tunnel, with a total length of 500 m, is proposed for investigation to see the effect of a blast wave, after tank rupture, in a fire, on a tunnel structure. Real tunnel (IDOM)

D4.3. Final report on analytical, numerical and experimental studies on explosions, including innovative prevention and mitigation strategies

with 5 ventilation ducts 1.2x1.8 m has been used as case study. The ventilation is hanged on a reinforced concrete slabs that forms the horizontal ceiling of the tunnel and is directly hit by the pressure wave of the tank explosion.

3.9.2 CFD Analysis (UU)

3.9.2.1 Numerical set-up

For simulation of the blast wave in a tunnel with cross-sectional area as shown in Figure 4, the following numerical setup was applied: large eddy simulation model with Smagorinsky-Lilly subgrid-scale for simulation of turbulence. The eddy dissipation concept model was used to simulate combustion, with one-step chemical reaction of hydrogen combustion in air and 4 species (H_2 , O_2 , N_2 , H_2O). The ideal gas equation of state was used for density calculation. The constant, $CFL=0.2$, was kept during the whole simulation, employing user-defined function (UDF). Initial conditions: 101,325 Pa; 293 K; non-slip boundary conditions and poly-hexa-core mesh with total number of control volumes: 479,134.

3.9.2.2 Computational results

The study of the blast wave after stand-alone tank rupture in a fire in a tunnel is initiated. The simulation demonstrated a strong influence of non-uniform pressure distribution at the ceiling in time, due to reflections and formation and propagation of Mach stem. The maximum pressure dynamics in time was transferred to partner DTU for FEM study of the reaction of the ceiling, separating road part of a tunnel from the ventilation duct.

3.9.3 FEM Analysis (DTU)

3.9.3.1 Object of the analysis

The ceiling slab is 10 m wide and anchored at the side walls of the tunnel in such a way that rotation of the slab ends is allowed. The slab is 35 cm high and reinforced with 16 mm diameter hot-rolled bars placed every 150 mm in both directions and both at the top and the bottom of the slab. The top reinforcement is placed at 35 mm from the top and the bottom reinforcement is placed at 55 mm from the bottom. A section of the slab can be seen in

Figure 83.

In Table 33 the mechanical properties of the slab concrete and steel reinforcement are listed. In the table, ε_{c1} is the concrete compressive strain at the peak strength, ε_{cu1} is the maximum concrete compressive strain at rupture, ρ_c is the density of the concrete, ρ_s is the density of the reinforcement, and Φ is the diameter of both upper and lower reinforcing bars.

Table 33. Material parameters

f_{ck} (MPa)	f_{ct} (MPa)	Concrete					Reinforcement		
		E_c (GPa)	ε_{c1} %	ε_{cu1} %	ρ_c (kg/m ³)	E_s (GPa)	f_y (MPa)	Φ (mm)	ρ_s (kg/m ³)
35	2.2	34	0.0225	0.35	2400	200	500	16	7850

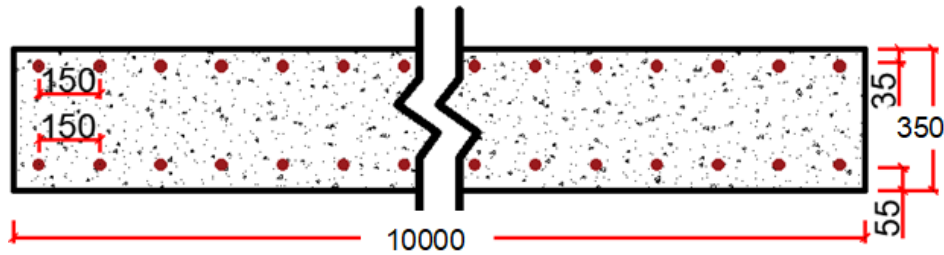
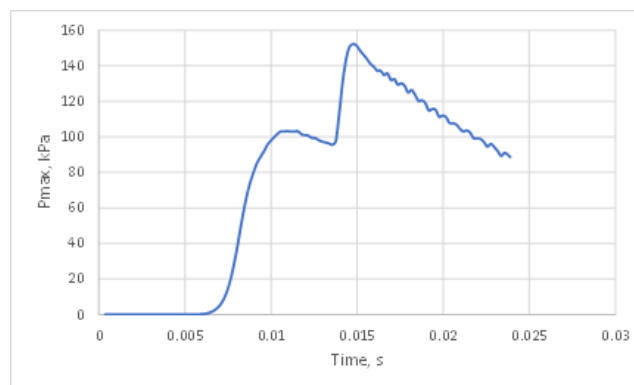


Figure 83. Cross-section of the investigated slab. Measures are in mm.

A simple hand-calculation of the static load-bearing capacity of the slab indicates that the slab can resist a uniform distributed load of 16 kN/m² in negative bending and slightly less in positive bending. This calculation is based on the usual assumption that the tensile strength of the concrete can be neglected, and a parabola-rectangle model can be considered for the concrete in compression and simplified by means of the so-called stress-block of compressive stresses. A more advanced calculation that include the tensile strength of the concrete and a compressive model with softening is carried out with the free software for sectional analysis developed by Technical University of Hamburg-Harburg (TUHH). This calculation gives a less approximated capacity of 18.3 kN/m² in negative bending and this value is used in paragraph 3.9.3.3 as comparison with the ultimate capacity obtained with the FE analysis, to validate the FE model.

3.9.3.2 Input pressure and characterization of the dynamic regime

Figure 84 shows the maximum pressure on the ceiling obtained from the CFD simulation of the stand-alone 62.4 L at 700 bar tank rupture described in the previous chapter 3.9.2. This maximum overpressure time-history is recorded in the areas of blast reflection in the corners. However, as a simplification, such pressure is uniformly applied on the slab bottom surface. As seen in Figure 84, the overpressure has a time duration $t_p = 0.024$ s and a peak value of 152 kPa.



D4.3. Final report on analytical, numerical and experimental studies on explosions, including innovative prevention and mitigation strategies

Figure 84. Maximum overpressure on the tunnel ceiling (stand-alone tank 62.4L, 700bar).

This peak pressure of 152 kN/m² is about 9 times bigger than the load capacity of the slab, which has been calculated as 18.3 kN/m² in negative bending. Thus, the slab would completely fail, if such pressure would be applied in a quasi-static way on the bottom surface of the slab. Nevertheless, the application of the action is dynamic and could therefore either amplify or de-amplify the slab response, depending on how much shorter the duration of the dynamic action is in comparison with the natural period of vibration of the slab T , as defined below.

The amplification or de-amplification of the response is typically measured by means of the dynamic amplification factor (DAF), defined as the ratio between the maximum displacement of the slab when exposed to the dynamic action $u_{\max, \text{dyn}}$ and when the action is applied in a quasi-static way $u_{\max, \text{st}}$.

$$\text{DAF} = u_{\max, \text{dyn}} / u_{\max, \text{st}} \quad (50)$$

Three different regimes are identified:

- a quasi-static regime, characterized by a duration of the action that is much longer than the natural period ($t_p \gg T$). This means that the elastic response of the structure is so fast in comparison to the action that there is no dynamic amplification of the response ($\text{DAF} = 1$). Therefore, just like in the static analysis, the structural response is only determined by the peak value of the action and by the stiffness of the structure, while the mass of the structure and the impulse of the force (defined as integral of the action in time) do not have significant influence.
- an impulsive regime, characterized by a duration of the action that is much shorter than the natural period ($t_p \ll T$). This means that the elastic response of the structure is slow in comparison to the action and, as a result, it cannot reach the static value of the response. This means that the dynamic amplification factor in impulsive regimes is lower than one ($\text{DAF} < 1$) and that the response does not depend on the peak value of the force, but only on the impulse of the force (in addition to the mass and stiffness of the structure). It also means that a significant delay between the peak of the action and the peak of the response can be expected, as the elastic response of the structure is still growing, when the action is ending.
- a dynamic regime, characterized by a duration of the action t_p that does not respect either of the two conditions above. In this regime, there is a positive dynamic amplification of the response ($\text{DAF} > 1$), which depends on the whole history of the load application (peak value, impulse), in addition to the mass and stiffness of the structure.

The following limits (Table 34) for the three regimes are found in literature, according to different authors:

Table 34. Limit for dynamic regimes in literature.

Regime	Mays & Smith 1995	TM 5-1300, 1990	UKOOA, 2003
Impulsive	$t_p / T < 0.064$	$t_p / T < 0.1$	$t_p / T < 0.3$
Dynamic	$0.064 \leq t_p / T \leq 6.4$	$0.1 \leq t_p / T \leq 6$	$0.3 \leq t_p / T \leq 3$

D4.3. Final report on analytical, numerical and experimental studies on explosions, including innovative prevention and mitigation strategies

Quasi-static	$1.4 < t_p / T$	$6 < t_p / T$	$3 < t_p / T$
--------------	-----------------	---------------	---------------

The natural period of vibration of a structural element is defined as the time it takes to complete a free oscillation. Such value is influenced by the mass and the stiffness of the element in a way that it increases if the mass of the element increases, or the stiffness of the element decreases. For a single degree of freedom system, i.e., a simple oscillator with concentrated mass m and stiffness k , the natural period can be expressed as:

$$T = 2 \pi (m/k)^{0.5} \quad (51)$$

For a model with distributed mass, such an elastic beam in bending having a section with moment of inertia I and made of a uniform material of stiffness E , the period T_i of each vibration mode i can be obtained with the following formula, where K_i is a constant that depends on the i vibration mode of the beam. $K_i = 9.87$ in case of a simply supported beam bending under self-weight (uniform distributed load/ mass).

$$T_i = \frac{2 \pi}{K_i} \sqrt{\frac{EI/L^4}{m}} \quad (52)$$

In case of a reinforced concrete slab, the stiffness and moment of inertia used in the formula must be calculated as those of a homogenized concrete section, where the steel is replaced by an equivalent amount of concrete. Such equivalent concrete must have the same centre of gravity of the steel and an area n time larger than the steel area, where $n = E_s/E_c$ is the ratio between the steel stiffness E_s and the concrete stiffness E_c . Thus, the reinforced concrete section is replaced with a section made of sole concrete, with stiffness E_c , area $A_{hom} = A_c + n A_s$, and moment of inertia $I_{hom} = I_c + n I_s$. By using such homogenized properties in the formula above (in particular E_c instead of E , I_{hom} instead of I and A_{hom} in the calculation of the mass), the natural period of the first mode of vibration of the slab can be obtained.

This value is also calculated numerically by means of a modal analysis in Ansys, by mean of a modal analysis on a 2D elastic model of the slab. In this model, SHELL181 squared elements of size 0.1 m are used to model the concrete and BEAM188 elements are used to model the top and bottom reinforcing bars. The material data and natural periods calculated both analytically and with Ansys are reported in Table 35 and indicate that the period of the slab T_1 is about one order of magnitude bigger than the duration of the dynamic overpressure t_p . As such, a significant dynamic de-amplification of the response could be expected and a full nonlinear dynamic analysis that includes the inelastic response of the material is carried out, to evaluate the slab response and whether it fails or is damaged by the explosion.

Table 35. Calculation data and results of the natural period of the simply supported R.C. slab.

	Concrete	Reinforc.	R.C. slab		Natural period T [s]	
			Length L [m]	B.C.	ANSYS	Analytical
Stiffness E [GPa]	34	2400				
Density ρ [kg/m ³]	200	7850	10	unif. loaded, simply sup.	0.1660	0.1637

D4.3. Final report on analytical, numerical and experimental studies on explosions, including innovative prevention and mitigation strategies

3.9.3.3 Implementation and validation of the model

A 2D model of the slab is implemented in Ansys in a transversal section of the tunnel. This simplification is motivated by the fact that, if the load on the slab is uniform, the problem is plane, as the slab is not restrained at the start and end section of the tunnel. This simplification is important for the feasibility of the analysis but limit the result to the case of a uniform pressure in the longitudinal direction of the tunnel, which is of course not the case, when a local tank explosion occurs at a certain point in the tunnel. In this case, the part of the slab further from the section where the explosion has occurred can sustain the section of the slab hit by the explosion, while this 3D effect is neglected, in case a plane problem is conservatively assumed. A more advanced 3D model of the slab should be implemented in case the solution is deemed too conservative and the slab response to a pressure wave variable along the direction of the tunnel is of interest.

The 2D model of the slab has been implemented with reference to a simply supported boundary and the section of the slab presented in Figure 83. However, due to the plane property of the problem, only a slab strip of depth 0.15 m is considered in the model. The concrete is modelled by means of PLANE182 elements, which are four-node element with two degrees of freedom at each node (see Figure 85, left), while the two steel bars are modelled as REINF263, which is a way of modelling the reinforcement embedded in the concrete with a smeared approach.

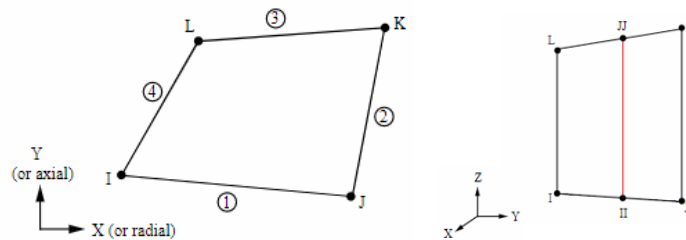


Figure 85. PLANE182 (left) and REINF263 elements (right) (ANSYS, 2022).

The material behaviour assumed for the concrete in compression and tension is a Drucker-Prager model with exponential HSD (Hardening-Softening-Dilatation) model for the inelastic part of the material response (Figure 86). The parameters of the model are calculated according to Eq. (56). In particular, the hardening yield function in compression Ω_c is given in Eq. (54) as a function of different strain range, while the yield function in the tension Ω_t is given by an exponential softening function where the volumetric energy dissipated in softening is proportional to the fracture energy in tension G_{ft} .

D4.3. Final report on analytical, numerical and experimental studies on explosions, including innovative prevention and mitigation strategies

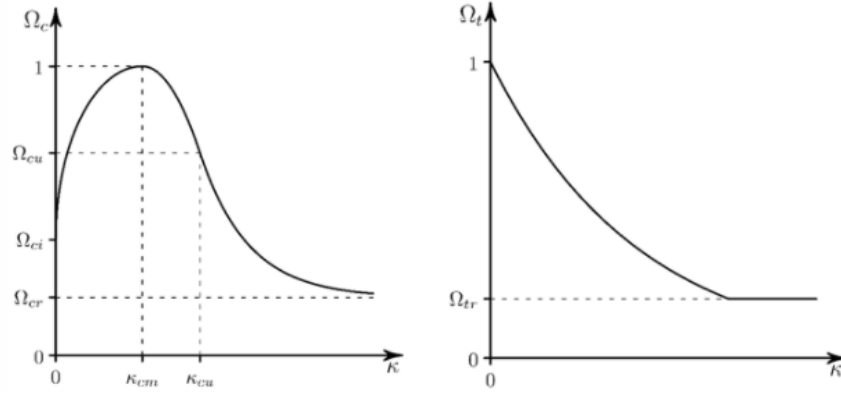


Figure 86. 2 HSD hardening yield function in compression Ω_c (left) and tension Ω_t (right) (ANSYS, 2022).

$$k < k_{cm} \rightarrow \Omega_c = \Omega_{ci} + (1 - \Omega_{ci}) \left(2 \frac{k}{k_{cm}} - \frac{k^2}{k_{cm}^2} \right)^{0.5} \quad (53)$$

$$k_{cm} < k < k_{cu} \rightarrow \Omega_c = 1 - (1 - \Omega_{cu}) \left(\frac{k - k_{cm}}{k_{cu} - k_{cm}} \right)^2 \quad (54)$$

$$k > k_{cu} \rightarrow \Omega_c = \Omega_{cr} + (\Omega_{cu} - \Omega_{cr}) \exp \left(2 \frac{\Omega_{cu} - 1}{k_{cu} - k_{cm}} \cdot \frac{k - k_{cu}}{\Omega_{cu} - \Omega_{cr}} \right) \quad (55)$$

$$\int_0^{\infty} \Omega_t dk = \frac{g_{ft}}{R_t} \quad (56)$$

$$g_{ft} = \max \left(\frac{G_{ft}}{h_i}, \frac{f_{ct}^2}{E_c} \right) \quad (57)$$

where k_{cm} is the plastic strain at uniaxial compressive strength, k_{cu} is the plastic strain at the transition from power law to exponential softening, Ω_{ci} is relative stress at start of nonlinear hardening, Ω_{cu} is residual relative stress at k_{cu} , Ω_{cr} is residual compressive relative stress, G_{ft} is mode I area-specific fracture energy, Ω_{cr} is residual tensile relative stress, f_{ct} is the uniaxial tensile strength, h_i is the effective element length, and E_c is the concrete Young's Modulus.

The value of the calculated material parameters are shown in Table 36, together with the value of the concrete uniaxial compression strength f_{ck} and some general data on the beam geometry.

D4.3. Final report on analytical, numerical and experimental studies on explosions, including innovative prevention and mitigation strategies

Table 36. Parameters of the concrete material model

Beam		Concrete material model					
Height H (m)	0.35	E_c (MPa)	34000	k_{cm}	0.00122	Ω_{cr}	0.63
Width w (m)	0.15	f_{ck} (MPa)	35	k_{cu}	0.00247	Ω_{cu}	0.79
Length L (m)	10	f_{ct} (MPa)	2.2	Ω_{ci}	0.4	Ω_{tr}	0.1
Boundary condition	simply-sup.	G_{ft} (N/m)	100	Density (kg/m ³)	2400	Poisson's ratio	0.2

The modelling of the nonlinear response of reinforce concrete element is a challenging problem, due to three main issue: the softening behaviour of the concrete in compression, the cracking of the concrete in tension, and the presence of steel bars with different ultimate deformation and material behaviour.

The use of a material with softening is known to lead to stress concentration and possible lack of objectivity of the solution and convergence issue. Such issue can be solved by means of regularization technique, as e.g., explained in (Bontempi & Malerba, 1997), but requires an attentive analysis of the results and careful validation of the model.

The cracking of the concrete is often not explicitly simulated but modelled instead as smeared cracking over the element mesh. This simplifies the model significantly, but creates a mesh dependency, as the fracture energy becomes dependent on the characteristic length of the element. In order to maintain the objectivity of the solution, the ultimate strain of the concrete in tension must be adjusted depending on the mesh used.

However, the interaction of the concrete and the steel poses limits on such adjusted value of the ultimate tensile strain, which should not exceed the yielding strain of the steel or the maximum elastic tensile strain of the concrete. This means, that the mesh size of the model cannot be refined as desired, as a corresponding maximum and minimum limit on the mesh characteristic length h should be respected (Carstensen, Jomaas, & Pankaj, 2013). Such limits are reported in the following equation, where: E_c is the elastic modulus of concrete; G_f is the fracture energy of the concrete; f_{ct} is the uniaxial tension strength of the concrete, E_s is the elastic modulus of steel; f_y is the yield strength of steel.

$$h_{max} = \frac{2G_f E_c}{f_{ct}^2} \quad h_{min} = \frac{2G_f E_s}{f_{ct} f_y} \quad (58)$$

This has consequences on the accuracy of the solution and on the computational effort to find convergence of the solving algorithm. As result, the implementation of a FEM of a concrete element is a delicate task and a through validation of the model is of outmost importance. In the following, the validation of the ultimate static capacity of the model is presented, with respect to compression, tension and bending. Then, the dynamic behaviour of the model is tested with respect to the elastic and inelastic response to a step function of the dynamic load.

D4.3. Final report on analytical, numerical and experimental studies on explosions, including innovative prevention and mitigation strategies

3.9.3.3.1 Static validation

3.9.3.3.1.1 Tension and compression benchmark

First a simulation of the slab loaded in pure compression and tension is presented. Such simulation is meant to benchmark the correct behaviour of the material and the capability of the model of following the softening phase of the material. Since the compression and tension are uniform along the slab length, only a segment of the slab can be used. Furthermore, since the problem is plane, it is not necessary to model the whole depth of the slab in the tunnel nor refer to a strip of 1 m, but any depth can be used, provided that the appropriate amount of reinforcement per meter depth is respected. This model assumes a slab strip with depth $w = 0.15$ m, which is equal to the distance between the bars. Therefore, the slab is modelled as a beam with a section having height $h = 0.35$ m, width $w = 0.15$ m, and only one top and bottom steel bar along the central vertical axis of the section. One end of the beam is restrained, while at the other end a uniform displacement is applied on all nodes first in the negative direction (compression) and then in the positive direction (tension). PLANE181 elements are used to model the concrete with a mesh size of 0.35 m.

The results of the static incremental analysis (Newton-Raphson) for the compressive and tensile benchmark are presented on the left and right chart of Figure 87, respectively. A good agreement of the peak force and corresponding displacement is shown in both cases, while the softening branch deviates just slightly from the expected solution and slightly underestimate the capacity at failure in compression. Overall, the results are deemed acceptable, and the model is considered validated for the static response in tension and compression.

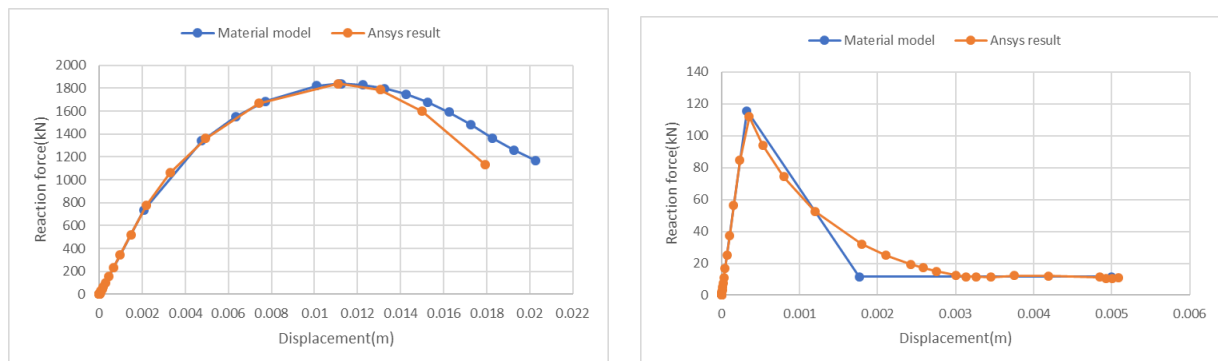


Figure 87. Results of the compressive (left) and tensile (right) reaction force vs. displacement of the free end obtained in Ansys (orange line) and comparison with the value calculated from the input material model (blue line).

3.9.3.3.1.2 Bending capacity

The ultimate bending capacity of the 10 m long simply supported, and uniformly loaded slab is investigated. Thanks to the symmetry of the problem about the vertical mid-span axis, only half of the problem can be modelled. This is done by considering only half-length of the slab and assuming a fixed (moment-resistant) restrain at one end, which simulate the symmetry condition and releasing the vertical displacement at the other end. The result is a cantilevered slab having a length of 5 m, but the same load bearing capacity of the 10 m long simply supported slab.

D4.3. Final report on analytical, numerical and experimental studies on explosions, including innovative prevention and mitigation strategies

Furthermore, as done in the compressive and tensile benchmarks, the width of the slab can be reduced, as the problem is plane. Therefore, only one strip of the slab of width 0.15 m will be considered with one steel bar at the top and one at the bottom, in the centre of the section. The validation is done with respect to the negative bending capacity, as the slab in the tunnel will be hit by an upward pressure on the bottom surface and first bended in negative bending. As seen in Figure 88, a vertical downwards load is applied to the beam (slab strip). However, in order to maintain the correct bending response, the section of the beam is reverted, so that the upper bar has a concrete cover of 55 mm, and the bottom bar has a concrete cover of 35 mm.

The model is built by using SHELL181 elements for modelling the concrete and REINF263 elements as reinforcement embedded into the concrete elements. The use of embedded steel elements allows to avoid using a very small mesh in the concrete rebar part and use mesh sizes that respect the limits indicated in the previous paragraph. In particular, the minimum mesh for this particular model is calculated to be 3.6 cm, which would not allow a very good discretization of the concrete cover of the steel in tension, which is 5.5 cm.

A dynamic solving algorithm is used to calculate the capacity, based on HHT integration method. The static solution is obtained by applying the load linearly over 10 s, which is a time much larger than the natural period of the cantilevered slab, so that a quasi-static regime is obtained, and the solution is not affected by inertia effects. The choice of using a dynamic algorithm to calculate the static capacity is motivated both by the fact that the final simulation of interest is a dynamic simulation and by the fact that the static incremental analysis based on Newton-Raphson or arc-length method have difficulty to converge and predict an accurate value of the capacity.

The results of the analysis are reported in Figure 89 and in Table 37 for three different sizes of a squared mesh: a larger mesh size of 20 cm (case 3), an intermediate mesh size of 10 cm (case 2), and a finer mesh size of 5 cm (case 1). The intermediate mesh size is the one that gives longer convergence and show the peak of the capacity, which is instead not fully reached in the analysis of the model with finer mesh and not very accurate in the analysis of the model with the coarse mesh. The resulting capacity is reported in the picture and in the table in term of reaction force at the support $R = p L$, where p is the value of the uniform load in kN/m and $L = 5$ m is the length of the cantilever beam. This value is compared with the expected value of the reaction force obtained by the simplified hand calculations and INCA2 calculations reported in paragraph 3.9.3.1. It is seen that the capacity predicted by the model in case 2 is the same as the one calculated with INCA2, while the other 2 cases give an underestimation of the capacity of ca. 7% with respect to the INCA2 value and only 4% with respect to the hand-calculated capacity, which is normally used for design purpose. Such error is quite small for fully plastic nonlinear analysis and therefore even such other two models would be deemed to give acceptable results.

D4.3. Final report on analytical, numerical and experimental studies on explosions, including innovative prevention and mitigation strategies

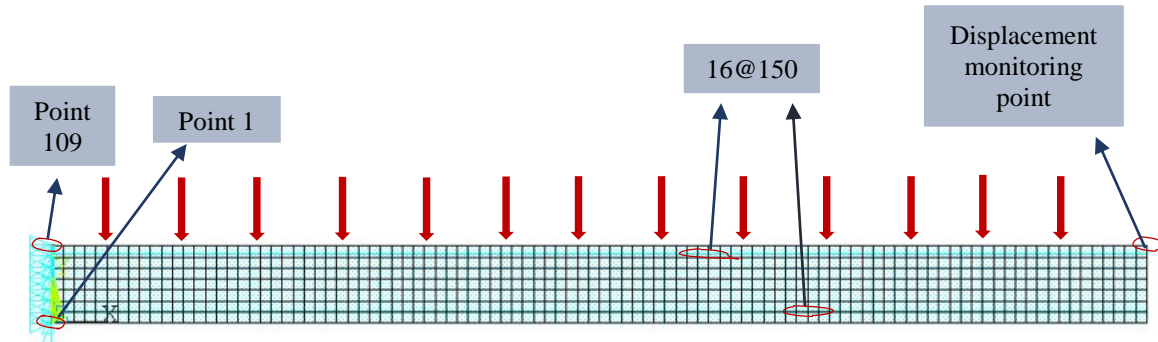


Figure 88. Model of the slab for validation of the bending capacity.

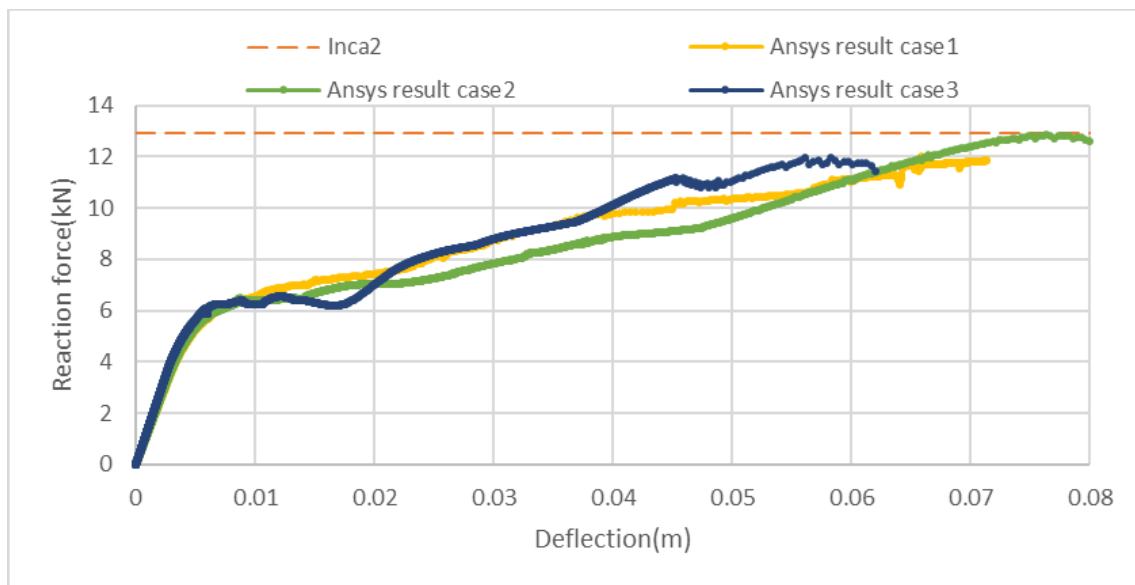


Figure 89. Reaction at support vs vertical displacement of the free end obtained for three different mesh sizes (continuous lines) and expected value of the capacity calculated in INCA2 (dotted line).

Table 37. Table 1. Reaction at support in the FEM for 3 different mesh and comparison with the expected values.

Type	Case3	Case2	Case1	Inca2	Hand-calc.
Grid size (m)	0.20	0.10	0.05	---	---
Max reaction (kN)	12.0	12.9	12.0	12.9	12.5

3.9.3.4 Outcomes of the analysis and evaluation of the results

After having validated the model in term of plastic response and dynamic response, the response of the simply supported 10 m long slab to the tank explosion is investigated. As explained above, the maximum pressure obtained in the CFD analysis and reported in Figure 84 is assigned to each bottom node of the slab and a dynamic analysis with direct integration HHT method is carried out. The results are

D4.3. Final report on analytical, numerical and experimental studies on explosions, including innovative prevention and mitigation strategies
reported in term of history of the displacement of the mid-span of the slab

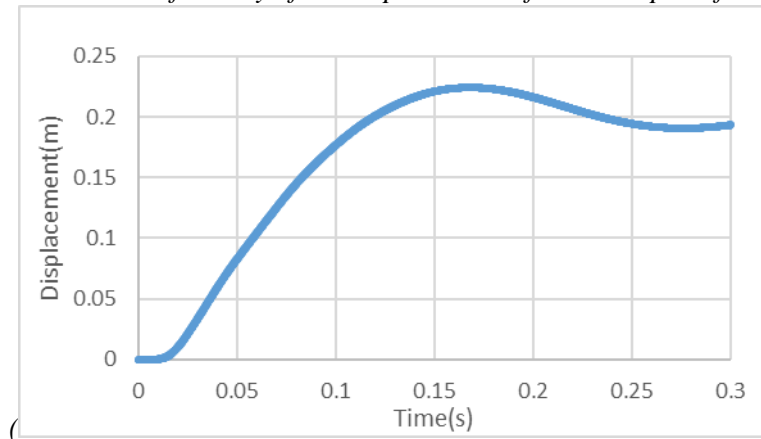


Figure 90), as well as plot of the strain at the time point when the maximum displacement is reached (Figure 91).

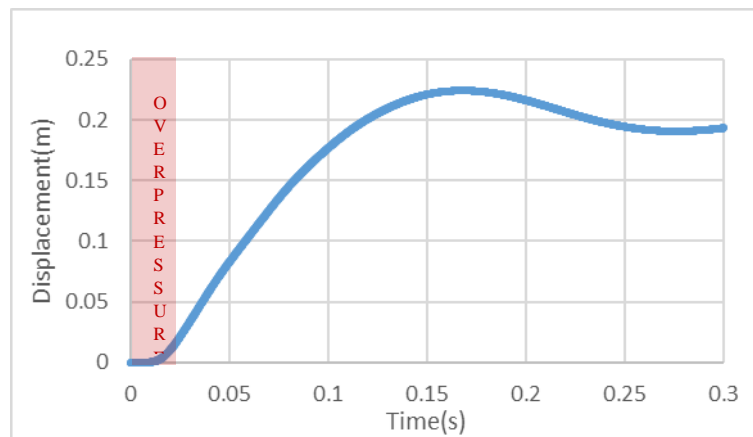


Figure 90. Deflection of the mid-span as function of time.

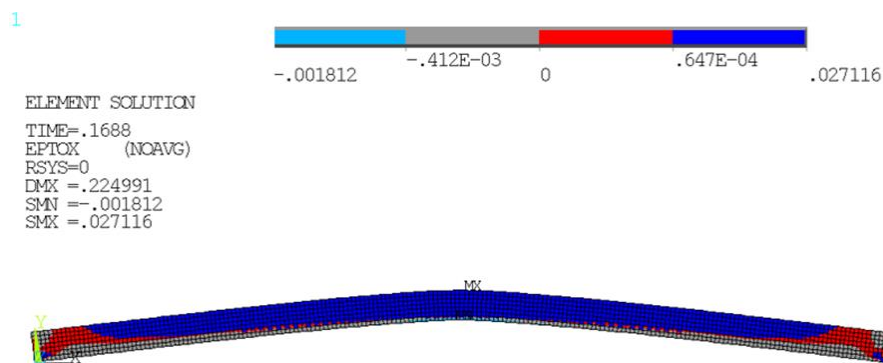


Figure 91. Plot of the strain at the time of the maximum deflection.

The plot also shows that, at this point, the majority of the beam section is cracked (blue color), which indicates that the pressure wave has induced a significant damage in the slab. However, no runaway of

D4.3. Final report on analytical, numerical and experimental studies on explosions, including innovative prevention and mitigation strategies
the mid-span is evident in the displacement history shown in

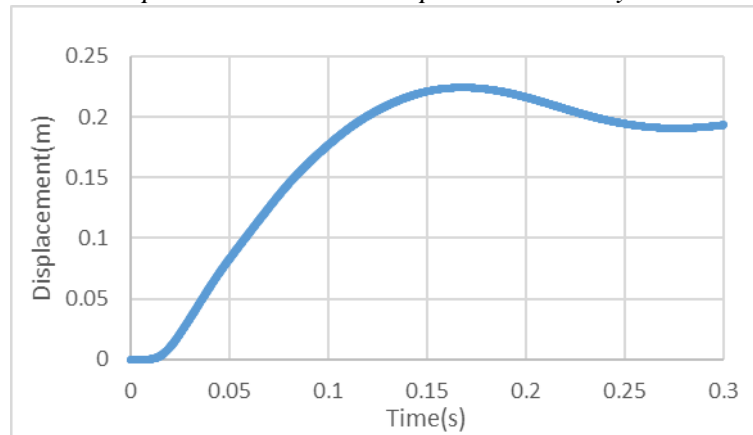


Figure 90, which would clearly indicate a collapse of the slab.

Nevertheless, the maximum deflection of the mid-span is about 22 cm, which is a quite significant displacement, corresponding to 1/45 of the slab length and thus being about 5.5 bigger than the service limit displacement $L/250$ used as design condition for horizontal elements in bending. In order to check whether the maximum deflection highlighted by the analysis could indicate a collapse of the slab, such value is compared with the limits used to indicate collapse by different regulations and summarized in Table 38.

Table 38. Limit on the maximum deflection for collapse according to different regulations.

Regulation	based on	formula	δ_{\max} [cm]
GSA	max plastic rotation	$\theta_{\max} = 0.063$ rad	31.5
BS476	fire limit	$\delta_{\max} = L^2/(400 \cdot H)$	71.4
ISO834-1	fire limit	$\delta_{\max} = L/20$	50.0

The slab deflection of 22 cm is within the limits indicated for collapse by the three regulations considered. A clear collapse condition is therefore not highlighted by the results of the analysis. Nevertheless, the high deflection and the large damage status of the slab suggest that reinforcement measures should be precautionary adopted, so that the slab can sustain the tank explosion. Such measures are even more recommendable, in consideration of the fact that the tank explosion could not be the only accidental event but be triggered by a concomitant fire or cause the explosion of the other hydrogen tanks of the bus.

3.9.3.5 Conclusions

A nonlinear dynamic analysis of a 2D model of a tunnel slab exposed to a tank explosion have been carried out. The results of the analysis show that, despite the overpressure caused by the tank explosion is significantly higher than the static capacity of the slab, the duration of the pressure wave is so short in comparison with the natural period of the slab, that the dynamic response is significantly de-amplified with respect to the static response. As a result, the deflection of the mid-span reaches a maximum displacement of 22 cm, but no runaway of the deflection is highlighted. However, an extended cracking of the beam and a permanent residual deflection of about 20 cm can be noted, which would require the substitution of the portion of the slab hit by the overpressure.

D4.3. Final report on analytical, numerical and experimental studies on explosions, including innovative prevention and mitigation strategies

The results have been obtained by means of a FE analysis of the nonlinear dynamic response of a 2D model of a transversal section of the slab. The effect of the explosion wave travelling along the length of the tunnel has not been included. Furthermore, the slab section has been uniformly loaded over the transversal length to the explosion pressure of one tank shown in Figure 84. The analysis is carried out at 20°C, thus implicitly assuming that no concurrent accident is considered - such as, e.g., a vehicle fire that might have triggered the explosion.

As such, the validity of the conclusions is limited by the assumptions done on the action and on the modelling. In particular, the response of the slab could be higher, if:

- some parts of the slab are exposed to a lower but longer overpressure, resulting in a dynamic amplification or at least a lower de-amplification of the response.
- the effect of the pressure wave along the tunnel cause more significant deformations or vibrations in the longitudinal direction of the slab
- the explosion of more than one tank occurs, because of the same accident.
- the tank explosion has been triggered by a vehicle fire, which had previously, or is simultaneously, acting on the slab.

D4.3. Final report on analytical, numerical and experimental studies on explosions, including innovative prevention and mitigation strategies

3.10 Simulations of flame acceleration and transition to detonation in tunnel structures (4.3, USN)

3.10.5 Background and accident scenario

For a scenario of a hydrogen-powered train in a rail tunnel that is essentially narrower than a typical road tunnel, hydrogen releases from TPRD of larger diameter would require sufficient air entrainment to assure the effective reduction of hydrogen concentration above and on sides of the train. High train speed and smaller TPRD diameter could ensure a decrease of flammable cloud. For a stopped in a tunnel train, a smaller diameter TPRD can reduce hydrogen concentration and the size of a flammable envelope to some extent.

For trains travelling in a tunnel, a larger release will form a large flammable mixture. Figure 92 shows the hydrogen mass flow into the air above the train to produce an average 30% hydrogen-air mixture as a function of air volumetric flow rate. The airflow rate of $80 \text{ m}^3/\text{s}$ corresponds to about 55 m/s train speed for 0.5 m height between train and tunnel ceiling and 6 m width and assuming a linear velocity profile (see Figure 92). For this scenario it is assumed the accidental release of hydrogen with a mass flow rate over 2 kg/s will produce a 30% hydrogen-air mixture along the length of the train. The mass flow rate of 2 kg/s can be from only one TPRD of 9 mm diameter or multiple TPRDs of the same total cross-section area for storage with NWP=70 MPa.

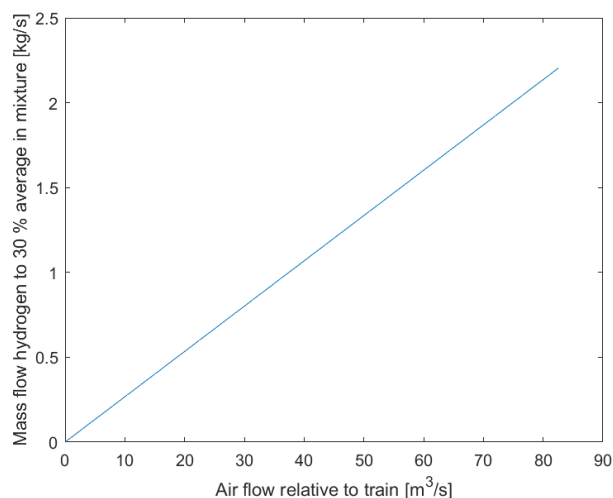


Figure 92. Hydrogen mass flow rate into air volume above the train to form 30% vol. hydrogen mixture as a function of volumetric air flow rate above the train in tunnel, assuming 6 m x 0.5 m free area above train.

3.10.6 Objectives

The objective of this task is to simulate flame acceleration and DDT, in scenarios of release of hydrogen from a train, in a tunnel. The narrow gap between train and tunnel ceiling, in addition to the train moving, can cause a combustible hydrogen-air mixture and lead to severe explosion. The outcome of the simulation work will be a method for simulating flame acceleration and DDT in such scenarios, including the effect of a moving wall and concentration gradients.

D4.3. Final report on analytical, numerical and experimental studies on explosions, including innovative prevention and mitigation strategies

Another outcome is recommendation for safe ventilation of hydrogen from trains.

3.10.7 Numerical simulation set-up

The CFD method that will be used in this work is a USN in-house code for flame acceleration, detonations, and shock waves. The code is based on the centred TVD scheme, FLIC, and includes combustion models for turbulent flames, chemical kinetics, and viscous stresses. The code has been used in simulations of flame acceleration, DDT, detonation propagation, blast waves and shock-flow interactions (Vågsæther, 2010). The simulations were performed on a 2D domain of 0.5 m height and 12 m for concentration gradients and 32 m long for velocity gradients. The domain is discretized using a spatial resolution of 1 mm, which is on the coarse side regarding simulation of DDT in hydrogen-air mixture. For the simulations of effect of concentration gradient, hydrogen concentration field was set to be between equivalence ratio of 0.46 and 1 or 16 to 30 vol%, see Figure 93. The presumed worst case of 30% average concentration is not presented to demonstrate that concentration gradients can significantly accelerate the flame even in “lean” in the average mixtures.

In the simulations on the effect of velocity gradient a velocity gradient of 110 s^{-1} was applied based on a typical high train velocity of 55 m/s in a tunnel leading to a strained flow field in the space between the train and the tunnel walls. A typical height between train roof and tunnel ceiling is 0.5 m for standard tunnel and train sizes.

Simulations with stationary homogenous gas mixture and a applying both velocity gradient and concentration gradient was also done in this work. The mixture is ignited in the center along the top wall for all simulations.

No other geometry than upper and lower wall was applied in the simulations. It is important to underline that presence of obstacles and wall roughness in the tunnel geometry could increase flame acceleration and promote DDT.

D4.3. Final report on analytical, numerical and experimental studies on explosions, including innovative prevention and mitigation strategies

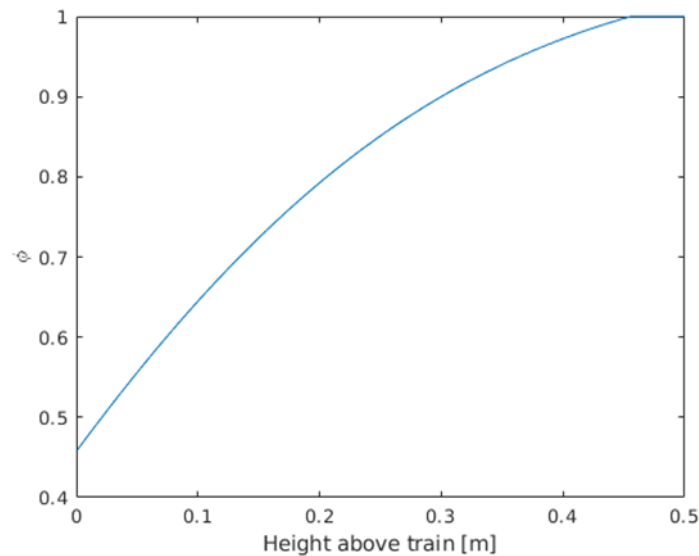


Figure 93. Hydrogen concentration distribution (gradient) used in the simulations (shown in terms of the equivalence ratio). A lean hydrogen-air mixture in the whole domain is used to keep reactivity low in simulations.

3.10.8 Results and conclusions

3.10.8.1 Effects of the concentration gradient

Figure 94 shows three snapshots of simulated pressure during flame acceleration in a rail tunnel volume above the train. Ignition is at the top and centre of the geometry. The middle frame (9.2 ms) shows destructive Mach-stems are forming towards the train roof. In the last frame (10.1 ms) DDT is seen on both sides, producing pressure up to 9 MPa due to detonation in the pre-compressed mixture.

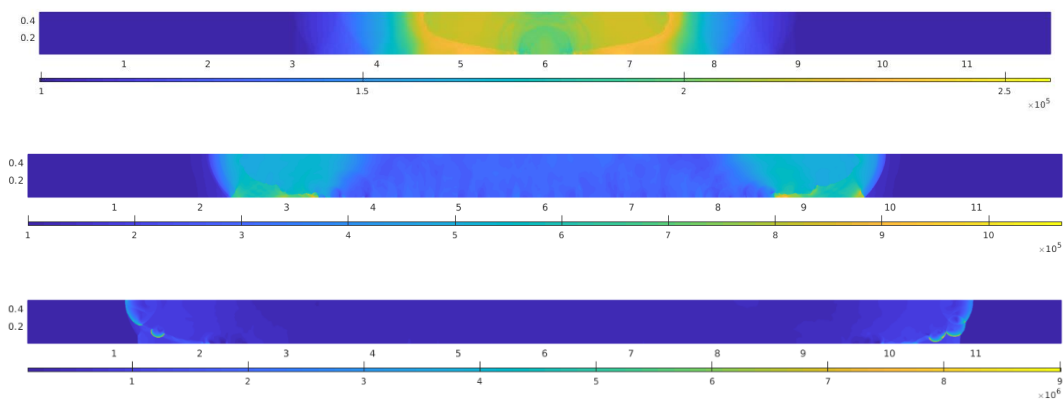


Figure 94. Top: 7 ms after ignition. Middle: 9.2 ms after ignition. Bottom: 10.1 ms.

3.10.8.2 Effect of velocity gradient

Figure 95 shows a pressure contour where the flame is close to the domain exit. The pressures in the domain reach 1 barg as the flow field in front of the propagating flame dominates over the initial strained flow field. Since the initial velocity field of strain rates of 110 s^{-1} will not,

D4.3. Final report on analytical, numerical and experimental studies on explosions, including innovative prevention and mitigation strategies significantly, contribute to flame acceleration up to DDT, the recommendation will be to keep high train velocity through tunnels for dilution of hydrogen during accidental release.

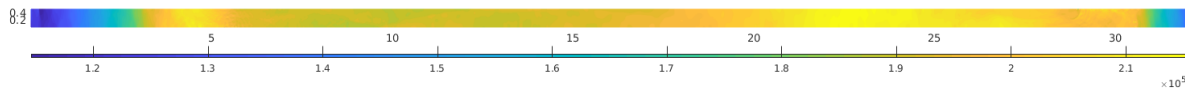


Figure 95. Simulated pressure during accelerated flame propagating in velocity gradient of 110 s^{-1} (0-55 m/s over 0.5 m) at 69 ms from the ignition. The domain is 32 m long.

3.10.9 Conclusion

Simulations with homogeneous gas mixture, in this simplified set-up, did not produce DDT in the tunnel geometry, even with velocity gradients up to 110 s^{-1} . Concentration gradients can increase flame area turbulence and lead to DDT in both stationary gas mixture and in a velocity gradient. A DDT occurring in such a scenario will lead to significant overpressures acting on a train, leading to large consequences. An important effect of reaching a detonation is that the explosion reaction rate will be high even in semi-confined or unconfined gas clouds.

4 Experiments (Task 4.4 / HSE)

4.1 Blast wave and fireball of tank rupture in tunnel: Demonstrations of car tank failure in fire experiments in one real tunnel (4.4.1, CEA)

4.1.5 Introduction

CEA is conducting tests on explosion of pressurized tanks in a full-scale tunnel geometry.

The tests were organized in two phases. The first one in October 2020 in which type II cylinders under 200 bar were used. The second in June 2021 in which type IV tanks of 78 liters under 700 bar were used as a source of compressed gas. In these tests, the blast waves overpressures are recorded as well as the fireball characteristics. This report focuses on fireballs analysis.

The relevant information regarding the test geometry, the detail of injection, the type of sensors as well as their locations are provided in two separate documents:

- For pre-tests of 2020:
Sauzedde et al, 2020. *CEA Experimental devices Tests of 2020. HyTunnel-CS project, 2020.*
- For the tests 2021:
Sauzedde et al, 2021. *CEA Experimental devices Tests of 2021. HyTunnel-CS project, 2021.*

The CEA contribution is organized as follows. In the first paragraph, the geometry used for the test is briefly described. Then, the different phases of the test and the test matrix are detailed. Finally, the results are provided for the behavior of large-scale fireballs. Some conclusions and recommendations follow.

D4.3. Final report on analytical, numerical and experimental studies on explosions, including innovative prevention and mitigation strategies

4.1.6 Test geometry

The relevant information regarding the test geometry, the type of sensors as well as their locations are provided in a separate document (Sauzedde et al., 2020). A schematic description of the test arrangement is provided in Figure . The tests were performed in the tunnel du Mortier (near Autrans village, Isère, France). This disused road tunnel is a horse-shoe type geometry with a total length of about 502 m. The slope is 3.6% and the tunnel is divided in two different sections. The one located on the Autrans side is made of a flat concrete ceiling arch and the second one on the Montaud side is raw limestone rocks. The tank to be exploded was installed in this second section for both test series. Explosions belts were used to open the tank circumferentially (Figure).



Figure 96. Example of tank equipped with a detonation belt.

The tunnel dimensions vary in the rocky section, an average height is close to 5.9 m, and the diameter is about 8.9 m. Two sidewalks are also present on each side of the road.

The monitoring system can be divided into two parts:

- The one related to overpressure recording along the tunnel length. Blast wave pencils were installed in the center of the road at approximately one meter height
- The one related to the fireball monitoring. Both sides of the tunnel were equipped with thin type-K thermocouples associated with an ionization gauge (Figure 97). The thermocouple is supposed to catch the hot gases and the ionization gauge the reactive waves. These devices were located along the tunnel wall at about 3 meters height at about 20 cm from the wall. They were installed at +/-5, 10, 15, 20 and 25 m from the explosion center. Two high-speed cameras (Phantom Miro M310 operated at about 10000 fps) were also located at about 100 m distance from the explosion in a protective box to record the shape of the fireballs.

D4.3. Final report on analytical, numerical and experimental studies on explosions, including innovative prevention and mitigation strategies

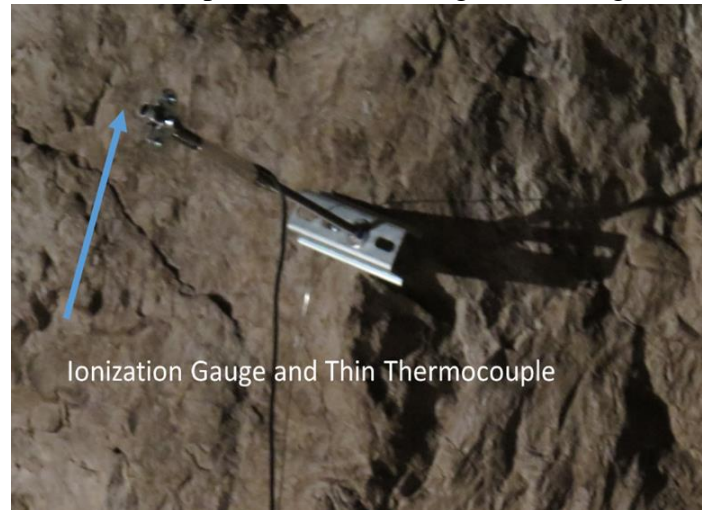


Figure 97. Measurement devices used to monitor fireballs.

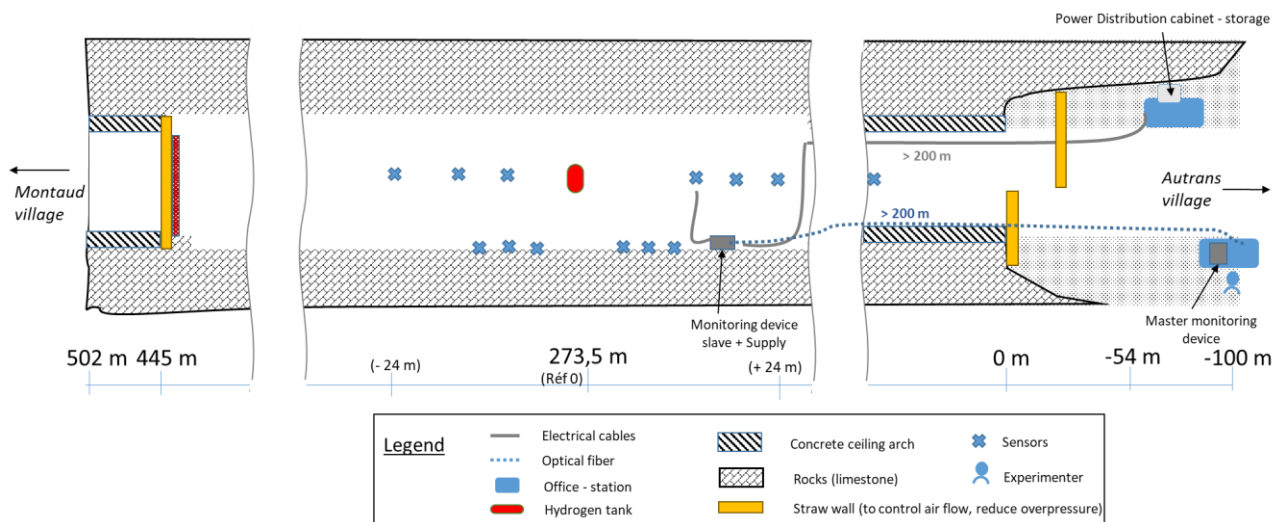


Figure 98. General sketch of the 2021 explosion and fireball tests.

4.1.7 Test sequence and test matrix

The test sequence is divided into three steps:

- Step 1: installation of the tank on a support in the center of the tunnel. The tank is oriented perpendicular to the tunnel axis in order to blow the fragments against the walls.
- Step 2: The tank is equipped circumferentially with a detonation belt to cut the tank into two pieces. The belt is ignited by a small charge of explosive in which a detonator is inserted.
- Step 3: ignition of the detonator and start of recording. The data acquisition frequency is 200 kHz for the blast sensors and 100 Hz for the thermocouples and ionization gauges.

Time zero has been set to the beginning of Step 3.

The two test matrices are given in Table 39 and the tests relevant for fireball analysis are only those in which the tank is pressurized with hydrogen. Only two tests were relevant during the 2020 campaign (pre-test 31 and 32). In the 2021 test series, data were lost during test 35.

D4.3. Final report on analytical, numerical and experimental studies on explosions, including innovative prevention and mitigation strategies

Table 39. Explosion test matrix.

	Type of Test 2020	Nb of test	Volume (litre)	Pressure (bar)	Configuration	Test n°
Test 2020	Explosion of solid explosives	10	-	-	0,160 kg	n°24
			-	-	0,702 kg	n°25
			-	-	1,350 kg	n°26
	Explosion of empty tank		50	-	Fragment	n°33
			32	-	Fragment	n°27
			150	-	Fragment	n°29
	Explosion of He tank		150	41	Tank III	n°28
			22	40	Tank IV	n°30
	Explosion of H ₂ tank		150	5 (He) 36 (H ₂)	Tank III	n°31
			50	47	Tank II	n°32
Test 2021	Explosion of empty tank	9	50	-	Fragment	n°31
			78	-	Fragment	n°33
	Explosion of He tank		50	200	Tank II	n°30
			78	650	Tank IV	n°34
	Explosion of H ₂ tank		50	194	Tank II	n°42
			78	90	Tank IV	n°32
				520	Tank IV	n°37
				580	Tank IV	n°35
				610	Tank IV	n°38

D4.3. Final report on analytical, numerical and experimental studies on explosions, including innovative prevention and mitigation strategies

In this document, the results of the 2021 tests are mainly described. References to the 2020 test results are given when necessary. As a reminder, these 2020 tests were performed with type II, type III, and type IV tanks with reduced pressures but at the same location in the tunnel.

Fireballs issued from different tank volumes from 50 to 78 liters and internal pressures from 90 to 610 bar are experienced in the 2021 test matrix. If fireball analysis is concerned, the first parameter to estimate is the mass of hydrogen (m_{H_2}) inside the tank (Table 40). It ranges from 566 g to around 2.8 kg for the performed tests. In the open literature, size of fireballs produced by hydrogen tanks put in a fire are also reported from different publications. A review has been recently published by Makarov et al. (2021). They gathered the different experimental data and issued a conservative correlation (1) to estimate the equivalent hemispherical radius.

$$R_{\text{hemisphere}} = 9.75 m_{H_2}^{1/3} \quad (59)$$

Zalosh and Weyand (Zalosh and Weyand, 2005) also issued experimental data about fireball size and duration t of fireball event in the form of different correlations (2) whereas the buoyancy or convection are dominant phenomena.

$$R_{\text{hemisphere}} \sim 5 m_{H_2}^{1/3} \quad (60)$$

$t = 0.47 m_{H_2}^{1/3}$ in convection dominated regime and $t = 2.6 m_{H_2}^{1/6}$ in buoyancy dominated regime.

Application of these correlations to the 2021 test conditions leads to fireballs greater than the dimensions of our tunnel if we consider the conservative ones. However, those of Zalosh et al lead a fireball smaller than the tunnel diameter for the first two test conditions (test 42 and 32). The three other tests will lead to fireballs filling completely the tunnel cross-section. The durations vary from 0.5 to 3 seconds depending on the convective or buoyant dominant expansion process.

Table 40. Some global characteristics of fireball tests performed in 2021

Volume	Pressure (bar)	Mass H ₂ (kg)	R _{hem.} (m)	t (s)	Test n°
50	194	0.725	4.5 - 8.8	0.4 – 2.5	n°42
78	90	0.558	4.1 - 8.1	0.4 – 2.4	n°32
	520	2.554	6.9 - 13.4	0.6 – 3.0	n°37
	580				n°35
	610	2.871	7.1 - 13.9	0.7 – 3.1	n°38

The derivation of the hemispherical radius of the fireballs is performed using the pictures taken by the high-speed cameras during the expansion of explosion process. The image processing method is explained in Figure 99. This method is based on a threshold gray levels image and contour detection. It is inherently a 2D process and the tools are programed in Python thanks to the OpenCV toolbox. The scale on the 2D plan is given by the tank diameter (pixel/mm).

D4.3. Final report on analytical, numerical and experimental studies on explosions, including innovative prevention and mitigation strategies

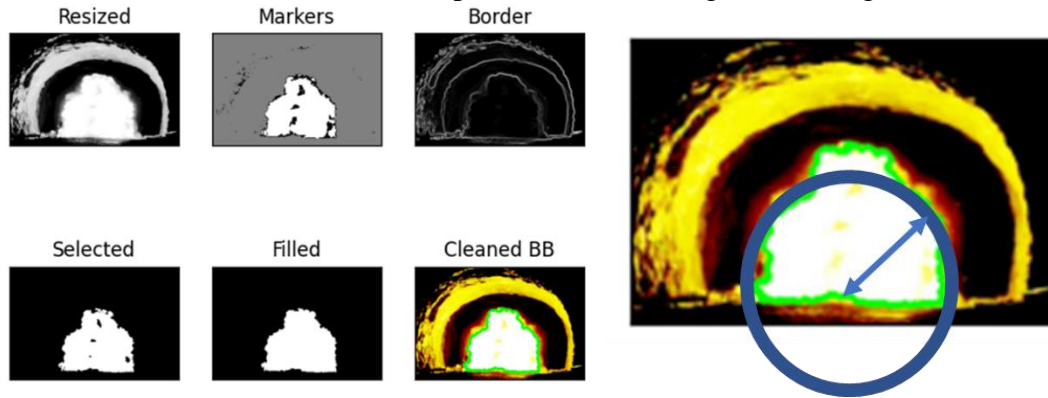


Figure 99. Post-processing method to derive the hemispherical radius of fireballs.

4.1.8 Test results

Before describing the results obtained for the 2021 tests, we recall the main lessons learned from the two 2020 tests. First, an image obtained by the high-speed camera is shown in *Figure 100*, left. We applied the same processing method as described above and identified a phenomenon of breathing of the fireball. This phenomenon does not appear in open areas. In the tunnel or any confined space, the shock waves produced by the explosion are reflected by the walls and return to the reaction zone and slow it down due to reverse velocities. This oscillatory process is clearly identified in *Figure 100*, right, and the period is of the order of 25 ms. It probably corresponds to a mixture of the sound velocities in the fresh and burnt gases brought back to the radius of the tunnel. This phenomenon probably has also an impact on the turbulent velocities to be used to calculate these fireballs in a confined environment. Such comparison will surely be very interesting to estimate the percentage of chemical energy involved in the creation of blast waves.

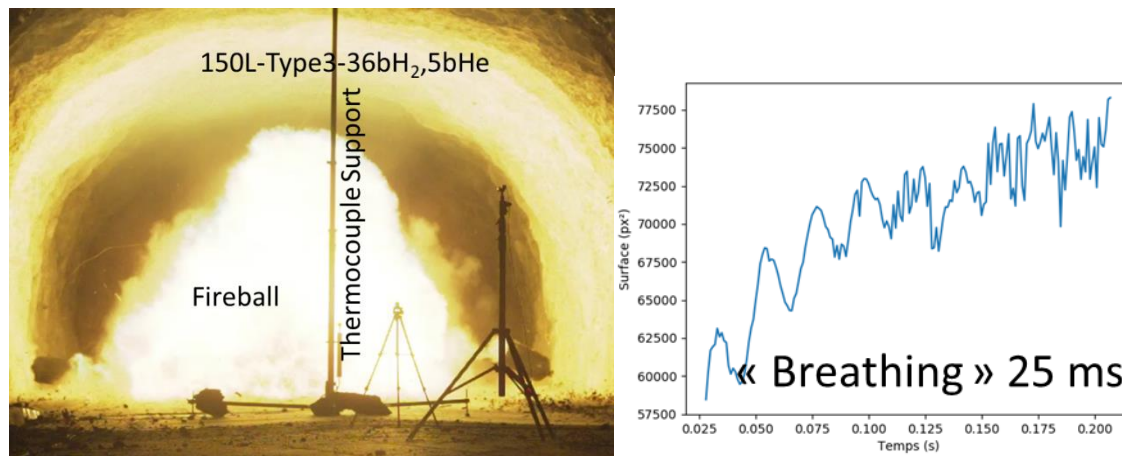


Figure 100. 2020 pre-test 31: Left – example of fireball picture. Right – post processing of fireball surface.

In addition, thermocouples installed in the upper part of the tunnel along a cable allowed to follow the progression of the hot gas cloud during the pre-test 32 (*Figure 101*).

D4.3. Final report on analytical, numerical and experimental studies on explosions, including innovative prevention and mitigation strategies

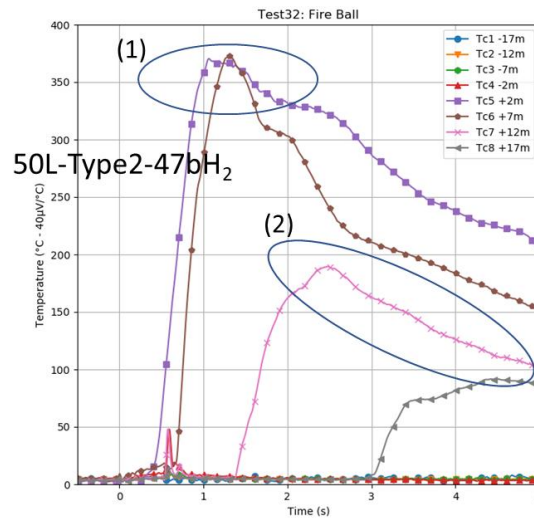


Figure 101. 2020 pre-test 32: Thermocouple measurements.

Two regimes are clearly identified:

1. A first wave propagating near the explosion center at a velocity close to 25 m/s.
2. A dilution of the convected hot gas cloud far from the explosion center. During this test, the ventilation velocity in the tunnel was measured at about 3.5 m/s which corresponds well to the measurements reported by two thermocouples located towards Autrans side (positive Y axis).

4.1.8.1 Morphology of the fireballs

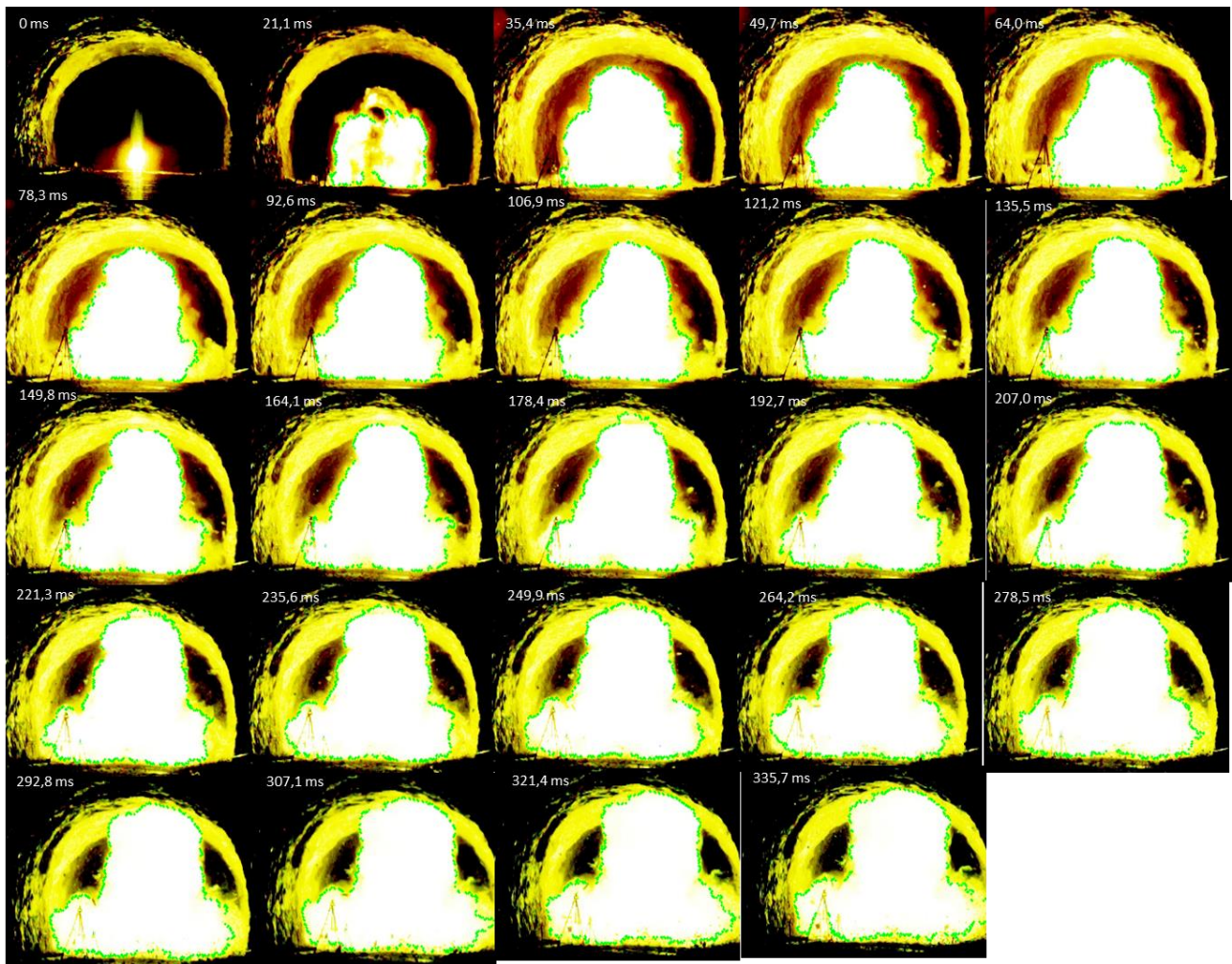


Figure 102. 2021 test 32: Shapes of the fireball.

On the images of the fireball of test 32 (*Figure 102*), one can see that the first glow comes from the ignition of the solid explosive initiating the explosion of the detonation belt. Then, the fireball is square shaped because of the specific shape of the detonation belt focusing the waves for the circumferential cutting of the tank. From 20 ms, the luminosity increases and the chemical reaction with hydrogen starts. At the beginning, a hemispherical ball develops. Then (60 ms), the reaction progresses with the two fragments of the tank which are expelled violently on the side walls, while the remainder of the fireball is slowed down by the pressure waves which reflect on the walls. In this test, the fireball does not spread over the entire cross-section of the tunnel and the sensors that we installed along the wall at 3 m height on the left are not a priori impacted by the reactive zone.

D4.3. Final report on analytical, numerical and experimental studies on explosions, including innovative prevention and mitigation strategies

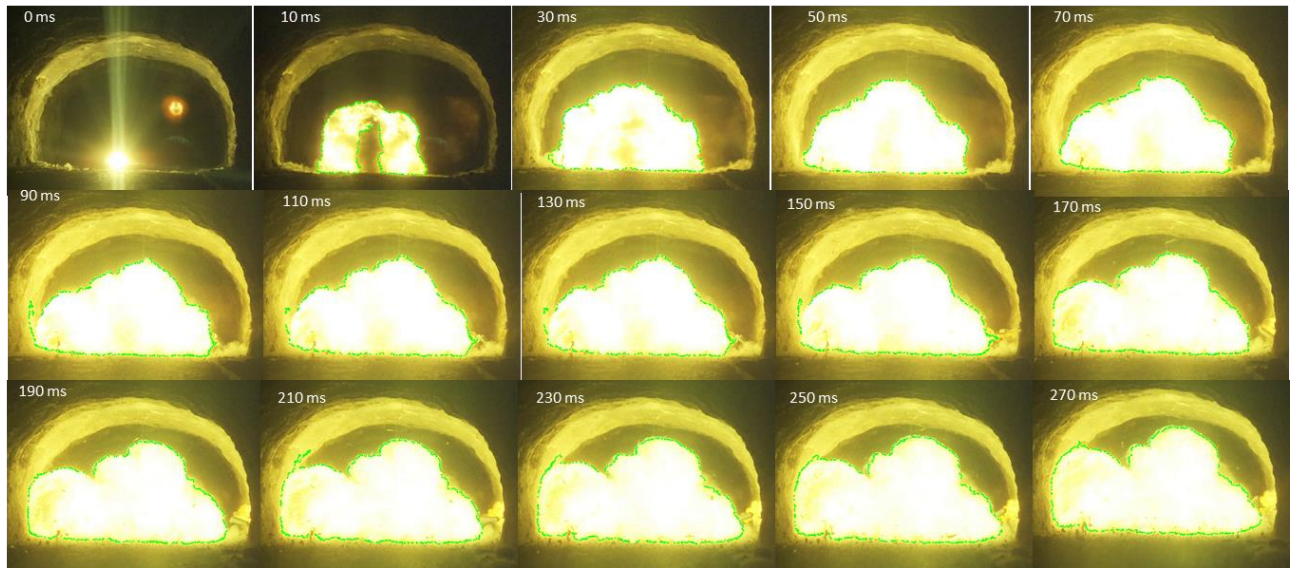


Figure 103. 2021 test 42: Shapes of the fireball.

If we increase the mass of hydrogen by increasing the pressure with a tank of smaller volume (*Figure 103*), the phenomena are slightly different and faster. We find the square shape of the fireball up to 10 ms. Then, the chemical reaction develops in a hemispherical way without progressing towards the top of the tunnel. The two fragments finally produce two almost distinct fireballs. In this test, the tank is not cut in the center; the fragment on the left is much smaller than the one on the right, which may explain the two fireballs.

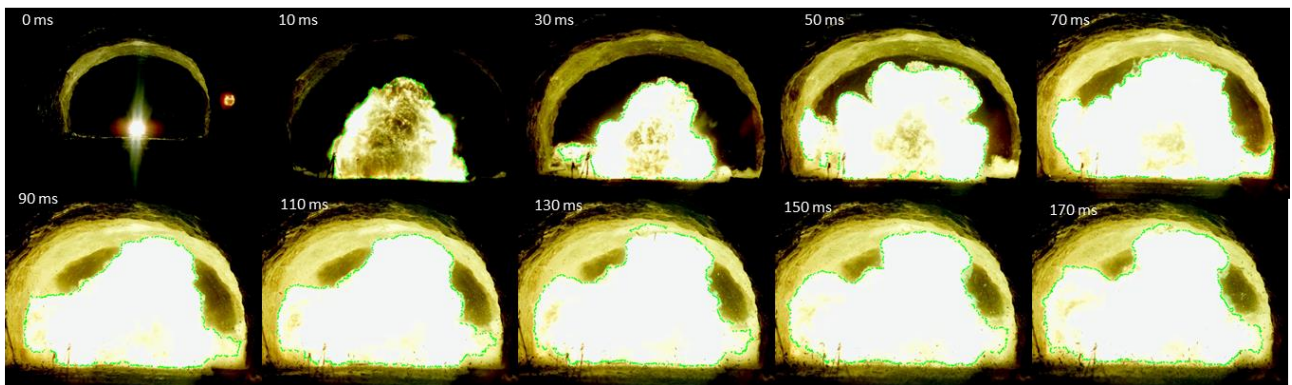


Figure 104. 2021 test 37: Shapes of the fireball.

The next two tests (tests 37 and 38 *Figure 104* and *Figure 105*) were carried out with a type IV tank of 78 liters and two internal pressures above 500 bar. The phenomena observed are relatively identical. The sequence of stages accelerates. The fireball is already luminous and hemispherical from 10 ms. Then, it progressively engulfs the whole cross-section of the tunnel only for test 38, i.e., the tank with the highest internal pressure. In the last image of test 38, the box containing the camera starts to move under the effect of the blast waves.

D4.3. Final report on analytical, numerical and experimental studies on explosions, including innovative prevention and mitigation strategies

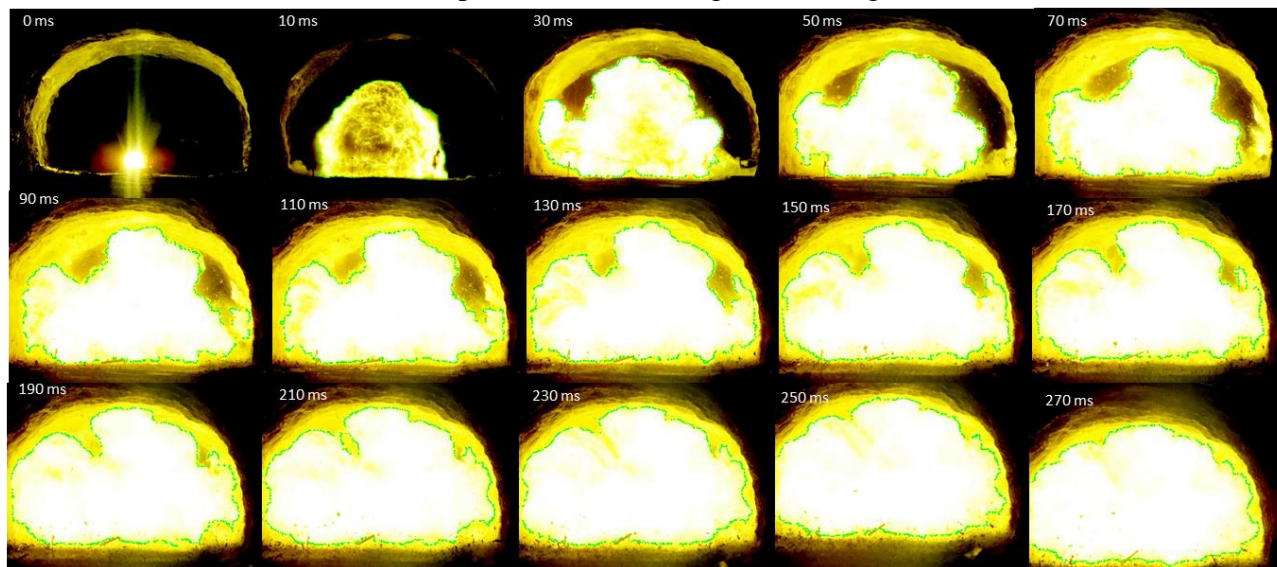


Figure 105. 2021 test 38: Shapes of the fireball.

4.1.8.2 Fireball characteristics

First, the evolution of the radius of the equivalent hemisphere (Figure 106) reflects quantitatively the observations made on the videos. Only the test 38 lead to the complete filling of the tunnel cross section by the fireball.

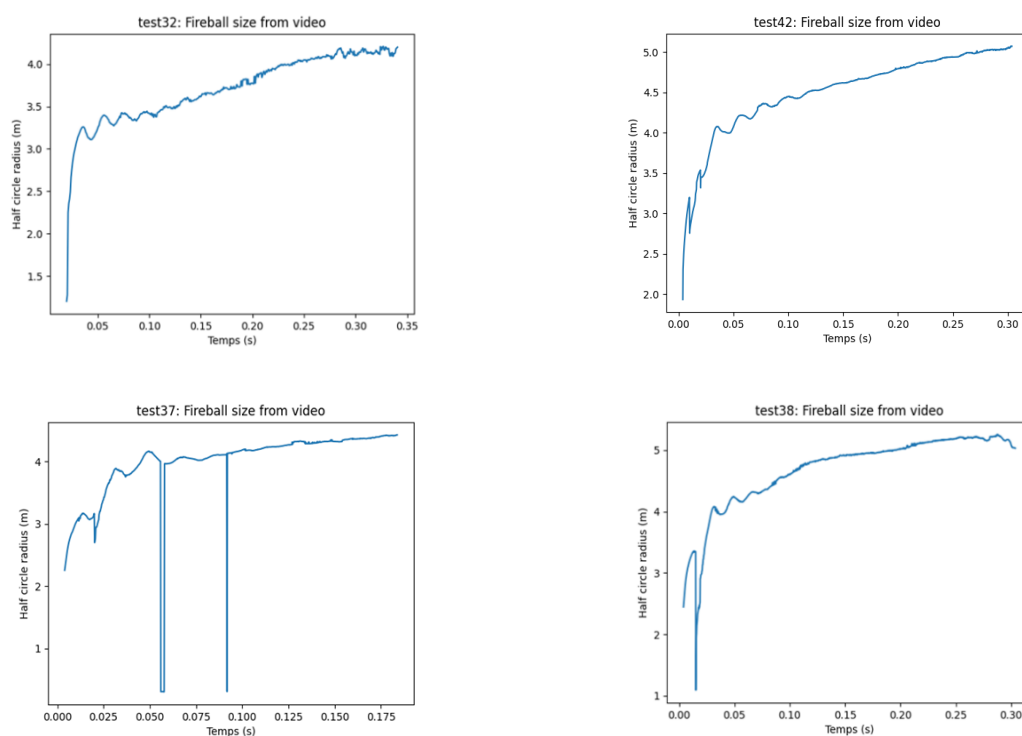


Figure 106. 2021 fireball tests: Evolution of the equivalent hemispherical radius.

The breathing of the fireball is observed on all the tests and the period tends to decrease with the increase of the mass contained in the tank (20 ms for the test 32). These values are lower

D4.3. Final report on analytical, numerical and experimental studies on explosions, including innovative prevention and mitigation strategies
than the one measured in 2020 (25 ms) with a tank containing a much lower mass of hydrogen. We also notice that the slower the global phenomenon the more pulses we can observe.

A photodiode was installed next to the camera about 100 meters from the explosion site. Its measured signal allows us to obtain the duration of the light emission by the fireball. The signal saturates very quickly (*Figure 107*) and desaturates at the end of the combustion. The duration of the presence of the fireball is of the order of a second in all the tests. If we keep the duration of the signal higher than 2V as a criterion, we obtain 1.070 s for the test 32, 1.303 s for test 42, 0.786 s for test 37, 0.672 s for test 38. The correlation with the inner pressure and the size of the tank is not straightforward.

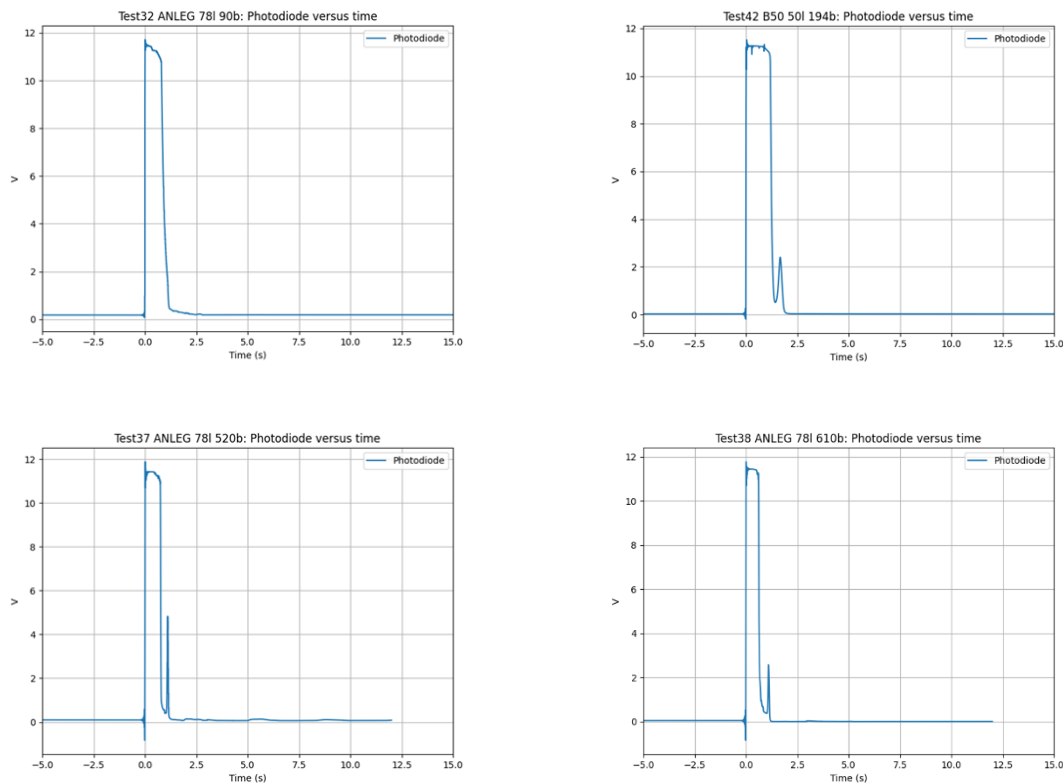


Figure 107. 2021 fireball tests: Photodiode measurements.

Note also the phenomenon observed in the four tests with the most hydrogen in the tank. A peak of intensity is recorded at the end of the combustion. We have no explanation for this.

A standard video camera (25 fps) was installed near the photodiode and the images recorded by this device (*Figure 108*) clearly show the light peak at the end of the combustion (920 ms). It is also surprising to see that a delayed light emission is also recorded between 2.4 and 2.9 seconds that would correspond to a re-ignition of the unburned hydrogen present in the tunnel by the shock wave reflected on the protective walls located at each exits.

D4.3. Final report on analytical, numerical and experimental studies on explosions, including innovative prevention and mitigation strategies

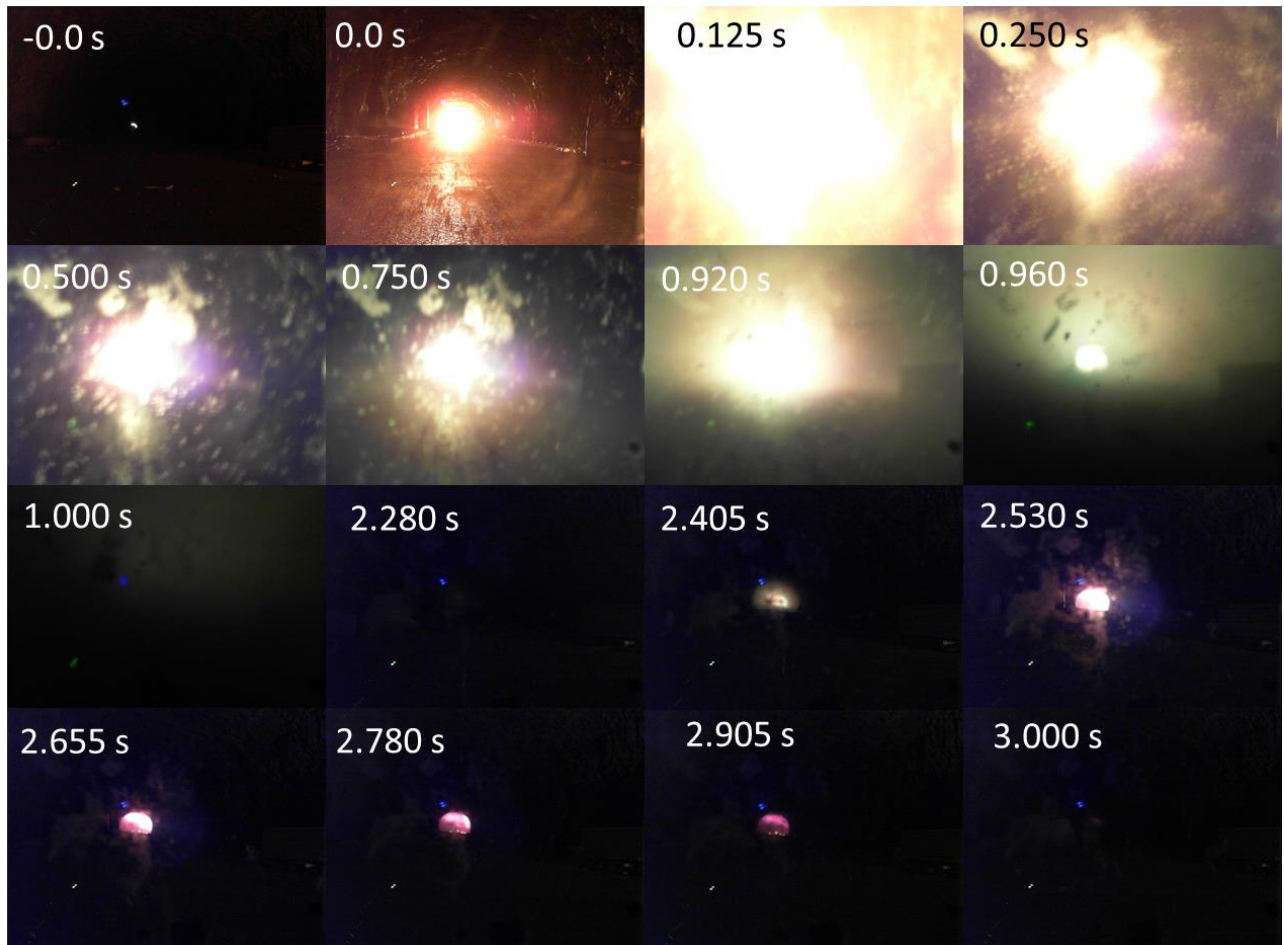


Figure 108. 2021 test 37: Video camera images.

The 2D ultrasonic anemometer was installed also nearby the photodiode. The recorded signal during three tests is presented in *Figure 109*.

Test 32

Test 42

Test 38

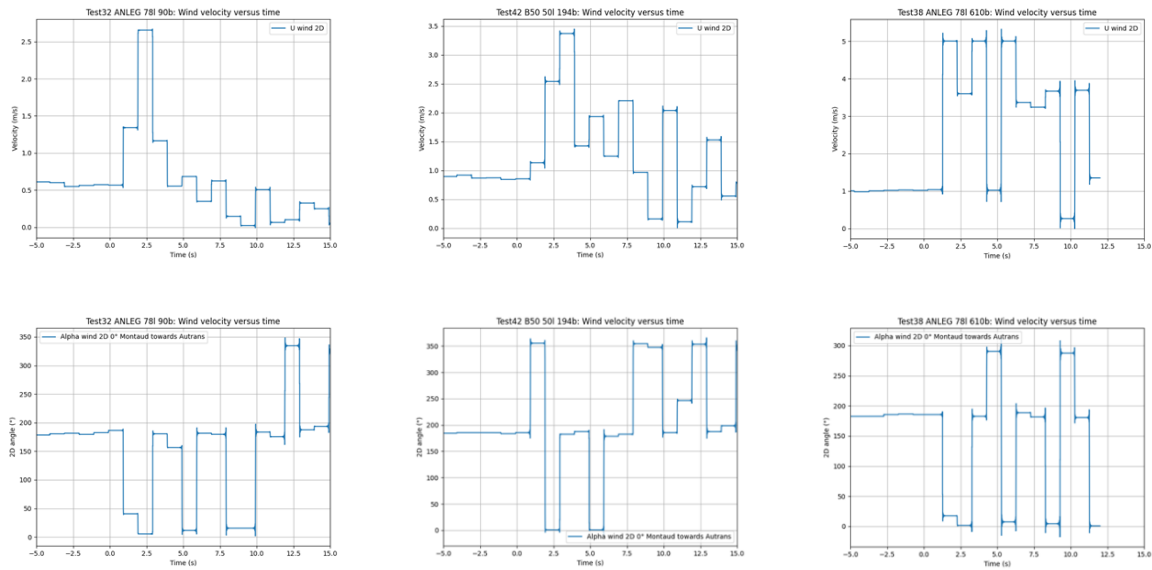
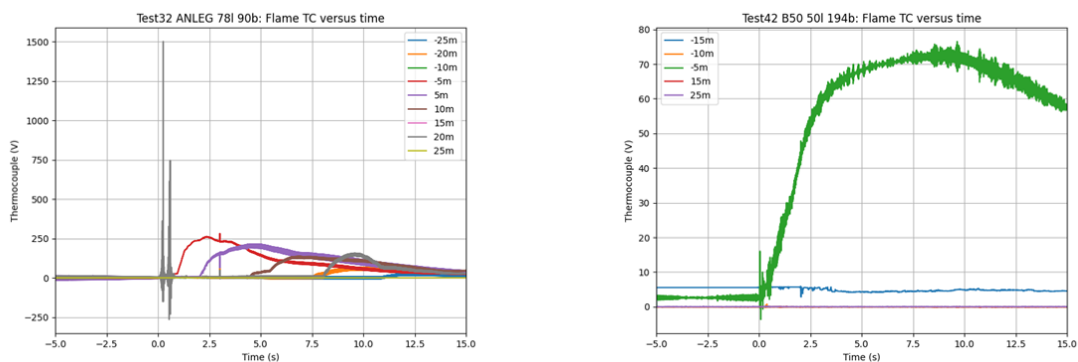


Figure 109. 2021 fireball tests: Ultrasonic anemometer measurements. Top velocity, Bottom Orientation.

This sensor is slow (~1 second response time) and we had calibrated it for a maximum speed of 5 m/s. Nevertheless, we note that after the initiation of the explosion, oscillations in the direction of the velocity are measured and that the characteristic time corresponds to the multiple reflections of the blast waves in the tunnel. The measured velocity increases with the violence of the explosion.

The measurements of the thermocouples (Figure 110) and ionization probes are unsatisfactory. They do not allow to obtain interesting information on the fireballs and these sensors were very quickly destroyed because of the violence of the explosions and their too weak robustness. We note only that during test 32 the thermocouples make it possible to measure the convection of the hot gas cloud on each side of the tunnel. In test 42, the fireball does not reach the wall, which is consistent with the images. Finally, in the last three tests, the thermocouple located at -5m shows that the fireball reaches the wall at this location, which is still consistent with the images.



D4.3. Final report on analytical, numerical and experimental studies on explosions, including innovative prevention and mitigation strategies

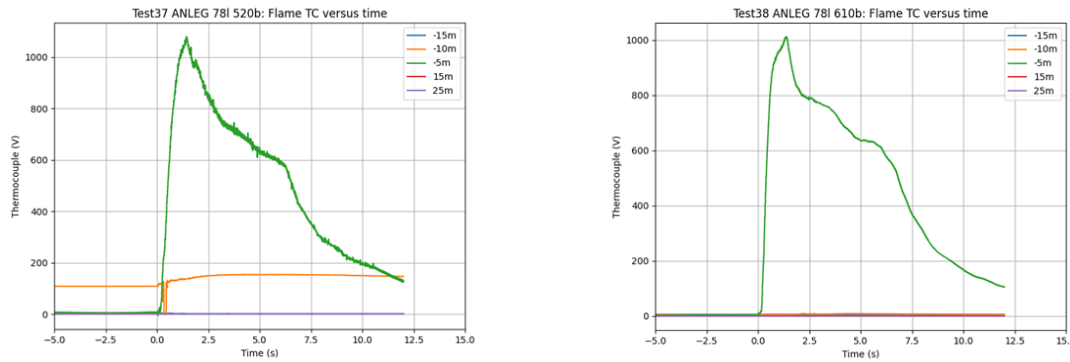


Figure 110. 2021 fireball tests: Thermocouple measurements.

4.1.9 Conclusions and recommendations

This document details the results obtained during explosion and fireball tests of pressurized tank filled with various pressure of hydrogen in the Mortier road tunnel. The main results show that:

- The morphology of the fireball inside the tunnel depends on the size and the pressure inside the tank.
- The breathing of the fireball supposed to be a consequence of shockwaves reflection is always recorded and the period of the oscillatory behavior decreases with the increase of the violence of the explosion.
- The predicted size of the fireball is in accordance with the correlation proposed by Zalosh et al for outdoor experiment.
- The duration of the fireball is also consistent with the correlation proposed by Zalosh et al. A peak of light intensity appears at the end of the combustion process during four tests, which is presently not explained. Secondary ignitions are also observed after pressure wave reflection.
- The sensors installed for the monitoring of fireballs failed early during the experiments. Consequently, no information on fireball velocity and the fireball stretching in tunnel axial direction can be obtained from those experiments.

These test results as well as those obtained during the 2020 campaign under 200 bar constitute a unique database for the understanding and validation of fireball models at the road tunnel scale.

4.2 Blast wave and fireball of tank rupture in tunnel: Experiments utilising the experimental tubular steel “explosion” tunnel (4.4.1, HSE)

4.2.5 Background

HSE, as part of its contribution to the HyTunnel-CS programme, will undertake a series of hydrogen ignition releases and explosion tests using its steel tunnel test facility, which is located on its test site at Buxton, Derbyshire, UK.

D4.3. Final report on analytical, numerical and experimental studies on explosions, including innovative prevention and mitigation strategies

4.2.6 Objectives

- To complete a series of scaled ignited releases of hydrogen from containment simulating the catastrophic failure of the pressure containment vessel.
- The foregoing releases to be undertaken using a vessel of up to 18 litre capacity with the releases being upwards from near ground level through a 100 mm diameter double bursting disc assembly, together with various levels of ventilation.
- To undertake a series of ignited scaled jet releases within the tunnel through blowing down a fixed capacity pressure vessel.
- The foregoing to be undertaken at different orientations and ventilation rates.
- To measure the pressure development, temperature, and associated flame speeds following ignition of the released hydrogen, for both the jet and catastrophic releases.
- To undertake two bonfire tests within the tunnel on a novel pressure vessel designed to leak but not burst.
- To generate from the foregoing test programme experimental data to support further development and validation of relevant physical models and risk assessment tools.

4.2.7 Description of test facilities

The experiments will be performed in the HSE test facility which consists of a circular steel tunnel; it is nominally 3.7 m in diameter and comprises 5 sections totalling 70 m in length. The central section is 8 m long and has a wall thickness of 55 mm. The outer sections have a wall thickness of 25 mm and together are approximately 31 m in length, each side of the central section. The central section is able to withstand static pressures up to 3 MPa. The outer sections are able to withstand static pressures up to 1.4 MPa. Both the central and outer sections can withstand higher dynamic pressures of at least 3 MPa resulting from a shock or blast wave travelling along the tunnel. The sections are aligned with each other to within the manufacturing tolerances, and the gaps between sections have been sealed to prevent any leakage of gas.

The tunnel enables the release of hydrogen from vessels simulating hydrogen storage in a typical fuel cell powered vehicle, i.e., with the capacity to store an appropriate quantity of hydrogen gas at pressures up to 70 MPa. The facility is equipped with the following ancillary equipment for the purpose of delivering the desired experimental objectives:

- axial fan,
- gas boosters,
- hydrogen storage tanks,
- gas release control system,
- sensors,
- data acquisition system.

There are two types of releases being undertaken, namely a blowdown release, representing the quasi-steady release through a pressure relief device and an instantaneous release, representing the catastrophic failure of the gas storage vessel. The amounts to be released and the rates of release were determined by consideration of full-size practical storage situations, scaled to our

D4.3. Final report on analytical, numerical and experimental studies on explosions, including innovative prevention and mitigation strategies
test tunnel. Two individual test vessels are used to store the hydrogen at pressures up to 700 bar.

The vessel used for the blowdown tests comprises three individual carbon fibre cylinders supplied by Luxfer, each with a capacity of 53 L and connected in parallel. To allow dispersion experiments, this blowdown vessel incorporates a suitably sized off-take to which a nozzle representing a TPRD or several TPRD's is attached.

The instantaneous release vessel was manufactured to our specification and has a total capacity of 18 L, but which can be reduced to a minimum of 5 L. It incorporates a double bursting disc assembly as a means of operation, thus allowing for the near instantaneous release of hydrogen gas, as required for HSE's contribution to this aspect of the research programme.

Both vessels are filled from standard hydrogen multi-cylinder packs, MCP's, and are operated remotely using an arrangement of commercially available control valves and gas boosters.

The whole of the tunnel floor has been concreted as this provides a secure mounting area for the instantaneous release vessel and for the scale models included in some of the tests. A metal plate has been secured directly under the vertically downwards pointing jet to act as a spreader plate for the jet during these tests, in order to prevent damage to the floor.

4.2.8 Scaling and accident scenarios assessed

The catastrophic releases are being undertaken using a 700-bar bespoke designed vessel with a capacity of between 5 to 18 litres. Its contents being released through a 100 mm diameter double bursting disc unit at an initial rate exceeding 200 kg/s. The initial shock wave is expected to develop an overpressure of some 55 bar with an initial velocity of about 2.3 km/s. Ignition may take place at the contact surface but if not, then an external ignition source will be provided. Examination of the ignition mechanism is being studied as part of the test programme, including delayed ignition.

Four scaled releases will be undertaken, characterised by the quantity released and the time scale of the releases. These will represent TPRD blowdowns from a representative car, bus and two trains as would occur in a typical full-sized tunnel. The actual representations have been derived following a study of the various accident scenarios. These have been scaled as described in the following sections using the method described by Hall and Walker (1997).

Based upon the accident scenario analysis carried out in HyTunnel-CS D1.3 (2019), we are proposing the following test programme for which the following assumptions are considered applicable:

1. In the case of normal TPRD operation in a fire, it is assumed that the total inventory is released through the TPRD's. All TPRD's opening at roughly the same time.
2. In the case of a spurious TPRD operation it is assumed that only one tank is involved.
3. In the case of TPRD malfunction it is assumed that only one tank will fail catastrophically in a fire.
4. A tunnel cross-sectional area is represented by a circle of the equivalent area.

D4.3. Final report on analytical, numerical and experimental studies on explosions, including innovative prevention and mitigation strategies

The hydrogen inventories carried by the three different types of vehicle, based on HyTunnel-CS D1.3 (2019), are as follows:

4.2.8.1 Car

Five makes of car were specified, all operating at 70 MPa. The hydrogen storage capacity of each car varies between 115 and 156 L, usually comprising two tanks, each of similar capacity. The average capacity is, therefore, taken to be 135 L, which is equivalent to a total mass of 5.4 kg hydrogen. The vent lines specified for the vehicles are usually between 2.0 mm and 4.0 mm in diameter, although a 4.2 mm diameter is used in some cases. The vent lines are directed downward from underneath the vehicle at 45 degrees backward. The TPRD diameter is quoted as 2.0 mm.

4.2.8.2 Bus

Three makes of bus are specified, all operating at 35 MPa. They use either four or nine roof mounted cylinders, each with a capacity between 74 and 205 L. Assuming an average of 210 L per tank in a four-tank pack, each containing 4.97 kg of hydrogen, gives a total capacity of around 40 kg. The vent line from the cylinders is directed upward from the top of the vehicle. The TPRD diameter is 3.3 mm and there are two fitted to each cylinder, giving a total of eight. Other buses have a slightly larger capacity with either 11 or 12 TPRD's fitted. Recently, Wrightbus have introduced a series of single decker buses with a hydrogen capacity of between 35-50 kg. In view of which we have used a 40 kg capacity (say five tanks) with ten TPRD's fitted as the basis for our modelling.

4.2.8.3 Train 1

Initially, only one make was considered, manufactured by GE Alstom. This is a two-carriage unit, each with 96 kg of hydrogen operating at 350 bar. Each unit has 24 cylinders each with a capacity of 175 L containing a total of 4.14 kg of hydrogen. We have assumed that only one carriage is involved in a fire. Each cylinder will have two TPRD's, diameter of 3.3 mm.

4.2.8.4 Train 2

A further model from the same manufacturer, GE Alstom, known as "Breeze", was also considered. This will carry a maximum total mass of 417 kg hydrogen at 350 bar pressure, contained in 72 cylinders, each with a capacity of 245 L. Each cylinder contains 5.8 kg of hydrogen and there are 36 cylinders in both the lead and trailing cars. We have assumed that only one carriage is involved in the fire, consequently the total inventory per car will be 209 kg. The tanks are arranged in cassettes, comprising nine tanks each. There are four cassettes per carriage, contained in a unit behind the cab. There are two cassettes on either side of the storage bay, assumed separated by a partition. Each cylinder has two TPRD's; hence each cassette has 18 TPRD's of 3.3 mm diameter. We assume that for modelling purposes only two cassettes (one side) would be involved in a fire. The inventory involved in a fire is therefore 105 kg with 36 TPRD's able to vent the inventory.

4.2.9 Tunnel scaling

Examples of the cross-sectional areas (area through which vehicles are travelling) of the various types of real-world tunnel considered in this scaling exercise are listed in Table 41 and Table 42 below.

D4.3. Final report on analytical, numerical and experimental studies on explosions, including innovative prevention and mitigation strategies

4.2.9.1 Road tunnels

Table 41. Examples of European road tunnels showing relevant geometry.

	Tunnel Description	Cross-section Area, CSA (m ²)	Equivalent Diameter, D (m)
1.	Single lane tunnel	24.10	5.54
2.	Double lane tunnel	39.50	7.09
3.	Gotthard tunnel, double lane	49.35	7.93
4.	Rennsteig tunnel, double lane	72.95	9.64
5.	Tyne tunnel (Original), double-lane	48.10	7.83
	Average (all tunnels)	46.80	7.61
	Average (double bore only)	52.48	8.12

4.2.9.2 Rail tunnels

Table 42. Examples of European rail tunnels showing relevant geometry.

	Tunnel Description	Cross-section Area, CSA (m ²)	Equivalent Diameter, D (m)
1.	High speed traffic, two rail	92.00	10.82
2.	Express traffic tunnel, two rail	79.20	10.04
3.	Metro type traffic, single rail	44.60	7.54
4.	Rectangular section urban rail, two rail	56.30	8.47
5.	Severn tunnel, two rail	60.00	8.74
6.	Channel tunnel single bore, single rail	53.50	8.25
	Average (all tunnels)	64.27	8.98
	Average (double-bore only)	71.88	9.52

4.2.9.3 HSE Buxton test tunnel

Relevant information on the geometry of the HSE Buxton test tunnel is given in Table 43 below.

Table 43. Geometry of the HSE Buxton test tunnel.

Radius	1.85 m
Depth of ballast	0.45 m
Area of segment containing ballast	0.75 m ²
Circular area of tunnel (no ballast)	10.75 m ²
Area through which vehicles travel	10.00 m ²
Equivalent diameter, D _{HSE}	3.57 m

4.2.10 Scaling criteria

An exercise to determine suitable scaling criteria was undertaken, full details of which can be found in Appendix A1. The applicable scaling criteria from that study are shown in Table 44.

D4.3. Final report on analytical, numerical and experimental studies on explosions, including innovative prevention and mitigation strategies

Table 44. Scaling factors to be applied for tests carried out at HSE Buxton.

Scaling factor, H, for tunnel diameter	D/D_{HSE}
Scaling factor for mass of stored hydrogen	H^3
Scaling factor for the mass flow rate	$H^{5/2}$
Scaling factor for the discharge time	$H^{1/2}$
Scaling factor for the airflow in the tunnel	$H^{1/2}$

Based on the tunnel geometry data in Table 41 and Table 42, average scaling factors for the two tunnel types (All tunnels, Double bore only) were obtained and then used to establish the scaled inventories for a car, bus and train in the relevant tunnels. Examples of calculated scaling factors are shown below and the complete calculation results, showing the scaling factor and the resulting scaled inventory for all 4 vehicle types, are shown in Table 45.

Examples:

Equivalent diameter of an average double bore road tunnel = 8.12 m, therefore:

$$H = \frac{D}{D_{HSE}} = \frac{8.12}{3.57} = 2.275$$

Equivalent diameter of an average double bore road tunnel = 9.52 m, therefore:

$$H = \frac{D}{D_{HSE}} = \frac{9.52}{3.57} = 2.665$$

D4.3. Final report on analytical, numerical and experimental studies on explosions, including innovative prevention and mitigation strategies

Table 45. Scaled hydrogen inventories for cars, buses and trains (values highlighted in bold i.e. double-bore only, are those to be used for the actual modelling exercise).

	Total Vehicle Inventory (kg)	Single Tank Inventory (kg)	Average scaling Factor, H	Average Mass Reduction (%)	Scaled Total Inventory (kg)	Scaled Inventory Single Tank (kg)
Car (700 bar)						
All Tunnels	5.4	2.7	2.13	10.35	0.56	0.28
Double bore only	5.4	2.7	2.275	8.49	0.46	0.23
Bus (350 bar)						
All Tunnels	40.0	4.97	2.13	10.35	4.14	0.51
Double bore only	40.0	4.97	2.275	8.49	3.40	0.42
Train 1 (350 bar)						
All Tunnels	96.0	4.14	2.513	6.30	6.05	0.26
Double bore only	96.0	4.14	2.665	5.28	5.07	0.22
Train 2 (350 bar)						
All Tunnels	105.0	5.80	2.513	6.30	6.62	0.37
Double bore only	105.0	5.80	2.665	5.28	5.54	0.31

4.2.11 Test rig for scaled releases

For the purpose of providing a test rig with suitable capacity to carry out the range of proposed tests, commercially available off-the-shelf cylinders will be used. These will be 700 bar cylinders, each with a 53 L capacity, designed specifically for hydrogen. It is expected that up to 3 of these cylinders, manifolded together to provide capacities between 53 L and 159 L, will be used.

The vessel inventories were scaled to match these volumes and were calculated, along with orifice diameters and mass flow rates, using the suite of programmes available at: <https://elab-prod.iket.kit.edu/>. The scaled values obtained are given in Table 46. The first four rows show the scaled inventories at 700 bar, for cars, and 350 bar, for buses and trains. The second four, highlighted in bold, give the values adjusted to the rig storage volume(s) of 53 L and 159 L.

D4.3. Final report on analytical, numerical and experimental studies on explosions, including innovative prevention and mitigation strategies

Table 46. Correlation of proposed hydrogen to actual tank inventories.

	Total Scaled Inventory (kg)¹	Pressure (bar)	Tank Volume (litres)	Single Tank Scaled Inventory (kg)¹	Pressure (bar)	Tank Volume (litres)
Car	0.46	700	12	0.23	700	6
Bus	3.40	350	145	0.42	350/700	18/11
Train 1	5.07	350	215	0.22	350/700	10/5
Train 2	5.54	350	251	0.31	350/700	13/8
Car	0.46	118	53	0.23	300	11
Bus	3.40	310	159	0.42	700	11
Train 1	5.07	510	159	0.22	290	11
Train 2	5.54	580	159	0.31	450	11

From the literature, the typical TPRD orifice sizes for cars, buses and trains are 2.0 mm, 3.3 mm and 3.3 mm respectively. Furthermore, cars have 2 cylinders; buses have 8 to 12 cylinders and trains have 18 to 24 cylinders. It is assumed in a fire scenario; the total inventories are discharged with all TPRD's open at the same time. The calculated equivalent diameter for this combined discharge area of the TPRD's is shown in Table 47 for each vehicle type.

¹ Scaled tank inventories from Table 45

D4.3. Final report on analytical, numerical and experimental studies on explosions, including innovative prevention and mitigation strategies

Table 47. Equivalent diameter of TPRDs on cars, buses and trains.

Orifice Dia. (mm) Single TPRD	Car: 2 TPRDs Equivalent diameter	Bus: 10 TPRDs Equivalent diameter	Train 1 48 TPRDs Equivalent diameter	Train 2 36 TPRDs Equivalent diameter
2.0 mm	2.83 mm	-	-	-
3.3 mm	-	10.44 mm	22.86 mm	19.80 mm

Using the above calculated equivalent diameters, the initial mass flow rates, and discharge times (to choke point) are obtained for the actual full-size inventories as shown in Table 48.

D4.3. Final report on analytical, numerical and experimental studies on explosions, including innovative prevention and mitigation strategies

Table 48. Initial mass flow rates and discharge times for full size and for scaled inventories.

	Total Inventory (kg)	Initial mass flow rates (kg/s)	Discharge times (secs)	²Scaled total inventory (kg)	Scaled initial mass flow rates (kg/s)	³Scaled discharge times (secs)	⁴Scaled orifice dia's used (mm)
Car 700 bar	5.4 (135 L)	0.215	168	0.46 (12 L)	0.0275	120 (111)	1.0
Bus 350 bar	40.0 (1700 L)	1.638	134	3.40 (145 L)	0.21	86 (89)	3.8
Train 1 350 bar	96.0 (4050 L)	7.85	67	5.07 (215 L)	0.677	41 (41)	6.7
Train 2 350 bar	105.0 (4450 L)	5.89	97	5.55 (235 L)	0.508	60 (60)	5.8

NB: The approach used is equally valid for other orifice sizes other than those used here.

If using standard 53 L size cylinders, then we can model the foregoing using different pressures but fixed volumes (multiples of 53 L) to give the same initial mass flow rates as shown in Table 49.

As an example, the jet from a car cylinder at 700 bar pressure with an orifice diameter of 1.0 mm is the equivalent of releasing at 118 bar through a 2.2 mm diameter nozzle, given the same initial mass flow rates. This is because the fully expanded jets, in both cases, have an initial fully expanded diameter of 16.8 mm at atmospheric pressure and thereafter, they both

² Numbers in brackets are the volumes in litres required for the inventory at the pressures shown at the start of each row

³ The values in brackets are those obtained from scaling the discharge time values shown in column three

⁴ These are the orifice diameters needed to give the correct scaled initial mass flow rates

D4.3. Final report on analytical, numerical and experimental studies on explosions, including innovative prevention and mitigation strategies

behave in the same manner, namely as a free turbulent jet, for which the decay characteristics are well documented in the literature.

Table 49. Scaled orifice size for experimental releases.

	Scaled total inventory (kg)	Scaled initial mass flow rates (kg/s)	Discharge times (s)	Scaled orifice diameters used (mm)
Car 118 bar	0.46 (53 L)	0.0275	70	2.2
Bus 310 bar	3.40 (159 L)	0.21	83	4.0
Train 1 510 bar	5.07 (159 L)	0.677	46	5.7
Train 2 580 bar	5.55 (159 L)	0.508	69	4.7

4.2.12 Scaling of airflow in HSE tunnel

HyTunnel-CS Deliverable D1.2, makes recommendations for the maximum required ventilation velocity in actual tunnels. This is stated to be 3.5 m/s based on physiological and fire-fighting needs. Based on this information, deliverable D1.3 has recommended a range of tunnel ventilation velocities for study: 1, 2, 3.5 and 5 m/s.

These values correspond to actual full-scale tunnel ventilation velocities and, according to the scaling rules which are being adopted, should be modified in line with the HSE tunnel being studied.

Based on the 11 tunnel examples (Table 41 and Table 42), the average scaling factor (H), for both road and train tunnels over the HSE tunnel has been shown to be 2.275 and 2.665 respectively (Table 45).

Scaling analysis (Appendix A1), which aims to match hydrogen / air buoyancy and ventilation dynamic head in real tunnels, with that in the HSE tunnel, concludes that the ventilation velocity (U) should scale according to:

$$U_{\text{actual}}/U_{\text{HSE}} = H^{1/2} \quad (61)$$

Applying this scaling criterion to the scaling factors (H) of 2.275 and 2.665, results in the HSE tunnel ventilation velocities shown in Table 50.

D4.3. Final report on analytical, numerical and experimental studies on explosions, including innovative prevention and mitigation strategies

Table 50. Scaled ventilation velocities in HSE tunnel.

Actual tunnel ventilation velocity (m/s)	HSE ventilation velocity (m/s)	
	Scale factor 2.275 (Car/Bus)	Scale factor 2.665 (Train)
1	0.66	0.61
2	1.33	1.22
3.5	2.32	2.14
5	3.31	3.06

4.2.12.1 Test programme

The first requirement of the test programme is to repeat the blowdown tests of HyTunnel-CS deliverable D2.1 but with immediate and delayed ignition of the releases. There will be 8 tests without the scaled models being present. The modelling work undertaken by both KIT and NCSRD will be used to give guidance regarding the initial cloud spread and hence, the ignition delay and ignition location. These tests will be done immediately after the un-ignited releases of HyTunnel-CS deliverable D2.1, without the scaled models in the tunnel and in the absence of the concentration sensors. These tests will then be repeated with the scaled models in the tunnel, giving a total of 16 tests.

A test will be carried out to look at single tank (spurious) releases, but this may not be necessary, as the largest single tank has almost the same capacity as the total release for a car, which is already planned. One test will cover this requirement.

There is a requirement to do some releases in the crown of the tunnel, having seen the modelling results which show that buoyancy has a major influence on the movement of hydrogen into the crown of the tunnel; we believe that the already planned ignited releases will also satisfy this requirement. If not, then one or two horizontal releases near the tunnel crown could be considered, with a maximum of two releases with and two without the models being present.

The instantaneous releases using the 18 L vessel, will provide data on blast / sound wave attenuation along the tunnel, which can be scaled up to full size tunnels using Sachs scaling. This includes verifying modelling of blast wave propagation along a tunnel with and without obstructions (scale models) being present. They will also enable us to examine visually the initial release behaviour, in particular auto-ignition at the contact surface. This is important as it is a basic tenet of the Ulster blast wave modelling. In practice there are four basic release scenarios all at 700 bar with quantities varying from 5 to 9 L. Wind speed is not thought to be a significant factor, so suggest use only one, the highest, or alternatively rely on the natural ventilation, as less risk of damaging the fans. The test results are likely to vary, therefore we will carry out two repeats for each test, making a total, with and without models, of no more than 18 tests.

In addition, a further four tests will be undertaken to look at the initial combustion behaviour; together with two further tests where the releases are done under a scaled car. Finally, two further tests will be undertaken using the full 18 L capacity of the test vessel, to extend the test envelope. The total number of tests for all this work would be 26 tests.

D4.3. Final report on analytical, numerical and experimental studies on explosions, including innovative prevention and mitigation strategies

Table 51. Proposed matrix of tests.

	Car		Bus		Train 1		Train 2	
Hydrogen quantity (kg).	0.45		3.40		5.07		5.55	
Orifice diameter (mm).	2.2		4.0		5.7		4.7	
Tunnel airflow (m/s)	1.25	2.4	1.25	2.4	1.25	2.4	1.25	2.4
Jet orientation.	D	D	U	U	U	U	U	U

4.2.13 Expected results

Pressure and heat flux profiles, together with flame speeds along the tunnel will be obtained for the various test conditions proposed. These are the four scaled vessel blowdowns, nozzle orientations and the ventilation flow velocities, together with the test results from the catastrophic releases.

Due to the COVID-19 outbreak and subsequent restrictions placed on businesses within the UK it has not been possible to complete work to the originally planned timescale. At the time of writing, the work to build and commission the test rig is complete and testing is due to commence in early March 2022. The experimental work is expected to be completed by the first week in June 2022. The timeline for the programme is detailed in Table 52.

All work that has been delayed will be captured and reported in the added deliverable D4.4. *Results of the deferred experimental programme and associated activities* and is due for completion by M41 (July 2022).

Table 52. Timeline of pre-test and experimental delivery activities.

<i>Blast wave and fireball of tank rupture in tunnel: Experiments utilising the experimental tubular steel “explosion” tunnel (HSE)</i>	<i>Due date</i>	<i>Report at project meeting (PM)</i>
Complete design, build and commissioning of test facility	M33	7th PM - Feb '22 (M36)
Commence test programme	M36	8 th PM – Jul '22 (M41)
Final results and conclusions for recommendations	M40	8 th PM – Jul '22 (M41)

4.3 Pressure decay after Hydrogen Tanks explosion tests in a full-scale tunnel

4.3.1 Introduction

Several pressurized tank rupture experiments have been conducted by CEA in June 2021 inside the Tunnel du Mortier located in the commune of Autrans in the Vercors, France. The tests can be divided into 3 categories: pressurized hydrogen gas tank rupture, pressurized helium tank rupture and a fragment of a tank rupture with a detonation belt (DB).

D4.3. Final report on analytical, numerical and experimental studies on explosions, including innovative prevention and mitigation strategies

The relevant information regarding the test geometry, the detail of injection, the type of sensors as well as their locations are provided in some separate documents:

- For pre-tests of 2020:
Sauzedde et al, 2020. *CEA Experimental devices Pre-tests of 2020*.
- For the tests 2021:
Sauzedde et al, 2021. *CEA Experimental devices Tests of 2021*.

This section is organized as follows. In Subsection 2, the geometry of the Tunnel, the tanks used for explosion tests, the pressure measurement devices as well as the test matrix are described. The test results are provided in Subsection 3, where maximum measured overpressure values are given for each test. These values are used for comparisons with an available universal correlation in Subsection 4. Some conclusions and recommendations follow.

4.3.2 Tunnel geometry, Measurement Devices and Experimental Matrix

The Tunnel du Mortier is 507 m long and is a disused straight road tunnel in the shape of a horseshoe (*Figure 111*). On the entrance (on Autrans side) the vault is concreted (Images 1 and 2) while the inside of the tunnel is in rough rock image 3 and 4). The concrete section is 133 m long, 7.5 m wide and 5.2 m high. The rocky area represents the rest of the length with a width of 8.9 m and a height of 5.6 m. The slope is 3.6% and there is no mechanical ventilation. Finally, another concrete section is located at the exit of the tunnel. The cross-section area in the “rock” part of the tunnel is approximately 41.3 m^2 while in the concrete part it is 33.0 m^2 .

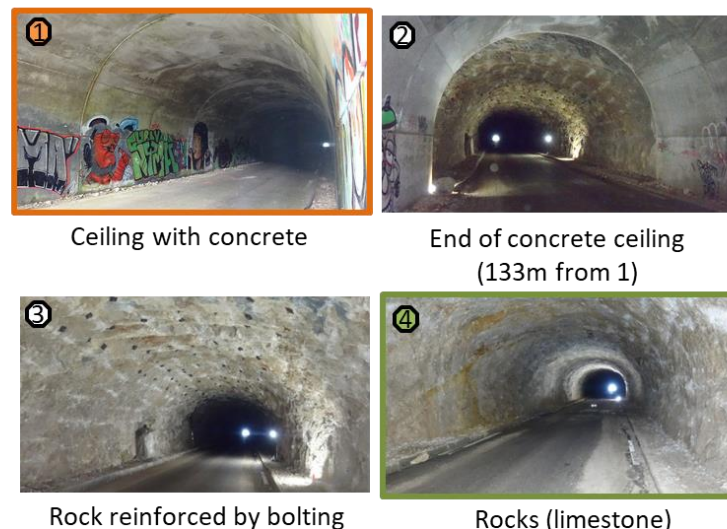


Figure 111: Tunnel geometry.

All explosion tests were performed in the tunnel du Mortier at a distance of 220 m from the main entrance on the Autrans side. Two straw walls were installed at each end of the tunnel to limit natural convection and to quench the pressure waves.

In order to capture the pressure waves during the explosion tests, seven PCB blast wave pencils were arranged in the tunnel at distances of 30 m, 50 m, 80 m, 110 m, 140 m, 170 m and 200 m from the tank (*Figure 112*, left, Table 53). These sensors are mounted on tripods approximately 70 cm above the ground (*Figure 112*, right). We mention that the pressure transducer at 200 m

D4.3. Final report on analytical, numerical and experimental studies on explosions, including innovative prevention and mitigation strategies

did not function properly during the tests and all the measurements from this transducer, apart from one measurement, were disregarded. The blast wave pencil installed at 80 m from a tank is equipped with two pressure transducers, denoted P3A and P3B in Table 53. They are mounted 10 cm apart to monitor the velocity of the blast waves.

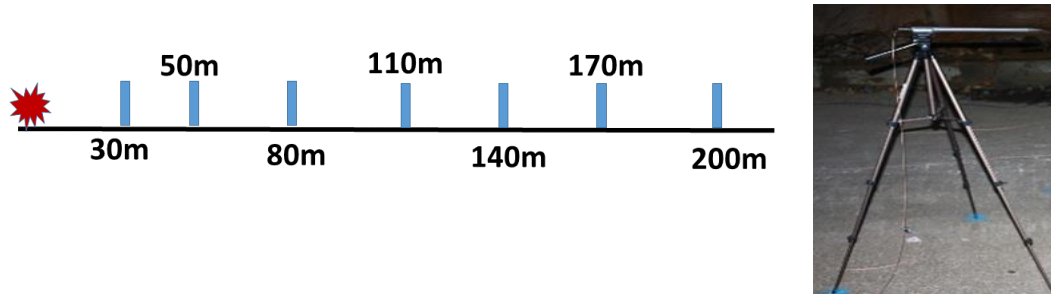


Figure 112 : Scheme of installation of blast wave pressure transducers (left) and photo of a PCB blast wave pencil.

Table 53. Blast wave sensors positions

Sensor	X (mm)	Y (mm)	Z (mm)
P1A	0	30000	685
P2A	0	50000	685
P3A	0	80000	685
P3B	0	80000	685
P6A	0	110000	685
P7A	0	140000	685
P8A	0	170000	685
P5A	0	200000	685

In some experiments presented in the literature (Zalosh & Wayandt, 2005), the tank is set on fire and if there is no depressurization means, the tank ends up exploding. To simplify the procedure and guarantee reproducibility, we have chosen to open the pressurized tank using a detonation belt of RAZOR type. This belt is located at the middle of the tank and a small sphere of explosive initiates its explosion (*Figure 113*). As far as possible, we tested the tanks with two different gases: helium or hydrogen. Systematically, for each tank, after the first explosion we kept a fragment and re-tested it with the detonating belt alone to measure its contribution. Type 2 and 4 tanks were used for these tests with different inner volumes (Table 62, *Figure 113*).

D4.3. Final report on analytical, numerical and experimental studies on explosions, including innovative prevention and mitigation strategies



Figure 113 : Tanks used for explosion experiments: TYPE II (left) and TYPE IV (right). The detonation belt is attached to each of the tanks.

Table 54. Specifications of Pressurized Tanks used in explosion tests

Tank name	Tank Volume (l)	Tank Masse (kg)	Tank length / ext. diameter (m)
TYPE II	50	60.5	1.45 / 0.3
TYPE IV	78	64.6	0.96 / 0.44

The Test Matrix is presented in Table 66. Two tests have been performed with helium gas inside (Test 30 and Test 34), four tests with hydrogen filled tanks (Tests 32, 42, 37, 38) and two tests with tank fragments (Tests 31 and 32). The hydrogen gas pressure varied between 90 bar and 610 bar. The detonation belt charge is kept constant for each Tank type, its energy is given in TNT equivalent units, i.e., 130 g for TANK II and 228 g for TANK IV (the Test 37 was performed with slightly lower charge, 221 g TNT). The outside air temperature was close to 15°C for all explosion tests. In the 2021 test series, data were lost during test 35.

D4.3. Final report on analytical, numerical and experimental studies on explosions, including innovative prevention and mitigation strategies

Table 55. Test Matrix

Test N°	Tank	Gas	Pressure (bar)	Detonation belt charge (g, TNT)	Temperature, °C
31	TYPE II (frag.)			130	
33	TYPE IV (frag.)			228	
30	TYPE II	He	185	130	15
34	TYPE IV	He	650	228	15
32	TYPE IV	H ₂	90	228	15
42	TYPE II	H ₂	194	130	15
37	TYPE IV	H ₂	520	221	15
38	TYPE IV	H ₂	610	228	15
35	TYPE IV	H ₂	580	NA	NA

4.3.3 Test results

The sample rate for all pressure transducers was 200 kHz. A pressure signal contains a certain amount of noise, which is manifested itself by high frequency oscillations. These oscillations could be due to acoustic waves inside the metallic structures supporting the pressure transducers as well as the acoustic waves propagating inside the tunnel solid floor. The “useful” oscillation frequencies are those related to acoustic/shock waves propagating through the tunnel atmosphere. The speed of these waves (see *Figure 114*) was close to 350 m/s. We remind that the tunnel width and height in the zone near the explosion are 8.9 m and 5.6 m, respectively. This gives us time scales of 51 ms and 32 ms corresponding to the times necessary for the acoustic waves to travel back and forth either between lateral walls or between the ceiling and the floor of the tunnel. These would correspond to oscillating frequencies of 20 Hz and 31 Hz, respectively. The pressure transducers were located midway between lateral walls of the tunnel, which means that the related frequency recorded by the transducers is close to 40 Hz.

We performed a Fourier transform of the pressure signals and, as an example, the related magnitude spectrum is presented in the *Figure 114* (right). One can see that the well-defined peak is present, corresponding to frequencies of around 40-50 Hz. Each pressure signal has been filtered using 4th order Butterworth low-pass filter with cut-off frequency of 100 Hz. The raw and filtered pressure signals recorded by transducer P1 are shown in *Figure 114* (left). In what follows, we shall present only filtered signals for all tests.

D4.3. Final report on analytical, numerical and experimental studies on explosions, including innovative prevention and mitigation strategies

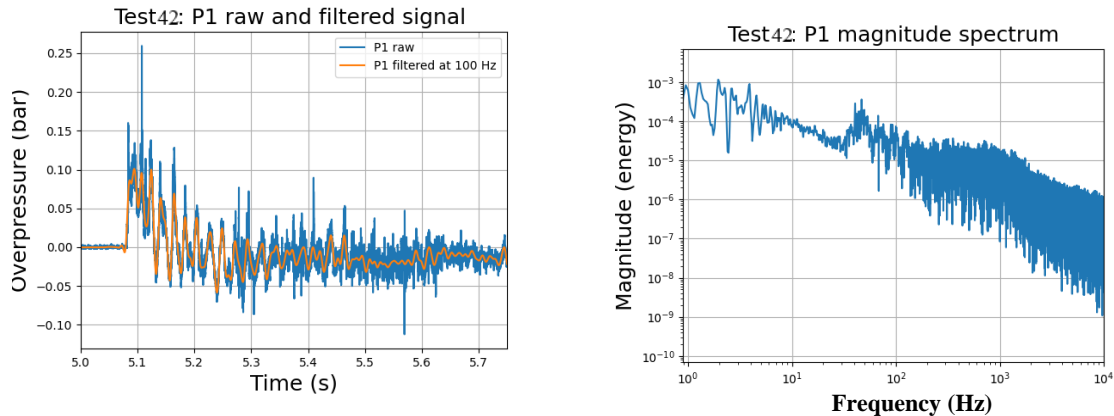


Figure 114 : Test 42. Raw and filtered pressure signal at P1 (left, 30 m from explosion) and the magnitude spectrum of the pressure signal (right).

Overpressure signals for Test 31 and Test 33 (Tanks fragment)

On Figure 115 and

Figure 116 we present the pressure evolution with time at different distances for the Test 31 and the Test 33, respectively. Three observations can be made:

First, we can separate the blast wave run-up distance on Zone 1, where pressure signals are dominated by reflections, and Zone 2, where the planar structure of the blast wave is observed, in the spirit of numerical observations reported in (Molkov & Dery, 2020). The transducers P1 (30 m), P2 (50 m) and P3 (80 m) are located in the Zone 1, while P6 (110 m), P7 (140 m) and P8 (170 m) - in the Zone 2. At a certain distance from the explosion, somewhere between 80 m and 100 m the secondary waves coalesce with the leading front and the resulting blast wave propagating as a planar structure.

Second, the pressure signal propagates with velocity close to 350 m/s which is slightly higher than the acoustic velocity, equal to 341 m/s ($T = 15^\circ\text{C}$).

Third, some non-physical oscillations are observed on the signals corresponding to the transducers P6 (110 m), P7 (140 m) and P8 (170 m). After additional analysis, these oscillations have been attributed to the perturbations created by the blast wave on the instrumentation box. This box, containing the recording equipment, was located approximately at 70 m from the explosion for initial few tests and at 100 m from the explosion, for the rest of the tests.

D4.3. Final report on analytical, numerical and experimental studies on explosions, including innovative prevention and mitigation strategies

Test 31 (TYPE II, frag.): Overpressure evolutions

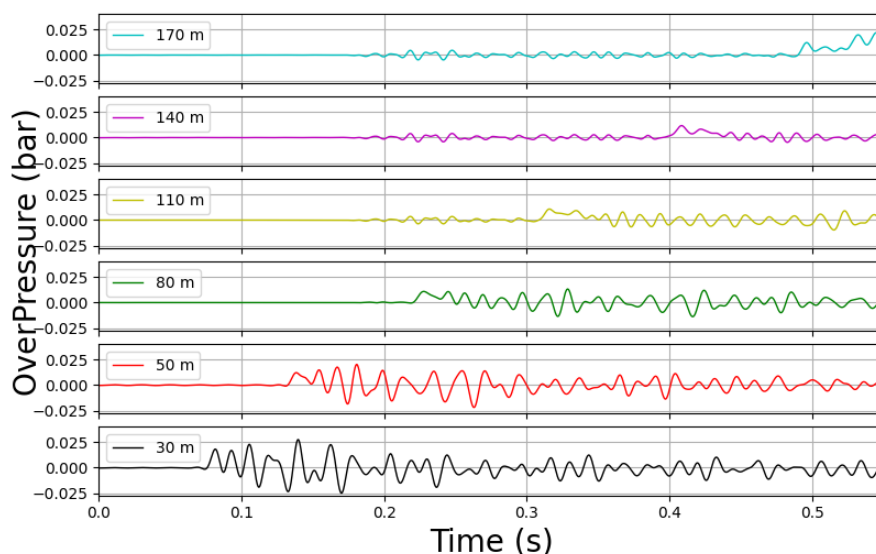


Figure 115: Test 31. DB of 130 g TNT. Overpressure evolutions at different distances.

The maximum pressure levels measured at the first pressure peak are reported in Table 67. We can observe that the maximum pressure attenuation with distance is limited due to focalisation of the blast wave energy along the tunnel. We mention that at 87 m from the explosion, the cross-section area of the tunnel diminishes from 41.3m^2 down to 33m^2 . This could explain the maximum pressure increase measured by the transducers located after that distance. Overall, almost all the maximum overpressure levels are lower than 20 mbar, which is considered as the threshold for indirect effects with respect to human health.

Test 33 (TYPE IV, frag.): Overpressure evolutions

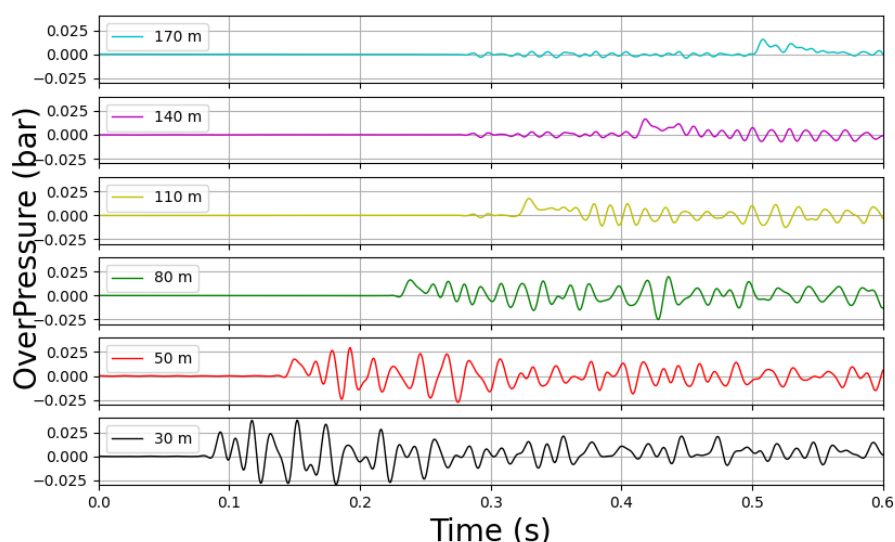


Figure 116: Test 33. DB of 228 g TNT. Overpressure evolutions at different distances

D4.3. Final report on analytical, numerical and experimental studies on explosions, including innovative prevention and mitigation strategies

Table 56. Tests 31-33 (fragments). Maximum overpressures recorded at different distances

Test	ΔP (mbar) @ 30 m	ΔP (mbar) @ 50 m	ΔP (mbar) @ 80 m	ΔP (mbar) @ 110 m	ΔP (mbar) @ 140 m	ΔP (mbar) @ 170 m
31	17.9	12.1	10.8	10.7	11.6	12.1
33	25.4	17.5	16.3	17.4	16.5	15.7

Overpressure signals for Test 30 and Test 34 (Tanks filled with Helium)

On Figure 117 and Figure 155 we present the pressure evolution with time at different distances for the Test 30 and the Test 34, respectively. These tests correspond to the pressurised helium tank rupture; thus, only mechanical energy input into the overpressure evolution is considered. The observations made in the previous paragraph are valid here as well. The pressure oscillations, at distances 30 m and 50 m from explosion, are of relatively high amplitude and some of the pressure peaks at later times are higher than the first pressure peak. Those pressure peaks must be considered with caution, as they could be the results of reflected pressure due to secondary waves propagation, and not the result of side-on pressure record. We deliberately cut the pressure signal P8 (170 m) (see Figure 155) due to the non-physical behaviour of the signal; the transducer falls due to explosion.

The maximum pressure levels measured at the *first* pressure peak are reported in Table 56 . We can observe, as before, that the maximum pressure attenuation with distance is limited due to focalisation of the blast wave energy along the tunnel. Overall, all the maximum overpressure levels are lower than 50 mbar, which is the threshold for irreversible effects with respect to human health (Test 30), and 140 mbar, representing the threshold for the first lethal effects (Test 34).

Test30(TYPE II He): Overpressure evolutions

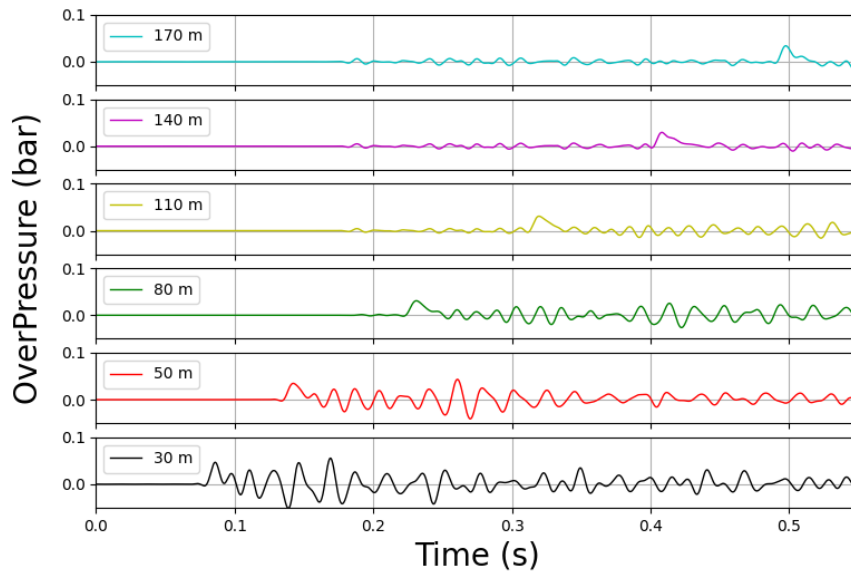


Figure 117: Test 30. He 185 bar, 50L Type II tank. Overpressure evolutions at different distances

Test34(TYPE IV, He): Overpressure evolutions

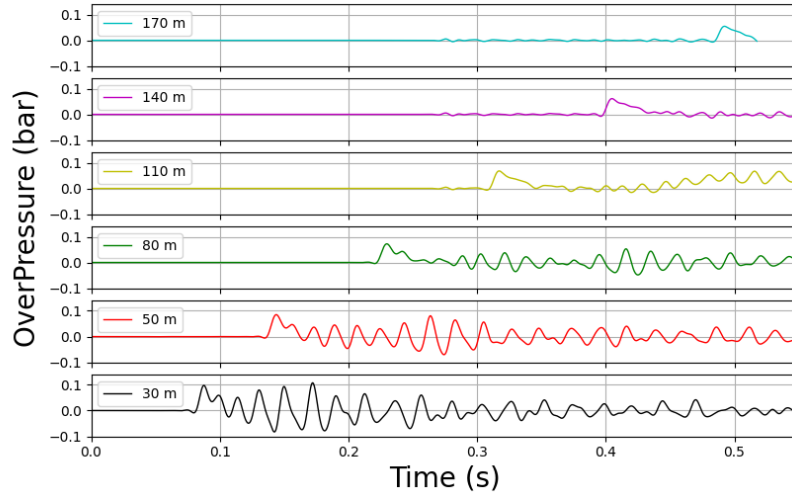


Figure 118: Test 34. He 650 bar, 78L Type IV tank. Overpressure evolutions at different distances.

D4.3. Final report on analytical, numerical and experimental studies on explosions, including innovative prevention and mitigation strategies

Table 57. Tests 30-34 (Helium tanks). Maximum overpressures recorded at different distances

Test	ΔP (mbar) @ 30 m	ΔP (mbar) @ 50 m	ΔP (mbar) @ 80 m	ΔP (mbar) @ 110 m	ΔP (mbar) @ 140 m	ΔP (mbar) @ 170 m
30	46.5	34.7	30.7	30.9	29.5	34.0
34	98.0	85.0	72.4	68.0	61.2	54.6

Overpressure signals for Test 32, 42, 37 and 38 (Tanks filled with Hydrogen)

On Figure 119 to Figure 122, we present the pressure evolution with time at different distances for the Tests 32, 42, 37 and 38, respectively. These tests correspond to the pressurised hydrogen tank rupture; thus, not only mechanical energy, but also chemical energy input into the overpressure evolution is considered. The observations made in the previous paragraph are valid here as well. As in the case with pressurized helium tanks, we deliberately cut some pressure signals (see Figure 119 to Figure 122) due to non-physical behaviour; the corresponding transducers fall due to explosion. In all Figures we show the zoomed part of the pressure signals near the first pressure peak.

In Figure 12 (bottom) we present the complete signal corresponding to the Test 38. We can see that the low frequency oscillations persist around zero value; they correspond to the acoustic waves travelling back and forth between two straw walls. The second pressure spike at approximately 1 second of the pressure signal at P7-140 m (red curve on Fig. 12, bottom) corresponds to the reflection of the blast wave from the straw wall closest to the Autrans entry.

Different behavior of the pressure peaks at close distances to the explosion point can be observed, in comparison to the previous tests. We can see that the first peak is not well defined; there are double or, sometimes, triple small peaks on the top of the main “global” peak. Moreover, the first small peak is not the highest one; very often, the second small peak has a higher value.

This behavior can be explained by recording of multiple pressure reflections or by initial liberation of chemical energy, or both. In the Figure 123 we present a sketch describing propagation of pressure waves due to explosion. A pressure transducer located at distance L from the explosion will record the first pressure peak at time t_L , corresponding to the shortest distance between the explosion and the transducer. Another pressure peak will be recorded when the blast wave, travelling upwards, hits the ceiling and is reflected towards the transducer via diagonal D at time t_{H+D} . Considering the averaged blast wave velocity of 350 m/s, we can readily compute the time difference (62) for a particular distance L .

$$\Delta t = t_{H+D} - t_L \quad (62)$$

This gives us a times scale: $\Delta t_{30m} = 17 \text{ ms}$, $\Delta t_{50m} = 16.6 \text{ ms}$. The measured time difference between the consecutive small peaks was close to these values.

D4.3. Final report on analytical, numerical and experimental studies on explosions, including innovative prevention and mitigation strategies

In Table 58 we present the maximum overpressure values at different distances. By default, the values corresponding to the first peak are presented; in the brackets we present the values of the corresponding second pressure peaks if *these values are higher than the corresponding values of the first peak*. From the results we can see that the maximum overpressure levels for the Tests 37 and 38 are higher than 200 mbar, the threshold for significant lethal effects with respect to human health.

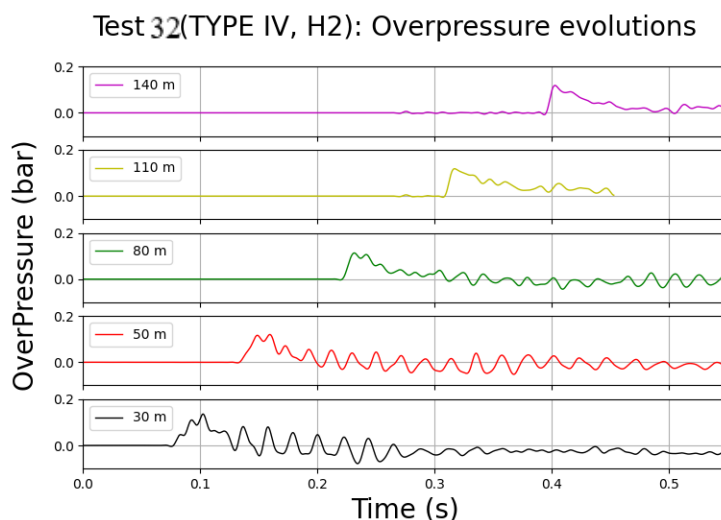


Figure 119: Test 32. H₂ 90 bar, 78L Type IV tank. Overpressure evolutions at different distances

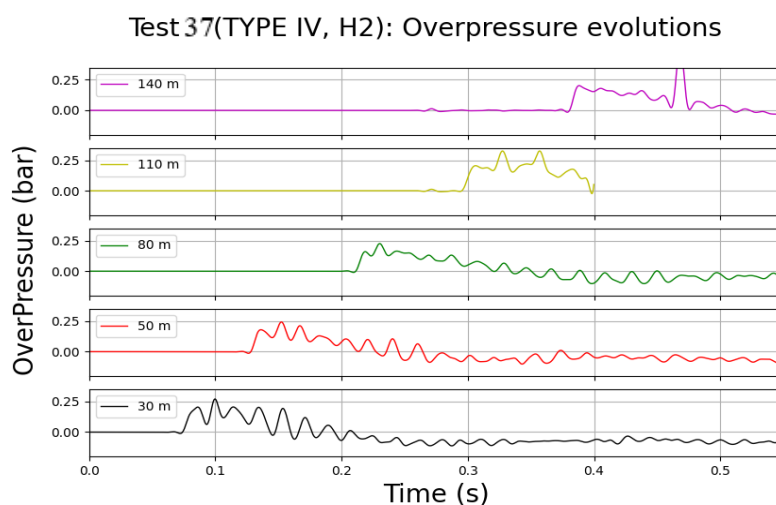


Figure 120: Test 42. H₂ 194 bar, 50L Type II tank. Overpressure evolutions at different distances

D4.3. Final report on analytical, numerical and experimental studies on explosions, including innovative prevention and mitigation strategies

Test 38(TYPE IV, H2): Overpressure evolutions

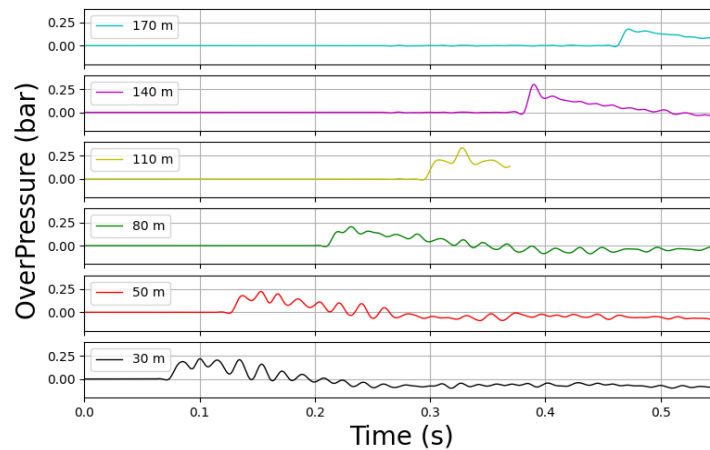


Figure 121: Test 37. H2 520 bar, 78L Type IV tank. Overpressure evolutions at different distances

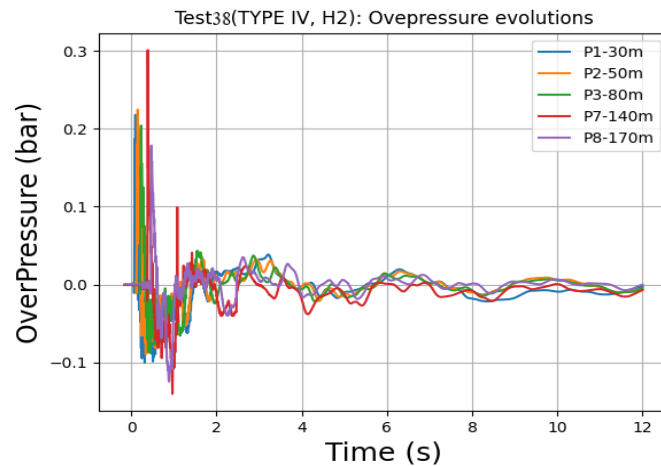


Figure 122: Test 38. H2 610 bar, 78L Type IV tank. Overpressure evolutions at different distances (top), the evolutions are shown for longer time scale (bottom).

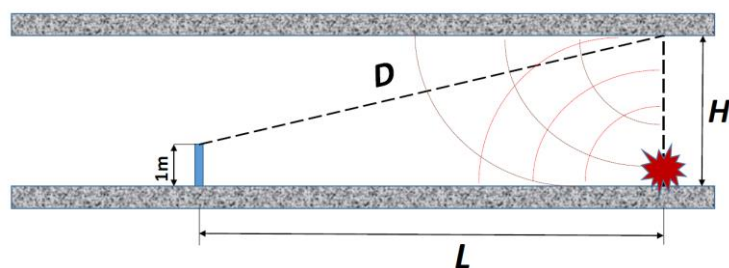


Figure 123: Sketch of the blast wave propagation near explosion zone.

D4.3. Final report on analytical, numerical and experimental studies on explosions, including innovative prevention and mitigation strategies

Table 58. Tests 32, 42, 37 and 38 (Hydrogen tanks). Maximum overpressures recorded at different distances

Test	ΔP (mbar) @ 30 m	ΔP (mbar) @ 50 m	ΔP (mbar) @ 80 m	ΔP (mbar) @ 110 m	ΔP (mbar) @ 140 m	ΔP (mbar) @ 170 m	ΔP (mbar) @ 200 m
32	110.4 (136.1)	116.8 (120.4)	113.4	118.2	118.7	----	----
42	101.0	97.7	92.2	100.4	----	84.8	79.8
37	205.0 (271.3)	179.6 (243.2)	160.1 (226.2)	205.5	202.2	----	----
38	187.1 (218.1)	180.5 (224.8)	151.2 (204.4)	205.5 (336.1)	301.3	178.6	----

Finally, on the *Figure 124* we present the blast wave velocity with respect to distance along the tunnel for the Tests 33, 34 and 38. The velocity values between adjacent pressure transducers are determined using time-of-arrival of the pressure signals and the corresponding distance between the transducers. We can see that on average, blast waves propagate with a velocity close to 350 m/s.

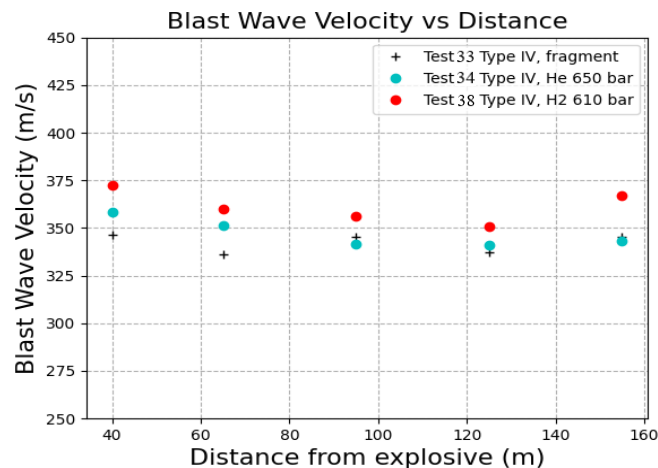


Figure 124 : Blast wave velocity as a function of distance for 3 tests.

4.3.4 Comparison with a correlation (Molkov & Dery, 2020)

The paper (Molkov & Dery, 2020) presents a universal correlation for blast wave decay after hydrogen tank in a tunnel fire. This correlation was developed using methods of similitude analysis and numerical experiments. In terms of energy, the total mechanical energy contained in the tank as well as the fraction of chemical energy (12% in the paper) is accounted for.

The best fit line (63) for the universal correlation is:

D4.3. Final report on analytical, numerical and experimental studies on explosions, including innovative prevention and mitigation strategies

$$\bar{P}_T = 0.22 \cdot \bar{L}_T^{-1.35} \quad (63)$$

while the conservative form of the correlation (64) is:

$$\bar{P}_T = 0.87 \cdot \bar{L}_T^{-1.35} \quad (64)$$

The correlation is expressed in terms of non-dimensional distance \bar{L}_T (65) and non-dimensional overpressure \bar{P}_T (66), where

$$\bar{L}_T = \frac{P_0 L A_T}{E \cdot AR^{0.5}} \cdot \frac{f L}{D_T} \quad (65)$$

$$\bar{P}_T = \frac{\Delta P}{P_0 \bar{L}_T} \quad (66)$$

The following values are taken for the analysis:

- Atmospheric pressure: $P_0 = 1 \text{ bar}$;
- Tunnel cross-section area: $A_T = 41.3 \text{ m}^2$ ($L < 87 \text{ m}$), and $A_T = 33 \text{ m}^2$ ($L > 87 \text{ m}$)
- Friction factor: $f = 0.0055$
- Aspect ratio: $AR = 1.6$ ($L < 87 \text{ m}$), and $AR = 1.4$ ($L > 87 \text{ m}$)
- Hydraulic diameter: $D_T = 6.6 \text{ m}$ ($L < 87 \text{ m}$), and $D_T = 6.0 \text{ m}$ ($L > 87 \text{ m}$).

The tests used for comparisons are presented in Table 59. One set of data from the pretest campaign of 2020 (Test 20), rupture of Type II tank of 50 L containing hydrogen at 47 bar, is added to the plot. The results were reported earlier; here we give the maximum overpressure levels, for completeness. The mechanical energy is computed using Abel-Noble equation of state of a real gas with constant $b = 7.69 \times 10^{-3} \frac{\text{m}^3}{\text{kg}}$. For further analysis, we consider 180% of the mechanical energy and 12% of the chemical energy (67), i.e.

$$E = 1.8 \cdot E_{ME} + 0.12 \cdot E_{CH} \quad (67)$$

We assume here that all energy of a DB is spent on a tank rupture.

The results are given in *Figure 125* (only the first overpressure peak is considered) and *Figure 126* (the second overpressure peak is considered). We can see that most of the data are below the best fit line of the correlation.

D4.3. Final report on analytical, numerical and experimental studies on explosions, including innovative prevention and mitigation strategies

Table 59. The tests used for comparison. The mechanical and chemical energies are given

Test N°	Tank	Pressure (bar)	Temperature, °C	Mechanical Energy, MJ	Chemical Energy, MJ
32	TYPE IV	90	15	1.60	66.92
42	TYPE II	194	15	2.09	86.94
37	TYPE IV	520	15	7.39	306.14
38	TYPE IV	610	15	8.31	344.13
20 from pretest of 2020	TYPE II	47	10	0.56	24.41

Table 60. Maximum overpressure values measured at different distances for pre-Test 20

Test	ΔP (mbar) @ 38 m	ΔP (mbar) @ 45 m	ΔP (mbar) @ 90 m	ΔP (mbar) @ 142 m	ΔP (mbar) @ 205 m
20 from pretest of 2020	80.0	72.1	60.5	58.2	58.1

D4.3. Final report on analytical, numerical and experimental studies on explosions, including innovative prevention and mitigation strategies

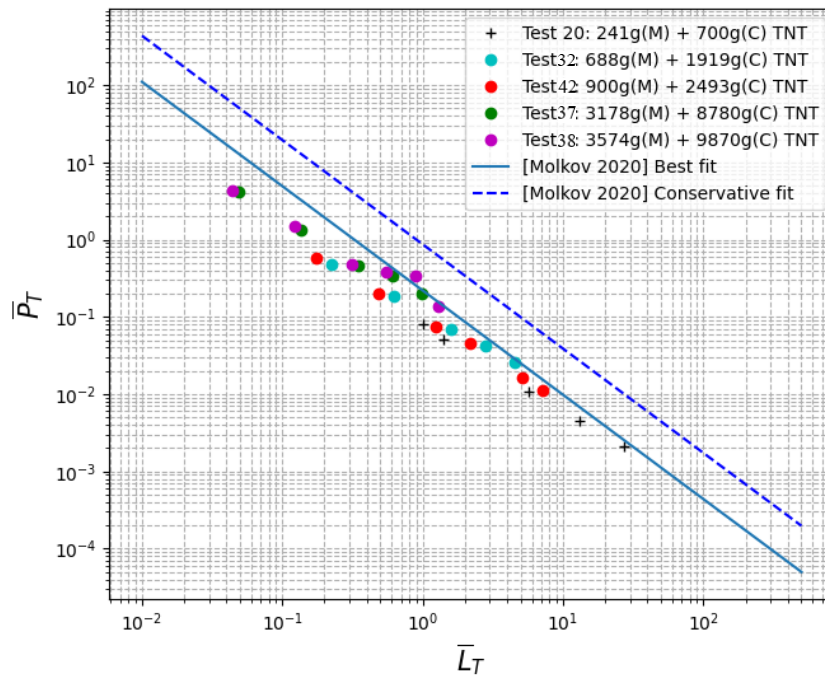


Figure 125: Comparison of experimental data with universal correlation. First peak of pressure is taken into account.

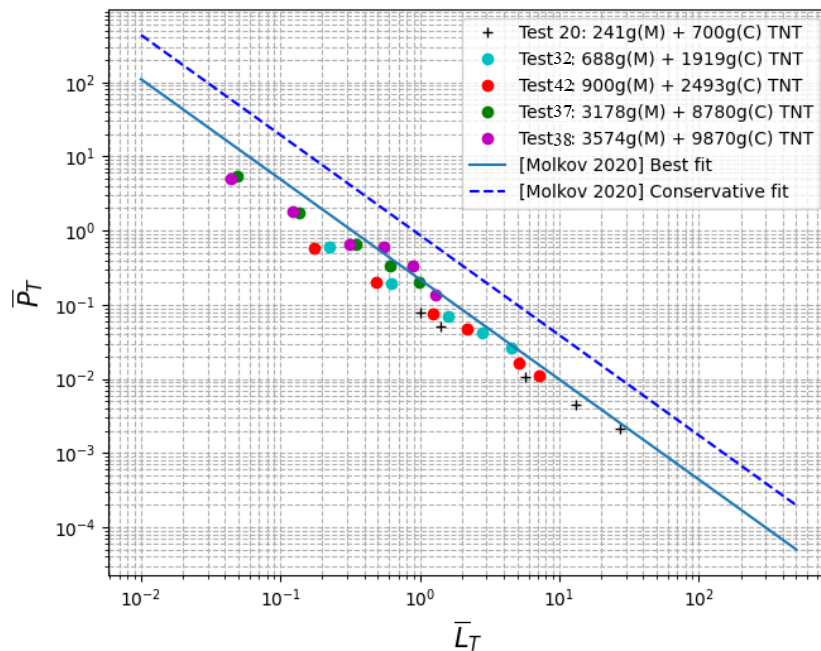


Figure 126: Comparison of experimental data with universal correlation. Second peak of pressure is taken into account.

D4.3. Final report on analytical, numerical and experimental studies on explosions, including innovative prevention and mitigation strategies

4.3.5 Conclusions and recommendations

This document details the results obtained during tank rupture experiments in the Mortier road tunnel. Two tests have been performed with helium gas inside, four tests – with hydrogen filled tanks and two tests - with tank fragments. The hydrogen gas pressure varied between 90 bar and 610 bar. The detonation belt charge is kept constant for each Tank type, its energy is given in TNT equivalent units, i.e., 130 g for TANK II and 228 g for TANK IV. Seven PCB blast wave pencils were installed in the tunnel to capture the pressure waves. The signals were analyzed in terms of maximum overpressures. The main results show that:

- Concerning the tests with fragment and detonation belts (Test 31 and 33), maximum overpressure levels are lower than 20 mbar at distances larger than 50m from the explosion, which is considered as the threshold for indirect effects with respect to human health.
- As of the tests with compressed helium gas, the maximum overpressure levels are lower than 140 mbar, representing the threshold for the first lethal effects (Test 30 and 34).
- Concerning the tests with compressed hydrogen gas, the maximum overpressure levels for the Tests 37 and 38 are higher than 200 mbar, the threshold for significant lethal effects with respect to human health.

In general, limited attenuation is observed along the tunnel. We mention that at 87 m from the explosion, the cross-section area of the tunnel diminishes from $41.3m^2$ down to $33m^2$. This could explain the maximum pressure relative increase measured by the transducers located after that distance.

The experimental results were compared with the universal correlation of (Molkov & Dery, 2020). It is shown that most of the data fall below the best fit line of the correlation, showing that despite its slightly conservative character, the correlation is applicable in such situations.

These test results constitute a unique database for the understanding and validation of energy release models at the road tunnel scale.

4.4 Deflagration of non-uniform cloud in a tunnel: Experiments on deflagration of non-uniform hydrogen-air cloud created by release in mock-up tunnel sections (4.4.3, PS)

4.4.5 Background

Accidentally released H_2 can accumulate below the ceiling of a, tunnel, garage or other roofs. Such scenarios can create local pockets of reactive H_2 /air-mixtures with concentration gradient. The combustion of such mixtures can lead to flame acceleration even detonation, thus, strong pressure loads and to structural damage.

4.4.6 Objectives

The aim of the experiment is to investigate the deflagration of stratified hydrogen-air mixture in tunnel-like structure with a rectangular cross section.

D4.3. Final report on analytical, numerical and experimental studies on explosions, including innovative prevention and mitigation strategies

4.4.7 Knowledge gaps and accident scenarios assessed

There is a lack of experimental data on the critical conditions for flame acceleration in semi-confined layer with concentration gradient.

4.4.8 Description

The tests were performed in H110 (A1) vessel of HYKA, as shown in Figure 127. The safety vessel H110 has main dimensions of 3.5 m id and 12 m length with a volume of 100 m³ and a design pressure of 100 bar. The vessel is used as a safety vessel. A rectangular sub-compartment of 9 x 3 x 0.6 m³ was used to study a combustion and detonation in a horizontal semi-confined layer of hydrogen air mixture, Figure 127 right. The safety vessel is equipped with measuring ports and windows for visual observations. A special gas-filling system allows the creation of a layer of hydrogen-air mixtures with a linear vertical concentration gradient from 0.1 to 1.1 % H₂/cm. The measuring system for combustion detection consists of an array of thermocouples (flame arrival time); fast pressure gauges (combustion pressure and shock wave); photodiodes and ion probes (flame arrival time, flame speed). The data acquisition system is based on multi-channel (64) ADC with a sampling rate of 1 MHz.

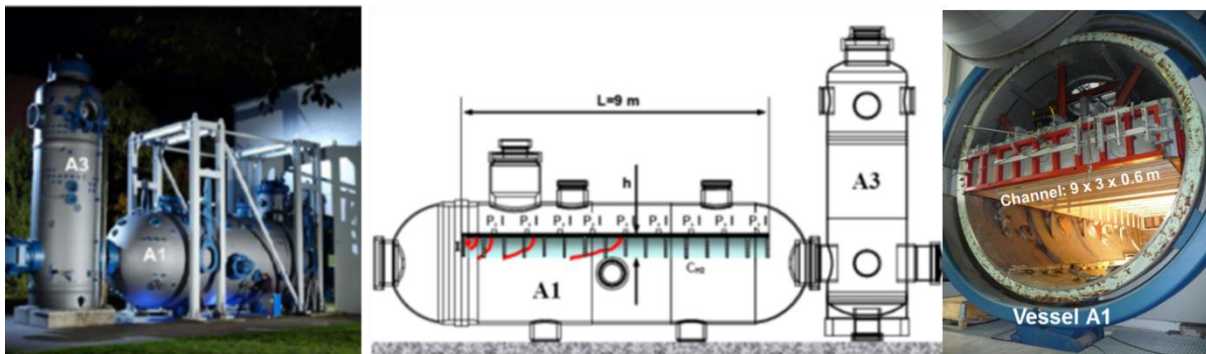


Figure 127. Test facility H110 (A1) of HYKA with large scale rectangular combustion channel 9 x 3 x 0.6 m³, open from below.

The mixture with concentration gradient were created as a thin layer under the ceiling by a special gas injection system. The non-uniform H₂-layer is quantified with a specific maximum H₂-concentration on the top (right below the ceiling) and a concentration slope of 0.3 - 0.6 % H₂/cm.

Technically, the hydrogen concentration gradient in the layer is controlled by injection of different air diluted hydrogen of 70 – 100 %H₂. The maximal hydrogen concentration on the top is controlled by the different injection pressures of 1.2 – 2 bar. By this way, the hydrogen inventory is controlled, accordingly. Figure 128 presents the hydrogen layers with different concentration gradients and peak concentrations in various cases.

D4.3. Final report on analytical, numerical and experimental studies on explosions, including innovative prevention and mitigation strategies

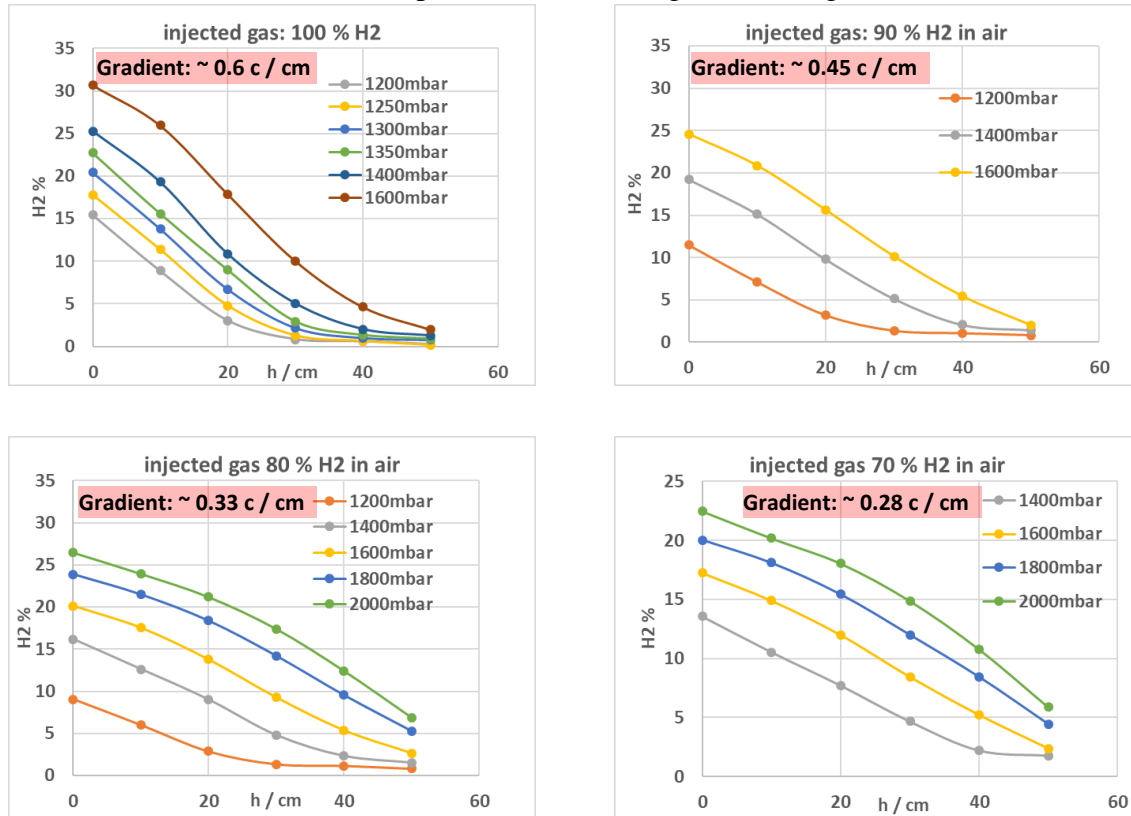


Figure 128. Various hydrogen layers are produced by injection of different air diluted hydrogen mixtures at different injection pressures.

In case of a uniform H_2 layer, the combustion channel full of uniform hydrogen-air mixture is separated by a thin foil on the bottom side of the channel. The layer height is 60 cm. The separation foil was cut short before ignition. The ignition was realized in a special perforated tube, acting as a line igniter.

To measure the flame propagation in 2D geometry, the rectangular combustion channel is equipped with fast pressure gauges (PCB) for combustion overpressure measurement and an array of ion probes for detection of the flame speed, respectively.

The designed test cases are summarized in Table 61, as the test matrix.

D4.3. Final report on analytical, numerical and experimental studies on explosions, including innovative prevention and mitigation strategies

Table 61. Test matrix of non-uniform and uniform hydrogen-air cloud in a tunnel.

Test Case	Injection Pressure, mbar	Injected H ₂ in Air, %	Nominal H ₂ Concentration Gradient, %/cm	H ₂ Conc. on the Ceiling, %
HyT240	1400	100	0.6	25.30
HyT241	1350	100	0.6	22.74
HyT242	1300	100	0.6	20.43
HyT243	1250	100	0.6	17.79
HyT244	1200	100	0.6	15.45
HyT245	1600	100	0.6	30.67
HyT246	2200	70	0.28	24.45
HyT247	2000	70	0.28	22.47
HyT248	1800	70	0.28	20.04
HyT249	1600	70	0.28	17.26
HyT250	1400	70	0.28	13.55
HyT251	1600	90	0.45	24.59
HyT252	1400	90	0.45	19.22
HyT253	1200	90	0.45	11.49
HyT254	2000	80	0.33	26.47
HyT255	1800	80	0.33	23.89
HyT256	1600	80	0.33	20.14
HyT257	1400	80	0.33	16.19
HyT258	1200	80	0.33	9.04
1		Uniform mixture	0	10
2		Uniform mixture	0	15
3		Uniform mixture	0	20
4		Uniform mixture	0	25
5		Uniform mixture	0	30

4.4.9 Results

4.4.9.1 Flame speed and combustion overpressure

The flame speed is computed based on the arrival times of the flame front at the ion probes positioned along the flame propagation passage. The test cases of HyT242 and HyT256 are taken as examples to show the measured flame speed, as shown in Figure 129. The data of the two columns of ion probes on the left (denoted as “links” or “li” in the figure) and right (as “rechts” or “re”) are applied to make comparison. According to the figure, both the flame speeds are subsonic, about 40 m/s.

D4.3. Final report on analytical, numerical and experimental studies on explosions, including innovative prevention and mitigation strategies

The combustion overpressures are also recorded by the PCB gauges, which are shown in Figure 129 too. The figure shows that the overpressure in Case HyT242 is about 0.13 bar, and Case HyT256 0.28 bar, respectively. It is certain that the mixture with a higher concentration gradient (HyT256) generates a higher overpressure.

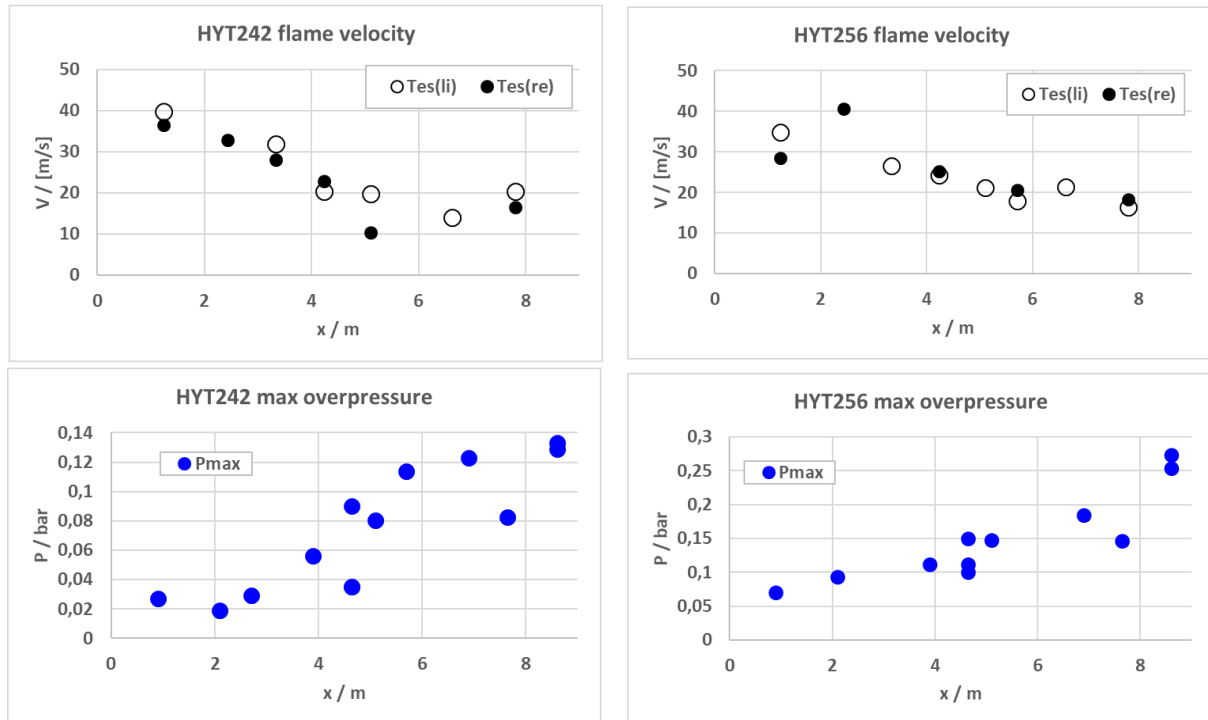
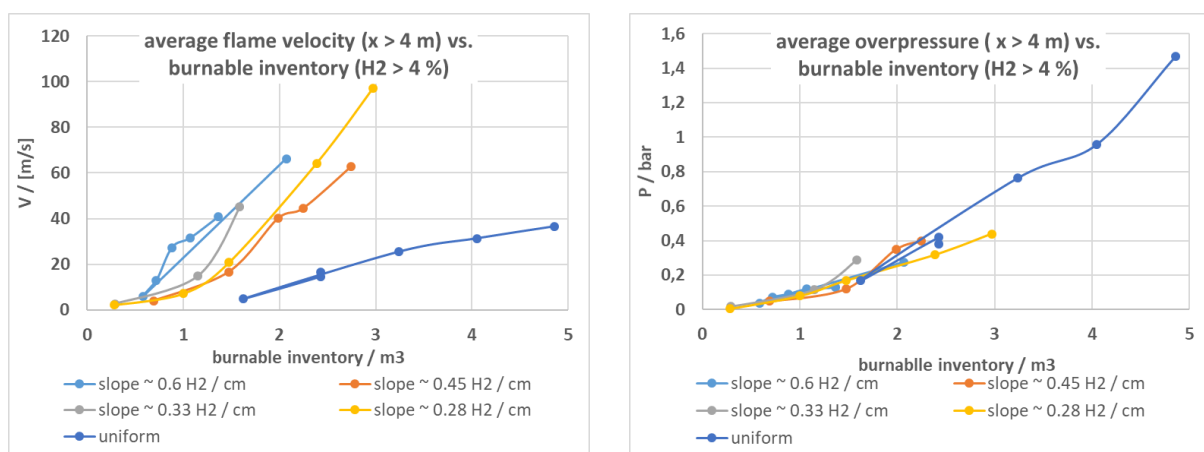


Figure 129. Measured flame speed and combustion overpressure in case HyT242 with H_2 concentration gradient of 0.6% H_2 /cm and max. H_2 concentration of 20% H_2 , case HyT256 with H_2 concentration gradient of 0.33% H_2 /cm and max. H_2 concentration of 20% H_2 .

4.4.9.2 Flame speed and combustion overpressure in non-uniform hydrogen-air mixtures

The measured flame speeds and combustion overpressures are compared for the various mixtures with different hydrogen concentration gradients, as shown in Figure 130.



D4.3. Final report on analytical, numerical and experimental studies on explosions, including innovative prevention and mitigation strategies

Figure 130. Flame speed (left) and combustion overpressure (right) comparisons between uniform and non-uniform mixtures with different hydrogen concentration gradients (slopes).

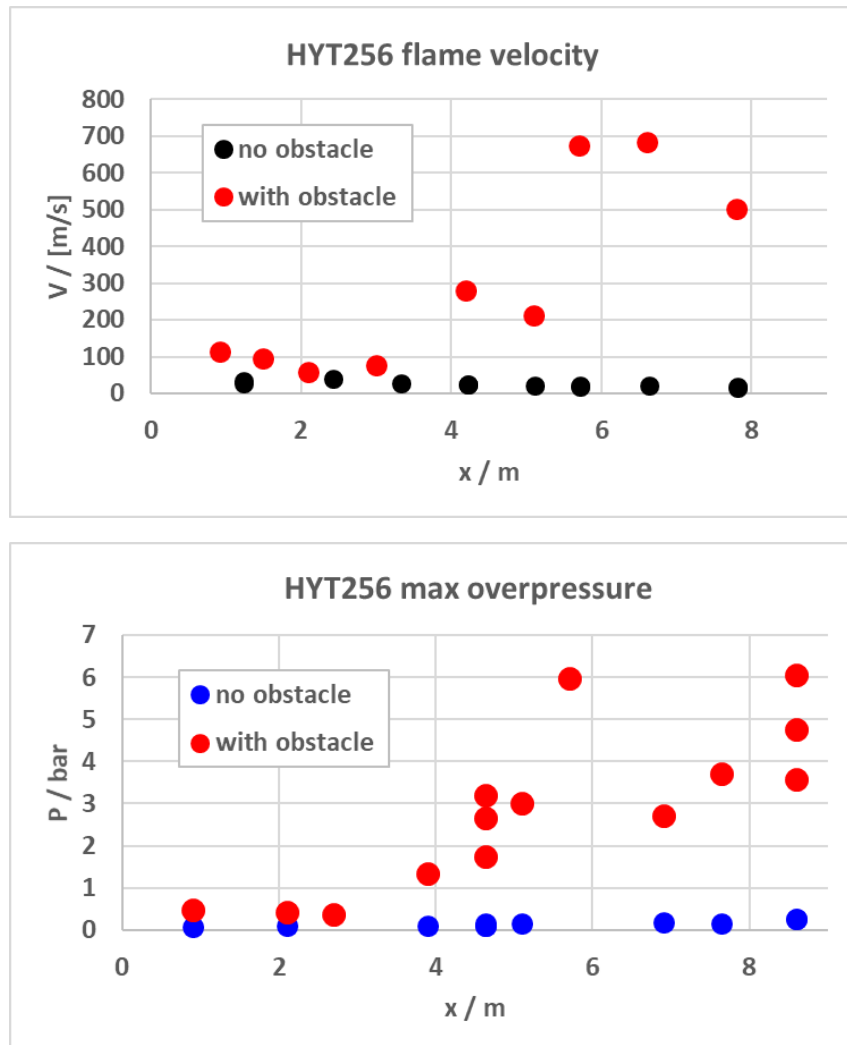
Figure 130 clearly indicates that, the mixture with a higher concentration gradient produces a faster combustion. It means flame acceleration occurs more likely to a stratified hydrogen cloud in each hydrogen inventory. In view of hydrogen safety, the layered hydrogen cloud is greater risk.

However, according to Figure 130, the combustion overpressure does not change much for different mixtures at a given hydrogen inventory. It is perhaps due to the smooth configuration of the combustion channel.

4.4.10 Influence of obstacles on stratified mixture combustion

As shown in Figure 127 (middle), obstacles can be installed in the combustion channel. The tests manifest that these obstacles can influence the combustion significantly.

The case HyT256 is taken as an example. The measured flame speeds and combustion overpressures are compared in Figure 131 with obstacles and without obstacles.



D4.3. Final report on analytical, numerical and experimental studies on explosions, including innovative prevention and mitigation strategies

Figure 131. Influence of obstacles on combustion in case of HyT256 with H_2 concentration gradient of 0.33% H_2 /cm and max. H_2 concentration of 20% H_2 .

The channel with obstacles is closer to the situation of a genuine tunnel. Figure 131 indicates obviously that, the original slow combustion without obstacles is transited to a supersonic flame by the obstacles, which produced a catastrophic overpressure of 6 bar.

4.5 Tests on effect of water sprays and mist systems on combustion and DDT (4.4.4, PS)

4.5.5 Background

Water injections like spray or mist generation systems are traditionally applied to extinguish fires in conventional accident scenarios. However, it might be a challenge for conventional fire protection systems when hydrogen vehicles are involved in a fire due to hydrogen release in confined spaces like traffic tunnels. It is still a question whether a water spray can effectively extinguish a hydrogen fire. Nuclear containment safety studies for water reactors have shown that water spray is not a sufficiently good extinguisher of hydrogen fires in some circumstances, but the injected water droplets and vaporised steam can change the composition of the atmosphere in the containment and the chemical sensitivities of the gas mixtures.

In case of hydrogen deflagration or detonation in confined spaces like tunnels, injected water mist interacts with the shockwave caused by explosion. The pressure waves are supposed to be attenuated by the interaction. The attenuation effect is still unclear and has to be investigated.

4.5.6 Objectives

The aim of the experiment is to test the suppression effect of water injection on the combustion of premixed hydrogen-air mixture.

4.5.7 Knowledge gaps and accident scenarios assessed

There is sparse data available regarding the dynamics of flame propagation in semi confined hydrogen-air mixture in presence of water spray or mist are available, see 2.5.3.

4.5.8 Description

The tests have been performed in H110 (A1) vessel of HYKA, a description of which can be found in 4.4.8. The longitudinal mid-point of the rectangular combustion channel 9 x 3 x 0.6 m³ will be equipped with a water spray system. The water spray system will be characterised by the design of the release nozzle and the water supply pressure. The test was performed with uniform H_2 layers. The open from below side of combustion channel was separated with a thin foil. The layer height is 60 cm. The separation foil was cut shortly before ignition. The ignition was performed in a special perforated tube which acts as line igniter. The flame propagates through the first half of the channel in dry atmosphere and enters the water spray section after 4.5 m, Figure 132.

D4.3. Final report on analytical, numerical and experimental studies on explosions, including innovative prevention and mitigation strategies

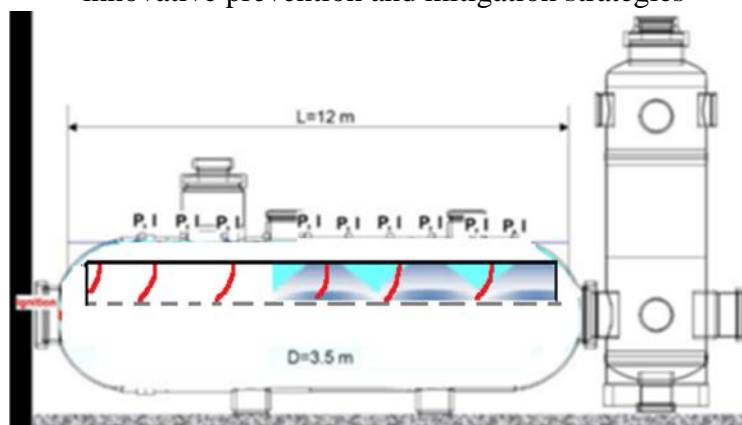


Figure 132. Test facility H110 (A1) of HYKA with large scale rectangular combustion channel $9 \times 3 \times 0.6 \text{ m}^3$ and section with water spray.

To measure the flame propagation in 2D geometry an array of sensors is necessary. The rectangular combustion channel will be equipped with 9 fast pressure gauges (PCB) for combustion pressure. An array of ion probes for detection of the flame arrival time will be placed in the dry section. Optionally, “single use” cameras or light detectors will be used in the wet zone.

The premixed hydrogen-air mixture fills in a rectangular domain $H \times W \times L = 0.6 \times 3 \times 9 \text{ m}$. The spray zone is 4.5 m long. The combustions with different hydrogen concentrations will be observed and measured with or without obstacles and with or without spray. The test matrix is shown in Table 62.

Table 62. Test matrix of water injection effect on hydrogen combustion and DDT.

With obstacles	No (deflagration)		Yes (fast flame or DDT)	
With spray	no	yes	no	yes
15 % vol H_2	1	4	7	10
20 % vol H_2	2	5	8	11
23 % vol H_2	3	6	9	12

4.5.9 Results

The suppression efficiency of water injection on hydrogen deflagration and fast flame or detonation will be proven by the tests' results.

4.5.10 Delivery timeline

The experimental work was completed ahead of M36 (February 2022), but the reporting was not. This will be completed by April 2022 and included in D4.4. *Results of the deferred experimental programme and associated activities* and is due for completion by M41 (July 2022).

D4.3. Final report on analytical, numerical and experimental studies on explosions, including innovative prevention and mitigation strategies

4.6 Effect of droplet size on mitigation of combustion and DDT (4.4.4, USN)

4.6.5 Background

In the literature, the availability of data on fire water spray is limited. Often the spray is described only by the orifice diameter of the firewater nozzles and spray angle. However, the flow properties of the spray (i.e., size distribution, velocity, and volume fraction of the droplets) are known to influence the suppression efficiency. Small droplets will follow the gas flow, evaporate quickly, cool the fire gases, and screen for heat radiation. In contrast, large droplets have high momentum and are more likely to reach the source of the fire and cool objects such as vehicles and surroundings. In explosion mitigation, the sizes of the droplets are important where small droplets can contribute to extinction and the large droplets have high inertia and can reduce the local gas velocities (Thomas 2000; Bjerketvedt & Bjørkhaug 1991). Increased turbulence can also have an effect. Thus, to evaluate the efficiency of a water spray system it is necessary to know the characteristics of spray.

Current research provides spray characteristics of a typical multipurpose mist nozzle using a laser-based shadow imaging technique.

4.6.6 Materials and method

The measurements are performed on the spray from a typical multipurpose high-pressure mist spray. Water for the spray is provided to the nozzle using a high-pressure water supply pump equipped with a pressure sensor. The characteristics of the spray are determined using a laser-based shadow-imaging system equipped with image processing software.

The measurement technique used to measure the characteristics of the mist spray is a laser-based shadow-imaging technique provided by LaVision. The main components of the setup are a dual cavity pulsed laser fitted with front optics (beam expander and a diffusor plate), a long-distance microscope, and a high-speed camera.

The measurements are performed on a Danfoss HNMP-5-10-1.19-00 nozzle with five separate micro nozzles attach to one common nozzle head. The micro nozzles are mounted at a half cone angle of 56° and an azimuthal angle of 72° with adjacent nozzles.

The laser is Photonic industry DM60-532 DH dual-head (dual cavity) laser with a wavelength of 532 nm (green). The laser is of the type DPSS (diode-pumped solid-state) Nd:YAG laser with two independently controlled laser cavities both with a repetition rate of 1.0 – 35.0 kHz and adjustable power. The high-speed camera is a Photron SA-Z type 2100K-M-32GB with a CMOS (Complementary Metal-Oxide Semiconductor) sensor with high resolution and high sensitivity. The sensor resolution is 1024 x 1024 pixels recording 12-bit monochrome images. The physical sensor size is 20.48 mm x 20.48 mm with a fill factor of 58 %. The Questar QM-1 by LaVision used for the experiments is a long-distance microscope lens designed to operate at focal lengths from 500-1500 mm. A given lens with a given magnification gives a field of view (FOV) and depth of field (DOF). The FOV is dependent on the setup, but the DOF is also droplet size dependent. To compensate for the droplet size dependency of the DOF, a calibration is performed on the setup. The calibration is performed before the experiment with the same settings for the camera, lens, and laser. A sizing standard is placed in the FOV and mounted on a perpendicular translation screw. In the current research, the range from 20 – 400 μm is selected.

D4.3. Final report on analytical, numerical and experimental studies on explosions, including innovative prevention and mitigation strategies

The shadow imaging technique previously described was used for measurements on the Danfoss mist nozzle. The combination of lenses gave a magnification of approximately 2.5 giving the field of view of 8.228 mm x 8.228 mm. The pixel resolution with the current setup was 8.04 µm/pixel.

The settings of the laser were adjusted by trial and error to give a proper measurement range of droplets and velocities. The repetition rate of the laser was set to 1.000 kHz and 20.00 µs spacing between image pairs. The current of the laser was set to 27.7 A and 27.5 A for cavity 1 and 2 respectively. This resulted in an average power of 7.9 and 8.2 W and a peak duration of about 140 and 160 ns. Using these numbers, the peak power of cavity 1 and 2 was 56 and 58 kW. The pulse energy was 7.9 and 8.2 mJ.

The in-frame movement during one exposure of droplets for a velocity of 10 m/s is 1.4 and 1.6 µm which is much less than one pixel of the image.

The inter-frame movement of droplets for a velocity of 10 m/s is 200 µm which is about 25 pixels with current magnification.

4.6.7 Results and discussion

25 measurements were performed of the mist spray at a single azimuth 940 mm below the tip of the nozzle. The location of the measurements ranged from centre to radius 600 mm with 25 mm intervals. This distance to the nozzle was the post-breakup region.

The supply water pressure was set to 100 bar with a water temperature of 12 °C and an air temperature of 20 °C.

The measurement was performed using a shadow-imaging setup from Lavision using Davis version 10.1.2.71878. The results were analysed using Particle Master with the settings in Table 63. The maximum velocity and eccentricity were determined by visual consideration of the shadow images.

Table 63. Settings for Particle Master

Property	Value
Normalization radius	75 pixels
Reduce Pixel Noise	Weak
Binarization Threshold	50 %
Minimum Slope	3.00 %
Minimum Shadow Area	25 pixels
Max velocity	10 m/s
Max eccentricity	120 %

Figure 141 (a) shows the mist spray and illustrates the optical depth (OD) of the spray. An estimate of the OD of the mist spray is made using an expression by Payri (2011). The expression below can be used to express the optical depth of a diesel spray.

$$OD = \frac{3}{2} \phi_f Q_e l \frac{1}{d_{32}} \quad (68)$$

D4.3. Final report on analytical, numerical and experimental studies on explosions, including innovative prevention and mitigation strategies

where ϕ_f is the volume fraction of water in the spray, Q_e is the extinction efficiency of the droplet and is assumed similarly equal here to 2.1, l is the path length and d_{32} is the Sauter mean diameter.

In the current research, the droplet density and Sauter mean diameter was measured for radial positions. Summarizing the contribution of all the intervals, the OD was found to be 2.4.

According to Payri (2011) the pure laser-based techniques like PDA, Mie scattering, and LIF generally perform well with OD less than unity but can give inaccurate measurements above due to multiple scattering. Shadow imaging is not equally dependent on OD other than providing blurred images.

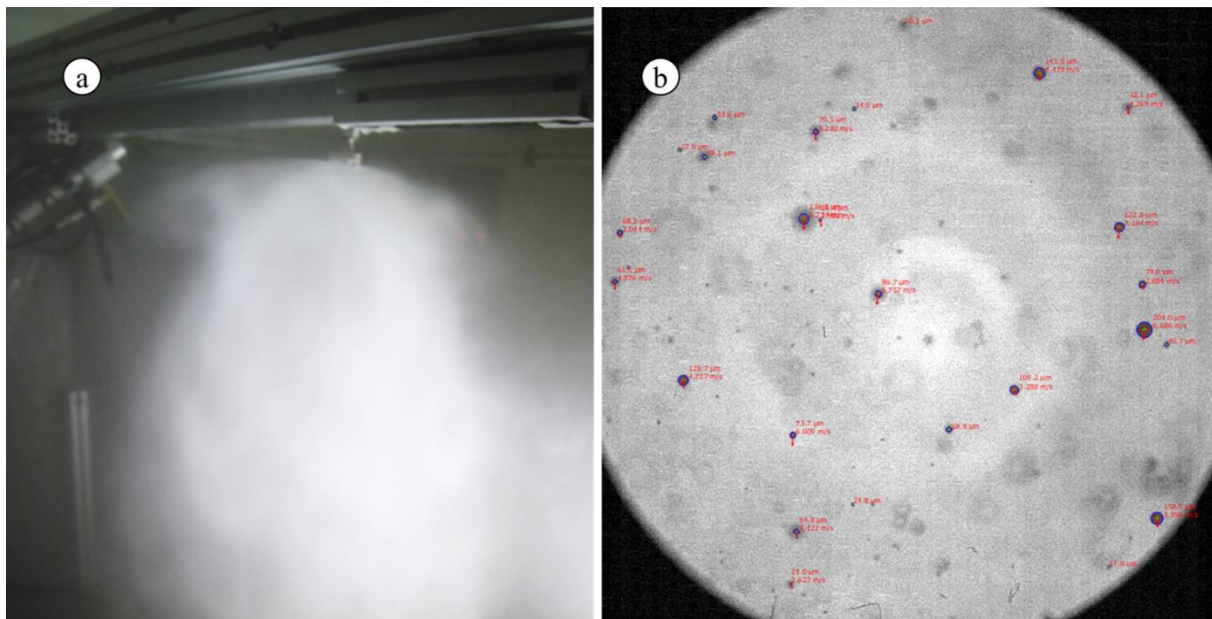


Figure 133. (a) Overview of mist spray, (b) shadow image with droplet data overlay from Particle Master by Davis

Lavision Particle Master measures the droplet diameter based on a single frame, Depth of Field (DOF) of every droplet, and velocity of droplets from adjacent frames. Automatically, this is used to calculate the properties: averaged diameters, droplet density, velocity, and fluxes from a given experiment. An example of the output of the image-processing tool Particle Master is shown in Figure 10b. The results from the measurements are given in the following figures.

As an indication of the performance of the mist nozzle, the volumetric flow of water is presented in Figure 134. The unit of the y-axis in the figure is arbitrary but indicates where most of the water is present radially in the mist spray. Most of the water is in the range of 100 to 300 mm from the centre, and just a small portion of the water is outside 500 mm. Azimuthal independence of the nozzle is assumed in the measurement.

D4.3. Final report on analytical, numerical and experimental studies on explosions, including innovative prevention and mitigation strategies

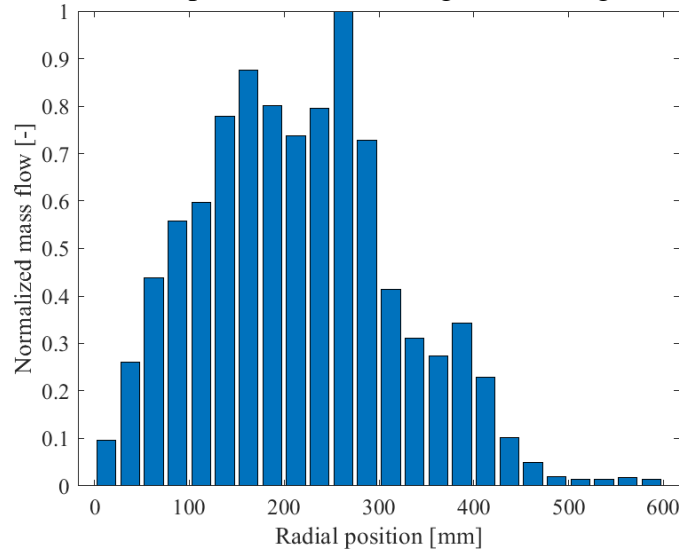


Figure 134. Normalized mass flow for 100 bar supply water pressure, 940 mm below mist nozzle.

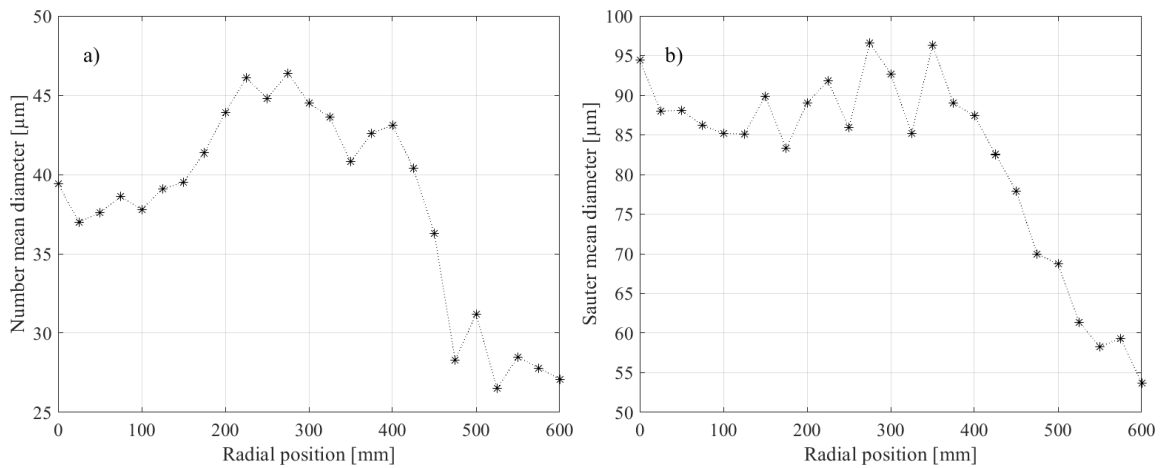


Figure 135. Number mean diameter for 100 bar supply water pressure, 940 mm below mist nozzle.

The number mean diameter (d_{10}) of the droplets recorded in this study is shown in Figure 135(a). The value averages around 40 μm in most of the spray considering the results shown in Figure 134 that most of the water is in the range between 100 and 300 mm.

The Sauter mean diameter shown in Figure 135(b) has an average value for the previously discussed range of about 90 μm . The Sauter mean diameter of the mist spray represents the averaged volume to surface ratio of the entire spray. The diameter is often in use when representing fire phenomena.

The measurements of the number mean and Sauter mean diameter is the same for a monodisperse droplet size distribution, and the difference of 40 μm to 90 μm indicates a wide range of droplet sizes.

A measure of the uniformity of the droplets is the span (Δ) of the distribution. The span is calculated using

$$\Delta = \frac{DV90 - DV10}{DV50} \quad (69)$$

D4.3. Final report on analytical, numerical and experimental studies on explosions, including innovative prevention and mitigation strategies

where DV90 is the diameter of the droplet that 90 % of the water (volumetric) is below. The DV10 and DV50 are defined in the same matter. A low value of span indicates a uniform size distribution. In Figure 136(a) the span is shown for the different radial positions in the mist spray. The average value in the previously discussed range is $\Delta = 1.2$.

The total number of droplets used to measure the characteristics of the spray is shown in Figure 136(b).

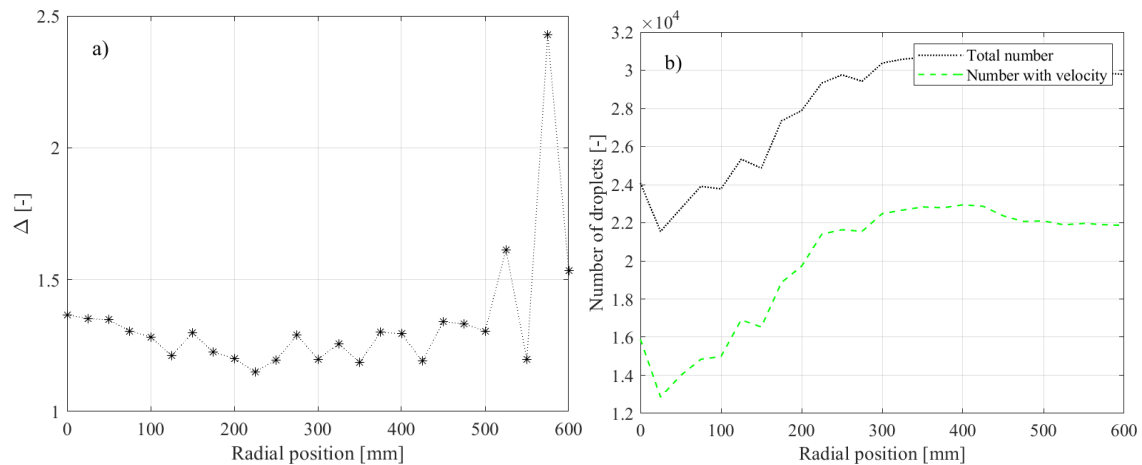


Figure 136. (a) Relative span factor- and (b) number of droplets for 100 bar supply water pressure, 940 mm below mist nozzle.

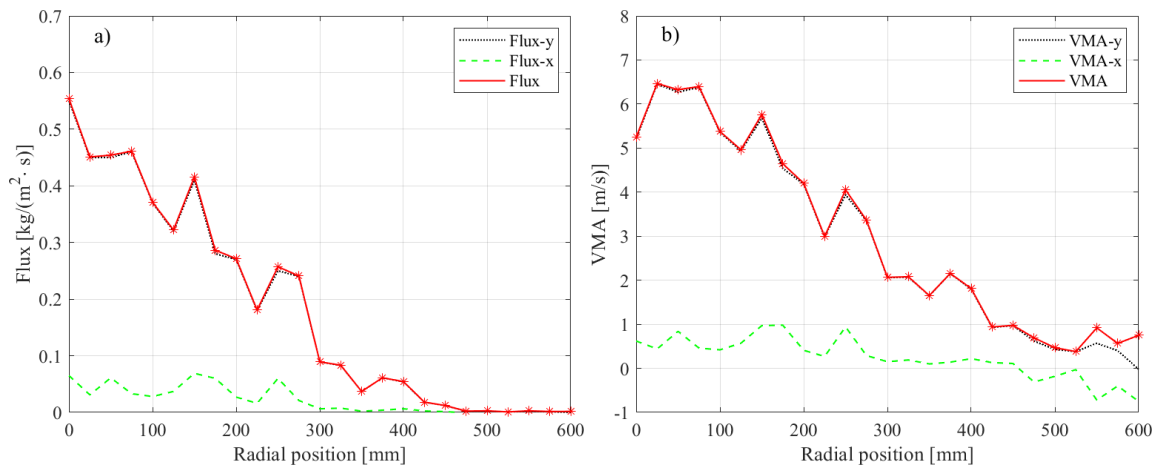


Figure 137. (a) Mass flux of water droplets- and (b) Mass averaged velocity for 100 bar supply water pressure, 940 mm below mist nozzle.

The mass flux of water is a measure of the amount of water per area and time in an area perpendicular to the mist nozzle. The mass of water is found by summing up the volume of all recorded droplets and multiplying by the density of water. The measurements are compensated for the DOF of droplets. The measurements show the mass flux to be highest at the centre of the spray, decreasing to the periphery (see Figure 137(a)). It is important to consider that the measurement is performed without any fire or external wind. This can change the mass flux dramatically for given positions.

D4.3. Final report on analytical, numerical and experimental studies on explosions, including innovative prevention and mitigation strategies

The velocity of the droplets is represented by the mass averaged velocity taking into account that larger droplets tend to move faster than smaller droplets. This is shown in Figure 137(b).

In the case of a fire or a gas explosion, the density of the droplets can influence the propagation of the reactions. In Figure 138 the droplet density is shown for ranging radial positions. The measurements show a decreasing density for increasing radial position. To convert droplet density to the volume fraction of water, it can be divided by 10^6 assuming the density of water to be 1000 kg/m^3 .

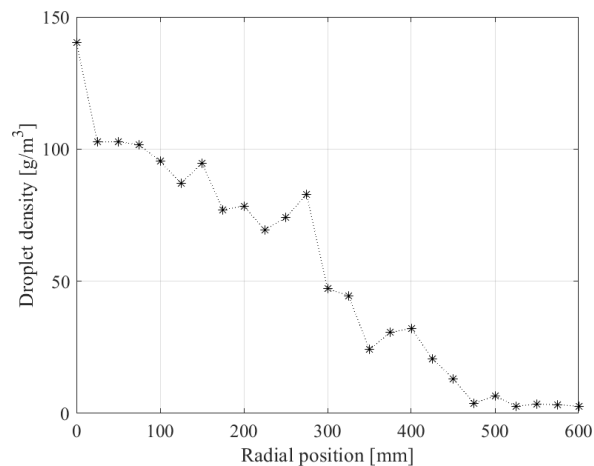


Figure 138. Droplet density for 100 bar supply water pressure, 940 mm below mist nozzle.

For a given position in the spray, the number- and volumetric size distribution (Figure 139) is given as an example for the same location in the spray. The figure shows both the bin count and the cumulative distribution. By comparing the two distributions, the volumetric distribution is skewed to the larger sizes indicating that the number distribution alone does not represent the characteristics of the mist spray.

D4.3. Final report on analytical, numerical and experimental studies on explosions, including innovative prevention and mitigation strategies

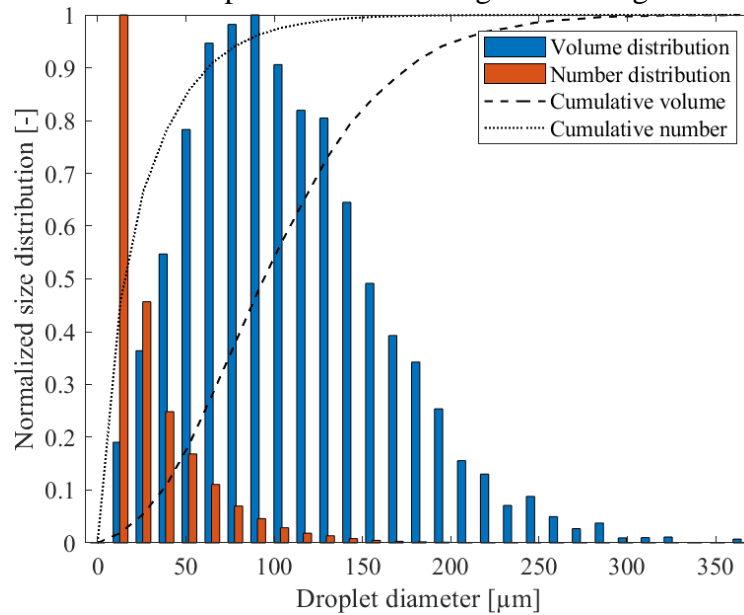


Figure 139. Example of Normalized distributions for 100 bar supply water pressure, 940 mm below, 75 mm radial to the mist nozzle.

By weighting the measurements by the normalized mass flow (given in Figure 134) for distributions and average diameters, the total values representing the entire mist spray can be found. This data represents all the measured droplets compensated for area increase with increasing radial distance. The data is referred to as the total values.

The total number distribution and total volume distribution of the mist spray are shown in Figure 140(a) and Figure 140(b), respectively. The number distribution shows a high end to the lowest detectable diameters indicating the method is likely to under-predict the number of the smallest droplets. The mode of the volume distribution is about the Sauter mean diameter. By comparing the two figures most of the total mass or volume of water in the spray exist as droplets around the Sauter mean diameter, but the highest number of droplets is

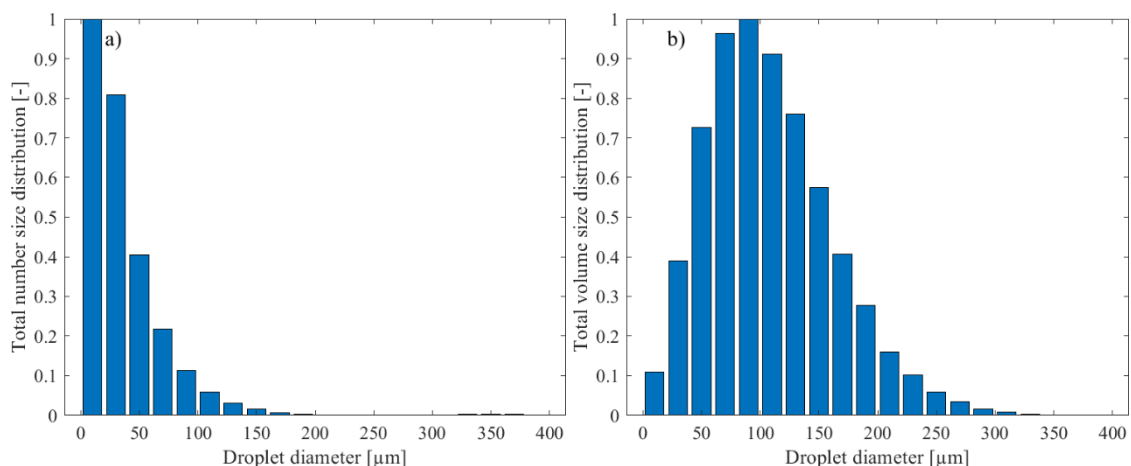


Figure 140. (a) Total number size distribution- and (b) total volume distribution for 100 bar supply water pressure, 940 mm below mist nozzle.

D4.3. Final report on analytical, numerical and experimental studies on explosions, including innovative prevention and mitigation strategies

The total properties of the entire spray compensated for mass flow differences radially are summarized in Table 64 and the numerical values of the distributions in Figure 139 are given in Table 65.

Table 64. Averaged properties of the entire spray

Averaged property	Value
d_{10}	42 μm
d_{32}	88 μm
v_{MA}	4.0 m/s
Droplet density	73 g/m^3

Table 65. Numerical values for droplet size distributions of mist spray.

Diameter [μm]	Number distribution	Volume distribution
10	37.6 %	1.7 %
30	30.4 %	6.0 %
50	15.2 %	11.2 %
70	8.2 %	14.8 %
90	4.3 %	15.4 %
110	2.2 %	14.0 %
130	1.1 %	11.7 %
150	0.6 %	8.8 %
170	0.3 %	6.2 %
190	0.1 %	4.3 %
210	0.1 %	2.5 %
230	0.0 %	1.6 %
250	0.0 %	0.9 %
270	0.0 %	0.5 %
290	0.0 %	0.3 %
310	0.0 %	0.1 %
330	0.0 %	0.0 %
350	0.0 %	0.0 %
370	0.0 %	0.0 %
390	0.0 %	0.0 %

By integrating the water mass flux over the entire measured area to get the total mass flow it is possible to compare with the mass flow put into the mist nozzle. For this study, about 50% of the water was represented in the measurements by the shadow imaging technique.

4.6.8 Concluding remarks

The characteristics of a general multipurpose mist nozzle with a K-factor=1.19 were measured with a laser-based shadow-imaging technique. The experiments were performed with supply water pressure equal to 100 bar at an axial distance of 940 mm for radial positions ranging from centre to 600 mm at a single azimuth. The mist nozzle is a general pendent nozzle head with 5 micro nozzles.

D4.3. Final report on analytical, numerical and experimental studies on explosions, including innovative prevention and mitigation strategies

The experiments were difficult to perform due to the high density of the water droplets. The optical depth (OD) was estimated to be about 2.4.

The number size distribution and number averaged diameter, d_{10} , of 42 μm was low for the entire spray, but the volume distribution shows the occurrence of droplets of 300+ μm .

The droplet density was averaged to be 73 g/m³ for the applied area with a radius of 600 mm.

4.7 Shock wave attenuation: tests on tank rupture in a tunnel with shock attenuation material / system (4.4.5, HSE)

4.7.5 Background

HSE will evaluate shock / blast wave attenuation by water sprays or mist systems only. A literature survey will be carried out and the findings, alongside data obtained by WP partners KIT, from work done in sub-task 4.4.4 and 4.4.5, will be used to establish the most effective water spray or mist system, for blast wave mitigation in a confined space.

4.7.6 Delivery timeline

This work has been delayed and will be reported in the added deliverable D4.4. *Results of the deferred experimental programme and associated activities*, due for completion by M41 (July 2022).

D4.3. Final report on analytical, numerical and experimental studies on explosions, including innovative prevention and mitigation strategies

4.8 Shock wave attenuation: Experiments on the effect of water spray / mist system on shock wave attenuation (4.4.5, PS)

4.8.5 Background

Water injections like spray or mist generation systems are traditionally applied to extinguish fires in conventional accident scenarios. However, it might be a challenge for the conventional fire protection systems when hydrogen vehicles are involved in fire, due to hydrogen release in confined spaces like traffic tunnels. It is still a question whether a water spray can effectively extinguish a hydrogen fire. Nuclear containment safety studies for water reactors have shown that a water spray is not sufficiently good at extinguishing hydrogen fires in some circumstances, but the injected water droplets and vaporized steam can change the composition of the atmosphere in the containment and the chemical sensitivities of the gas mixtures.

In the case of hydrogen deflagration or detonation in confined spaces like tunnels, injected water mist interacts with shockwave caused by an explosion. The pressure waves are supposed to be attenuated by the interaction. The attenuation effect is still unclear and must be investigated.

4.8.6 Objectives

The aim of the experiment is to investigate the attenuation effect of water injection on the shock wave of hydrogen detonation.

4.8.7 Knowledge gaps and accident scenarios assessed

In view of fire protection, water sprays bring both advantages and disadvantages. The advantage is to cool down the hot gases of combustion, while the disadvantage is that the spray action can, in some circumstances, intensify the turbulent effect in gas flow then to intensify the combustion of gaseous fuel like hydrogen.

4.8.8 Description

The experiments were performed in the safety vessel V220 (A2), as shown in Figure 141. The safety vessel, with an inner diameter = 6 m and a height = 8 m provides a volume of 220 m³. It is designed for a static overpressure of 11 bar and temperatures up to 150 °C. The vessel is equipped with a number of vents and ports and windows for optical access. The largest two flanges with an inner diameter = 1.890 m are parallel and located near the ground. Inside the safety vessel a defined H₂ detonation will be initiated. Figure 141A, shows a sketch of the experimental set-up. A H₂ detonation will be performed in the combustion unit with 4 g H₂ provided as stoichiometric H₂ / air mixture, Figure 141B, The cube-shaped 4 g H₂ combustion unit (0.5 x 0.5 x 0.5 m) is covered with thin plastic film and produces an unconfined H₂ detonation. Figure 141C, shows the dimensionless pressure in air blast wave, versus distance in free field tests. The emitted shock wave will be used to investigate the shock wave attenuation by water spray / mist. The water sprinkler system used is described in HyTunnel-CS D3.1 (2019), sub task 3.4.6.

D4.3. Final report on analytical, numerical and experimental studies on explosions, including innovative prevention and mitigation strategies

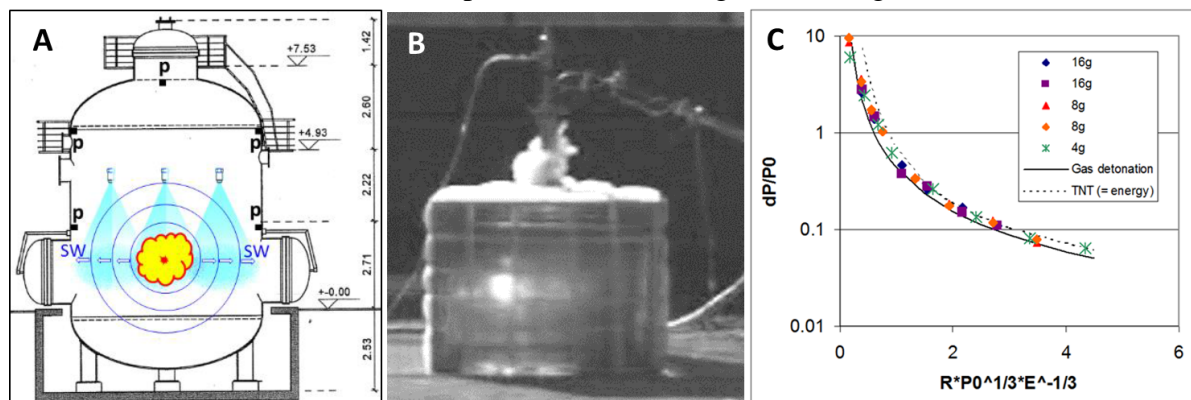


Figure 141. Test facility V220 (A2) of HYKA for attenuation of water spray on hydrogen detonation shock waves. A) Sketch of the set up for suppression tests of water spray on shock waves. B) Combustion unit with 4 g H_2 provided as stoichiometric H_2 /air mixture. C) Results of free field tests of combustion units.

Fast pressure sensors were used to precisely measure, the shock wave history. Additionally, a high-speed camera was used to record the global interaction of the shock wave with the spray.

A stoichiometric hydrogen-air mixture containing 4 g of hydrogen in a region of 0.5 x 0.5 x 0.5 m is ignited. The propagation of shock waves is recorded and measured with or without different water injection configurations. The test matrix is shown in Table 66. The basic test without spray and mist will be repeated as minimum twice.

Table 66. Test matrix of attenuation of water injection on shock wave of hydrogen detonation.

Water mass flow rate, kg/min	0	low	high
Spray	1	2	4
Mist		3	5

4.8.9 Results

The efficiency of water injection to attenuate shock waves gained from H_2 detonation will be concluded based on the experimental data.

4.8.10 Delivery timeline

The experimental work was completed ahead of M36 (February 2022), but the reporting was not. This will be completed by April 2022 and included in D4.4. *Results of the deferred experimental programme and associated activities* and is due for completion by M41 (July 2022).

4.9 Shock wave attenuation: Tests on shock wave attenuation by using shock absorbing materials, soft bulkheads and sacrificial pre-evacuated volumes (4.4.5, PS)

4.9.5 Objectives

The aim of the experiment is to investigate the attenuation effect of absorbing materials on the shock wave of hydrogen detonation.

D4.3. Final report on analytical, numerical and experimental studies on explosions, including innovative prevention and mitigation strategies

4.9.6 Description

The experiments were performed in the safety vessel V220 (A2). The experimental set-up is the same as described in section 4.4 for the tests without spray or mist. The emitted shock wave from a cube-shaped 4 g H₂ combustion unit was used, to investigate the shock wave attenuation by different absorbing materials. Probes of selected absorbing materials with an area of 1 m² will be fixed, at the same level of the combustion tube, on the wall of the safety vessel. Three fast pressure sensors were placed in front of the test probes to precisely measure the incoming shock wave history and the answer reflected from the absorbing materials. The reference will be the shock wave reflected from the steel body of the vessel.

Fast pressure sensors were used to measure precisely, the shock wave histories from the reflection on the absorbing materials. Optionally, high-speed cameras were used to record the shock wave reflection behaviour of the tested material.

Different absorbing materials with different thickness were applied to test their attenuation effect of shock wave of hydrogen detonation. The test matrix is shown in Table 67. The final selection of the absorbing materials is in process.

Table 67. Test matrix of absorbing materials' attenuation effect on shock wave.

Absorbing material	Polystyrol	Silicon	Rubber
Thickness, 10 cm	1	3	5
Thickness, 20 cm	2	4	6

4.9.7 Results

The efficiency of absorbing materials to attenuate detonation shock wave will be concluded based on the experimental data.

4.9.8 Delivery Timeline

The experimental work was completed ahead of M36 (February 2022), but the reporting was not. This will be completed by April 2022 and included in D4.4. *Results of the deferred experimental programme and associated activities* and is due for completion by M41 (July 2022).

4.10 Safety technology to prevent tank rupture: Development and manufacturing of four leak no burst composite type IV tanks prototypes for testing in a tunnel fire at CEA and HSE tunnels (4.4.6, UU)

4.10.5 Introduction

Hydrogen-powered vehicles (HPVs) are being developed and deployed in different parts of the world. As with conventional vehicles, there may be unfortunate scenarios arising in the event of an accident: a vehicle fire, for example due to faulty wiring; or a crash of one or multiple vehicles, leading to the ignition of fuel spilled from a gasoline-fuelled vehicle and resulting in a fire.

One of the main concerns of the firefighters approaching the HPV, which will also be the same for compressed natural gas (CNG) vehicles, is the potential for an explosion of the stored

D4.3. Final report on analytical, numerical and experimental studies on explosions, including innovative prevention and mitigation strategies
compressed gas to occur whilst firefighting and rescue activities are being undertaken leading to a fatal blast wave and fireball.

Taking hydrogen cars on London roads as an example, an excellent study on the risks associated with the explosion of an onboard storage tank, using QRA was carried out by Dadashzadeh et al. (Dadashzadeh et al., 2018). The risk would appear to be acceptable if the time from fire start to tank rupture, i.e., FRR, was up to 50 min. However, the reality is that currently, the FRR of hydrogen tanks is only 6-12 minutes (Makarov et al., 2016; Weyandt, 2006, 2005). TPRD and similar means have a comparatively high non-zero probability of a failure to initiate (Dadashzadeh et al., 2018). This would cause tank rupture in a fire, as for example in cases with smouldering fire and CNG tank explosion in the US (Hawkes, 2016; NJ, 2019; Today, 2016). There are certainly ways to increase the FRR of tanks beyond 6-12 min, such as fireproof blankets or intumescent paint (Webster, 2010). However, none of these yet demonstrates that the FRR is increased for a few hours, at least beyond a car fire duration of 2 hours (Mangs and Keski-Rahkonen, 1994).

A technology that would fully exclude a tank rupture in a fire is the ultimate solution and such a solution was developed by UU, i.e., leak-no-burst (LNB) safety technology for composite Type IV gas tanks (Molkov et al., 2018b).

4.10.6 Safety technology description

The UU's intellectual property (IP) "Composite vessel for hydrogen storage" (Molkov et al., 2018b) describes the tank structure. Namely, it has at least one mouthpiece (boss), polymer liner (limiting hydrogen permeation to the regulated level), primary fibre reinforced polymer (FRP) layer and thermal protection layer (TPL) that can also be made of FRP, but of different properties. Figure 142 demonstrates the scheme of the LNB tank in longitudinal middle cross-section.

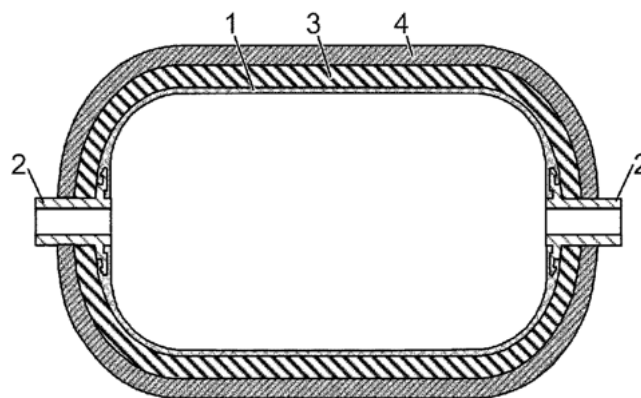


Figure 142. Schematic view of the LNB tank cross-section: 1-liner, 2-bosses, 3-primary FRP layer, 4-TPL layer (Molkov et al., 2018)

Figure 143 shows the currently used "original" and LNB tank behaviour in a fire. Both tanks have a liner and a primary FRP layer. Under fire conditions, the composite material degrades. Firstly, the polymer resin is thermally degraded and hence, the fibre reinforcement becomes unable to bear the pressure load exerted by the hydrogen from within. Thus, the resin degradation front propagates through the wall.

D4.3. Final report on analytical, numerical and experimental studies on explosions, including innovative prevention and mitigation strategies

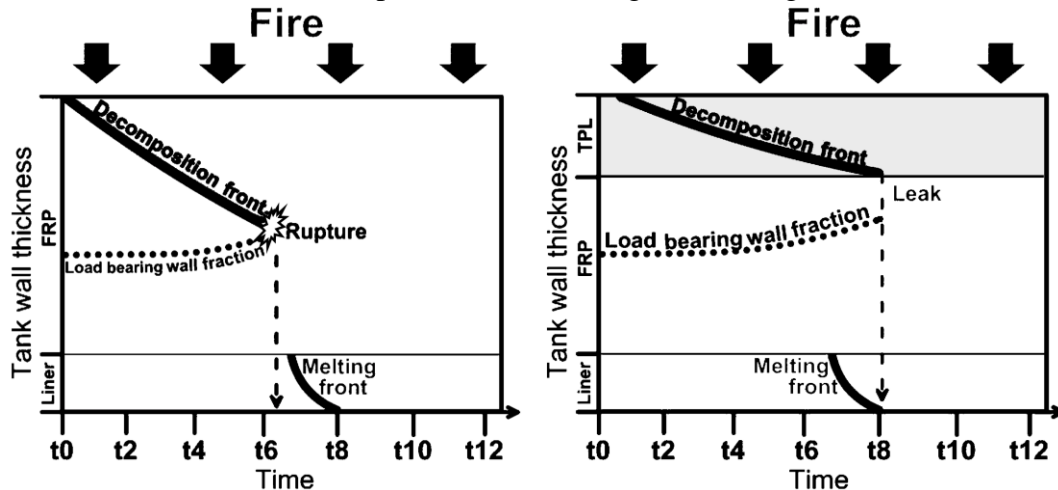


Figure 143. Schematic of LNB safety technology for composite Type IV tanks: original tank (left) and LNB tank (right) in a fire

The tank composite wall is designed to withstand the tank nominal working pressure (NWP) times the coefficient, called safety factor (SF). SF for CFRP is 2.25, i.e., the tank wall can withstand 225% NWP. Since we know that $NWP=700$ bar, then the composite is designed to hold $700 \text{ bar} \times 2.25=1575$ bar. Inversely, if we would like to know what wall fraction holds 700 bar, we take the reciprocal of the SF, $1/2.25=0.44$. Thus, the tank will be able to hold NWP and not explode in a fire, if the fire degrades the composite wall fraction less than $1-0.44=0.56$. However, hydrogen temperature and pressure inside the tank grows in time due to heat transfer from a fire.

This results in an increase of the amount of the wall fraction bearing the constantly increasing load. The tank will rupture when the decomposition front reaches the growing, in time, load-bearing wall fraction, see Figure 143 (left). The liner performance due to heat transfer is also very important. It has a melting temperature less than the decomposition temperature of the resin. It is assumed, that when the liner between the hydrogen and FRP is melted, i.e., melting front goes through its entire thickness, hydrogen would start leaking and being released through the composite, which is hydrogen-pervious, compared to liner material. On the left of Figure 143 the liner is not completely melted; hence, no hydrogen release is initiated.

Figure 143 (right) shows the behaviour of the LNB tank in a fire. The difference of LNB tank design with the original tank is in the additional TPL layer. TPL has lower thermal conductivity and FRP has higher thermal conductivity. The thermal parameters of the liner, TPL and FRP and their thickness are identified and arranged in a way to make the liner melt before the resin decomposition front reaches the load-bearing fraction of the wall.

The leaks distributed over the wall surface cool down the wall material to some extent and thus, reduce the speed of convergence of the decomposition and load-bearing fraction fronts. The pressure in the tank is dropping at the same time, thus preventing tank rupture.

The prototypes were developed at HySAFER but manufactured and successfully tested by other sub-contracting parties. The prototypes were developed to validate the safety technology for high-pressure storage tanks of 7.5 L and 700 bar. Above 40 tank manufacturers/OEMs worldwide were explored.

D4.3. Final report on analytical, numerical and experimental studies on explosions, including innovative prevention and mitigation strategies

4.10.7 Proof of the successful technology operation in other projects

The first prototypes had a CFRP primary layer and glass fibre reinforced polymer (GFRP) outer TPL layer. These prototypes were tested in USA in engulfing fire, and they leaked without rupture. The second LNB tanks also had CFRP primary layer and the TPL layer made of basalt fibre reinforced polymer. All tanks were successfully tested. The list of prototypes is given in Table 68.

Table 68. List of the first successful LNB prototypes.

Prototype name	Volume	NWP	Extra wall thickness	Test result (leak/rupture)
The first prototypes				
COPV1-4	7.5 L	700 bar	20.8 mm	Leak
COPV1-5			28 mm	Leak
The second prototypes				
COPV2-2	7.5 L	700 bar	2 mm	Leak
COPV2-3			1 mm	Leak
COPV2-4			0.5 mm	Leak
COPV2-5			0 mm (original tank wall thickness)	Leak

Figure 144 shows the exteriors of the first and the second prototypes.



D4.3. Final report on analytical, numerical and experimental studies on explosions, including innovative prevention and mitigation strategies

Figure 144. Finished LNB tank prototypes following UU design: left – the first prototypes, right – the second prototypes.

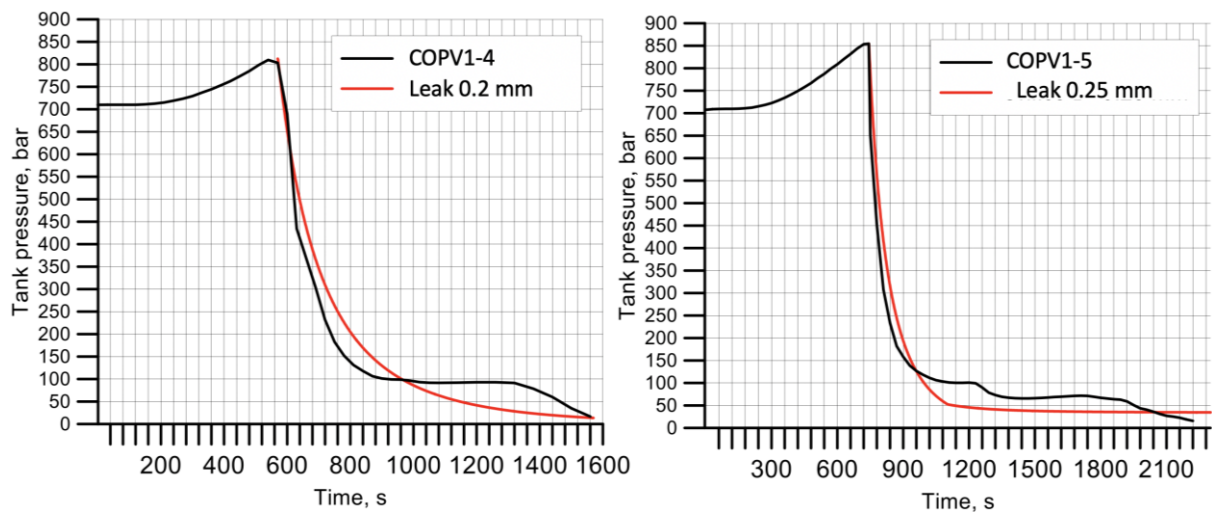


Figure 145. Pressure histories of the first prototypes in fire tests: COPV1-4 and COPV1-5.

Figure 145 shows the pressure readings inside the first prototypes, i.e., COPV1-4 and COPV1-5 (black curves). The red curves show the approximate predictions of the leaks' sizes, as rough reproductions of the pressure curves during the leaks.

Figure 146 shows the pressure and temperature readings inside the tank COPV2-5.

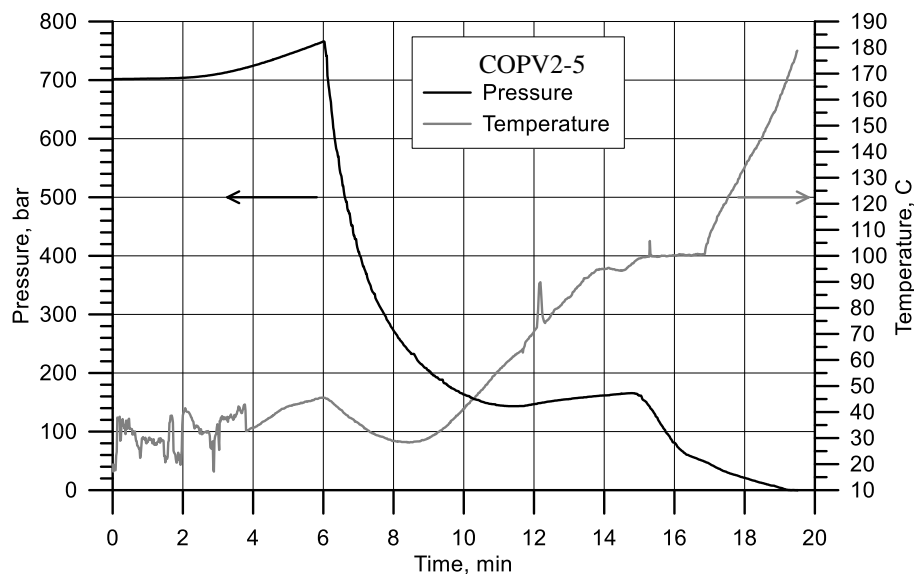


Figure 146. Pressure and temperature histories of the COPV2-5 tank prototype in a fire test.

Figure 147 shows snapshots of fire test with COPV5 tank. The test was conducted following GTR#13, i.e., initiated localised fire was followed by engulfing fire.

D4.3. Final report on analytical, numerical and experimental studies on explosions, including innovative prevention and mitigation strategies

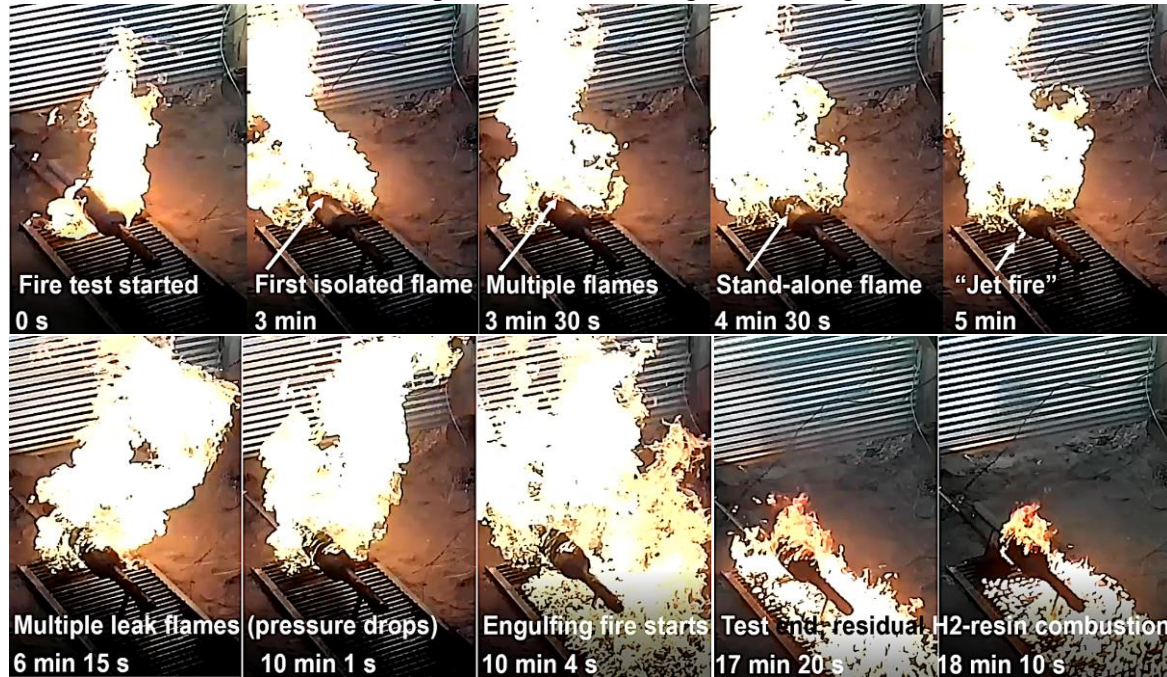


Figure 147. Snapshots of COPV2-5 LNB prototype performance in a fire test.

The sharp decrease of hydrogen pressures inside the tanks demonstrates the start of blowdown due to leaks. For example, for COPV2-5 in Figure 146 it is observed in the fire test at the time of about 6 min. In Figure 147, the snapshot at the time “6 min 15 s” is the first after the pressure in the tank starts to decrease. It doesn’t show any significant, visible change in the burner flame. The difference with the previous photo, “5 min” (before the leak start) is only in that there are a few more tiny flames around the tank surface. During the release, started at 6 min and until 10 min (snapshot “10 min 1 s”) and after, there is no visible change in combustion around the tank. The engulfing fire was initiated at about 10 min. There is no noticeable change in the small flames at the tank surface from the time when the flame is localised, throughout the engulfing fire and until the end of the test. The duration of the fire test, as defined by the drop of the tank inner pressure to atmospheric was 19 min 30 s. Hence, the hydrogen release time lasted for about 13 min 30 s. It was assessed that the estimated leak size (total leak as summarised from all the small leaks across the tank surface) as an equivalent to a diameter of TPRD is about ~0.3 mm.

It is assumed that hydrogen is released through the composite wall in the form of microleaks of different sizes. Not all microleaks can support microflames. They cannot burn in the form of microflames if the flow rate is below the quenching limit (3.9-5.0 $\mu\text{g/s}$ (Butler et al., 2009; Lecoustre et al., 2010; V. Molkov, 2012)) or above the blow-off limit. Microflames cannot be seen by eye (30 s exposure in a dark room is needed). The visible flames are rather either resin combustion flames, or hydrogen flames, together with resin combustion, or hydrogen flames through relatively big channels (leak channel sizes are unidentified). This justifies “no variation” in the visible picture of small flames around the tank surface when the release has started.

4.10.8 Design and manufacture of the LNB tank prototypes in HyTunnel-CS project

In total 10 LNB tank prototypes were designed and manufacture in HyTunnel-CS project. The volumetric capacity is $V=7.5$ L, nominal working pressure $P=700$ bar. The prototypes designs

D4.3. Final report on analytical, numerical and experimental studies on explosions, including innovative prevention and mitigation strategies were built basing on the original Type IV composite overwrapped tanks with minimum burst pressure ratio 2.25 and with HDPE liner. The description of LNB tank prototype designs, including components and objectives of testing is given in Table 69.

Table 69. List of LNB prototypes designed and manufactured in Hy-Tunnel-CS project: materials and objectives.

No	Liner	FRP	TPL	Wall+	Objectives of fire testing series
1	L2	C1	B	+2 mm	Burst test: definition of burst pressure ratio
2 ^a	L2	C1	B	+2 mm	Effect: fibre + resin in protection layer on leak/flame size and P dynamics in the same laboratory (USN) (#2 vs #3)
3 ^a	L2	C1	C2	+2 mm	Effect: fibre + resin in protection layer on leak/flame size and P dynamics in the same laboratory (USN) (#2 vs #3)
4 ^a	L1	C1	C2	+2 mm	Effect: liner type on leak (flame size) and pressure dynamics (#3 vs #4)
5 ^b	L1	C1	C2	+2 mm	Effect: burner/laboratory and repetition of experiment (#4 vs #5)
6 ^a	L2	C1	B	0	Effect: liner type on leak (flame size) and pressure dynamics for original thickness (#6 vs #7)
7 ^a	L1	C1	B	0	Effect: liner type on leak (flame size) and pressure dynamics for original thickness (#6 vs #7)
8 ^b	L1	C1	B	+2 mm	Effect: fibre + resin in protection layer on leak/flame size and P dynamics in the same laboratory (CEA) (#5 vs #8)
9 ^c	L1	C1	B	+2 mm	Performance in a "new" fire scenario – jet fire impingement from nearby storage
10 ^c	L1	C1	B	+2 mm	Performance in a "new" fire scenario – jet fire impingement from nearby storage, experiment repetition (#9 vs #10)

Notes:

^a - prototypes planned be tested at USN, ^b - prototypes planned to be tested at CEA, ^c - prototypes planned to be tested at HSE.

L1 – liner 1 (HDPE cross-linked), L2 – liner 2 (HDPE not cross-linked), C1 – carbon fibre reinforced polymer 1, C2 – carbon fibre reinforced polymer 2, B – basalt fibre reinforced polymer.

Figure 148 shows an example of the burst pressure achievement for prototype No 1. This is to demonstrate that the prototype burst pressure ratio is above that stated for composite overwrap pressure vessels of 2.25 in (Commission Regulation, 2010).

D4.3. Final report on analytical, numerical and experimental studies on explosions, including innovative prevention and mitigation strategies

COPV 1 Burst Data Trace

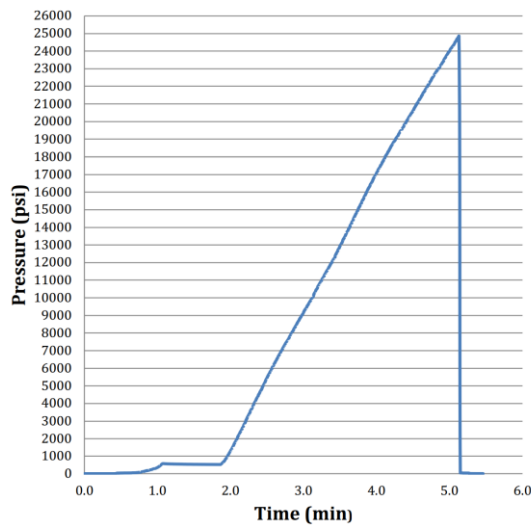


Figure 148. Example of achievement of the burst pressure for prototype No 1: $P_{burst}=24,917 \text{ psi}=1718 \text{ bar}$, giving the burst pressure ratio 2.45.

Table 70 lists the results of hydro burst and hydro static tests of the LNB prototypes.

Table 70. List of results of LNB prototypes undergone hydro burst and hydrostatic tests.

No	Prototype hydro burst pressure	Prototype hydro static pressure	% of NWP (700 bar)
1	1718 bar (24,914 psi)	N/A	245%
2	N/A	1,059 bar (15,365 psi)	151%
3	N/A	1,061 bar (15,393 psi)	152%
4	N/A	1,059 bar (15,363 psi)	151%
5	N/A	1,061 bar (15,391 psi)	152%
6	N/A	1,059 bar (15,355 psi)	151%
7	N/A	1,060 bar (15,370 psi)	151%
8	N/A	1,060 bar (15,374 psi)	151%
9	N/A	See prototype No 7	
10	N/A	See prototype No 8	

The prototypes exterior is depicted in Figure 149.

D4.3. Final report on analytical, numerical and experimental studies on explosions, including innovative prevention and mitigation strategies



Figure 149. The exteriors of the LNB prototypes (No 1-7 are shown).

4.11 Safety technology to prevent tank rupture: Tests on prototypes of “leak no burst” composite type 4 tanks at CEA

4.11.1 Introduction

Hydrogen Fuel Cell Electric Vehicles (HFC EVs) represent an alternative to replace current internal combustion engine vehicles. The use of these vehicles with storage of compressed gaseous hydrogen (CGH_2) or cryogenic liquid hydrogen (LH_2) in confined spaces, such as tunnels, underground car parks, etc., creates new challenges to ensure the protection of people and property and to keep the risk at an acceptable level. Several studies have shown that confinement or congestion can lead to severe accidental consequences compared to accidents in an open atmosphere. It is therefore necessary to develop validated hazard and risk assessment tools for the behavior of hydrogen in tunnels. The HYTUNNEL-CS project sponsored by the FCH-JU pursues this objective. Among the experiments carried out in support of the validation, the CEA is conducting tests on Leak No Burst (LNB) tanks in a full-scale tunnel geometry.

Two tests were performed in which the LNB tanks were engulfed in a localized fire up to the time of the start of the leakage. Then, the fire was shut down and the depressurization of the LNB tank was monitored as well as the behavior of the gaseous atmosphere around the tested tank.

The relevant information regarding the test geometry, the detail of injection, the type of sensors as well as their locations are provided in one document:

For the tests 2021:

Sauzedde et al (2021), *CEA Experimental devices Tests of 2021*.

D4.3. Final report on analytical, numerical and experimental studies on explosions, including innovative prevention and mitigation strategies

The report is organized as follows: in a first paragraph, the geometry used for the test is described. Then, the different phases of the test are detailed. Finally, the results are provided for the behavior of the tank but also that of the gaseous atmosphere surrounding it with conclusions at the end.

4.11.2 Test geometry

Two 7.5L tanks were tested. The first one has the number X04022021-COPV8 and the second one is X04022021-COPV5. These tanks are placed on a burner at the localized fire area.

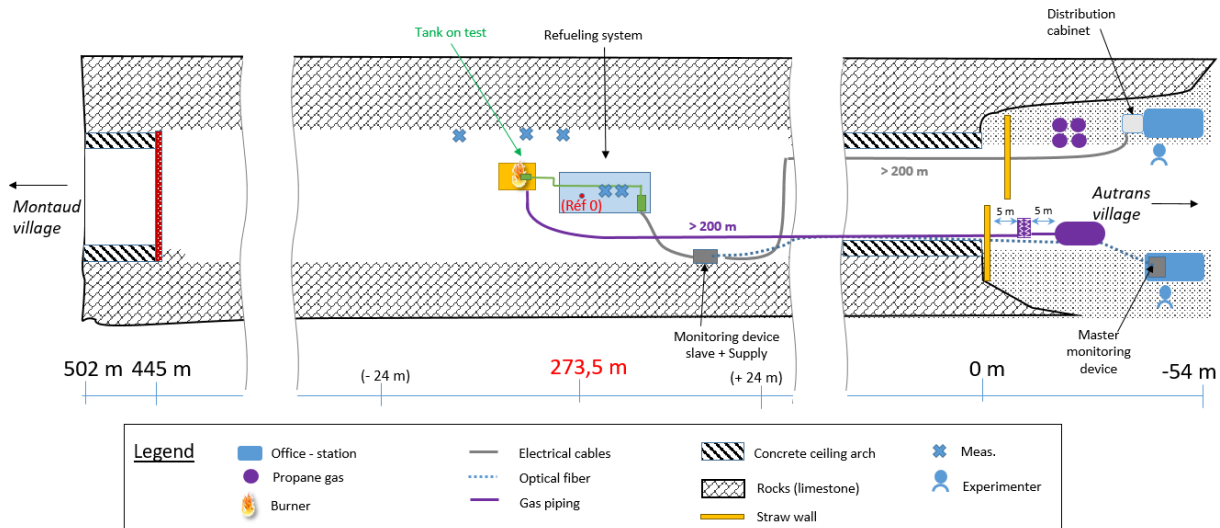
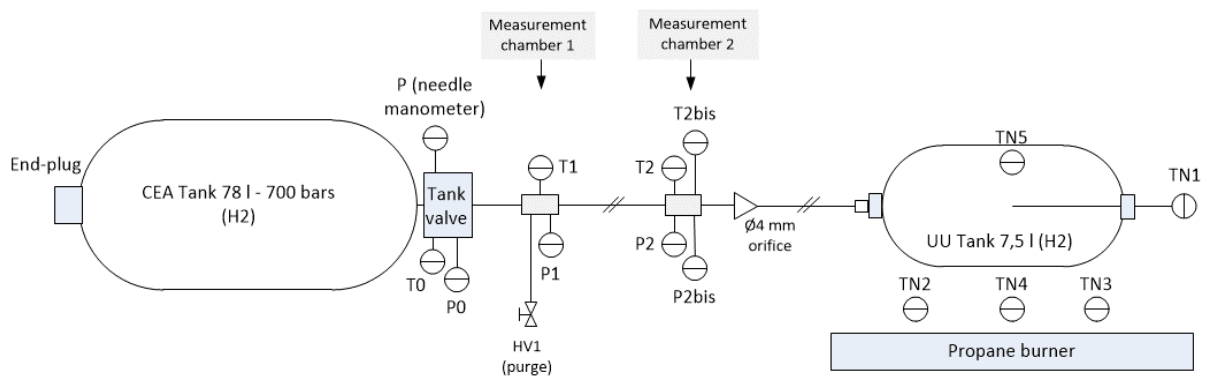


Figure 150. Schematic representation of the test.

Both tests were performed in the tunnel du Mortier at approximately 275 m from the main entrance on the Autrans side (Figure 150). This allowed us to use the hydrogen release system designed for the tunnel dispersion tests. For this purpose, we have a 78-litre master tank containing hydrogen under a pressure of about 700 bar. This tank is connected to the tank to be tested via a pipe comprising several elements, which we describe in detail in the following. After initially filling the LNB tank with about 5 bar of nitrogen to dilute the air, the solenoid valve is opened to connect the two tanks and fill the LNB tank. When the pressure is stabilized, the valve is closed. Then the burner is lit only in the localized fire area.



D4.3. Final report on analytical, numerical and experimental studies on explosions, including innovative prevention and mitigation strategies

Figure 151. Sketch of the two tanks and the associated measuring devices.

4.11.3 Description of the piping system

The volume of the gas between the solenoid valve and the inlet of the LNB tank has been calculated to provide these data to the modelers. This total volume was estimated to 1 litre. The different parts are depicted in Figure 152 and the associated free volumes are reported in

Table 71. The geometry of the manufactured TPRD indicated as an orifice of Ø 4 mm in the PID (Figure 151) is detailed.

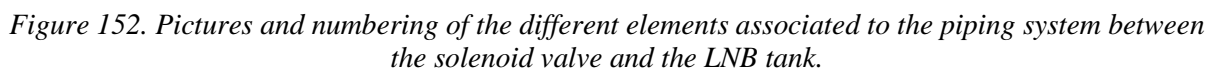
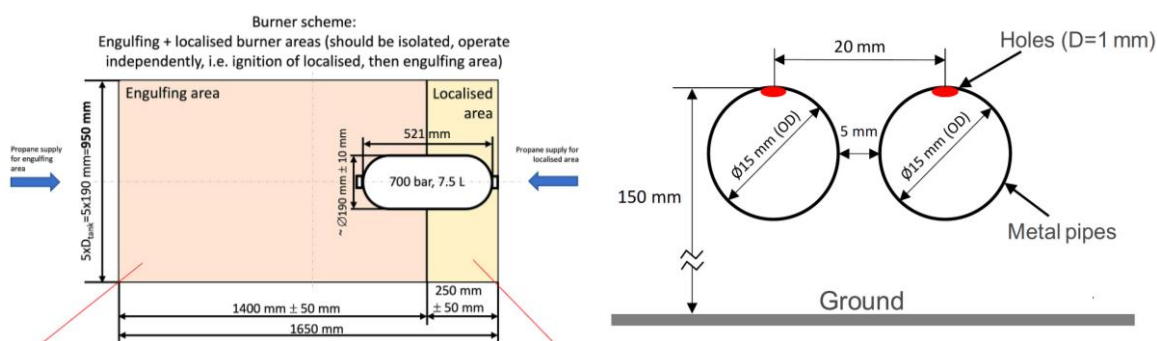


Table 71. Description and estimated internal volumes of the various parts of the connection between the main tank valve and the LNB tank.

N°	Element	Length (cm)	Ø int (cm)	V (cm3)
0	Solenoid valve	23,5	0,75	10,38
1	Flexible pipe	150	0,6	42,41
2	Meas. chamber n°1 with fittings*	21	1,27	26,60
3	Rigid pipe	82	1,11252	79,71
4	Union fitting*	13	1,5	22,97
5	Rigid pipe	193	1,11252	187,61
6	Meas. chamber n°2 with fittings*	28	1,2	31,67
7	Rigid pipe	6	1,11252	5,83
8	"TPRD 4mm" + 1 fitting	See plan		12,32
9	Rigid pipe	63	1,11252	61,24
10	"T" with fittings	15	1,5	26,51
11	Rigid pipe	387,5	1,11252	376,68
12	Bulkhead fitting	14	1,5	24,74
13	Rigid pipe	90,5	1,11252	87,97
14	Connection to tank	7	1,5	12,37
			Total	1009,03

The propane burner was designed according to the principles described in Figure 153. It consists of two zones to simulate a localized and an engulfing fire.



The picture of the burner before the tests is provided in Figure 154.

D4.3. Final report on analytical, numerical and experimental studies on explosions, including innovative prevention and mitigation strategies

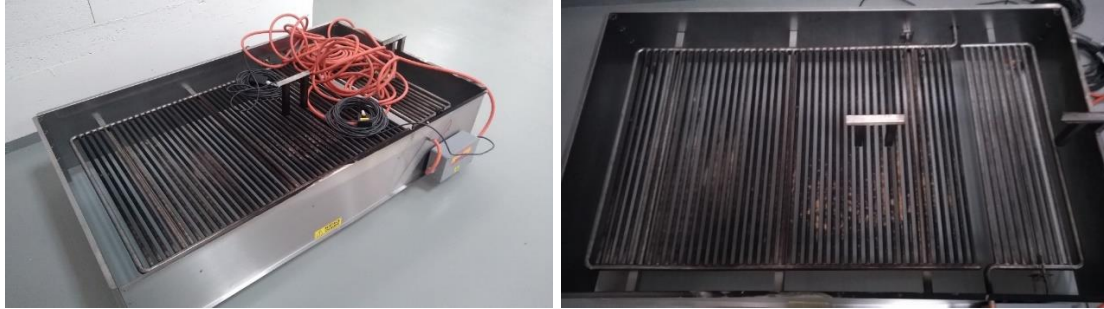


Figure 154. Picture of the propane burner with the two zones on the right picture: engulfing area (left side) and localized area (right side).

The dimensions of the ramps are:

- For the localized fire 300x900 mm with 9 pipes.
- For the engulfing fire 1340x900 mm with 43 pipes.

The pipes have an outer diameter (O.D.) of 16 mm and a thickness of 1 mm. They are made of stainless steel 304L. The spacing between pipes is 30 mm and the upper holes have a diameter of 1.5 mm and are located every 30 mm. A single tube of 21.3 mm O.D. and 1.3 mm thickness feeds each burner. The ramps are installed in a box (353 mm height for the surrounding plate and 80 mm for the 4 supporting tubes located at the four corners) and located 310 mm above the floor. The burner is fed by a propane tank with liquid extraction and evaporators. The propane flow rate during the operation of the different parts of the burner (localized, engulfing and localised + engulfing) was measured during qualification tests at different pressure levels at the supply (evaporator outlet) and with the same piping. The flow meter then failed and we do not have the time monitoring of the flow during the performed tests.

However, an operator oversaw checking the adjustment of the supply pressure during the tests to guarantee the desired flow rate to achieve a heat release rate (HRR) of 1 MW/m². UU has provided two propane mass flowrates to satisfy the requested HRR: 4.2 g/s for the localized fire and 23.4 g/s for the engulfing fire.

The position of the burner is depicted in Figure 155.

D4.3. Final report on analytical, numerical and experimental studies on explosions, including innovative prevention and mitigation strategies

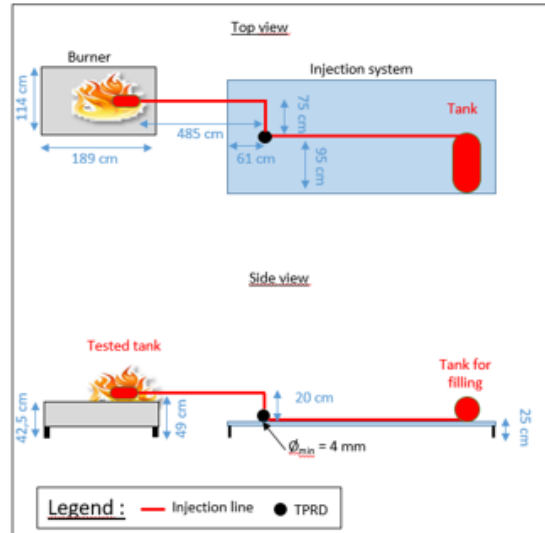


Figure 155. Position of the burner.

4.11.5 Measurement devices

During the tests, the pressure inside the LNB tank is monitored by the pressure sensor P1 (WIKA, 0-750bar, 0.25% BFS) installed on the first measurement chamber (Figure 151). Other pressure sensors are mounted on the connecting pipe in the measurement chambers: P0 inside the main tank (PRIGNITZ, 0-1000bar, between -40°C and 105°C 2%FS), P2 (same type as P1) and P2BIS (same type as P0) inside the second measurement chamber.

Five N-type thermocouples of 1 mm in outer diameter have been installed on the LNB tank. TN1 is used to monitor the temperature inside the LNB tank. TN5 is devoted to the upper surface temperature. The three others (TN2, TN3 and TN4) are used to monitor the gas temperature between the burner and the LNB tank below the tank. The exact position of the thermocouples is described in Figure 156. Three other temperatures are provided in the results, and they correspond to T0 (K-type thermocouple inside the main tank), T1 and T2 (T-type thermocouples inside the first and the second measurement chambers).

D4.3. Final report on analytical, numerical and experimental studies on explosions, including innovative prevention and mitigation strategies

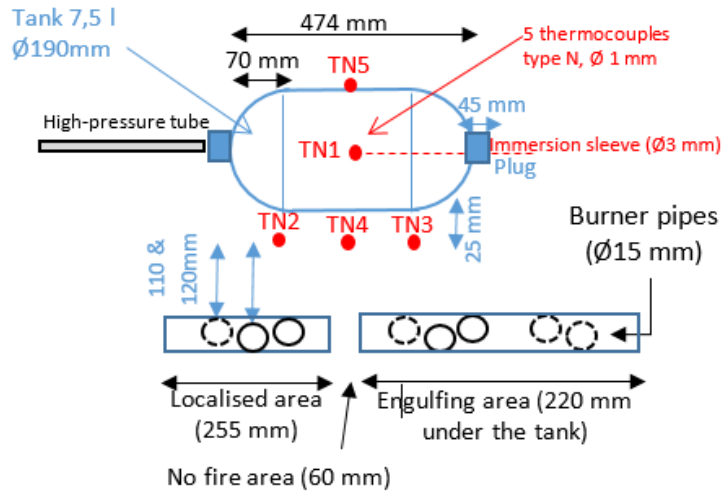


Figure 156. Location of dedicated N-Type thermocouples.

Seven heat flux sensors (CAPTEC 30x30mm) monitor the radiative heat flux (IR and visible): two are installed nearby the burner, four on the main chassis and one at 5 m back of the burner (Figure 157). Their exact positions can be viewed in a separate document (Sauzedde et al., 2020).



Figure 157. Location of the radiative heat flux sensors.

The tunnel is also fully equipped with sensors to monitor the gas temperature, the hydrogen concentration, and the relative humidity as well as the wind velocity. These sensors were not connected to the main objectives of these tests. Consequently, only the relevant information is reported in this document. The location of these sensors is reported in a separate document (Sauzedde et al., 2020) with the reference point (0,0,0) on top of the TPRD. The x axis is directed horizontally towards the walls of the tunnel, the y axis is oriented along the tunnel axis with the positive direction going to Autrans side and the z axis is oriented vertically. The slope of the tunnel is 3.6% and Autrans side corresponds to the upper part.

D4.3. Final report on analytical, numerical and experimental studies on explosions, including innovative prevention and mitigation strategies

4.11.6 Test sequence

The test sequence is divided into several phases:

- Phase 1: connection of the tested empty tank to the main pipe.
- Phase 2: injection of about 5 bar of nitrogen into the tested tank for inertisation purposes. The solenoid valve of the main tank is closed, and nitrogen is injected from a pressurized bottle through the purge line (HV1).
- Phase 3: filling of the LNB tank. The solenoid valve of the main tank is open to connect the LNB and the main tank together. The pressure inside the LNB tank is monitored via the different pressure sensors installed along the pipe. When the pressure is stabilized, the solenoid valve is closed.
- Phase 4: degradation of the LNB tank by the localized fire. At the beginning of the phase, the burner is switch on with a constant power of 1 MW/m² and only in the localized fire area. This phase ends when the LNB tank starts to leak.
- Phase 5: depressurization of the damaged LNB tank. Just after the start of the leakage, the localized fire is switched off and the pressure decrease inside the LNB tank is monitored. This phase ends when the pressure inside the LNB tank stays almost constant for at least 10 minutes.
- Phase 6: if the pressure inside the tank is not the atmospheric pressure, the burner is then switched on to restart the leakage process and finally depressurize the LNB tank.

Time zero has been set to the beginning of Phase 4.

D4.3. Final report on analytical, numerical and experimental studies on explosions, including innovative prevention and mitigation strategies

4.11.7 Test results

In the following paragraphs, the two tests, which are nearly identical, are compared. The first column corresponds to test 1 (Test 19 in the global test matrix of CEA tests) and the second to test 2 (Test 20).

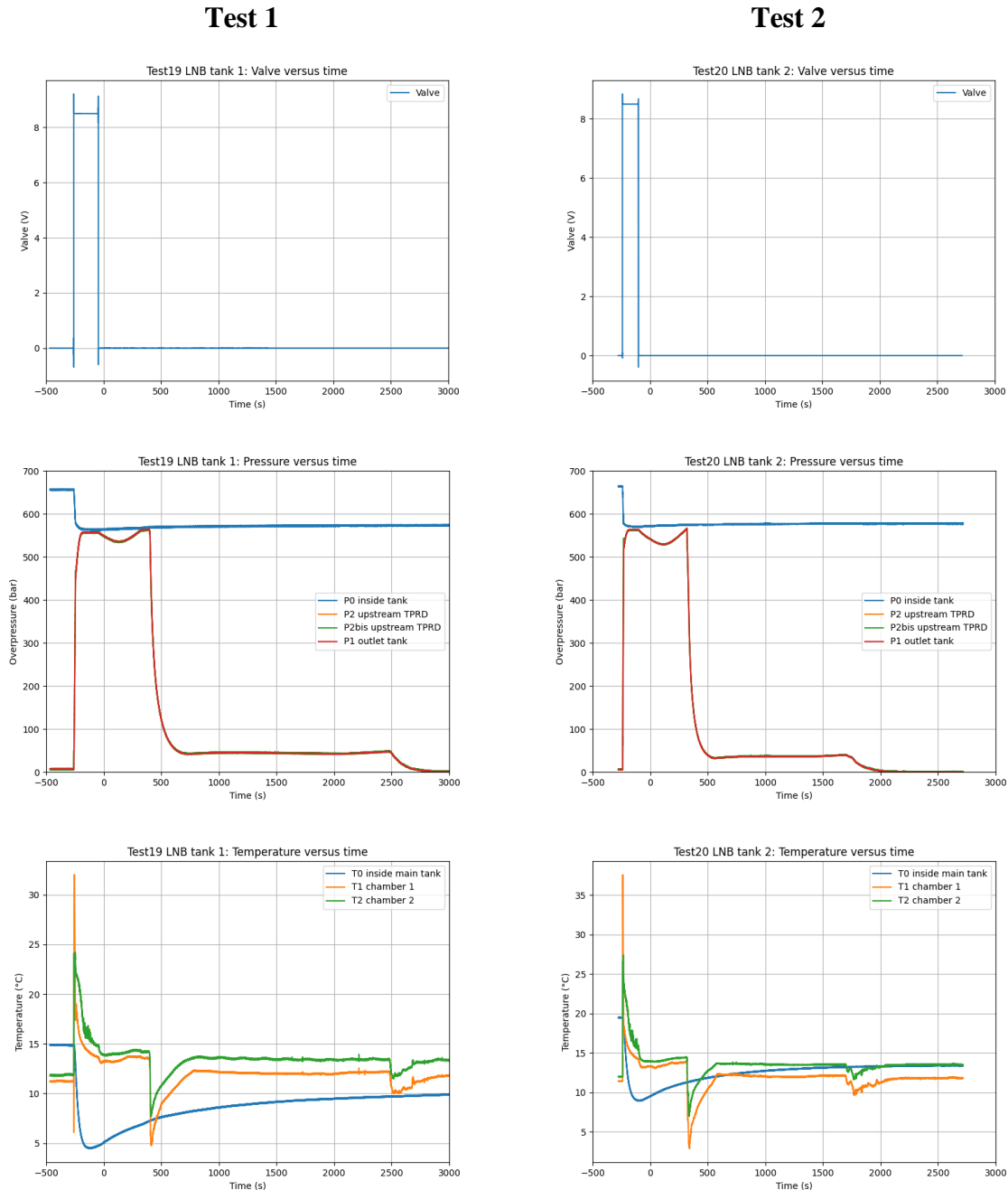


Figure 158. Inside tanks and pipes behavior – Top: solenoid valve opening to fill the LNB tank – Center: Overpressure in the main tank and in measurement chambers – Bottom: Temperature in the main tank and in the measurement chambers.

First, the test sequence begins with the opening of the solenoid valve between the main tank and the LNB tank (Figure 158 Top). In both tests, the filling time is very short (< 200s). For the pressure (Figure 158 Center), the main tanks had been filled to 700 bar when hot which

D4.3. Final report on analytical, numerical and experimental studies on explosions, including innovative prevention and mitigation strategies

gives at the time of the test about 650 bar (Figure 158 Center P0). The LNB tank is therefore filled with a pressure between 540 and 550 bar (Figure 158 Center P1).

This rapid filling of the LNB tank induces an increase in internal temperature, which reaches about a hundred degrees (Figure 159 Top TN1). Then, the evacuation of this heat takes time, and a thermal transient is observed (Figure 159). This cooling induces a slight pressure drop (Figure 158 Center P1) but as the burner is activated during this transient (at time zero), the heat input by the fire leads to a pressure increase. The two effects compensate each other. For a possible numerical simulation, it was therefore essential to consider the filling phase.

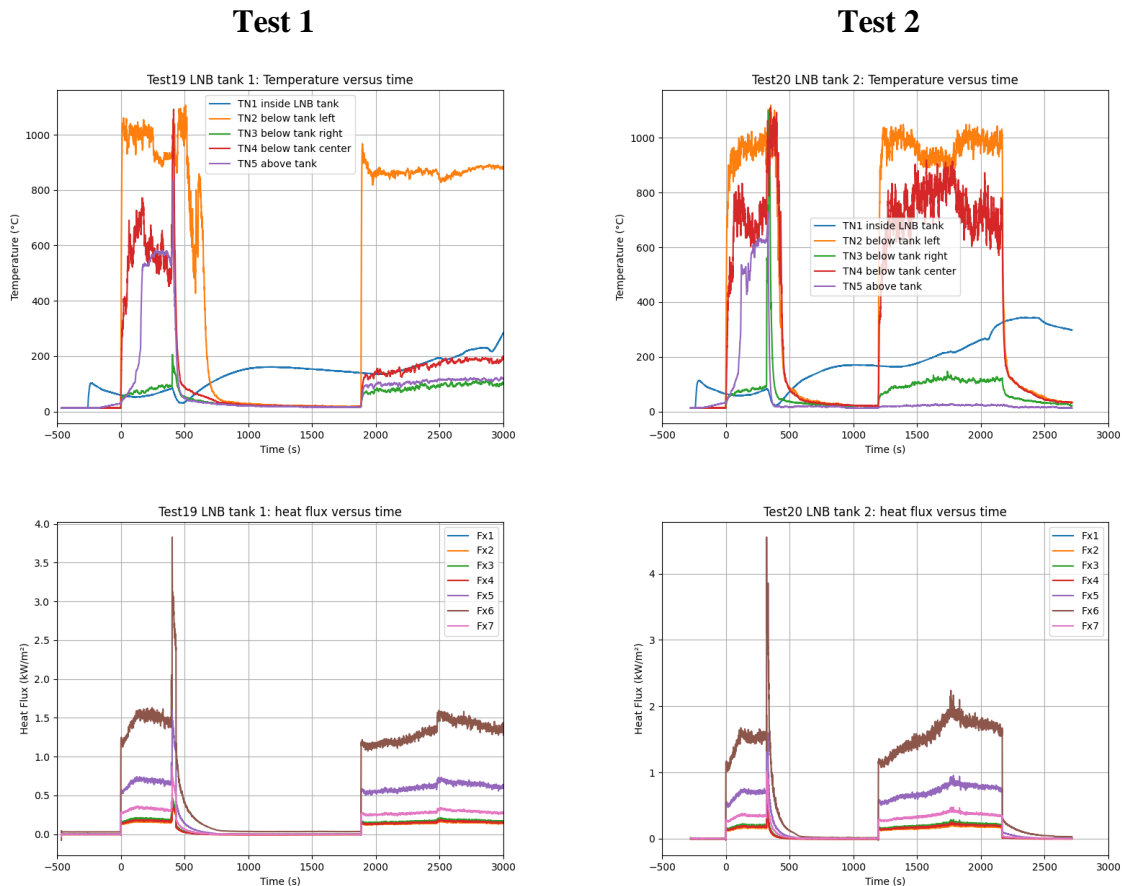


Figure 159. Behavior around the LNB tanks – Top: Temperatures – Bottom: Radiated heat fluxes.

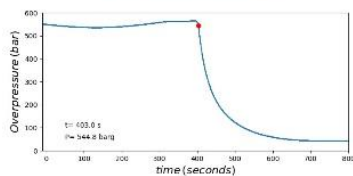
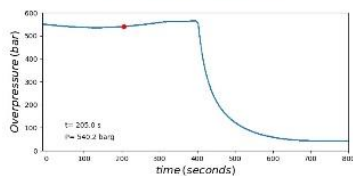
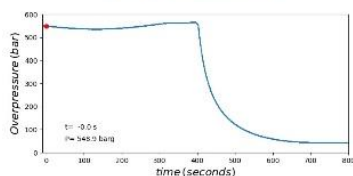
Then, the burner causes an increase in internal pressure (Figure 158 Center P1), a heating of the external envelope of the tank (Figure 159 Top TN5) and a beginning of degradation from the outer envelope to the inner one. This phase is globally very reproducible in both tests. The localized fire only affects the part of the tank closest to the chassis and, in particular, the TN3 thermocouple undergoes only a slight temperature increase. The temperature measured on the upper surface (TN5) reaches in both cases a plateau around 600°C. This phase 4 continues until the beginning of the leak of the LNB tank. The leakage time is different in the two tests, it is shorter in test 2 than in test 1 (Table 72). This difference can perhaps be explained by the different nature of the composition of the tank's inner liner. The numerical simulation will be able to confirm or deny this hypothesis.

D4.3. Final report on analytical, numerical and experimental studies on explosions, including innovative prevention and mitigation strategies

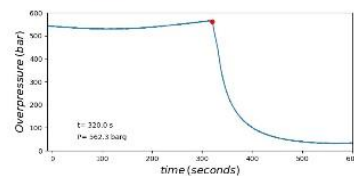
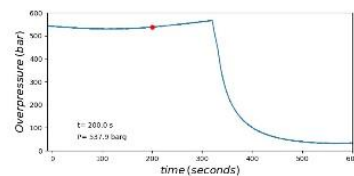
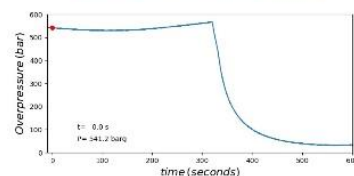
Table 72. Time occurrence of the main events.

Event	Test 1	Test 2
Start of the burner	0 s	0 s
Start of leakage	402 s	319 s
Stop of the burner	433 s	332 s
Stop of flames on the tank	761 s	600 s
Restart of the burner	1882 s	1195 s
Restart of the leakage	~2480 s	~1700s

Test 1



Test 2



D4.3. Final report on analytical, numerical and experimental studies on explosions, including innovative prevention and mitigation strategies

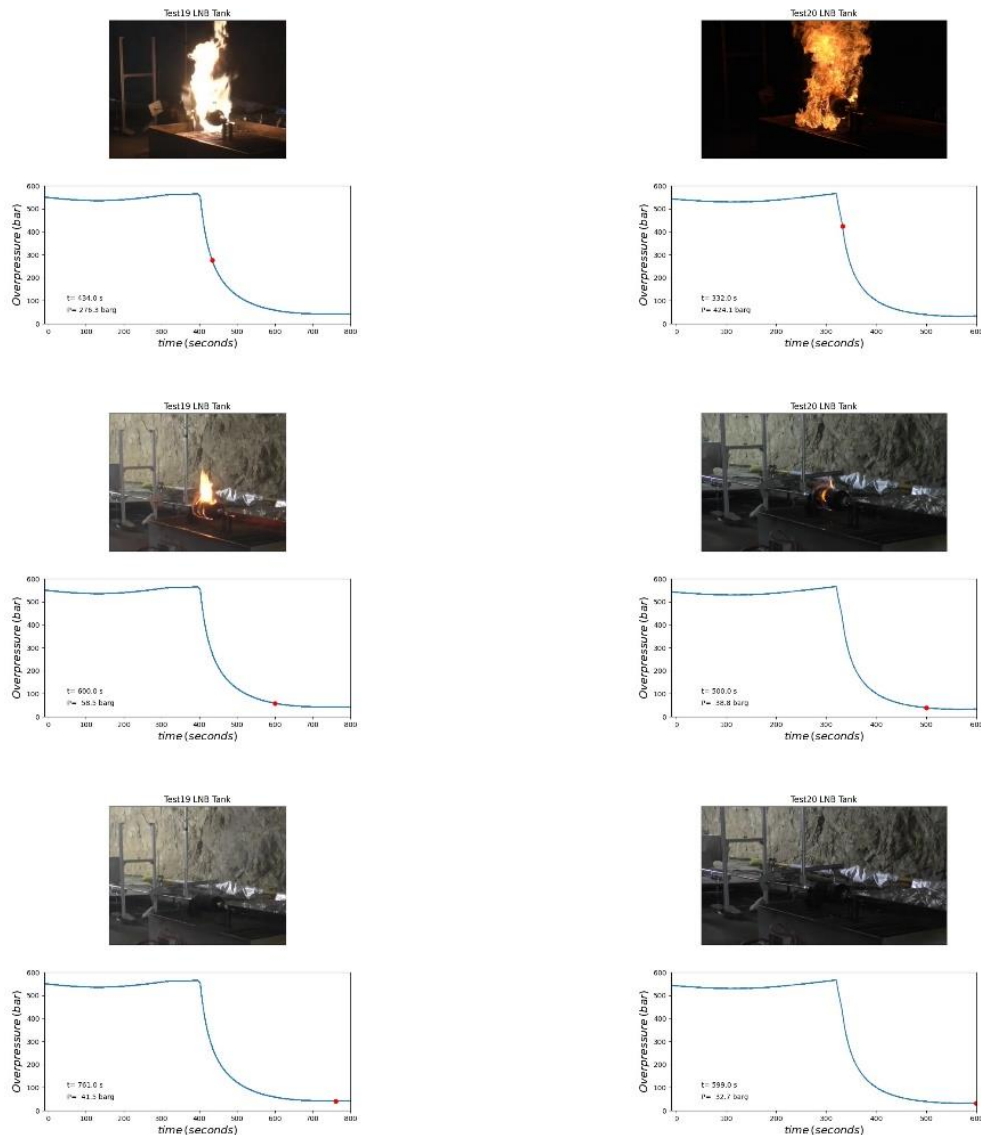


Figure 160. Synchronized behavior between overpressure inside the LNB tank and picture of the fire during phase 4 and 5.

At the beginning of the leak, there is a strong visual change of the flame, which grows strongly (Figure 160 third image). This is followed by a strong increase in the radiated flux (Figure 159 Bottom) and a very loud whistling noise of gas leakage. It seems that in test 1 the sudden depressurization has modified the position of some thermocouples.

In particular, the TN4 thermocouple has probably moved away because its measured temperature drops very suddenly (Figure 159 Top) while on the images, the flames continue to affect the zone where it is supposed to be located

After a few seconds of leakage, the burner is stopped, and the combustion continues around the tank (Figure 160 Fourth image). It is necessary to wait a few minutes before seeing the flames disappear. At this moment, the pressure in the tank has not fallen to the level of atmospheric pressure but to a value around a few tens of bar (about 43 bar in test 1, and 33 bar for test 2).

D4.3. Final report on analytical, numerical and experimental studies on explosions, including innovative prevention and mitigation strategies

This value does not decrease anymore for at least 15 minutes (waiting time during test 1). In the second test, as the phenomena were identical, the waiting time was shorter (only about 10 minutes). During this phase, the only measured quantity that increases is the temperature inside the LNB tank due to heat transfer (Figure 158 Top TN1).

After the waiting time, the burner is restarted (Figure 159 Bottom Fx6). Temperatures rise again and it takes between 400 and 600 seconds for the leak to restart. As in the first phase, the tank in test 2 reacts faster than in test 1. Since in both cases the internal pressure is much lower, the restart of the leak is much less impressive. The fire was maintained until the tanks were completely depressurized.

As for the thermocouples placed around the tank (Figure 159 Top), the absence of reaction of TN4 shows that it has probably changed position. Moreover, TN5 also seems to have been affected by the first phase. For the other measured quantities, this does not bring any particular information. Examination of pictures taken after the tests have shown that in the first test, TN2 has moved upward but has stayed within the fire and TN4 and TN5 have changed position. In the second test, TN5 has been thrown away.

Concerning the flow rate of the release, it has been calculated with the method of the mass balance in the bottle. In this method, the temperature and pressure in the nearest measuring chamber (P2 and T2) are used to determine the density variation (ρ_{gas}). The mass of the gas is computed using the obtained density and the volume of the tank (V_{tank}). The mass flow rate (56) $Q_{m_{\text{mass balance method}}}$ is computed using the mass balance method for the complete duration of the blowdown period.

$$M_{\text{gas}} = P_{\text{gas}} \times V_{\text{tank}} \quad Q_{m_{\text{mass balance method}}} = \frac{\Delta M_{\text{gas}}}{\Delta T} \quad (70)$$

The logarithmic scale is considered in Figure 161 for a better visualisation of the mass flow.

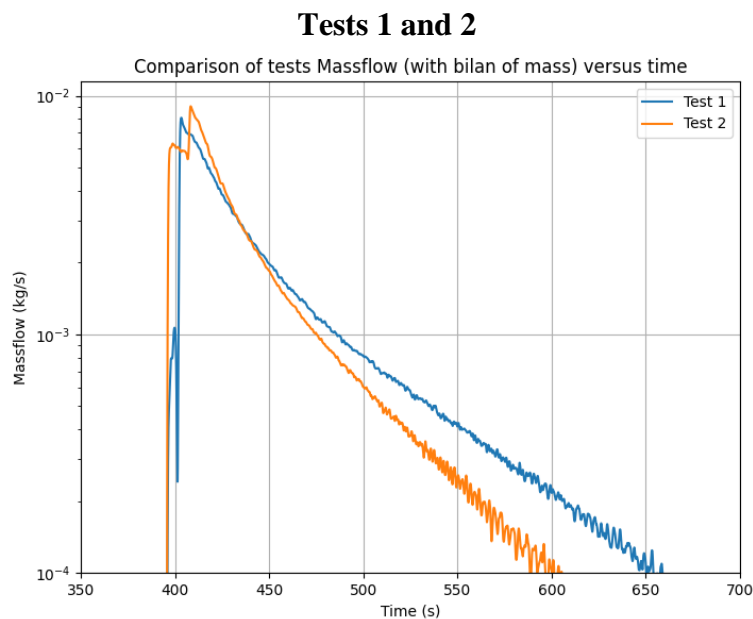


Figure 161. Mass flow rate of the leaks for test 1 and 2.

D4.3. Final report on analytical, numerical and experimental studies on explosions, including innovative prevention and mitigation strategies

For the two tests we observed a leak in two times with an increasing of the mass flow in the beginning. The mass flow evolution is afterwards different for the two tanks. The mass flow of the test 1 drops more slowly as the test 2.

This mass flow can be compared with a simulation of a gas release through a calibrated orifice using the sonic nozzle method. This method uses the theoretical model “Barré de Saint Venant” to compute the mass flow for a sonic regime $Q_{m_{\text{sonic nozzle method}}}$, which can be encountered at the exit of the TPRD of the experimental setup. The geometry and the surface quality are not considered in this method and is corrected by introducing the discharge coefficient (C_d). However, in the absence of data on this coefficient for the cases of leaks through a porous membrane, the $C_d = 1$ is considered.

$$Q_{m_{\text{sonic nozzle method}}} = C_d \cdot S \cdot \sqrt{\gamma \cdot P \cdot \rho \times \left(\frac{2}{\gamma + 1} \right)^{\frac{\gamma+1}{\gamma-1}}} \quad (71)$$

The surface of this calibrated orifice allows to find an approximation of diameter equivalent of the gas released in the tank.

D4.3. Final report on analytical, numerical and experimental studies on explosions, including innovative prevention and mitigation strategies

In Figure 162 the mass flow simulation of a gas release through an orifice of 0.58 mm fits properly to the mass flow of the LNB tank. The values of equivalent diameter found with this method are, for the test 1, 0.58mm and, for the test 2, 0.65mm.

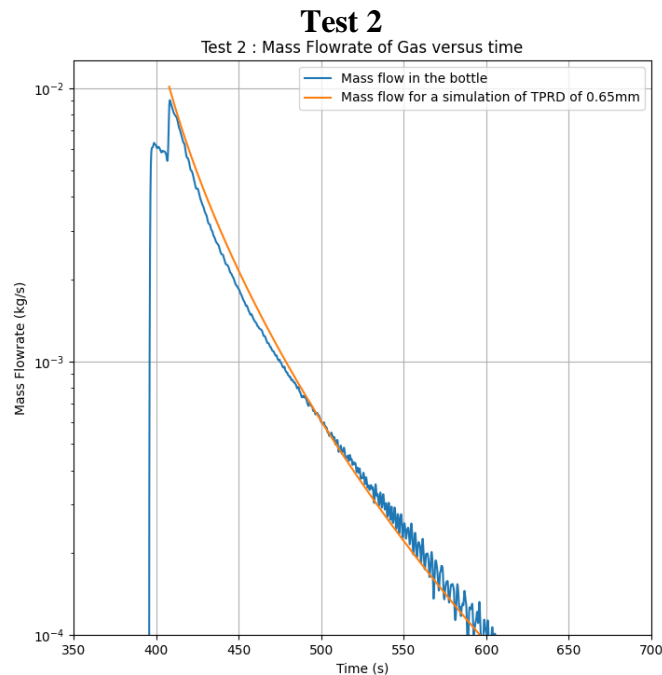


Figure 162. Comparison of mass flow rate's test 2 (Simulated and calculated).

The measurements made in the tunnel do not provide much information for these two tests. However, the measurements with the 2D anemometer show a flow when the burner is in operation (Figure 163 Top). It seems that the flow at this sensor located at (0, +17.6, +1.6) is mainly directed from the burner to the tunnel exit on the Autrans side. Nevertheless, oscillations of the direction are noted (Figure 163 Bottom).

D4.3. Final report on analytical, numerical and experimental studies on explosions, including innovative prevention and mitigation strategies

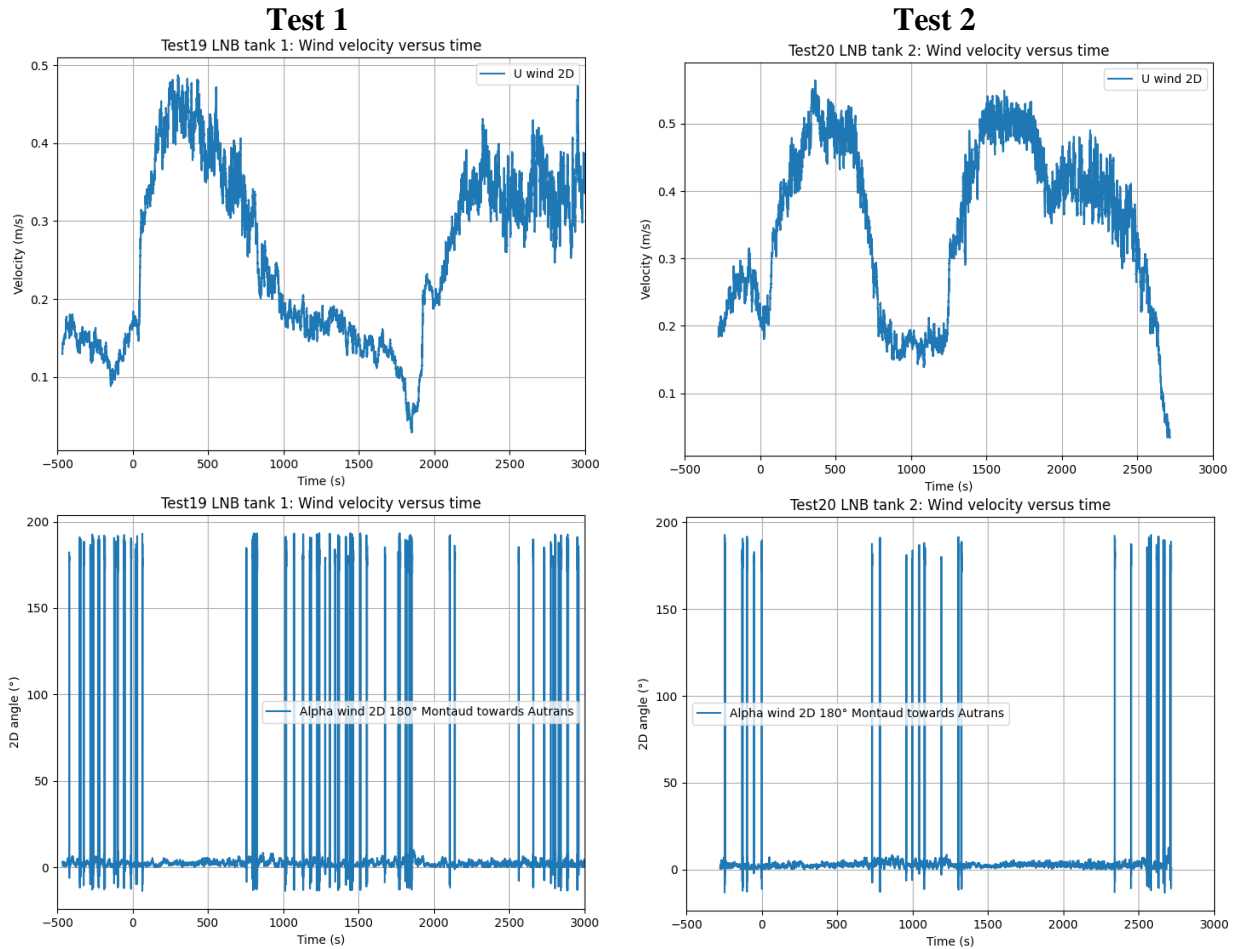


Figure 163. Measured wind velocity and angle during the tests.

Finally, the sensors installed in the upper part of the tunnel allow highlighting the flow of hot gases from the burner (Figure 164). On masts 3 and 8, the temperature increases can reach 7-10°C whereas at +/- 50m (masts 1 and 10) this value is only 3-5°C. The highest values are measured towards Autrans, which confirms the anemometer measurement.

The hydrogen measurements have only shown some thermal deviations.

D4.3. Final report on analytical, numerical and experimental studies on explosions, including innovative prevention and mitigation strategies

Test 1

Test 2



Figure 164. Measured gas temperature close to the top of the tunnel at different distances along the tunnel axis.

D4.3. Final report on analytical, numerical and experimental studies on explosions, including innovative prevention and mitigation strategies

4.11.8 Conclusions

This document summarizes the initial conditions, the boundary conditions, and the results of two tests of the behavior of 7.5 LNB tanks under approximately 550 bar of hydrogen when placed in a localized fire. The sequence adopted assumes that the fire is extinguished just at the start of the leak. The mass flow rate of the leaks is equivalent of gas release through a hole of about 0.6 mm. This situation generates a kind of reclosing of the leakage paths and thus a residual pressure in the tank between 30 and 40 bar. This new phenomenon, which is reproducible, will therefore require a more complete analysis involving detailed numerical simulations and probably expertise from the designers.

5 References

- Arntzen, B. J., 1998. Modelling of Turbulence and Combustion for Simulation of Gas Explosions in Complex Geometries.
- Battersby, P.N., Averill, A.F., Ingram, J.M., Holborn, P.G. & Nolan, P.F., 2012. Suppression of hydrogen-oxygen-nitrogen explosions by fine water mist: Part 2. Mitigation of vented deflagrations. *International Journal of Hydrogen Energy*, 37(24), pp.19258–19267.
- Bassan, S., 2016. Overview of traffic safety aspects and design in road tunnels. *IATSS Res.* 40, 35–46.
- Birch, A.D., Brown, D.R., Dodson, M.G. & Swaffield, F., 1984. The structure and concentration decay of high-pressure jets of natural gas. *Combustion Science and Technology*, 36(5–6), pp.249–261.
- Bjerketvedt, D., Bjørkhaug, M. Experimental investigation — Effect of water sprays on gas explosions. Prepared by Chr. Michelsen Institute for the Department of Energy. UK. OTH 90 316. HMSO. London, 1991.
- Bollinger LE, Fong MC, Edse R., 1961. Experimental measurements and theoretical analysis of detonation induction distance. *Am Rocket Soc J* 1961; 31:588.
- Butler, M.S., Moran, C.W., Sunderland, P.B., Axelbaum, R.L., 2009. Limits of hydrogen leaks that can support stable flames. *Int. J. Hydrogen Energy* 34, 5174–5182.
- C. Smith, A., J. Sapko, M., 2005. Detonation wave propagation in underground mine entries 58.
- Cao, X. yan, Bi, M. Shu, Ren, J. Jie & Chen, B., 2019. Experimental research on explosion suppression affected by ultrafine water mist containing different additives. *Journal of Hazardous Materials*, 368, pp.613–620.
- Chen, C., Rodi, W., 1980. Vertical turbulent buoyant jets - a review of experimental data. Pergamon Press, Oxford.
- Ciccarelli, C. Dorofeev, S., 2008. Flame acceleration and transition to detonation in ducts, *Progress in Energy and Combustion Science*, Volume 34, Issue 4, 2008, Pages 499-550
- Cirrone, D., 2018. Hazards from catastrophic failure of high-pressure hydrogen storage, PhD Thesis, Ulster University.
- Commission Regulation, 2010. No 406/2010 implementing Regulation (EC) No 79/2009 of the Parliament and of the Council on type-approval of hydrogen-powered vehicles. Off. J. Eur. Union.
- Curran, D.R., Norway, Forsvarets forskningsinstitutt, 1966. Underground storage of ammunition: experiments concerning accidental detonation in an underground chamber. Norwegian Defence Construction Service, Kjeller, Norway.
- Dadashzadeh, M., Kashkarov, S., Makarov, D., and Molkov, V., 2017. Socio-Economic Analysis and Quantitative Risk Assessment Methodology for Safety Design of Onboard

- D4.3. Final report on analytical, numerical and experimental studies on explosions, including innovative prevention and mitigation strategies
Storage Systems, in International Conference on Hydrogen Safety, Hamburg, 2017, vol. 184.
- Dadashzadeh, M., Kashkarov, S., Makarov, D., Molkov, V., 2018. Risk assessment methodology for onboard hydrogen storage. *Int. J. Hydrogen Energy* 43, 6462–6475. <https://doi.org/10.1016/j.ijhydene.2018.01.195>
- Dadashzadeh, M., Makarov, D., Kashkarov, S., Molkov, V., 2019. Non-adiabatic under-expanded jet theory for blowdown and fire resistance rating of hydrogen tank. Presented at the International Conference on Hydrogen Safety, Adelaide, Australia.
- Danfoss Fire Safety A/S, 2013. SemSafe Watermist Systems product catalogue, Nozzle Type HNMP-5-10-1.19-00 P, Odense, Denmark, 2013.
- Daubech, J., Simon, J., 2016. Un-ignited and ignited high pressure hydrogen releases: Concentration - Turbulence mapping and overpressure effects. <https://doi.org/10.1016/j.jlp.2015.05.013>
- Dorofeev, S.B., Sidorov, V.P., Efimenko, A.A., Kochurko, A.S., Kuznetsov, M.S., Chaivanov, B.B. et al., 1995. Fireballs from deflagration and detonation of heterogeneous fuel-rich clouds. *Fire Safety Journal* 1995, 25, pp. 323–336. [https://doi.org/10.1016/0379-7112\(96\)00008-2](https://doi.org/10.1016/0379-7112(96)00008-2).
- Dorofeev, S.B., Sidorov, V.P., Kuznetsov, M.S., Dvoinishnikov, A.E., Alekseev, V.I., Efimenko, A.A., 1996. Air blast and heat radiation from fuel-rich mixture detonations. *Shock Waves* 1996, 6, pp. 21–28.
- Dorofeev, S.B., Sidorov, V. P., Kuznetsov, M. S., Matsukov, I. D., Alekseev, V. I., 2000. Effect of scale on the onset of detonations. *Shock Waves*, 2000, v. 10, pp. 137-149
- Dorofeev, S.B., Kuznetsov, M.S., Alekseev, V.I., Efimenko, A.A., Breitung, W., 2001. Evaluation of limits for effective flame acceleration in hydrogen mixtures. *Journal of Loss Prevention in the Process Industries*, 2001, Vol 14/6, pp. 583-589. DOI: [http://dx.doi.org/10.1016/S0950-4230\(01\)00050-X](http://dx.doi.org/10.1016/S0950-4230(01)00050-X)
- European Maritime Safety Agency, 2015. Risk acceptance criteria and risk-based damage stability. Final report, part 1 : risk acceptance criteria.
- Fang, Y., Zou, Y.-L., Zhou, J., Yao, Z., Lei, S., Yang, W., 2019. Field Tests on the Attenuation Characteristics of the Blast Air Waves in a Long Road Tunnel: A Case Study. *Shock Vib.* <https://doi.org/10.1155/2019/9693524>
- Friedrich, A. Grune, J. Sempert, K. Kuznetsov, M, Jordan, T., 2019. Hydrogen combustion experiments in a vertical semi-confined channel, *International Journal of Hydrogen Energy*, Volume 44, Issue 17, 2019, Pages 9041-9049
- Friedrich, A., Vesper, A., Jordan, T., 2021. PRESLEY D5.4. Summary of experiment series E5.1 (Ignited discharge) results.; 2021
- Gavrikov, A.I., Efimenko, A.A., Dorofeev, S.B., 2000. A model for detonation cell size prediction from chemical kinetics, *Combustion and Flame*, Volume 120, Issues 1–2, 2000, Pages 19-33

- Page 233 of 243

- D4.3. Final report on analytical, numerical and experimental studies on explosions, including innovative prevention and mitigation strategies
- HyTunnel-CS D4.1, 2019. Deliverable 4.1 Detailed research programme on explosion in underground transportation systems.
- HyTunnel-CS D4.4, 2022. Deliverable D4.4 Results of the deferred experimental programme and associated activities, July 2022
- Jallais, S., Vyazmina, E., Miller, D., Thomas, K., 2017. Hydrogen Jet Vapor Cloud Explosion: A Model for Predicting Blast Size and Application to Risk Assessment. American Institute of Chemical Engineers 2017 Spring Meeting / 13th Global Congress on Process Safety, At San Antonio, TX.
- Kashkarov, S., Li, Z.Y., Molkov, V., 2017. Hazard distance nomograms for a blast wave from a compressed hydrogen tank rupture in a fire. 7th International Conference Hydrogen Safety. ICHS7.
- Kashkarov, S., Li, Z., Molkov, V., 2020. Blast wave from a hydrogen tank rupture in a fire in the open: Hazard distance nomograms. *Int. J. Hydrogen Energy* 45, 2429–2446. <https://doi.org/10.1016/j.ijhydene.2019.11.084>
- Kashkarov, S., Makarov, D., Molkov, V., 2018. Effect of a heat release rate on reproducibility of fire test for hydrogen storage cylinders. *International Journal of Hydrogen Energy*, *International Journal of Hydrogen Energy* 43, 10185–10192.
- Kato, M. & Launder, B.E., 1993. The modelling of turbulent flow around stationary and vibrating square cylinders. In Ninth Symposium on Turbulent Shear Flows. Kyoto, Japan, August 16-18.
- Kim, Y., Makarov, D., Kashkarov, S., Molkov, V., 2015. Modelling heat transfer in an intumescent paint and its effect on fire resistance of on-board hydrogen storage.
- Kudriakov, S. Studer, E. Kuznetsov, M. Grune, J., 2013. Experimental and numerical investigation of hydrogen-air deflagration in the presence of concentration gradients. Submitted to ICONE21, July 29- August 2, 2013, Chengdu, China. <https://doi.org/10.1115/ICONE21-16910>
- Kurenkov, A. & Oberlack, M., 2005. Modelling Turbulent Premixed Combustion Using the Level Set Approach for Reynolds Averaged Models, *Flow, Turbulence and Combustion*, 2005, 74:387–407.
- Kuznetsov, M, Alekseev, V, Bezmelnitsyn, A, Breitung, W, Dorofeev, S, Matsukov, I, Vesper, A, Yankin, Yu. 1999. Effect of obstacle geometry on behavior of turbulent flames, Report No. FZKA-6328, Forschungszentrum Karlsruhe/Preprint No. IAE-6137/3, RRC “Kurchatov Institute,” 1999.
- Kuznetsov, M, Singh, RK, Breitung, W, Stern, G, Grune, J, Friedrich, A, Sempert, K, Vesper, A., 2003. Evaluation of structural integrity of typical DN15 tubes under detonation loads. Report Forschungszentrum Karlsruhe, December 2003.
- Kuznetsov, M, Matsukov, I, Alekseev, V, Breitung, W, Dorofeev, S., 2005b. Effect of boundary layer on flame acceleration and DDT. In: *Proceedings of 20th international colloquium on the dynamics of explosions and reactive systems*, Montreal, Canada, 2005b.

D4.3. Final report on analytical, numerical and experimental studies on explosions, including innovative prevention and mitigation strategies

- Kuznetsov, M., Grune, J., Friedrich, A., Sempert, K., Breitung W. and Jordan, T. 2011. Hydrogen-Air Deflagrations and Detonations in a Semi-Confined Flat Layer, In: Fire and Explosion Hazards, Proceedings of the Sixth International Seminar (Edited by D. Bradley, G. Makhviladze and V. Molkov), 2011, pp 125-136, http://dx.doi.org/10.3850/978-981-08-7724-8_02-05
- Kuznetsov, M., Yanez, J., Grune, J., Friedrich, A., Jordan, T., 2015. Hydrogen Combustion in a Flat Semi-Confined Layer with Respect to the Fukushima Daiichi Accident, Nuclear Engineering and Design, Volume 286, May 2015, Pages 36-48
- Kuznetsov, M., Xiao, J., Hu, P., 2019. Stratified Hydrogen Combustion and Water Spray Mitigation Tests in a Containment of 220 m³, Proc. of the Ninth International Seminar on Fire and Explosion Hazards (ISFEH9), Edited by Snegirev A., Liu N.A., Tamanini F., Bradley D., Molkov V., and Chaumeix N., Published by Saint-Petersburg Polytechnic University Press, ISBN: 978-5-7422-6498-9, DOI: 10.18720/spbpu/2/k19-129, pp. 1293-1305 (2019)
- Lachance, J., Tchouvelev, A., Engebo, A., 2011. Development of uniform harm criteria for use in quantitative risk analysis of the hydrogen infrastructure. Int. J. Hydrog. Energy 36, 2381–2388. <https://doi.org/10.1016/j.ijhydene.2010.03.139>
- Laffitte P, Dumanois P. 1926. Influence of pressure on the formation of the explosive wave. Compt Rend Acad Sci Paris 1926; 183:284.
- Lafleur, C., Bran-Anleu, G., Muna, A.B., Ehrhart, B.D., Blaylock, M., Houf, W.G., 2017. Hydrogen Fuel Cell Electric Vehicle Tunnel Safety Study.
- Lamoureux., N., Djebaili-Chaumeix, N., Paillard, C.E., 2002. Laminar flame velocity determination for H₂-air-stream mixtures using the spherical bomb method, J. Phys. IV France, 12, Pr7-445-Pr7-458.
- Landau, L. D. and Lifshiz, E. M., 1986. Hydrodynamics, Edition 3, Nauka, Moscow, 1986, 736
- Landucci, G., Argenti, F., Tugnoli, A., Cozzani, V., 2015. Quantitative assessment of safety barrier performance in the prevention of domino scenarios triggered by fire. Reliab. Eng. Syst. Saf. 143, 30–43.
- Landucci, G., Gubinelli, G., Antonioni, G., Cozzani, V., 2009. The assessment of the damage probability of storage tanks in domino events triggered by fire. Accid. Anal. Prev. 41, 1206–1215.
- Lecoustre, V.R., Sunderland, P.B., Chao, B.H., Axelbaum, R.L., 2010. Extremely weak hydrogen flames. Combust. Flame 157, 2209–2210.
- Li, Y.Z., 2019. Study of fire and explosion hazards of alternative fuel vehicles in tunnels. Fire Saf. J. 110, 102871. <https://doi.org/10.1016/j.firesaf.2019.102871>
- Liang, Y. & Zeng, W., 2010. Numerical study of the effect of water addition on gas explosion. Journal of Hazardous Materials, 174(1–3), pp.386–392.
- Lindstedt, RP, Michels, HJ., 1989. Deflagration to detonation transitions and strong deflagrations in alkane and alkene air mixtures. Combust Flame 1989; 76: 169–81.

- D4.3. Final report on analytical, numerical and experimental studies on explosions, including innovative prevention and mitigation strategies
- Lundberg J., 2021. Characterization of a Medium Velocity Deluge Nozzle for Offshore Installations, *J. Loss Prev. Process Ind.* (2021), vol. 71, no. March, 104510.
- Makarov, D., Kim, Y., Kashkarov, S., Molkov, V., 2016. Thermal protection and fire resistance of high-pressure hydrogen storage, in: *Eight International Seminar on Fire and Explosion Hazards (ISFEH8)*. Hefei, China.
- Makarov, D., Hooker, P., Kuznetsov, M., Molkov, V., 2018. Deflagrations of localised homogeneous and inhomogeneous hydrogen-air mixtures in enclosures. *Int. J. Hydrog. Energy* 43, 9848–9869. <https://doi.org/10.1016/j.ijhydene.2018.03.159>
- Makarov, D., Shentsov, V., Kuznetsov, M. et Molkov, V. 2021. Hydrogen Tank Rupture in Fire in the Open Atmosphere: Hazard Distance Defined by Fireball. *Hydrogen*, vol. 2, no 1, 2021, doi: 10.3390/hydrogen2010008.
- Mangs, J., Keski-Rahkonen, O., 1994. Characterization of the Fire Behaviour of a Burning Passenger Car. Part I: Car Fire Experiments. *Fire Safety Journal* 23, 17–35.
- Miller, D., Eastwood, C.D., Kelly Thomas, J., 2015. Hydrogen jet vapour Cloud explosion: test data and comparison with predictions. In *Proceedings of the 11th Global Congress on Process Safety*; 2015.
- Moen, I. O., Donato, M., Knystautas, R., Lee, J. H. S., 1981. The influence of confinement on the propagation of detonations near the detonability limit. *Symp. (Int.) Combust.*, 18th, pp. 1615-23. Pittsburgh, Pa : Combust. Inst
- Molkov, V., Makarov, V. and Bragin, M. V., 2009. Physics and modelling of under-expanded jets and hydrogen dispersion in atmosphere, *Physics of Extreme States of Matter*, pp. 146–149.
- Molkov, V., 2012. *Fundamentals of Hydrogen Safety Engineering*. bookboon.com.
- Molkov, V. and Bragin, M., 2015. Hydrogen–air deflagrations: Vent sizing correlation for low-strength equipment and buildings, *International Journal of Hydrogen Energy*, Volume 40, Issue 2, 1256-1266.
- Molkov, V., Kashkarov, S., 2015. Blast wave from a high-pressure gas tank rupture in a fire: Stand-alone and under-vehicle hydrogen tanks. *Int. J. Hydrogen Energy* 40. <https://doi.org/10.1016/j.ijhydene.2015.07.001>.
- Molkov, V., Cirrone, D., Shentsov, V., Dery, W., Kim, W., Makarov, D., 2018a. Blast wave and fireball after hydrogen tank rupture in a fire, in: *Advances in Pulsed and Continuous Detonations*.
- Molkov, V., Makarov, D., Kashkarov, S., 2018b. Composite Pressure Vessel for Hydrogen Storage. PCT International Application P119851PC00.
- Molkov, V., Dery, W. 2020. The blast wave decay correlation for hydrogen tank rupture in a tunnel fire, *International Journal of Hydrogen Energy*, 31289-31302

- D4.3. Final report on analytical, numerical and experimental studies on explosions, including innovative prevention and mitigation strategies
- Molkov, V., Dadashzadeh, M., Kashkarov, S., Makarov, D., 2021. Performance of hydrogen storage tank with TPRD in an engulfing fire. *Int. J. Hydrog. Energy*.
<https://doi.org/10.1016/j.ijhydene.2021.08.128>
- Molkov, V., Cirrone, D., Shentsov, V., Dery, W., Kim, W., Makarov, D., 2021b. Dynamics of blast wave and fireball after hydrogen tank rupture in a fire in the open atmosphere. *International Journal of Hydrogen Energy*, Volume 46, Issue 5, 2021, Pages 4644-4665,
- Momferatos, G., Giannissi, S.G., Tolia, I.C., Venetsanos, A.G., Vlyssides, A. & Markatos, N., 2021. Vapor cloud explosions in various types of confined environments: CFD analysis and model validation. *Loss Prevention and Safety Promotion in the Process Industries*, accepted.
- National Highway Traffic Safety Administration (NHTSA), 2015. Traffic safety facts 2015: a compilation of motor vehicle crash data from the fatality analysis reporting system and the general estimates system.
- NJ, 2019. WATCH: Garbage truck explodes in fireball, rips hole in nearby house [WWW Document]. NJ.com.URL
https://www.nj.com/mercer/2016/01/garbage_truck_explosion_damages_hamilton_house.html (accessed 6.1.19).
- Nylon 12, 2020. Wikipedia. Overview of materials for High Density Polyethylene (HDPE), Extruded [WWW Document], URL
<http://www.matweb.com/search/DataSheet.aspx?MatGUID=482765fad3b443169ec28fb6f9606660> (accessed 11.22.17).
- Particle Master Shadow, Product-Manual for DaVis 10.1, LaVision GmbH, Göttingen, 2020.
- Payri, F., Pastor, J.V., Payri, R., Manin, J.. Determination of the optical depth of a DI diesel spray. *J Mech Sci Technol* **25**, 209–219 (2011). <https://doi.org/10.1007/s12206-010-1024-x>
- Papoulis, A., 1965. Probability, random variables, and stochastic processes, 3rd ed., New York: McGraw-Hill.
- Reliability Analysis Centre, 1991. Non electronic parts reliability data.
- Reynolds, W.C., The Element Potential Method for Chemical Equilibrium Analysis: Implementation in the Interactive Program STANJAN Version 3, Dept. of Mechanical Engineering, Stanford University, Palo Alto, California, January 1986.
- Road Tunnel Association (RTA), 2019. UK & Eire Road Tunnel Directory [WWW Document]. URL UK & Eire Road Tunnel Directory (accessed 6.28.19).
- Roberts, AF., 1981. Thermal radiation hazards from releases of LPG from pressurised storage. *Fire Safety Journal*, 4, pp. 197–212.
- Royle, M., Willoughby, D.B., 2010. Consequences of catastrophic releases of ignited and unignited hydrogen jet releases. *Int. J. Hydrogen Energy* 36, 2688–2692.
<https://doi.org/10.1016/j.ijhydene.2010.03.141>

- D4.3. Final report on analytical, numerical and experimental studies on explosions, including innovative prevention and mitigation strategies
- Rudy, W. Kuznetsov, M. Porowski, R. Teodorczyk, A. Grune, J. Sempert, K., 2013. Critical conditions of hydrogen–air detonation in partially confined geometry. Proceedings of the Combustion Institute, Volume 34, Issue 2, 2013, Pages 1965-1972, ISSN 1540-7489
- SAE J2601, 2016. SURFACE VEHICLE STANDARD (No. (R) Fuelling Protocols for Light Duty Gaseous Hydrogen Surface Vehicles).
- Sauzedde, F., Martin, M. Forero, D. Studer, E., 2020. CEA Experimental devices Tests of 2020. HYTUNNEL-CS project report, 2020
- Sauzedde, F., Martin, M. Forero, D. Studer, E., 2021. CEA Experimental devices Tests of 2021. HYTUNNEL-CS project report, 2021
- Schwer, D.A. & Kailasanath, K., 2007. Numerical simulations of the mitigation of unconfined explosions using water-mist. Proceedings of the Combustion Institute, 31 II(2), pp.2361–2369.
- Shen, C., Ma, L., Huang, G., Wu, Y., Zheng, J., Liu, Y., Hu, J., 2018. Consequence assessment of high-pressure hydrogen storage tank rupture during fire test. J. Loss Prev. Process Ind. 55, 223–231. <https://doi.org/10.1016/j.jlp.2018.06.016>
- Shentsov, V., Makarov, D., Dery, W., 2019. Stand-alone hemisphere-tank rupture in tunnel fire: effect of hydrogen inventory on blast wave strength in far field, in: 9th International Seminar on Fire and Explosion Hazards (ISFEH9). 21-26 April 2019, Saint Petersburg, Russia.
- Shentsov, V., 2020. Effect of blast wave after tank rupture in a fire on a tunnel structure. Digital Stakeholder' Workshop (HyTunnel-CS project), 4-5 May 2020.
- Skjeltorp, A., 1968. One-Dimensional Blast Wave Propagation (No. FORTIFIKATORISK NOTAT-48/69). NORWEGIAN DEFENCE CONSTRUCTION SERVICE OSLO OFFICE OF TEST AND DEVELOPMENT.
- Song, Y. & Zhang, Q., 2019. Quantitative research on gas explosion inhibition by water mist. Journal of Hazardous Materials, 363, pp.16–25
- Takeno, K., 2019. Private communication.
- Takeno, K., Okabayashi, K., Kouchi, A., Nonaka, T., Hashiguchi, K., Chitose, K., 2007. Dispersion and explosion field tests for 40 MPa pressurized hydrogen 32, 2144–2153. <https://doi.org/10.1016/j.ijhydene.2007.04.018>
- Tamura, Y., Takahashi, M., Maeda, Y., Mitsuishi, H., Suzuki, J., Watanabe, S., 2006. Fire Exposure Burst Test of 70MPa Automobile High-pressure Hydrogen Cylinders, in: Society of Automotive Engineers of Japan Annual Autumn Congress 2006. Presented at the Society of Automotive Engineers of Japan Annual Autumn Congress 2006, Sapporo.
- Teodorczyk, A., Lee, J.H., Knystautas, R., 1988. Propagation mechanism of quasi-detonations. 22nd Symposium (Int.) on Combustion. The Combustion Institute, Pittsburgh, pp 1723–1731.

- D4.3. Final report on analytical, numerical and experimental studies on explosions, including innovative prevention and mitigation strategies
- Thomas, G., 2000. On the conditions required for explosion mitigation by water sprays. *Process safety and environmental protection* 78(5): 339-354.
- Today, 2016. Caught on Camera: Natural-gas powered garbage truck explodes [WWW Document]. Today. URL <https://www.today.com/video/caught-on-camera-natural-gas-powered-garbage-truck-explodes-609780803613> (accessed 6.1.19).
- Tolias, I. C. and A. G. Venetsanos, 2018. An improved CFD model for vented deflagration simulations – Analysis of a medium-scale hydrogen experiment. *International Journal of Hydrogen Energy* 43(52): 23568-23584.
- Tolias, I. C. and A. G. Venetsanos, 2019. Evaluation of an improved vented deflagration CFD model against nine experimental cases. 8th International Conference on Hydrogen Safety (ICHS2019). Adelaide, Australia.
- Tolias, I.C., Venetsanos, A.G., Kuznetsov, M. & Koutsoukos, S., 2020. Evaluation of an improved CFD model against nine vented deflagration experiments. *International Journal of Hydrogen Energy*, 46(23), pp.12407–12419
- Tolias, I.C. & Venetsanos, A.G., 2018. An improved CFD model for vented deflagration simulations – Analysis of a medium-scale hydrogen experiment. *International Journal of Hydrogen Energy*, 43(52), pp.23568–23584.
- United Nations Economic Commission for Europe, 2013. Global Registry. Addendum 13: Global technical regulation No. 13. Global technical regulation on hydrogen and fuel cell vehicles. UNECE.
- van Wingerden K., Wilkins B., Bakken J., and Pedersen G., 1995. The Influence of Water Sprays on Gas Explosions. Part 2: Mitigation, *J. Loss Prev. Process Ind.* (1995), vol. 8, no. 2, 61–70.
- Vågsæther, K, 2010. Modelling of gas explosions, PhD Thesis, <http://hdl.handle.net/11250/2437792>
- Venetsanos, A., E. Papanikolaou and J. Bartzis, 2010. The ADREA-HF CFD code for consequence assessment of hydrogen applications. *International Journal of Hydrogen Energy* 35(8): 3908-3918.
- Verbecke, F., Molkov, V. and Makarov, D., 2009. VLES of lean hydrogen-air deflagrations in a closed vessel 5.7 m high, *International Conference on Hydrogen Safety*, Ajaccio 2009.
- Veser, A. Breitung, W. Dorofeev, S. B., 2002. Run-up distances to supersonic flames in obstacle-laden tubes, *J. Phys. IV France*, 12, No 7, 2002, pp333-340, <https://doi.org/10.1051/jp4:20020301>
- Webster, C., 2010. Localized Fire Protection Assessment for Vehicle Compressed Hydrogen Containers (Final No. DOT HS 811 303).
- Weyandt, N., 2006. Vehicle bonfire to induce catastrophic failure of a 5000-psig hydrogen cylinder installed on a typical SUV. Southwest Research Institute report for the Motor Vehicle Fire Research Institute.

D4.3. Final report on analytical, numerical and experimental studies on explosions, including innovative prevention and mitigation strategies

- Weyandt, N., 2005. Analysis of Induced Catastrophic Failure Of A 5000 psig Type IV Hydrogen Cylinder (No. 01.06939.01.001). Southwest Research Institute report for the Motor Vehicle Fire Research Institute.
- Yakhot, V., 1988. Propagation velocity of premixed turbulent flames. Comb. Sci. Tech., 60, 191, 1988.
- Yakhot, V. and Orszag, S. A., 1986. Renormalization Group Analysis of Turbulence, J. Sci. Comput. , vol. 1, no. 1, 1–51.
- Ye, J., Chen, Z., Fan, B. & Xie, B., 2005. Suppression of methane explosions in a field-scale pipe. Journal of Loss Prevention in the Process Industries, 18(2), pp.89–95.
- Yoshida, A., Okawa, T., Ebina, W. & Naito, H., 2015. Experimental and numerical investigation of flame speed retardation by water mist. Combustion and Flame, 162(5), pp.1772–1777.
- Zabetakis, M.G., 1964. Flammability characteristics of combustible gases and vapors (No. BM--BULL-627, 7328370). <https://doi.org/10.2172/7328370>
- Zalosh, R., Weyandt, N., 2005. Hydrogen fuel tank fire exposure burst test. SAE Pap. 2005-01-1886.
- Zimont, V.L. and Lipatnikov, A.N., 1995. A numerical model of premixed turbulent combustion of gases, Chem. Phys. Reports, Vol. 14(7), 993-1025.

Appendices

A1. Scaling criteria

The objective of a steady state scaled experiment is to match the concentration of hydrogen in the downstream flow and the proportion of the tunnel over which the flow is distributed. The defined variables are described in Figure 165.

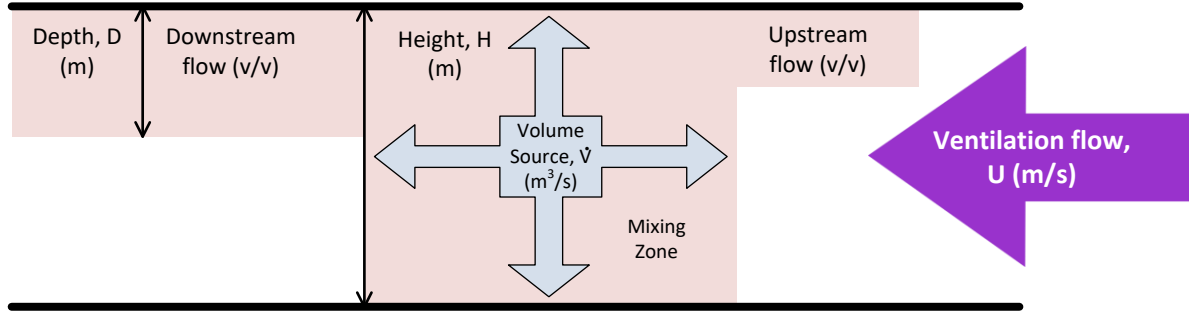


Figure 165. Schematic diagram showing modelling of jet and tunnel ventilation interactions.

$$C_{model} = C_{fullscale} \quad (72)$$

$$\frac{D_{model}}{H_{model}} = \frac{D_{fullscale}}{H_{fullscale}} \quad (73)$$

Assume there is a mixing zone, of limited size, around the source where the flow is dominated by source momentum. Outside this zone, the flow is controlled by the interaction between the buoyant gas and the tunnel flow.

If the downstream flow occupies the same proportion of the model as in the full scale tunnel area then mass conservation gives:

$$C \propto \frac{\dot{V}}{UH^2} \quad (74)$$

Since hydrogen is very light, the density difference associated with the downstream flow is:

$$\frac{\Delta\rho}{\rho_0} \sim C \quad (75)$$

If $\Delta P_{buoyancy}$ is the buoyancy head associated with the flow:

$$\Delta P_{buoyancy} \propto Hg\rho_0 C \quad (76)$$

D4.3. Final report on analytical, numerical and experimental studies on explosions, including innovative prevention and mitigation strategies

The dynamic head associated with the tunnel flow is:

$$\Delta P_{tunnel\ flow} \propto \rho_0 U^2 \quad (77)$$

If these are in the same proportion, then the tendency for back flow and the stability of the downstream layer will be matched for the model and full-scale flow when:

$$\rho_0 U^2 \propto H g \rho_0 C \quad (78)$$

$$Or \quad C \propto \frac{U^2}{H} \quad (79)$$

This equation implies that the tunnel flow speed should be scaled as \sqrt{H} .

$$U \propto \sqrt{H} \quad (80)$$

Combining this with (74) gives

$$\dot{V} \propto H^{5/2} \quad (81)$$

A1.1 Matching the mixing zone by choice of source momentum

The velocities associated with a jet source with a momentum flux, M , vary with scale as

$$M \propto H^2 U_{source}^2 \quad (82)$$

The edge of the mixing zone corresponds to locations where $U_{source} \sim U_{tunnel}$

The mixing zones will have similar shapes at different scales if

$$U_{source} \propto \frac{\sqrt{M}}{H} \propto U_{tunnel} \quad (83)$$

$$Since \quad U_{tunnel} \propto \sqrt{H} \quad (84)$$

This means that the mixing zones will be similar if

$$M \propto H^3 \quad (85)$$

D4.3. Final report on analytical, numerical and experimental studies on explosions, including innovative prevention and mitigation strategies

In summary, the appropriate scaling relationships between the tunnel flow, U , the hydrogen volume flow, \dot{V} , and the tunnel diameter, H , for a *steady* release experiment in a model tunnel is:

$$U \propto H^{\frac{1}{2}} \quad (86)$$

$$\dot{V} \propto H^{\frac{5}{2}} \quad (87)$$

If U and \dot{V} are chosen in this way then the concentration in the flow, developing around the source will be the same and the relationship between the buoyancy head associated with the release and the dynamic head of the flow will be the same. This means there will be a similar tendency for the gas to be blown down stream or flow backwards at high level.